UNIVERSIDAD COMPLUTENSE DE MADRID
FACULTAD DE CIENCIAS QUÍMICAS

TESIS DOCTORAL

Dinámica y Estereodinámica de la Fotodisociación Molecular por Cartografía y Tomografía de Imágenes de Iones

Dynamics and Stereodynamics of Molecular Photodissociation by Slice and Velocity Map Ion Imaging

MEMORIA PARA OPTAR AL GRADO DE DOCTOR

PRESENTADA POR

Javier Cachón Ortiz

DIRIGIDA POR

Luis Bañares Morcillo
Pedro Recio Ibáñez

Madrid

UNIVERSIDAD COMPLUTENSE DE MADRID
FACULTAD DE CIENCIAS QUÍMICAS

Dinámica y Estereodinámica de la Fotodisociación Molecular por Cartografía y Tomografía de Imágenes de Iones

Dynamics and Stereodynamics of Molecular Photodissociation by Slice and Velocity Map Ion Imaging

TESIS DOCTORAL

Javier Cachón Ortiz

Directores

Luis Bañares Morcillo

Pedro Recio Ibáñez

Madrid, 2024

UNIVERSIDAD COMPLUTENSE DE MADRID

FACULTAD DE CIENCIAS QUÍMICAS

Programa de doctorado en Química Avanzada

Dinámica y Estereodinámica de la Fotodisociación Molecular por Cartografía y Tomografía de Imágenes de Iones

Dynamics and Stereodynamics of Molecular Photodissociation by Slice and Velocity Map Ion Imaging

TESIS DOCTORAL

Javier Cachón Ortiz

Directores

Luis Bañares Morcillo

Pedro Recio Ibáñez

Madrid, 2024

Abstract/Resumen

This Doctoral Thesis falls within the field of Molecular Dynamics of Chemical Reactions. It focuses on the dynamics of molecular photodissociation, where a chemical bond is broken due to photon absorption. While seemingly simple, this process can become complex, involving multiple potential energy surfaces and interactions between electronic states, such as non-adiabatic couplings and conical intersections. This complexity results in multidimensional problems and varied reaction pathways after photon absorption.

The present research employs nanosecond pulsed lasers combined with pump (excitation) and probe (detection) techniques on molecular beams, along with ion imaging methods. The molecular beam, comprising the molecule under study and a carrier gas, is intersected by two laser pulses. The first pulse excites and dissociates the molecule, and the second pulse ionizes the resulting fragments. Resonant multiphoton ionization is used to enhance absorption cross-sections of multiple photons. The ions generated are extracted and detected using a position sensitive detector (microchannel plate) and a phosphor screen to produce ion images which contain all the dynamical and stereodynamical information about the photodissociation process.

Experimental observables, such as identifying reaction products, determining quantum states, measuring absorption cross-sections, and analyzing energy and angular distributions, help determine dissociation pathways and reaction mechanisms. Theoretical calculations of electronic structures of the molecules under study further aid in elucidating these mechanisms, verifying the accuracy of the theoretical models and potential energy surfaces.

Key findings of the present work include the ultraviolet photodissociation dynamics of methylamine (CH_3NH_2) into H-atom, and CH_3 and NH radical fragments and a comparative study of the stereodynamics of various alkyl iodides and bromo-iodomethane by looking at atomic fragment alignment. The thesis concludes with significant insights into molecular dynamics and stereodynamics, and the validation of theoretical models.

Esta Tesis Doctoral se enmarca en el campo de la Dinámica Molecular de Reacciones Químicas. Esta se centra en la dinámica de la fotodisociación molecular, un proceso en el cual un enlace químico se rompe debido a la absorción de un fotón. Aunque aparentemente simple, este proceso puede volverse complejo, ya que involucra múltiples superficies de energía potencial e interacciones entre estados electrónicos, como los acoplamientos no adiabáticos e intersecciones cónicas. Esta complejidad da lugar a problemas multidimensionales y a diversas vías de reacción tras la absorción del fotón.

La investigación presentada en esta tesis emplea láseres pulsados de nanosegundos combinados con técnicas de bomba (excitación) y sonda (detección) en haces moleculares, junto con métodos de formación de imágenes de iones. El haz molecular, que contiene la molécula en estudio y un gas portador, es alcanzado por dos pulsos láser. El primer pulso excita y disocia la

molécula, mientras que el segundo ioniza los fragmentos resultantes. Se utiliza ionización multifotónica resonante para mejorar la sección eficaz de absorción de múltiples fotones. Los iones generados son extraídos y detectados mediante un detector sensible a la posición (placa de microcanales) y una pantalla de fósforo, produciendo imágenes de iones que contienen toda la información dinámica y estereodinámica sobre el proceso de fotodisociación.

Las magnitudes experimentales observables, como la identificación de los productos de reacción, la determinación de los estados cuánticos, la medición de secciones eficaces de absorción y el análisis de las distribuciones de energía y ángulos, permiten determinar las vías de disociación y los mecanismos de reacción. Además, los cálculos teóricos de estructuras electrónicas de las moléculas en estudio contribuyen a esclarecer estos mecanismos y a verificar la precisión de los modelos teóricos y las superficies de energía potencial calculadas.

Los principales hallazgos de este trabajo incluyen el estudio de la dinámica de fotodisociación ultravioleta de la metilamina (CH_3NH_2) en fragmentos radicales H, CH_3 y NH, así como un estudio comparativo de la estereodinámica de diversos yoduros de alquilo y del bromoyodometano, analizando la alineación de los fragmentos atómicos. La tesis concluye con importantes aportes a la comprensión de la dinámica molecular y estereodinámica, además de la validación de modelos teóricos.

Agradecimientos

Quiero expresar mi sincero agradecimiento a mi director de Tesis, Luis Bañares, por su orientación, conocimientos y apoyo a lo largo de este proceso. Su dedicación y guía han sido fundamentales para mi desarrollo académico y poder terminar esta tesis. También agradezco a Pedro Recio, mi co-director de Tesis, y a Sonia Marggi Poullain, que me aconsejaron y ayudaron tanto en los análisis como en el laboratorio, en los momentos clave. Su apoyo ha sido decisivo para el progreso de mi investigación.

A mis compañeros de universidad, David, Nacho, Kushal, Mariu, gracias por trabajar junto a mí y las pausas para comer, especialmente después de haber estado más en soledad debido al haber empezado cuando aún había cierto riesgo del bicho. Espero que vuestros futuros académicos o de otro tipo, os lleven a buen puerto.

A mis compañeros de piso presentes y pasados, Sergio, Pedro, Jaime, Cris, Enzo y Berto, les agradezco el haberme acompañado en el viaje de independencia y cambio de ciudad (además de la formación del *ghetto* cántabro en Madrid). Espero que todo lo que hemos compartido aquí se traslade allá donde quiera que terminemos todos. Al resto de mis amigos, gracias por estar siempre presentes al volver a Santander, apoyándome desde la distancia.

A Javier y Mariela, cuya amistad se forjó a partir de los famosos “martes de jazz” que tan poco tiempo duraron, pero que intensos fueron. El tiempo pasado jugando a la brisca o debatiendo cosas de física en la cafetería han llevado hasta este punto. Después habrá que ir al CDs a por una cerveza.

Finalmente, y con la mayor importancia, a mis padres. Os agradezco profundamente vuestro respaldo incondicional y vuestra constante motivación. Sin vuestro apoyo, todo este trabajo no habría sido posible. Se que uno de los dos se quedará más tranquilo una vez esté terminado este trabajo (Al otro no creo que le preocupe demasiado). No me olvido del resto de mi familia; hermano, tíos, primos, y demás relaciones de parentesco extrañas que han aportado su granito de arena estando conmigo o simplemente preguntando de vez en cuanto.

Chapter 1 Introduction

1.1. General introduction

This Doctoral Thesis is centred around the realm of Molecular Dynamics of Chemical Reactions. The research focuses on identifying various molecular-level observables that provide comprehensive insights into the fundamental mechanisms of chemical reactions, typically involving the formation or breaking of chemical bonds.

Among the diverse processes in Molecular Dynamics, this Thesis specifically examines the dynamics of molecular photodissociation. Photodissociation involves breaking a chemical bond upon absorption of one or more photons, being interpreted as a half-collision process. While this process might appear straightforward when considered within a single electronically excited state of the molecule and a single reaction coordinate, which requires only the energy of the absorbed photon to surpass the bond energy, the reality is usually more difficult to analyse. Depending on the molecule's complexity, multiple potential energy surfaces linked to different electronic states may be involved, making the dynamics of the molecule a multidimensional problem. Additionally, interactions between different excited potential energy surfaces, such as non-adiabatic couplings and conical intersections between various electronic states, can further complicate the photodissociation process, creating multiple reaction pathways depending on the potential energy landscape of the molecule. This process can also involve redistribution of the available energy after absorption of one or more photons among the various degrees of freedom of the molecule.

To study molecular photodissociation dynamics, numerous techniques can be employed. In this Thesis, nanosecond pulsed lasers are used in conjunction with the pump (excitation) and probe (detection) technique on a molecular beam, combined with ion imaging methods. The molecular beam, consisting of the molecule under study (parent molecule) and a carrier gas, typically a noble gas, is intersected by the two laser pulses in a pump-probe experiment. The initial pump pulse excites and dissociates the molecule, creating a distribution of photoproducts. Later, after a short delay time, the probe pulse ionizes one or more fragments arising from the photodissociation process. A resonant multiphoton ionization scheme of defined quantum states is generally employed to enhance the photoionization cross-section. The resulting ions are extracted using an electric field and detected with position-sensitive microchannel plates (MCP) coupled to a phosphor screen, and the phosphorescence detected by a charge couple device (CCD) camera. This results on velocity-map imaging or slice imaging experiments.

The experimental observables provide a reflection of the photodissociation process under study. Identifying reaction products, determining their quantum states, measuring absorption cross-sections, and kinetic energy and angular distributions of the fragments, determining the lifetimes of the excited states, and obtaining the adiabatic ionization energy (AIE) are all crucial properties in identifying the dissociation pathways taken by the molecule, the evolution of the generated wave packet, and identifying conical intersections (CIs) and non-adiabatic couplings between electronic states, to resolve the reaction mechanisms. Furthermore, elucidating these

mechanisms is supported by indispensable theoretical calculations of the electronic structure of the studied molecules. This joint approach also serves to validate the accuracy and reliability of the theoretical calculations and models, which will subsequently influence the precision of new potential energy surfaces found for the molecules under study.

The PhD Thesis is organized in the following chapters:

Chapter 1. Introduction. This chapter introduces the most relevant concepts of molecular photodissociation, detailing the most relevant observables such as kinetic energy and angular distributions, and molecular photoionization.

Chapter 2. Methodology. This chapter details the experimental setups used to carry out the experiments. These setups include the nanosecond pulsed laser systems, the velocity map ion imaging apparatuses, as well as the fundamentals of each technique employed.

Chapter 3. Results on the dynamics and stereodynamics of molecular photodissociation. This chapter first presents the results obtained for the ultraviolet (UV) photodissociation of methylamine (CH_3NH_2) into different fragment channels, including H, CH_3 and NH. By examining its molecular dynamics and thus the different dissociation channels and the time of action, information about the quantum structure and photochemistry of the molecule is readily obtained. Following this, the results of the stereodynamics study, in particular the atomic fragment alignment, comparing several alkyl iodides (RI) and bromo-iodomethane (CH_2BrI) are shown. In these molecules, special attention is paid to the analysis of the iodine atom fragment alignment parameters, so that by obtaining experimental measurements using all possible combination of the linear polarization of the incident electric field of both the excitation laser and the probe laser, their stereodynamical information is obtained.

Chapter 4. General conclusions. This chapter presents the most important conclusions reached in this Doctoral Thesis.

1.2. Fundamentals of Molecular Photodissociation

Molecular photodissociation is a common consequence of the absorption of one or several photons by a molecule. Upon absorption, the molecule reaches a higher energy state which allows it to either suffer a dissociative process, ionize through dissociative ionization processes, or release this energy via a deactivation process that may be radiative, such as fluorescence or phosphorescence, or non-radiative (including internal conversion, intersystem crossing, or vibrational relaxation). The discussion in this Thesis is centered on electronic dissociation processes. Specifically, we center in those processes where a standard molecule AB, in its fundamental electronic state, is excited to a higher electronic state AB*, through the absorption of visible or ultra-violet (UV) radiation $nh\nu$, which represents *n* photons of energy $h\nu$. This absorption may result in the dissociation of the molecule into fragments in specific quantum states, as described by the following reaction:

$$\mathrm{AB} + nh\nu \rightarrow \mathrm{AB}^* \rightarrow \mathrm{A}(\alpha) + \mathrm{B}(\beta) \qquad (1.1)$$

where, $\mathrm{A}(\alpha)$ and $\mathrm{B}(\beta)$ are either atomic or molecular fragments formed in specific quantum states (electronic, vibrational, and rotational) α and β, respectively. Likewise, in a non-dissociative molecular photoionization process, the fragments produced are typically an ion (the cation of the molecule that absorbed the photon) and an electron extracted after ionization.

For photodissociation to take place, the photon's energy absorbed must exceed the energy of any bond within the molecule. The molecular bond is, then, prone to breakage through a complex process where the absorbed energy is redistributed across the molecule's various degrees of freedom. This redistribution leads to the formation of fragments, each in specific quantum states and possessing defined kinetic energy. The allocation of this energy among the fragments adheres to the principle of energy conservation. As a result, the energy provided by the photon or photons, along with the internal energy of the starting molecule, will be used to break the bond, select the quantum states of the generated fragments, and supply them with a certain amount of kinetic energy.

If the photons provide enough energy to produce fragments in various quantum states, it is possible for a single fragment to appear in two distinct quantum states. This occurrence results in several dissociation pathways. In each pathway, the fragments are propelled in different directions of the space, originating from a common point, the center-of-mass of the original molecule, to conserve linear momentum with a velocity vector of constant magnitude. The three-dimensional distribution of fragments is referred to as Newton's sphere, which will be further detailed in the following.

1.2.1. Types of Molecular Photodissociation

Photodissociation processes are dependent on the quantum structure of the molecule, meaning that the dynamics observed will be different for quantum levels of both the initial state of the molecule and the final states of the fragments. According to the possible multiple electronic states present for the molecule, a wide range of scenarios are possible. Therefore, photodissociation processes can be categorized into two main types based on the molecular electronics state's relevant in the dissociation [1].

One of the simplest photodissociation processes involves a repulsive excited electronic state. The dissociation process takes the generic molecule AB in its ground electronic state to a repulsive excited state after absorption of a photon. The excited molecule, AB*, will rapidly dissociate through this repulsive state into products A and B in their respective quantum states. Known as *direct photodissociation*, this process is illustrated in Figure 1.1. Typically, the absorbed photon has a wavelength in the UV region for polyatomic molecules, and its energy must be sufficient so that the sum of the photon's energy and the molecule's internal energy (E_{int}) exceeds the bond dissociation energy, D_0. This process produces fragments with high kinetic energy and occurs very quickly, typically within a timescale shorter than a single vibrational period of the molecule, around several tens of femtoseconds (1 fs = 10^{-15} s) [2].

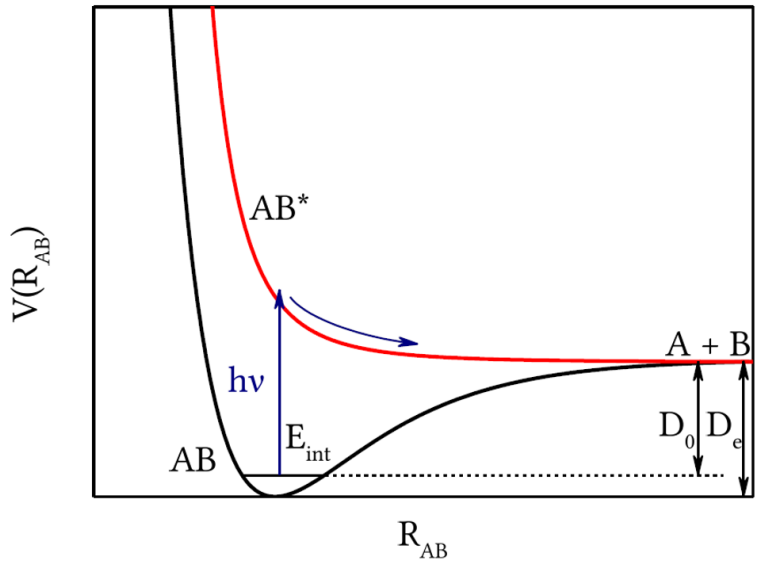

FIGURE 1.1: *SCHEMATIC REPRESENTATION OF A DIRECT PHOTODISSOCIATION PROCESS. A GENERIC MOLECULE AB IN ITS GROUND ELECTRONIC STATE (BLACK CURVE) ABSORBS A PHOTON WITH ENERGY* $h\nu$*, AND IT IS EXCITED, AB*, TO A REPULSIVE EXCITED ELECTRONIC STATE (RED CURVE), LEADING TO THE FORMATION OF REACTION PRODUCTS A AND B IN SPECIFIC QUANTUM STATES.* D_e *REPRESENTS THE DISSOCIATION ENERGY OF THE MOLECULE FROM THE MINIMUM OF THE POTENTIAL ENERGY CURVE, WHILE* D_0 *IS THE DISSOCIATION ENERGY ACCOUNTING FOR THE MOLECULE'S INTERNAL ENERGY (ZERO-POINT ENERGY). FIGURE ADAPTED FROM [3].*

Direct photodissociation processes can manifest within a single bound electronic state if the photon energy surpasses the bond dissociation energy (D_0). Figure 1.2 presents scenarios where direct dissociation occurs within a single bound state, the ground state. In Figure 1.2(a), the molecule AB absorbs a high energy photon, promoting it to vibrational overtones that lie above the dissociation energy threshold, thereby inducing dissociation into fragments A and B. Figure 1.2(b) illustrates the multiphoton absorption process involving a specific number of infrared (IR) photons. As the selection rules governing ro-vibrational transitions near the dissociation threshold, which constitute a quasi-continuum, become less strict, multiphoton excitation to these states becomes available.

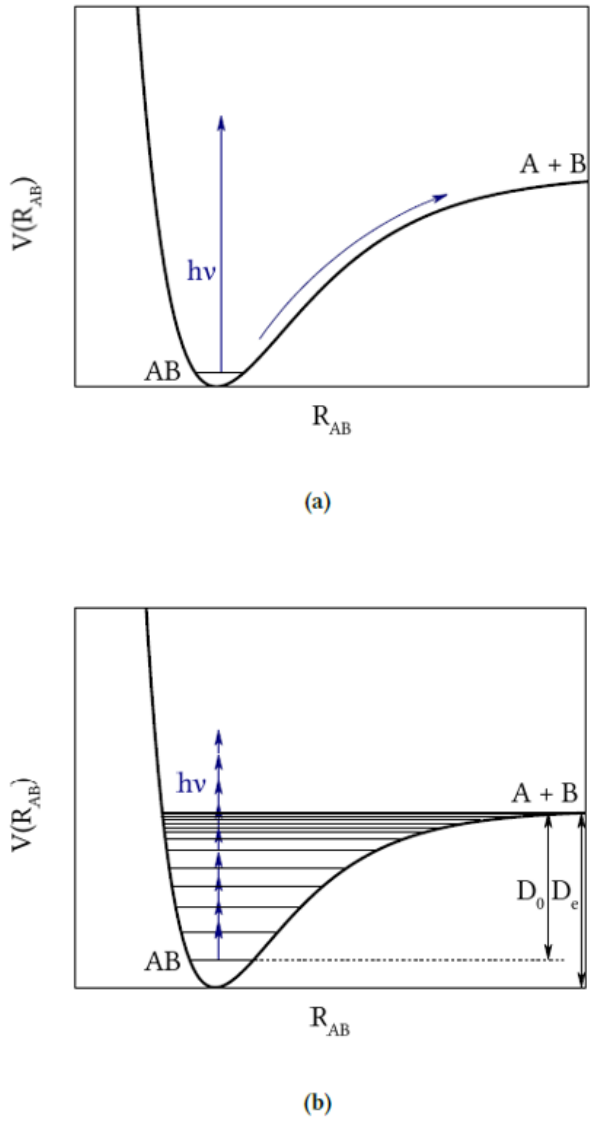

FIGURE 1.2: *SCHEMATIC REPRESENTATION OF DIRECT PHOTODISSOCIATION IN A SINGLE ELECTRONIC STATE, THE GROUND ELECTRONIC STATE, RESULTING FROM EITHER (A) ABSORPTION OF A HIGH ENERGY PHOTON THAT EXCEEDS THE BINDING ENERGY OR (B) ABSORPTION OF A HIGH NUMBER OF PHOTONS IN THE INFRARED (IR) RANGE THROUGH MULTIPHOTON ABSORPTION. FIGURE ADAPTED FROM [3].*

The second category of dissociative processes involves those with a potential barrier that the system must overcome to achieve dissociation. These processes are known as *indirect photodissociation*. Upon absorbing one or more photons, the molecule AB is excited to a metastable electronic state, characterized by a local energy minimum. The evolution of the excited molecule (AB*) dictates the specific dissociation mechanism that occurs.

If the bound excited state is coupled with a repulsive electronic state, photodissociation occurs through non-adiabatic coupling between these states. This coupling allows the excited molecule AB* to evolve and dissociate via the repulsive state. The mechanism, known as *electronic predissociation* (illustrated in Figure 1.3(a)), occurs over longer timescale than direct dissociation. The process is directly related to the transition probability from the bound state to the repulsive state, which is determined by the coupling strength between these two states.

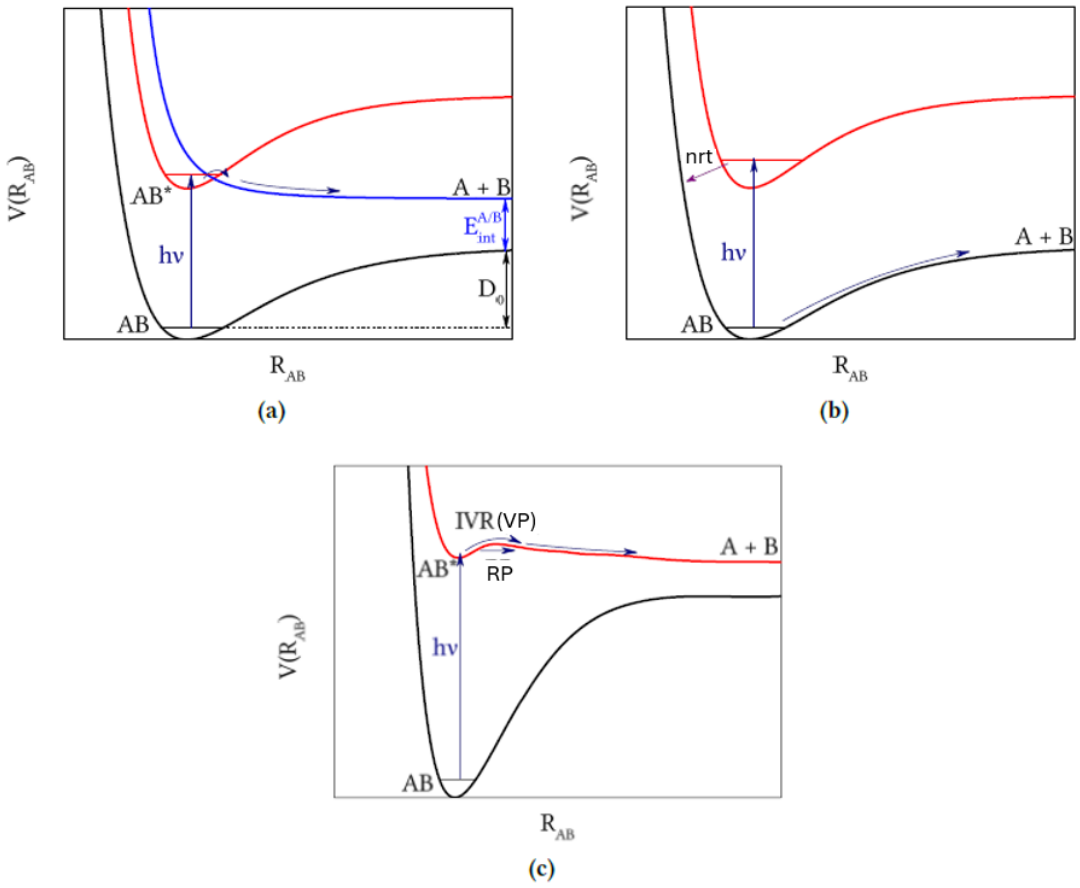

FIGURE 1.3: *SCHEMATIC REPRESENTATION OF INDIRECT PHOTODISSOCIATION MECHANISMS. IN (A), AN ELECTRONIC PREDISSOCIATION IS SHOWN WHERE AN EXCITED BOUND STATE (RED CURVE), POPULATED BY THE ABSORPTION OF A PHOTON WITH ENERGY* $h\nu$*, IS COUPLED WITH A REPULSIVE ELECTRONIC STATE (BLUE CURVE) THROUGH WHICH DISSOCIATION OCCURS. IN (B), THE MOLECULE IS EXCITED TO A BOUND STATE THAT IS NOT COUPLED WITH ANY REPULSIVE STATE, SO THE ONLY DISSOCIATION PATHWAY IS THROUGH INTERNAL CONVERSION VIA A NON-RADIATIVE TRANSITION (NRT) TO THE GROUND STATE, WHICH THEN DISSOCIATES. IN (C), VIBRATIONAL (VP) OR ROTATIONAL (RP OR TUNNELING EFFECT) PREDISSOCIATION OCCURS DUE TO EXCITATION TO A QUASI-BOUND STATE. FIGURE ADAPTED FROM [3].*

Conversely, if the excited state lacks coupling with any repulsive electronic state, and the photon's energy falls short of the excited state's barrier, internal conversion may take place, as illustrated in Figure 1.3(b). This is typically facilitated by conical intersections, enabling a non-radiative transition to the ground state, which subsequently dissociates to form the products A and B. The process adheres to the principles of energy conservation, dictating that the electronic energy held by the molecule AB* must be conserved into vibro-rotational energy of the ground state, significantly exceeding the state's dissociation energy.

The last possibility of indirect dissociation is shown in Figure 1.3(c). Here, the molecule absorbs a photon which is excited to a quasi-bound state, where a small potential barrier prevents the bond from breaking. The molecule may then dissociate through one of two

pathways: either by redistributing its intramolecular vibrational energy among its various degrees of freedom (vibrational predissociation, VP) or by tunneling effect (rotational predissociation, RP). The lifetime of this mechanism depends on the efficiency of vibrational energy transfer or, in the case of tunneling, on the width of the barrier.

1.2.2. Kinematics of Molecular Photodissociation

If we consider equation (1.1), which depicts an AB molecule absorbing a photon with energy $h\nu$ and transitioning to an electronically excited state before dissociating into fragments A and B, the energy balance can be expressed by the following equation:

$$E_{\text{int}}\,(AB) + E_{tr}(AB) + nh\nu = E_{\text{int}}\,(A) + E_{\text{int}}\,(B) + E_{tr}(A) + E_{tr}(B) + D_0 \qquad (1.2)$$

where D_0 represents the bond energy between A and B (dissociation energy), E_{int} denotes the internal energy of the parent molecule or its resulting fragments, E_{tr} refers to their translational energy, and $nh\nu$ is the energy provided by the n photons involved in the absorption process [4].

Considering certain criteria, the equation mentioned can be simplified as follows: $E_{\text{int}}\,(AB)$, the internal energy of the AB molecule, can be considered negligible because it is part of a molecular beam where supersonic expansion cools the internal ro-vibrational degrees of freedom to very low temperatures. Furthermore, by selecting the center-of-mass (CM) coordinate system, $E_{tr}(AB)$ is set to zero. With these simplifications, the total available energy of the system, E_{disp} , can be defined as:

$$E_{\text{disp}} = nh\nu - D_0 = E_{\text{int}}\,(A) + E_{\text{int}}\,(B) + E_{\text{tr}}\,(A) + E_{tr}(B) \qquad (1.3)$$

Similarly, it is possible to define a total translational energy of the system, E_T, defined by:

$$E_T = E_{tr}(A) + E_{tr}(B) = \frac{1}{2}m_A|\vec{v}_A|^2 + \frac{1}{2}m_B|\vec{v}_B|^2 \qquad (1.4)$$

where m_A and m_B represent the masses of the fragments A and B respectively, and $|\vec{v}_A|$ and $|\vec{v}_B|$ are the magnitudes of the velocity vectors for each fragment. Additionally, due to the selection of the center-of-mass (CM) reference system and by conservation of linear momentum, the following relationship is established:

$$m_A\vec{v}_A + m_B\vec{v}_B = 0 \qquad (1.5)$$

and, simplifying in equation (1.4), the translational energy of each of the fragments can be expressed as:

$$E_{tr}(A) = \frac{m_B}{m_A + m_B} E_T \tag{1.6}$$

$$E_{tr}(B) = \frac{m_A}{m_A + m_B} E_T \tag{1.7}$$

where $\frac{m_B}{m_A+m_B}$ and $\frac{m_A}{m_A+m_B}$ are mass factors. Thus, the relationship between the total translational energy of the system and the available energy then becomes:

$$E_T = E_{\text{disp}} - E_{\text{int}}(A) - E_{\text{int}}(B) = nh\nu - D_0 - E_{\text{int}}(A) - E_{\text{int}}(B) \tag{1.8}$$

Thus, since D_0 is usually a known value, having been experimentally or theoretically obtained, the resulting translational energy distributions provide information about the process that has taken place, as well as the possible photodissociation channels present.

1.2.3. Formation of Newton's Spheres

As previously mentioned, in any photoionization process the fragments produced through the cleavage of the bond of the parent molecule will expand following a three-dimensional distribution. This is referred to as a Newton's sphere. The energy scheme followed by photoionization events was shown in equation (1.1) [1].

Fragments with the same velocity vector spread out in space, creating Newton's spheres. These spheres, illustrated in Figure 1.4, result from the fragments being ejected in opposite directions. In photodissociation processes, the energy available is distributed among the fragments in a way that ensures both momentum and energy conservation. Newton's spheres are produced through multiple iterations of the photodissociation processes directed in specific spatial orientations.

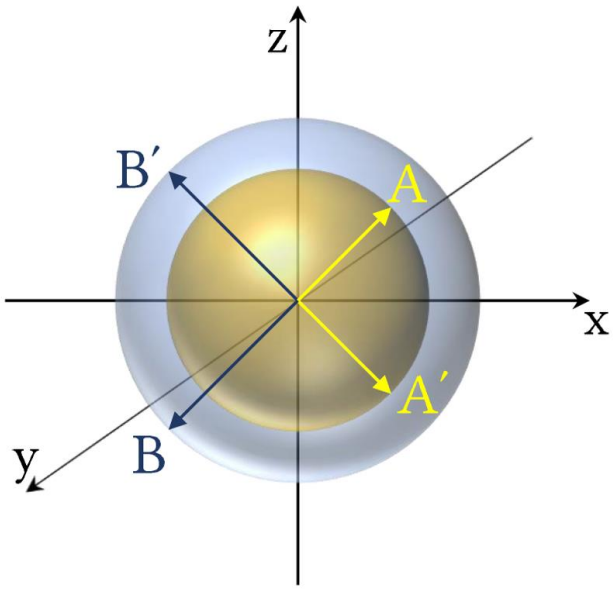

FIGURE 1.4: *NEWTON'S SPHERES IN VELOCITY SPACE FORMED BY THE SET OF* n *EVENTS FOR THE PHOTODISSOCIATION OF THE HYPOTHETICAL MOLECULE AB. THE FIGURE REPRESENTS TWO EVENTS, A-B AND A'-B', WHERE* $v_A = v'_A$ *IS THE RADIUS OF NEWTON'S SPHERE FOR FRAGMENT A, AND* $v_B = v'_B$ *IS THE RADIUS FOR FRAGMENT B. ADDITIONALLY,* v_A *AND* v_B *ARE THE VELOCITIES OF THE RESPECTIVE FRAGMENTS. OBSERVING THE RADII OF THE SPHERES,* $v_A < v_B$ *, WHICH IMPLIES THAT, DUE TO THE CONSERVATION OF MOMENTUM, THE MASS OF FRAGMENT A IS GREATER THAN THAT OF FRAGMENT B.*

Figure 1.4 displays two Newton's spheres that showcases the specific scenario of molecule AB undergoing photodissociation into fragments A and B, as depicted in the photodissociation mechanism shown in equation (1.1). The radius of each Newton's sphere is indicative of the velocity of the respective fragments. Furthermore, in Figure 1.4 that the radius of the golden sphere is smaller than that of the silver sphere, indicating that the velocity of fragment A is lower than that of fragment B. This implies that the mass of fragment A is greater than that of fragment B, a relationship that stems from the principle of conservation of linear momentum [5].

All Newton's spheres created by a photodissociation processes are concentric to each other. By measuring their sizes, one can derive information about the velocity distribution of the fragments in scalar form. Additionally, analyzing the likelihood of the fragments being ejected into specific areas of the sphere provides insights into the angular distribution (anisotropy) of the process being examined.

In general, by analyzing Newton's spheres, it is possible to gain relevant information of the kinematics and anisotropy of photodissociation processes. Over time, various techniques have been developed to measure Newton's spheres generated during these processes. The most prevalent methods include time-of-flight spectroscopy and ion Velocity Map Imaging (VMI). Both techniques rely on the generation and detection of ions, though they differ in the timing of ion creation. With the VMI mapping technique, ions are produced immediately after the formation of Newton's spheres, allowing for their subsequent expansion and detection. Conversely, in the time-of-flight technique, Newton's spheres are ionized post-expansion. In this PhD Thesis, the VMI technique along with its data management has been employed when direct measuring methods, mainly Slice Imaging (SI), could not be used. These methods will be described in detail in Chapter 2.

1.2.4. Molecular Photodissociation Experimentally: REMPI and TOFMS

Earlier sections described the fundamental principles of a photodissociation reaction, highlighting the importance of measuring specific observables to ascertain the physical and chemical properties of the photodissociation process. This section will present the main experimental techniques used in the study of photodissociation processes.

Historically, one of the first ways used to collect fragment information from a photodissociation process was by measuring fragment arrival times from the interaction region between molecules and lasers using a quadrupolar mass spectrometer as a universal detector. The neutral fragments would be ionized by electronic impact and then detected. This approach is referred to as Photofragment Translational Spectroscopy (PTS). A limitation of this technique is that the resolution of the detected distribution was not high enough to discern different rovibrational levels and to obtain a high-quality angular distribution. To address this issue, techniques such as Resonance Enhanced Multiphoton Ionization (REMPI) and Time-Of-Flight Mass Spectrometry (TOFMS) were integrated. This REMPI method can selectively detect specific quantum states of a single fragment, thereby eliminating cross-contamination in the translational energy distributions from other fragments. Consequently, the translational energy information exclusively reflects the specific dissociation channel being studied and the energy profiles of the fragment and its co-fragments [2], [5].

The initial challenge in investigating molecular photodissociation involves identifying and characterizing the fragments produced by the reaction. Often, these fragments emerge in several different quantum states, requiring a certain level of spectral resolution for their individual detection. Here, tunable nanosecond pulsed lasers present an essential role in detection, as they can achieve the high spectral resolution necessary to discriminate said states. Among the spectroscopic detection methods used, laser-induced fluorescence (LIF) and REMPI are the most common. For the purposes of this PhD Thesis, the REMPI technique was exclusively used and then will be the only explanained.

Thanks to the high spectroscopic resolution provided by nanosecond pulsed lasers, and by using the REMPI technique, it is possible to detect different quantum states of a single fragment and selectively ionize specific dissociation products. REMPI achieves this by the resonant absorption of multiple photons to ionize the selected fragment, which may be simple atoms or small molecules and radicals. The most basic REMPI setup involves the absorption of two photons, either of identical or different wavelengths. Here, the first photon excites the atom or molecule to a resonant electronic state, while the second photon provides the energy necessary to exceed the ionization threshold. For example, the REMPI (1+1') method is utilized to detect hydrogen (H) atoms using the transition $1s(\,^2S_{1/2}) \leftarrow 2p(\,^2P_{1/2})$ via a 121.6 nm photon (Lyman-α line). Subsequently, a 364.8 nm photon is used to access the corresponding H^+ ion. Similarly, the REMPI (3+1) method, illustrated in Figure 1.5, involves absorbing four 364.8 nm photons to resonantly ionize the H atom, achieving access to the $2p(^2P_{1/2})$ state by absorbing three photons, and one more to ionization [6].

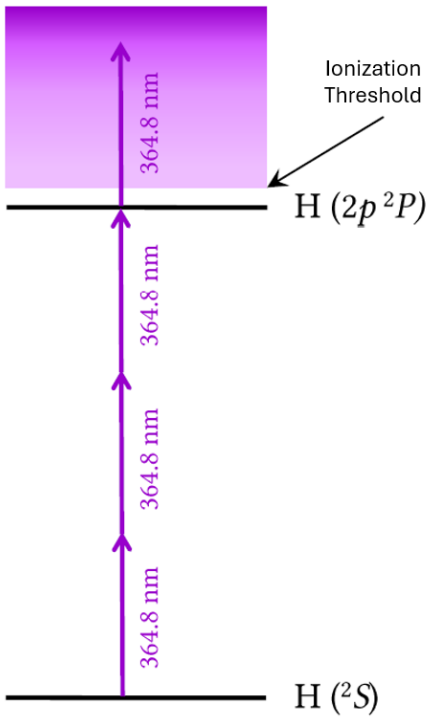

FIGURE 1.5*: (3+1) REMPI SCHEME FOR DETECTING A HYDROGEN ATOM. IT INVOLVES THE RESONANT ABSORPTION OF FOUR PHOTONS AT 364.8 NM. THIS PROCESS OCCURS THROUGH THE THREE-PHOTON TRANSITION FROM* $\mathbf{1s}(\,^2\boldsymbol{S}_{1/2}) \leftarrow \mathbf{2p}(\,^2\boldsymbol{P}_{1/2})$ *[6].*

A key characteristic that offers significant insights into a photodissociation process is the distribution of translational and internal energy among the fragments. This distribution is crucial because any surplus energy the molecule still has after absorbing photons is converted into either translational or internal energy of these fragments. The translational energy of the products specifically provides essential data on the dynamics of photodissociation, indicating, for instance, whether potential barriers are present or not. Mass spectrometry is one of the primary methods employed in these analyses.

Doppler spectroscopy is another commonly used technique that allows making accurate measurements of a fragment velocity when Doppler shift resulting from absorption becomes relevant [7], [8], [9].

Another significant advancement in the detection of Newton's spheres, and thus in the translational energy distributions, was the introduction of a bidimensional 2D flat detector screen. This allows for spatial resolution and therefore, obtaining a 2D image of the distribution of the fragment. The integration of these bidimensional detectors with the REMPI technique brought further development of the VMI technique, which will be discussed in the next chapter.

In a photodissociation process, the fragments can display polarization. This phenomenon is analyzed by measuring the vector correlation between three vectors: the transition dipole moment (**μ**), the angular momentum of the fragments (**J**, if rotational), and the relative speed of the fragments (**v**). Relationships between these vector magnitudes can be explored using Doppler profiles, time-of-flight velocity profiles, or 2D ion images, employing techniques such as

LIF or REMPI. The correlation between these vectors reveals valuable information about the quantum structure of the molecule and it will be explained further in the next section.

1.2.5. Spatial Distribution and Polarization of Fragments. Anisotropy of Photodissociation

In every photodissociation process, the fragments are ejected in various directions forming Newton's spheres, as previously described. While this might imply that the spatial distributions of the fragments are isotropic and lack any defined distribution, the reality is that the probability of fragment ejection is not uniform across all directions of the three-dimensional space. As a result, Newton's spheres often exhibit an anisotropic distribution of fragments. This anisotropy is influenced by the orientation of the transition dipole moment relative to the molecular system's coordinates. The spatial distribution of these fragments can be quantified through the angle between the polarization vector of the laser pulse's electric field, denoted as $\boldsymbol{\varepsilon_p}$, and the velocity vectors in the center of mass (CM) coordinate system, $\boldsymbol{v_A}$ and $\boldsymbol{v_B}$, for fragments A and B in the dissociation of a AB molecule [1], [2].

For a transition between two electronic states to occur through the absorption of a linearly polarized photon, certain conditions must be met. First, the transition must be allowed by electric dipole rules, meaning that the transition dipole moment, $\boldsymbol{\mu}$, must align parallel to the polarization vector of the incident radiation, $\boldsymbol{\varepsilon_p}$. In diatomic molecules, the nature of the transition depends on the symmetry of the involved electronic states. This differentiates two primary scenarios: *parallel transitions*, where the symmetries of the involved states are identical (e.g., $\Sigma \leftrightarrow \Sigma$ or $\Pi \leftrightarrow \Pi$), meaning the transition dipole moment, $\boldsymbol{\mu}$, aligns parallel to the internuclear axis of the molecule. The other scenario considers *perpendicular transitions*, where the symmetries differ (e.g., $\Pi \leftrightarrow \Sigma$), and $\boldsymbol{\mu}$ is perpendicular to the internuclear axis. Consequently, the angular distributions measured between the polarization vector and the velocity vector of the fragment provide a direct indication of the orientation of the dipole moment relative to the internuclear axis, revealing the nature of the electronic transition. In polyatomic molecules, however, the transition dipole moment may align along any of the three axes *x*, *y*, or *z*, which are determined by the molecule's symmetry group and the symmetries of the involved electronic states. In such molecules, certain transitions may be forbidden due to symmetry constraints. This complexity introduces challenges discerning angular distributions, as the orientation of fragment emissions in relation to the transition dipole moment can vary significantly. Thus, understanding these angular distributions requires careful consideration of the molecular symmetry and the specific electronic transitions involved[1], [2], [4].

The relationship between the velocity vector of the fragments and the transition dipole moment can lead to an anisotropic angular distribution of the fragments, particularly when the rotational period of the molecule is longer than the duration of the molecule's dissociation. This scenario is typical in fast dissociation processes like direct dissociations. In such cases, the quick separation of fragments doesn't allow the molecule enough time to rotate, thereby preserving the alignment between the transition dipole moment and the emission directions of the fragments. Conversely, if the rotational period of the molecule is less or equal to the dissociation time, the alignment between the velocity vector of the fragments and the polarization vector of the laser pulse becomes blurred. This happens because the molecule has sufficient time to rotate before the fragments are ejected. Such a scenario is typical in indirect photodissociation

processes like electronic predissociation (Figure 1.3(a)), where the extended interaction time allows the molecule to undergo significant rotational movements, thereby losing the initial orientation information. Furthermore, it's important to highlight that the angular distribution information may become blurred when the excitation involves multiple electronic states with varying probabilities. This scenario leads to a blend of different dissociative processes reflected in the angular distributions, which significantly makes their analysis and interpretation more difficult.

Zare and Herschbach [8], [10], [11] developed an analytical treatment of the angular distribution of the fragments resulting from a photodissociation process induced by excitation with a single photon of linearly polarized light, given by the following equation:

$$I(\theta)_{\text{dis}} = \frac{\sigma}{4\pi}[1 + \beta P_2(\cos\ \theta)] \tag{1.9}$$

where $I(\theta)_{\text{dis}}$ is the spatial intensity distribution of a certain fragment, θ is the angle between the laser radiation polarization vector ($\boldsymbol{\varepsilon_p}$) and the emission velocity vector of said fragment, σ is the absorption cross-section, β is the anisotropy parameter, and $P_2(\cos\theta)$ is the Legendre polynomial of order 2, defined as $\left(\frac{1}{2}\right)(3\cos^2\theta\ -\ 1)$.

According to equation (**1.9**), the topologies of the fragment distributions will vary based on the values assumed by the anisotropy parameter β. Figure 1.6 illustrates the three limiting cases for the values of β. A limiting value of β equal to 2 suggests a parallel transition (right panel of Figure 1.6), characterized by a lobular distribution of fragments following the pattern of $\cos^2\theta$:

$$I(\theta)_{\text{dis}} \propto \frac{1}{4\pi}(3\cos^2\theta) = \frac{3}{4\pi}\cos^2\theta \tag{1.10}$$

If the anisotropy parameter β takes the limit value of -1, then a perpendicular transition will be present (left panel of Figure 1.6, and the distribution of the fragments will be toroidal, of the type of $\text{sen}^2\theta$:

$$I(\theta)_{dis} \propto \frac{1}{4\pi}\left(1 - \frac{3}{2}\cos^2\theta + \frac{1}{2}\right) = \frac{3}{8\pi}(1 - \cos^2\theta) = \frac{3}{8\pi}\text{sen}^2\theta \tag{1.11}$$

Finaly, in the case where β takes a value of 0 (central panel of Figure 1.6, two different cases can be deduced, that have already been mentioned. it could be that the excitation occurs into two states of different symmetries or that the rotational period of the molecule is higher than the reaction time as can occur in indirect processes.

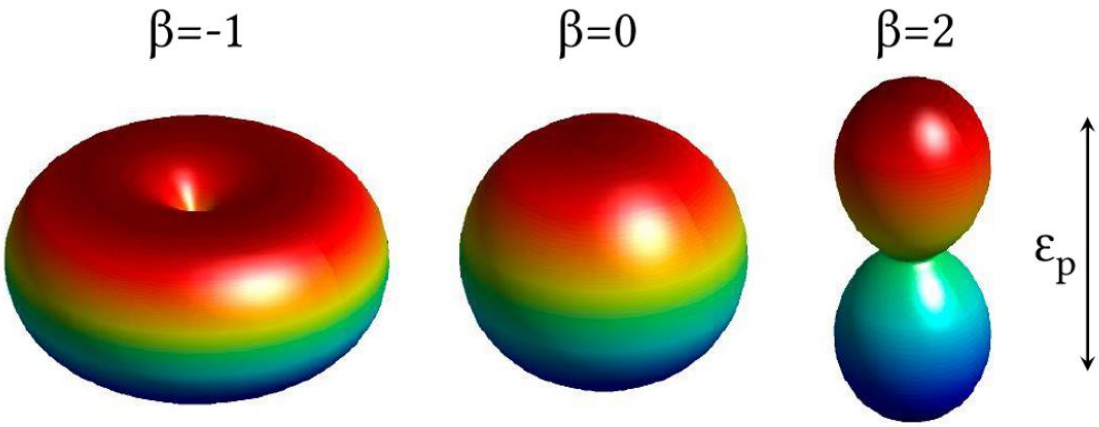

FIGURE 1.6: *THREE-DIMENSIONAL REPRESENTATION RESULTING FROM SOLVING EQUATION (1.9) FOR DIFFERENT VALUES OF THE ANISOTROPY PARAMETER β. WHEN β IS -1, LEFT PANEL, THE DISTRIBUTION OF THE FRAGMENTS IS TOROIDAL OR $\boldsymbol{sin^2}\,\theta$ (PERPENDICULAR TRANSITION). IF β IS 0, CENTRAL PANEL, AN ISOTROPIC DISTRIBUTION IS OBTAINED, WITH THE SAME PROBABILITY OF FINDING THE FRAGMENTS IN ANY DIRECTION IN SPACE. IN CASES WHERE β IS 2, RIGHT PANEL, THE DISTRIBUTION OF THE FRAGMENTS IS LOBULAR OR $\boldsymbol{cos^2}\,\theta$ (PARALLEL TRANSITION).*

Equations (1.9), (1.10) and (1.11) detail the spatial distribution of the fragments relative to the polarization vector of the photolysis laser, yet they do not consider the photons from the subsequent probe pulse that are absorbed by the fragment for ionization. The REMPI technique, employed in this PhD Thesis to detect atomic and molecular fragments, is sensitive to both the velocity and the polarization of the fragments. This means that the spatial distribution of the products must be adjusted according to the probability of detection to produce the corresponding intensity distribution, denoted as $I(\theta)_{\text{int}}$, in the following manner:

$$I(\theta)_{\text{int}} = I(\theta)_{\text{dis}} \times I(\theta)_{\text{det}} \tag{1.12}$$

Thus, the intensity distribution for a REMPI (n+m) scheme, where n is the number of photons involved in the resonant stage and m those involve in the ionization stage of the REMPI process, that uses linearly polarized light will be defined by the following equation:

$$I(\theta)_{int} = \frac{\sigma}{4\pi}[1 + \beta P_2(\cos\theta)] \sum_{i=0}^{2n} c_i P_i(\cos\theta) \tag{1.13}$$

where $P_i(\cos\theta)$ are the respective Legendre polynomials. Simplifying equation (1.13) yields:

$$I(\theta)_{\text{int}} = \frac{\sigma}{4\pi} \sum_{i=0}^{2n+2} \beta_i P_i(\cos\,\theta) \tag{1.14}$$

where β_i are the anisotropy parameters that allow for the description of the phenomenology of the dissociation and polarization of the fragments, despite lacking a specific physical meaning. This polarization of the fragments can signify the presence of certain alignments between the fragment's angular momentum and either the transition dipole moment or the emission vector of the fragment.

Equation (1.14) is defined based on the polarization of the lasers and the type of REMPI (n+m) scheme used. If the pump and probe lasers are linearly polarized only even Legendre polynomials appear. And if the REMPI detection scheme is of the type (2+1), then n will take a value of 2 [7], [11], [12], [13], so equation (1.14) becomes:

$$I(\theta)_{\text{int}} = \frac{\sigma}{4\pi}[1 + \beta_2 P_2(\cos\,\theta) + \beta_4 P_4(\cos\,\theta) + \beta_6 P_6(\cos\,\theta)] \tag{1.15}$$

1.3. Alignment Parameters

The Slice Imaging (SI) technique, which will be explained later in detail, offers a direct measurement of the central slice of the 3D distribution of photofragments generated during a photodissociation process. One of the main benefits of this technique is that it does not require any mathematical transformation to map the photofragment distribution, as it is the case for the VMI technique. As a result, the slice images can be easily interpreted to extract important dynamical information. The analysis requires images captured using four combinations of pump and probe laser polarizations: X(pump)X(probe), XZ, ZX, and ZZ configurations. In this setup, the XYZ coordinate system represents the laboratory frame, with both lasers counterpropagating along the Y axis and the molecular beam traveling along the Z axis (the time-of-flight axis). Among the laser polarizations configurations, the XX images include all the stereodynamical information, such as the anisotropy of the dissociation process and the orientation and/or alignment of the photoproducts. Meanwhile, in the XZ images, the probe polarization vector is perpendicular to the detection plane, resulting in the loss of information related to the angular momenta of the products. Similarly, ZX images lack information about the anisotropy of the dissociation process, as is the pump laser polarization the one perpendicular to the detection plane. Finaly, the ZZ images do not contain any dynamical information and are used as a reference to prevent systematic errors related to the good alignment of the lasers or imperfections of the micro-channel plate (MCP) detector.

Photofragment alignment is crucial for understanding the underlying dynamics of a photodissociation process and is one of the important pieces of information that can be derived from the images. The laboratory intensity distribution for a one-photon dissociation process, followed by (n + m) REMPI detection, can be described by the following expression [13]:

$$I(\theta_{\text{pump}}) \times I(\theta_{\text{probe}}) = [1 + \beta P_2(\cos\theta_{\text{pump}})] \times \sum_{k=2}^{2n+m} 1 + A_0^k P_k(\cos\theta_{\text{probe}}) \tag{1.16}$$

where $I(\theta_{\text{pump}})$ and $I(\theta_{\text{probe}})$ represent the intensity distributions associated with the photolysis and detection processes, respectively. Here, θ_{pump} and θ_{probe} indicate the angles between the photolysis and probe polarization directions relative to the recoil direction. The parameter β is the dissociation anisotropy parameter, while the parameters A_0^k are the photofragment polarization parameters. $P_k(\cos\theta)$ denotes the *k*-th Legendre polynomial.

When linearly polarized pump and probe laser pulses are used, the experiment is insensitive to photofragment orientation, meaning that the *k* index takes only even values. Furthermore, for (2+1) REMPI detection, as used in the stereodynamic experiments of this Thesis, the expansion is truncated at $k = 4$. Therefore, equation (**1.16**) should be expressed as an expansion of Legendre polynomials up to $k = 4$ [12], [14] :

$$I(\theta)^{FG} = 1 + \beta_2^{FG} P_2(\cos\,\theta) + \beta_4^{FG} P_4(\cos\,\theta) + \beta_6^{FG} P_6(\cos\,\theta) \tag{1.17}$$

where F and G denote the photolysis and probe polarization directions, respectively, relative to the slicing plane. The parameters β_k^{FG} represent the anisotropy parameters in the laboratory frame. These phenomenological β_k^{FG} parameters encapsulate all the dynamical and geometrical information about the process. To extract the relevant dynamical data, β_k^{FG} must be converted into a different set of parameters.

Rakitzis and Zare described the stereodynamics of molecular photodissociation using a set of polarization parameters, denoted as $a_p^k(p)$ [13]. In subsequent publications, Rakitzis developed useful expressions for various laboratory geometries and dynamical problems [12]. Notably, he established a relationship between the anisotropy parameters in the laboratory frame, β_k, and the molecular frame polarization parameters, $a_p^k(p)$, through expressions involving the coefficients $A_p^k(p)$, which in several cases are related to isotropic A_0^k(iso) or anisotropic A_0^k(aniso) contributions:

$$\begin{aligned}\beta_2 N = c\beta + s_2\left\{A_0^2(\text{iso}) + \frac{1}{7}[2A_0^2(\text{aniso}) + cA_1^2 - 2cA_2^2]\right\} \\ + s_4\left\{\frac{1}{21}\left[6A_0^4(\text{aniso}) + \sqrt{30}cA_1^4 + \sqrt{15}cA_2^4\right]\right\}\end{aligned} \tag{1.18}$$

$$\begin{aligned}\beta_4 N = s_2\left\{\frac{1}{35}[18A_0^2(\text{aniso}) - 12cA_1^2 + 3cA_2^2]\right\} \\ + s_4\left\{A_0^4\,(\text{iso}) + \frac{1}{77}\left[20A_0^4\,(\text{aniso}) + \sqrt{30}cA_1^4 + 6\sqrt{15}cA_2^4\right]\right\}\end{aligned} \tag{1.19}$$

$$\beta_6 N = s_4\left\{\frac{1}{35}\left[15A_0^4\,(\text{aniso}) - 2\sqrt{30}cA_1^4 + \sqrt{15}cA_2^4\right]\right\} \tag{1.20}$$

where *N*, proportional to the population, is given by:

$$N = 1 + s_2\left\{\frac{1}{5}[A_0^2\ (\text{aniso})\ + cA_1^2 + cA_2^2]\right\} \tag{1.21}$$

The s_k are the k-th order sensitivity factors (normalized so that $s_0 = 1$), and c is a constant that can be either 1 or -1/2, depending on whether the photolysis laser is linearly or circularly polarized, respectively. In this thesis, $c = 1$ because only linear polarization of the photolysis laser has been used. The $A_q^k(p)$ coefficients in equations (1.18)-(1.21) are related to the $a_q^k(p)$ parameters, and are employed to simplify the equations.

Equations (1.18)-(1.21) represent the key findings of Rakitzis work (presented as equations 7a–7d in reference [12]). These equations provide a range of simplified expressions that facilitate the analysis of the experimental data [12], [15], [16]. The $a_q^k(p)$ parameters are divided into three groups based on the transition dipole moment of the one-photon excitation process: $a_q^k(\parallel)$, $a_q^k(\perp)$ and $a_q^k(\parallel,\perp)$. In the case of a one-photon *pure parallel transition*, described by $\beta = 2$ and $q = 0$, only the $a_0^k(\parallel)$ parameters are relevant. For a one-photon *pure perpendicular transition*, characterized by $\beta = -1$ and $q = 0{,}2$, only the parameters $a_q^k(\perp)$ are relevant. Additionally, the $a_q^k(\parallel,\perp)$ parameters account for contributions from the interference between parallel and perpendicular transitions.

Rakitzis has converted equations (1.18)-(1.21) into easily applicable expressions for pure perpendicular transitions, as well as for the more complex interference cases [15], [16]. However, he did not develop the equivalent set of equations for purely parallel transitions as well as mixed cases where there are contributions from both the parallel and perpendicular transitions. In the following paragraphs, the corresponding set of equations for *parallel transitions* are shown, considering the interference from perpendicular transitions:

$$A_0^k(iso) = a_0^k(\parallel) \tag{1.22}$$

$$A_0^k(\text{aniso}) = 2a_0^k(\parallel) \tag{1.23}$$

$$A_1^k = \sqrt{\frac{8}{3}}\text{Re}\left[a_1^k(\parallel,\perp)\right] \tag{1.24}$$

$$A_1^k = 0 \tag{1.25}$$

Substitution of equations (1.22)-(1.25) into equations (1.18)-(1.21) results in the following equations:

$$\begin{aligned}\beta_2 N = \beta + s_2&\left\{\frac{11}{7}{a_0}^2(\parallel) + \frac{1}{7}\sqrt{\frac{8}{3}}\text{Re}\left[{a_1}^2(\parallel,\perp)\right]\right\} \\ &+ s_4\left\{\frac{12}{21}a_0^4(\parallel) + 4\sqrt{5}\text{Re}\left[a_1^2(\parallel,\perp)\right]\right\}\end{aligned} \tag{1.26}$$

$$\beta_4 N = s_2\left\{\frac{36}{35}a_0^2(\|) - 12\sqrt{\frac{8}{3}}\mathrm{Re}\left[a_1^2(\|,\perp)\right]\right\} + s_4\left\{\frac{117}{77}a_0^4(\|) + \frac{4}{77}\sqrt{5}\mathrm{Re}\left[a_1^4(\|,\perp)\right]\right\} \tag{1.27}$$

$$\beta_6 N = s_4\left\{\frac{10}{11}a_0^4(\|) - \frac{8}{33}\sqrt{\frac{8}{3}}\mathrm{Re}\left[a_1^4(\|,\perp)\right]\right\} \tag{1.28}$$

$$N = 1 + s_2\left\{\frac{1}{5}\left[2a_0^2(\|) + \sqrt{\frac{8}{3}}\mathrm{Re}\left[a_1^2(\|,\perp)\right]\right]\right\} \tag{1.29}$$

For experimental results that can be fitted to equation (1.17) with $\beta_6 = 0$, the second-order sensitivity parameter s_4 is also zero. Therefore, the relationship between the measured β_k^{FG} and the alignment parameters β, $a_0^4(\|)$, and $\mathrm{Re}\left[a_1^k(\|,\perp)\right]$ for the three geometries (XX, XZ, and ZX) is given by:

$$\beta_2^{XX} = \frac{\beta + \frac{s_2}{7}\left\{11a_0^2(\|) + \sqrt{\frac{8}{3}}\mathrm{Re}\left[a_1^2(\|,\perp)\right]\right\}}{1 + \frac{s_1}{5}\left\{2a_0^2(\|) + \sqrt{\frac{8}{3}}\mathrm{Re}\left[a_1^2(\|,\perp)\right]\right\}} \tag{1.30}$$

$$\beta_4^{XX} = \frac{12s_2\left\{\frac{3}{35}a_0^2(\|) + \sqrt{\frac{8}{3}}\mathrm{Re}\left[a_1^2(\|,\perp)\right]\right\}}{1 + \frac{s_1}{5}\left\{2a_0^2(\|) + \sqrt{\frac{8}{3}}\mathrm{Re}\left[a_1^2(\|,\perp)\right]\right\}} \tag{1.31}$$

$$\beta_2^{XZ} = \frac{\beta + s_2 a_0^2(\|)}{1 + \frac{1}{2}s_2 a_0^2(\|)} \tag{1.32}$$

$$\beta_2^{ZX} = s_2 a_0^2(\|) \tag{1.33}$$

Chapter 2 Methodology and experimental Setups

2.1. Laser Systems

In the realm of laser physics and its applications, the choice of experimental setup is crucial to the success of the experiments. The precision, versatility, and power of the laser systems directly influence the scope and quality of research outcomes. This chapter introduces the laser setup at the *Centro de Láseres Ultrarrápidos* (CLUR) at Universidad Complutense de Madrid (UCM), delving on its components, functionalities, and the reason behind its configuration. In general terms, the main system that was used consisted on two dye lasers (Sirah Cobra-Strech) pumped by two Nd:YAG lasers (Quanta-Ray Pro-190 and 230) whose setup scheme is shown in Figure 2.1.

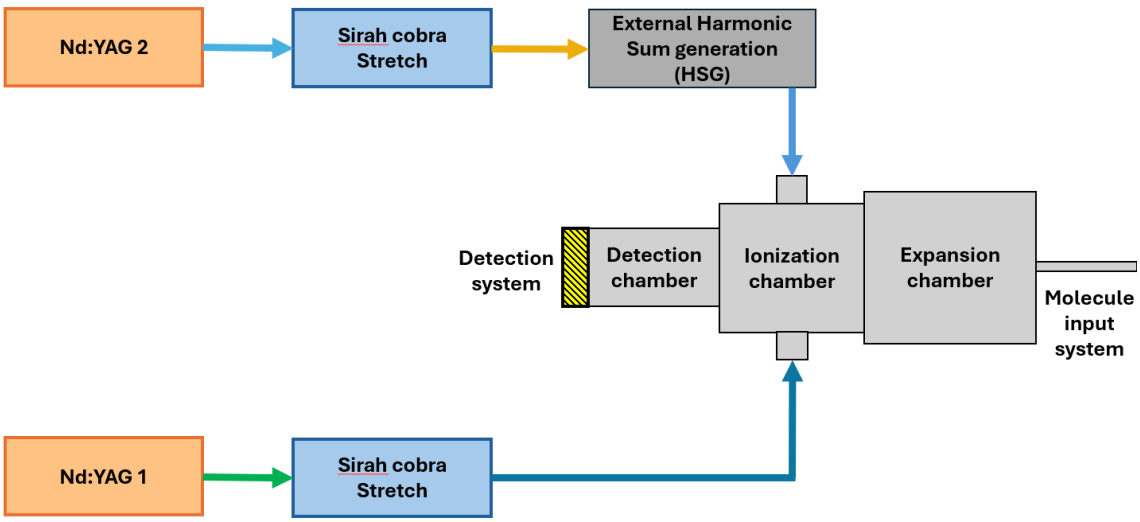

FIGURE 2.1: *SCHEMATIC REPRESENTATION OF THE EXPERIMENTAL SETUP AT CLUR THAT WAS USED IN THIS THESIS.*

2.1.1. Nd:YAG Lasers

Nd:YAG lasers, Figure 2.2(a), short for neodymium-doped yttrium aluminum garnet lasers, are solid-state lasers widely used across various fields for its versatility and efficiency. The laser medium in these lasers is a crystal of yttrium aluminum garnet (YAG) doped with neodymium ions (Nd^{3+}), Figure 2.2(b), which serve as the active laser source. When relaxing after an excitation, these ions emit fundamental light at 1064 nm, in the infrared region of the spectrum. To accomplish the excitation, Xe lamps, Figure 2.2(b), discharge into the active laser medium, inside a cavity made up of two gold reflectors, Figure 2.2(b), generating a pulse of light in a first phase in the oscillator cavity (yellow rectangle in Figure 2.2(c)). Later, this pulse is sent to a similar second cavity (blue rectangle in Figure 2.2(c)), where it is amplified. All the cavities are water-cooled to dissipate the heat generated by the lamps. For the purpose of our experiments,

these lasers were made to work at a nominal output energy of 1 W, although they may reach up to 3.5 W if needed, a repetition rate of 10 Hz and pulse width of around 10 ns.

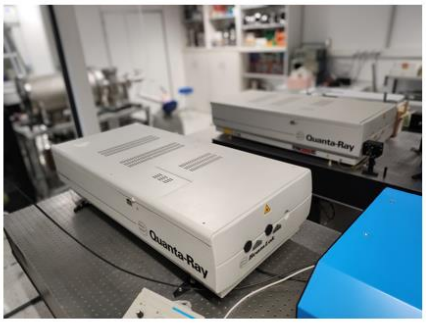

(a) Quanta-Ray Lasers

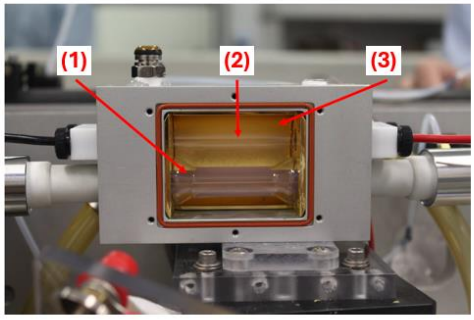

(b) Amplification chamber Laser cavities

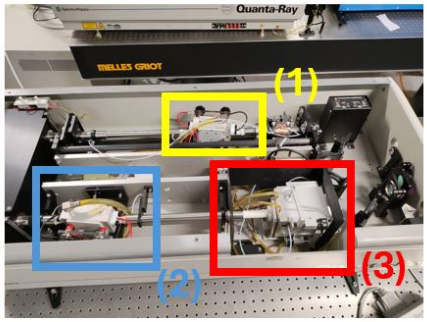

(c) Inside of Nd:YAG laser

FIGURE 2.2: *(A) QUANTA-RAY PRO (190 FRONT AND 230 REAR) LASERS FROM SPECTRA PHYSICS. (B) THE AMPLIFICATION CHAMBER OF THE QUANTA-RAY PRO 190 LASER, WHERE THE ND:YAG CRYSTAL (1), THE XE LAMP (2), AND THE GOLD REFLECTOR (3) ARE ALLOCATED. (C) TOP VIEW OF THE QUANTA-RAY PRO 190 LASER TO DISTINGUISH THE DIFFERENT SECTIONS: THE OSCILLATOR (YELLOW RECTANGLE), THE AMPLIFIER (LIGHT BLUE RECTANGLE), AND THE HARMONIC GENERATION UNIT (RED RECTANGLE).*

2.1.2. Harmonic Generation

The harmonic generation process is used to achieve shorter wavelengths from the fundamental radiation emission of the laser. The standard way of doing this is by taking advantage of the non-linear optical properties of certain materials. In this case, Beta Barium Borate crystals (b-BaB_2O_4), or BBO for short, are used. When laser radiation goes through this kind of crystals, a polarization induction effect is undergone by the material due to the incident photons. When two of them coincide at the material they are recombined into a photon with double frequency which will be phased matched with the rest of photons that undergo the same process. It is also possible to recombine photons of different frequencies to obtain their frequency sum. This means that by adding fundamental frequencies to a doubled frequency photon we can obtain the odd numbered harmonic as well. Due to the multi-event nature of the process, it is very inefficient when considering energy conversion. Usually, the favored output has an efficiency rate of 5% to 10%. Therefore, the output power consists of a mixture of both the harmonic radiation and the fundamental input. In order to clean the output radiation as much as possible, dichroic mirrors of the adequate wavelength are used to filter the undesirable radiation. A schematic representation of the wave-mixing process is shown in

Figure 2.3.

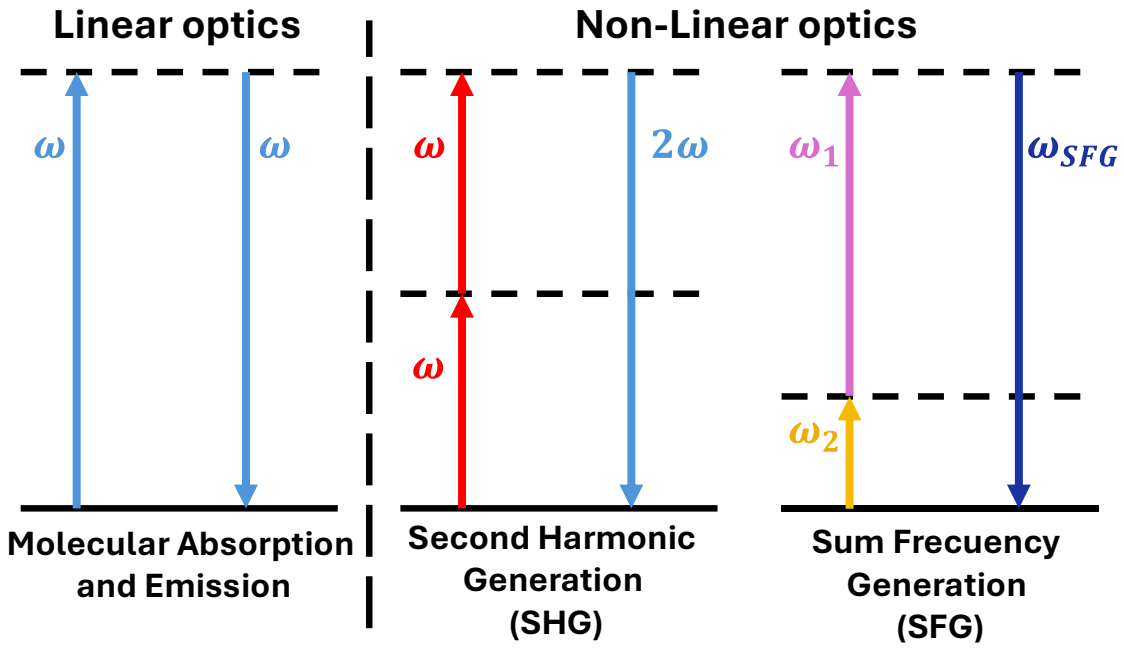

FIGURE 2.3: GENERAL *DIAGRAM OF THE LINEAR AND NON-LINEAR INTERACTIONS OF LIGHT WITH MATTER WHERE FREQUENCY SUM IS OBSERVED AS A MULTI-PARTICLE EVENT TO GENERATE PHOTONS WITH GREATER FREQUENCY THAN THE PHOTONS IN THEIR INITIAL STATE.*

The harmonic generation module is set at the exit of the amplifier, red rectangle in Figure 2.2(c). There, the 1064 nm laser radiation that enters, can be doubled in frequency, or sum to its second harmonic, to achieve output wavelengths of 532 nm (second harmonic) and 355 nm (third harmonic), respectively. The module is also coupled with another BBO crystal after the first one, so the fourth harmonic, 266 nm, can also be obtained. However, this was not used in this Thesis. The maximum energies that can be achieved with this setup are around 400 mJ working at 532 nm and 250 mJ working at 355 nm when the fundamental laser of the 1064 nm has a value of energy of 1J.

2.1.3. Dye lasers

Harmonic generation alone falls short when considering our needs to obtain a specific wavelength in the UV. This aspect is key for the quality and success of the experiments carried out during this Thesis. To solve this problem, the output of the Nd:YAG lasers, 532 nm or 355 nm, is sent into two dye lasers (Sirah Cobra-Stretch) which are able to select the wavelength to the hundredth of nanometer. Figure 2.4 show the general setup of (a) the two-laser system, and (b) the inside of the laser cavity with the dye containers and grating of one of the dye lasers. How these parts interact to achieve a tunable coherent laser beam is explained in the following.

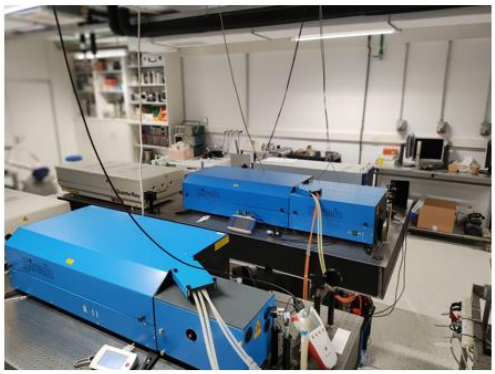

(a) General nano-second laser system

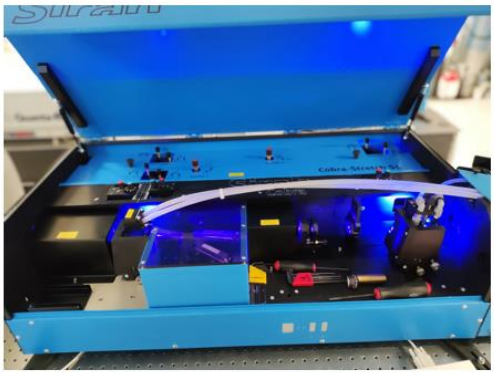

(b) Inside of Sirah Cobra-Stretch

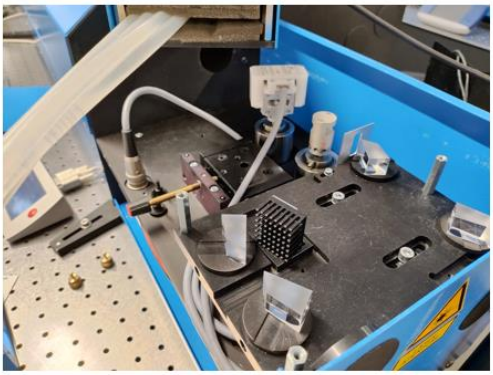

(c) Frequency Conversion Unit (FCU)

FIGURE 2.4: *(A) IMAGE SHOWING THE NANOSECOND LASER SYSTEM, WHICH CONSISTS OF TWO ND:YAG LASERS (BEIGE) AND TWO SIRAH COBRA-STRETCH DYE LASERS (BLUE). (B) INTERIOR OF ONE OF THE SIRAH COBRA-STRETCH DYE LASERS. (C) IMAGE PROVIDING A DETAILED VIEW OF ONE OF THE FREQUENCY CONVERSION UNITS (FCU).*

As mentioned earlier, the laser radiation from the Nd:YAG is sent into the dye laser, usually the second or third harmonic. Here it first goes through an active medium consisting of a solution of an organic dye. These organic molecules are chromophores capable of emitting fluorescence after having been excited at a given excitation wavelength. In Figure 2.5 the fluorescent emission spectra for several chromophores can be seen. By choosing the chromophore (dye), their concentration and solvent, a wide range of wavelengths can be achieved, albeit with different energy output efficiencies.

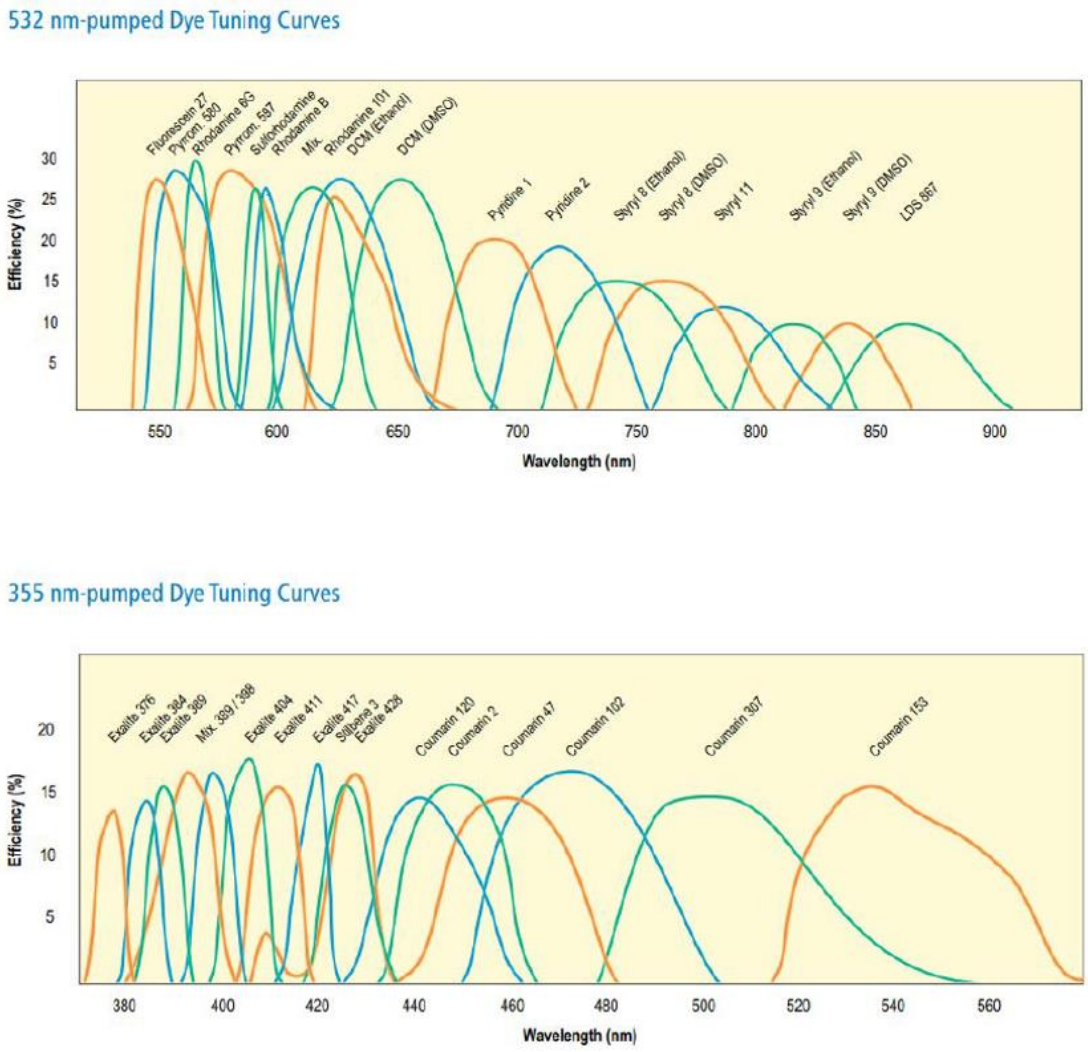

FIGURE 2.5: *FLUORESCENCE EMISSION CURVES FOR DIFFERENT ORGANIC DYES AS A FUNCTION OF EMISSION WAVELENGTH. THE UPPER GRAPH SHOWS THE FLUORESCENCE EMISSION SPECTRA OF THE VARIOUS DYES WHEN EXCITED AT 532 NM, WHILE THE LOWER GRAPH SHOWS THE SPECTRA WHEN EXCITED AT 355 NM. IMAGE TAKEN FROM THE SIRAH LASER MANUAL [17].*

The whole laser system can be described in different phases and its diagram is shown in Figure 2.6.

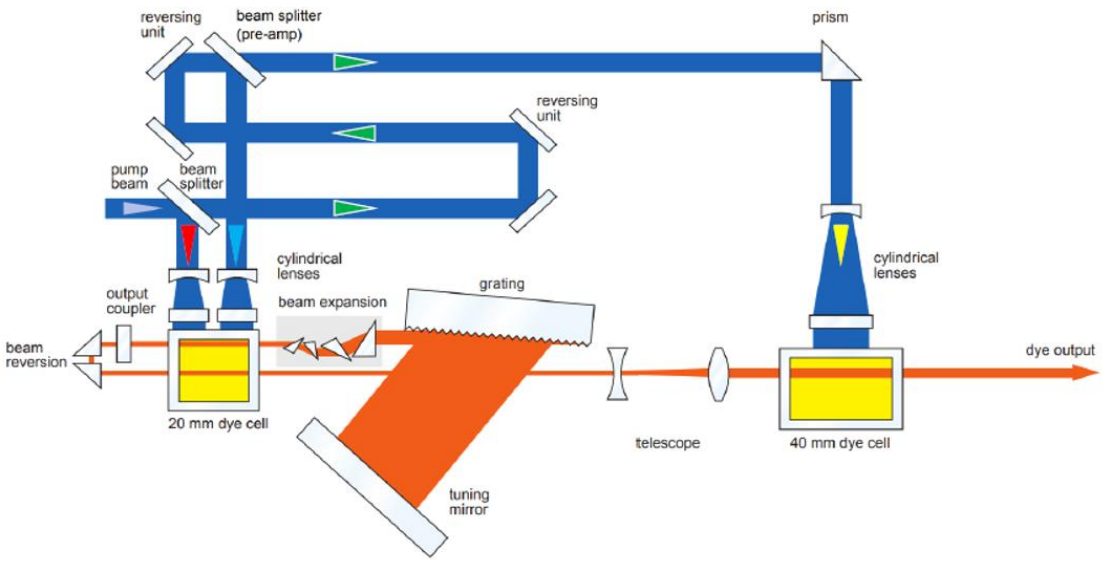

FIGURE 2.6: *OPTICAL DIAGRAM OF THE PARTS OF THE SIRAH COBRA-STRETCH DYE LASER. TAKEN FROM THE SIRAH LASER MANUAL [17].*

In the first phase, a beam splitter directs 10% of the pump laser energy (red arrow in Figure 2.6) to the oscillator cell (a quartz cell of 20 mm side) where the dye solution circulates. After being excited, the dye emits fluorescent radiation that is directed to the resonant cavity. This resonant cavity is formed by a diffraction grating and a tuning mirror, a beam expander used to illuminate the total length of the grating, and the output coupler. Only the wavelength of the fluorescent emission spectrum that is diffracted in the first order on the diffraction grating will be tuned in the resonant cavity. At the output of the resonant cavity, the generated laser radiation has a maximum pulse energy of 2 mJ. This energy output is sent to the second part of the dye laser, the pre-amplification phase, by a pair of prisms. In this second phase, and after a delay line (green arrows) used to match temporally the pulses, another beam splitter directs another 10% of the pump laser energy to another part of the same cell (blue arrow). At this point, the generated laser pulse from the oscillator coincides with the pump laser pulse, producing an increase in energy up to a maximum of 20 mJ per pulse. A telescope modifies the beam profile to adapt it to the last phase of the laser, the amplifier. A prism sends all the remaining energy of the pump laser to the amplifier cell (yellow arrow), a cylindrical cell of 40 mm length and 5 mm diameter. The main difference between the two types of cells is the final beam profile of the laser radiation. At the output of the amplification phase, the energy can be very divergent depending on the dye used, covering an energy range between 20 mJ and 100 mJ. Finaly, the output laser radiation faces another BBO crystal to obtain the second harmonic of the fundamental emission (Figure 2.4(c)).

2.2. Ion Imaging Techniques

In general, the experiments carried out in this Thesis are framed within the Velocity Map Imaging (VMI) and Slice Imaging (SI) techniques. These techniques allow for high resolution measurements of the angular and velocity distributions of the products generated in photodissociation processes. The experiments of these thesis were performed at CLUR, UCM, and at the *Foundation for Research and Technology* (FORTH) Institute at Heraklion, Crete, Greece.

2.2.1. Velocity Map Imaging of Ions (Velocity Map Imaging)

Before the 1980s, there were no ways to directly measure both the angular distribution, and the translational energy distribution of the fragments produced by a molecular photodissociation process. Having to rely on indirect methods to obtain these experimental results [9], [18]. By the end of that decade and beginning of 1990s, it was first introduced by Chandler and Houston [REF] a way to measure the three-dimensional Newton sphere. This was accomplished by "crushing" the Newton sphere into a two-dimensional plane detector combined with Time-of-Flight Mass Spectrometry (TOFMS). After this, with the help of different mathematical methods, it was possible to extract the translational energy as well as the angular distribution directly from the image produced by the "crushed" Newton sphere. This novel experimental process was named the Ion Imaging technique.

The first published ion image by Chandler and Houston in 1987 is shown in Figure 2.7(a) [19]. It was a measurement of CH_3I photodissociation, excited in the UV at 266 nm, producing the photofragment $CH_3(v=0)$. This fragment was detected through a REMPI (2 + 1) scheme of the $3p_z$ Rydberg state at 333.45 nm. After ionization occurs, a homogeneous electrostatic field was applied to a set of metallic plates to redirect the ions into the plane detector corresponding to the image presented.

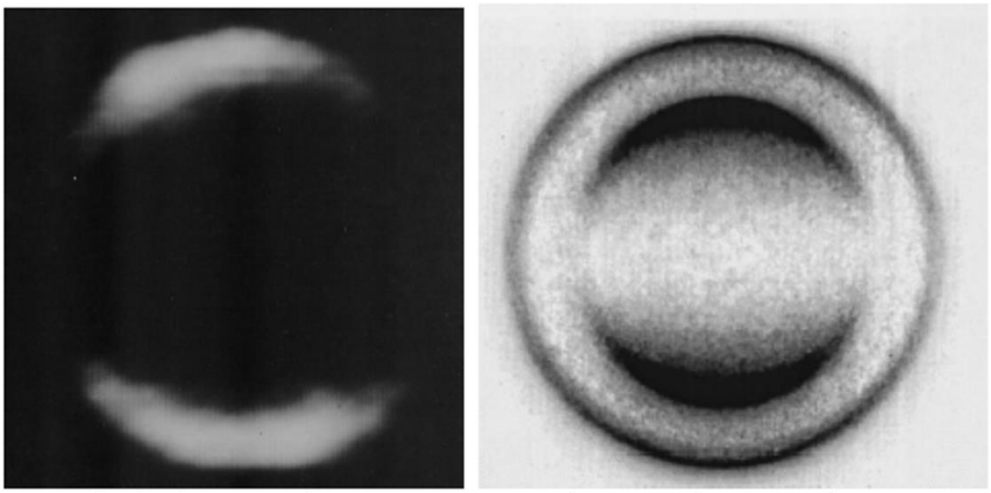

(a) First ion image obtained in 1987 (b) Ion image obtained by Eppink and Parker

FIGURE 2.7: *EVOLUTION OF THE ION IMAGING TECHNIQUE. (A) THE FIRST IMAGE OF ION FRAGMENTS FROM THE PHOTODISSOCIATION OF CH_3I OBTAINED BY CHANDLER AND HOUSTON IN 1987* [20]. *(B) ION IMAGE OBTAINED BY EPPINK AND PARKER* [21] *IN 1998 FOR THE SAME MOLECULE AFTER IMPROVING THE TECHNIQUE AND IMPLEMENTING VELOCITY MAP IMAGING (VMI).*

The experiment delivered successful results, as it was capable of simultaneously providing details about both the angular and the translational energy distribution of the fragments through the measurement of an image. However, the impact of this achievement was diminished by the poor quality of the image, which appeared irregular and blurry. This issue arose because the photolysis laser affected a broad area of the molecular beam, causing

numerous ions to hit various parts of the detector. In their setup, Chandler and Houston utilized a modification of the Wiley-McLaren (WM) spectrometer [22], as illustrated in Figure 2.8(a), where only the repeller (R) plate was subjected to voltage while the extractor (E) and accelerator (G) plates were connected to the ground. Although the WM spectrometer is highly regarded for its high mass resolution in time-of-flight mass spectrometers and is frequently used in ion imaging experiments, it encounters a drawback due to the ions being affected by the presence of a grid on the extractor plate that the fragments must go through [23], [24], [25].

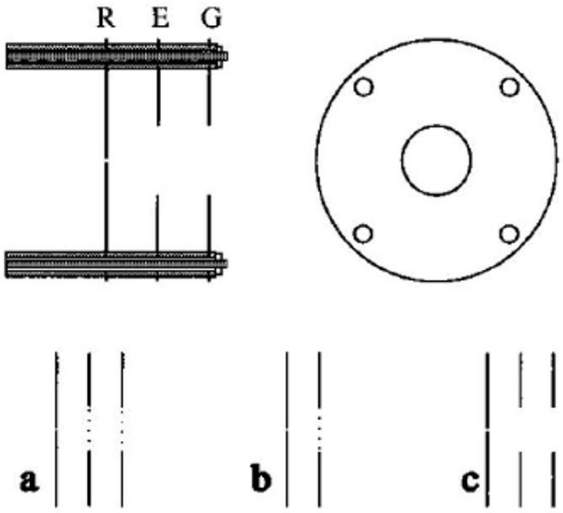

FIGURE 2.8: *DETAILED VIEW OF THE DIFFERENT EXPERIMENTAL SETUPS FOR ION EXTRACTION, TAKEN FROM REFERENCE* [26]*, WHERE "R" IS THE REPELLER PLATE, "E" THE EXTRACTOR PLATE, AND "G" THE GROUND ELECTRODE OR ACCELERATOR PLATE. SETUP (A) IS A WILEY-MCLAREN SYSTEM, (B) A CONVENTIONAL ION IMAGING SYSTEM, AND (C) THE VMI CONFIGURATION*.

To mitigate the distortions caused by the grids on the extractor and accelerator plates, the accelerator plate was removed, resulting in a simplified two-plate system comprising only the repeller and extractor plates, as depicted in Figure 2.8(b). This configuration became much more prevalent in ion imaging experiments [27], [28], [29], [30]. However, the challenges associated with the grid usage persisted. To limit the deflection of the ion path as effectively as possible, it was necessary to use a grid with wire spacing no larger than the diameter of the Newton sphere when it goes through. Although this adjustment significantly reduced trajectory deviations, it also led to a reduction in ion transmission through the grid, highlighting a trade-off between trajectory accuracy and ion throughput.

Eppink and Parker addressed the limitations associated with both the Wiley-McLaren system and the two-plate system by introducing an innovative gridless open plate extraction system, as illustrated in Figure 2.8(c) [26]. They discovered in their analysis of Chandler and Houston's experiment that ions sharing the same kinetic energy were not hitting the detector at the same point, leading to reduced image resolution. On top of the lack of grid, they also made use of an uneven electrostatic field to extract ions, therefore enhancing the clarity and resolution of the images produced. An illustrative outcome of this improvement is the ion image depicted in Figure 2.7(c), showing the molecular photodissociation of CH_3I when excited at 305 nm and the

ion image of CH_3(v=0) captured through a REMPI (2+1) scheme at 333.45 nm [21]. This new modification was addressed as the Velocity Map Imaging (VMI) technique.

In 2006, Papadakis and Kitsopoulos advanced the VMI technique by innovating a new two-plate system consisting of a repeller and an extractor, where the repeller plate alone receives voltage application. They introduced modifications to the plate design, offering two configurations: one with a grid and another without. Figure 2.9 illustrates these revised designs for the ion sphere extraction system. This innovative approach simplifies the system by requiring voltage application only to the repeller plate, while also achieving focusing conditions at a predetermined distance between the repeller and extractor plates. This last design has been adopted by the VMI machine at FORTH and, with minor adjustments, by the VMI system at CLUR, details of which will be discussed later.

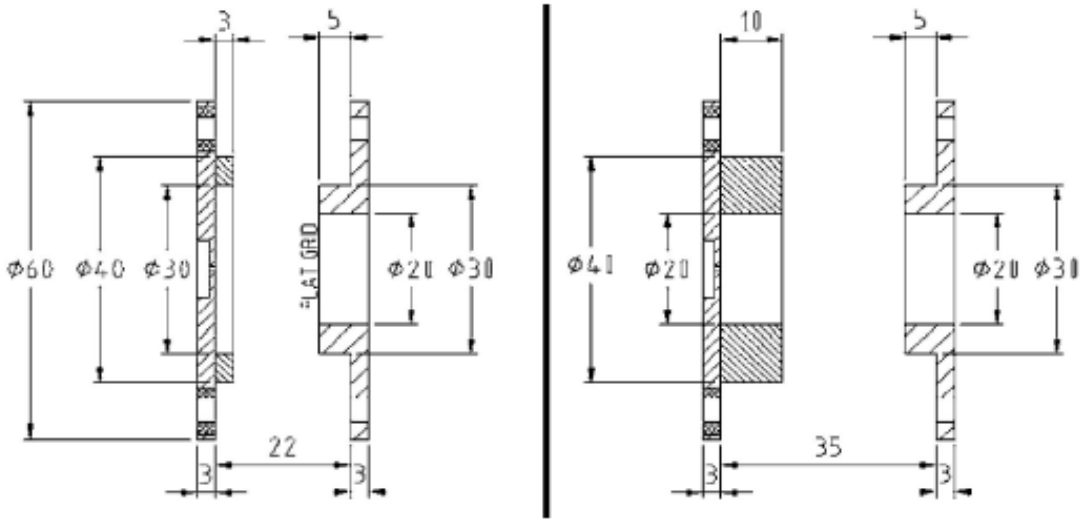

FIGURE 2.9: *SCHEMATICS OF THE MODIFICATION MADE TO THE REPELLER AND EXTRACTOR PLATES [16] TO ACHIEVE VMI WITH A SINGLE VOLTAGE APPLIED TO THE REPELLER PLATE. ON THE LEFT SIDE, THE DESIGN FOR THE EXTRACTOR PLATE WITH A GRID IS SHOWN, AND ON THE RIGHT, THE DESIGN FOR THE EXTRACTOR PLATE WITHOUT A GRID.*

2.2.2. VMI Image Reconstruction Methods

Despite the great advantage of the development of VMI, the Newton spheres are “crashed” against the detector plane, i.e. the ion image represents a 2D projection on a plane of the 3D object. Then, the analysis of the 2D images requires a reconstruction of the images to obtain information about the velocity and anisotropy of the photofragments.

Numerous approaches are available for the reconstruction of VMI images, being the symmetry that appears in the two-dimensional image the deciding factor behind which one to use. This symmetry is defined by the laser pulses' polarization vectors. In cases where the image possesses a cylindrical geometry, indicated by the laser pulses' polarization vectors being parallel both amongst themselves and to the detector plane, inversion techniques are applied.

Alternatively, for images where cylindrical symmetry is not observed, direct convolution techniques must be used [31].

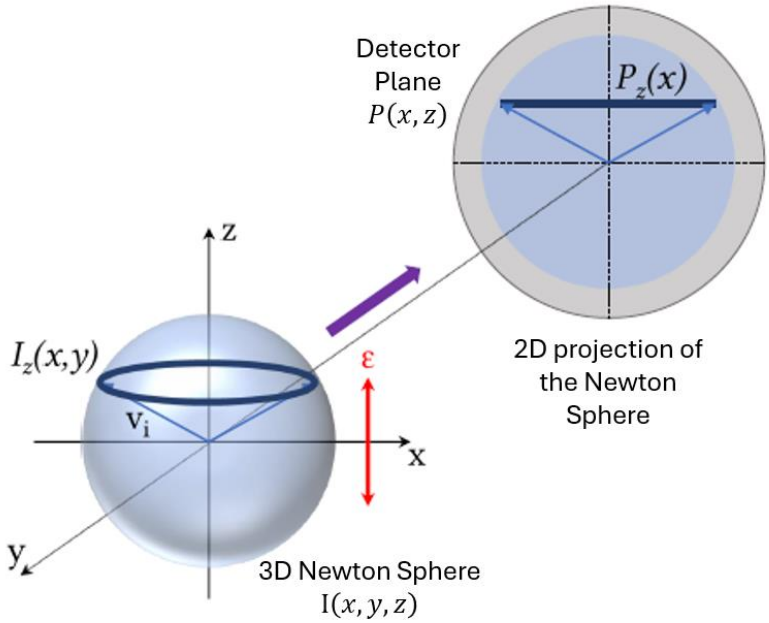

FIGURE 2.10: *SCHEMATIC REPRESENTATION OF NEWTON'S SPHERE WITH CYLINDRICAL SYMMETRY ALONG THE Z-AXIS AND ITS PROJECTION ONTO THE DETECTOR PLANE. THE DETECTOR IS POSITIONED PERPENDICULARLY TO THE Y-AXIS, WHICH IS THE PROPAGATION DIRECTION (INDICATED BY THE PURPLE ARROW). THE LASER PULSES PROPAGATE ALONG THE X-AXIS, WITH THEIR POLARIZATION VECTOR (ε) ALONG THE Z-AXIS.*

Direct convolution techniques consist of creating a simulation of the experiment based on a series of 2D images derived from the initial 3D distributions. Through an iterative process, this simulation is matched against experimental data until the outcome agrees with the experimental results [32]. Due to the complexity behind the mathematical development of said method and since it was not used in any experiment presented in this Thesis, it will not be further explained here. We will center, instead, on the inversion methods.

Figure 2.9 shows the Newton sphere made of an intensity function in the three-dimensional space $I(x,y,z)$. Any given cross section of said sphere is then defined as:

$$I_z(x,z) = \int_{-\infty}^{\infty} I(x,y,z)dy \tag{2.1}$$

For every 3D distribution $I(x,y,z)$, there are infinite projections of a 2D function with cylindrical symmetry along the z-axis, referred to as $I_z(x,y)$. Projecting these 2D functions, yields infinite series of intensity profiles for *x* across each *z* value, namely $P_z(x)$. This makes it possible to analyze the problem line-by-line, meaning that, for each distinct *z* value is possible to define the problem as a one variable function. Therefore, by focusing on a singular line along

the *x*-axis at a specific *z* value, designated as $z = z_0$, one can define a function solely dependent on x, $f(x)$. Considering this into equation (2.1), we obtain:

$$f(x) = P(x, z_0) = \int_{-\infty}^{\infty} s(x, y)dy = 2\int_{0}^{\infty} s(x, y)dy \tag{2.2}$$

where $s(x, y)$= $s(x, y, z_0)$ represents a slice of the 3D distribution that is perpendicular to the *z*-axis, the axis of cylindrical symmetry. Therefore, to extract the data encapsulated in $s(r)$, it is essential to use the experimental function $f(x)$. When cylindrical symmetry is assumed for $s(x, y)$, equation (2.2) can be transformed into polar coordinates by using the change of variable of the form $r^2 = x^2 + y^2$, leading to:

$$f(x) = 2\int_{x}^{\infty} \frac{s(r)r}{\sqrt{r^2 - x^2}} dr \tag{2.3}$$

Equation (2.3) is known as the Abel transform and is the basis for several image reconstruction methods[33]. The inverse Abel transform can be obtained by applying a Fourier Transform (FT) to equation (2.3) and by doing a variable change of the kind $r^2 = x^2 + y^2$:

$$s(r) = \frac{1}{\pi}\int_{r}^{\infty} \frac{df/dx}{\sqrt{x^2 - r^2}} dx \tag{2.4}$$

By combining equations (2.2)-(2.4), it is possible to perform the reconstruction of the initial distribution *s(r)* for every segment $P_z(x)$ within the projected image. However, the process of integrating equation (2.4) can be challenging, notably due to a singularity when $r^2 = x^2$, which in turn causes the enhancement of noise levels when in proximity to said singularity. As a result, noise amplification occurs along the symmetry axis of the image. Given that images might display asymmetries attributed to noise or discrepancies between the ionization laser's bandwidth and the Doppler profile of the fragments, Smith and Keefer [34] suggested to apply a FT to equation (2.2):

$$F\{f(x)\} = \int_{-\infty}^{\infty}\int_{-\infty}^{\infty} s\left(\sqrt{x^2 + y^2}\right) e^{-2\pi i x q} dxdy \tag{2.5}$$

Since the cero order Bessel function is defined as:

$$J_0(z) = \frac{1}{2\pi}\int_{0}^{2\pi} e^{-iz\cos\theta} d\theta \tag{2.6}$$

then the following expression is obtained by doing a change into polar coordinates on equation (2.5):

$$F\{f(x)\} = 2\pi \int_0^\infty rs(r)J_0(2\pi rq)dr \tag{2.7}$$

In this equation, the right-hand side represents the zero-order Hankel transform of $s(r)$. Given that the Hankel transform has the property of being its own inverse, it is possible to retrieve the original distribution $s(r)$ by applying the Hankel transform to the Fourier transform of the projected intensity,

$$s(r) = H[F\{f(x)\}] = 2\pi \int_0^\infty qJ_0(2\pi rq)\left[\int_{-\infty}^\infty f(x)e^{-2\pi xq}dx\right]dq \tag{2.8}$$

This equation greatly reduces the problem of high noise amplification at the singularity point. However, it does not completely erase it since the Bessel function has a high oscillation intensity for values close to zero [35].

Another approach to the inversion was introduced by Reisler and her team [36]. This method involves using a collection of base functions for the expansion of the original 2D projection. These base functions are analytical projections resembling Gaussian shapes. The coefficients from this expansion carry the essential details required for reconstructing the 3D velocity distribution. Named the BASEX method, short for Basis Set Expansion, this technique allows for the reconstruction of the 3D distribution to be expressed *via* two coordinates, $I = I(r, z)$, where *z* denotes the image's axis of symmetry and *r* the distribution's radius. Consequently, this function projection onto the detector plane can be articulated through the Abel integral,

$$P(x, z) = 2\int_{|x|}^\infty \frac{rI(r, z)}{\sqrt{r^2 - x^2}}dr \tag{2.9}$$

The experimental measurement of the projection $P(x, z)$ occurs in a two-dimensional space, represented as $(x_i, z_i) = (i, j)$; and is dependent on the pixel count of the Charged Coupled Device (CCD) camera, used to observe the 2D Newton spheres. The overall number of pixels is described by $N_x \times N_y$, which usually falls within the range of 105 to 106 pixels. Consequently, this process yields a digitized projection function, P, with specific elements P_{ij} based on:

$$P_{ij} = 2\int h(x - x_i, z - z_i)dxdz \int_{|x|}^\infty \frac{rI(r, z)}{\sqrt{r^2 - x^2}}dr \tag{2.10}$$

where the function $h(x, z)$ serves as an instrumental function. For the BASEX technique, the function $I(r, z)$ is expanded into base functions $f_k(r, z)$ in the following manner:

$$I(r,z) = \sum_{k=0}^{k-1} C_k f_k(r,z) \tag{2.11}$$

This allows the velocity distribution function $I(r,z)$ in 3D, and its projection, to be described as an expansion of the base set using coefficients:

$$P_{ij} = \sum_{k=0}^{k-1} C_k G_{kij} \tag{2.12}$$

where G_{kij} can be expressed as:

$$G_{kij} = 2\int\int h(x-x_i, z-z_i)dxdz \int_{|x|}^{\infty} \frac{r f_k(r,z)}{\sqrt{r^2-x^2}} dr \tag{2.13}$$

This expression can be rewritten in matrix form as $P = CG$ where *C* is the coefficient vector $C = (C_0, \dots, C_{k-1})$ and *G* is the base projection matrix $G = (G_0, \dots, G_{k-1})^T$.

Given that the number of base functions could potentially be greater or lesser than the CCD camera's pixel count, it is possible for the problem to either have too many degrees of freedom or to be over constrained. In the former case, the inverse of *G* (G^{-1}) cannot be established, yet it is essential for calculating the coefficients *C*. To resolve this, Tikhonov [37] introduced a regularization method detailed as follows:

$$C = PG^T(GG^T + q^2 I)^{-1} \tag{2.14}$$

where q represents the regularization parameter and I denotes the identity matrix. After deriving the C matrix in line with equation (2.14), it becomes possible to reconstruct the inverted image using equation (2.11). While the BASEX approach is an improvement over earlier techniques, it still does not fully address the issue of noise present along the symmetry axis of the image.

In all previously discussed, image reconstruction methods introduce noise along the image's symmetry axis, potentially distorting the original 3D distribution velocity and angular data. To avoid this issue, García and his team [38] introduced the pBASEX method. This approach introduces the use polar coordinates over cartesian ones, better aligning with the symmetrical nature of radiation-matter interactions in the gas phase. Due to the nature of this coordinate shift, the noise from the 3D distribution reconstruction tends to be focused on the center of the image, which is usually (although not always) an area where there is no critical information.

2.2.3. Slice Imaging Methods

As described in Section 2.2.1, the Velocity Map Imaging (VMI) technique marked a breakthrough in performing molecular photodissociation experiments. Nonetheless, it encounters two primary challenges: noise production along the image's axis of symmetry or its center during reconstruction, and the requirement for cylindrical symmetry throughout the experiment to be able to be applied. To address these issues, the VMI method coupled with the ion slicing technique, known as Slice imaging (SI), was introduced [39], [40], [41].

Slice imaging focuses on capturing the central slice (thus the name) of the Newton sphere. Consequently, the slice image provides directly the angular and velocity distributions of the fragment resulting from the photodissociation process under investigation, by-passing the needs for the use of image reconstruction techniques. The basic principle for this method to work consists of "stretching" the Newton sphere on its propagating direction, so the central slice is only measured discarding the rest by using a short duration gating on the detector.

This method was first introduced by Kitsopoulos and coworkers [39], who called it Pulsed Field Velocity Tomography, or simply *Pulsed Slicing*. Soon later both, Suits [40], and Liu [41], presented separately an experimental setup named Continuous Field Velocity Map Imaging, or *DC slicing*. The main distinction between these slicing techniques is the method by which the ion sphere is elongated. These techniques are widely recognized and frequently cited in scientific literature, though they are not the only slice imaging methods available. Figure 2.11 shows different slice imaging approaches and highlights the distinctions between them [42].

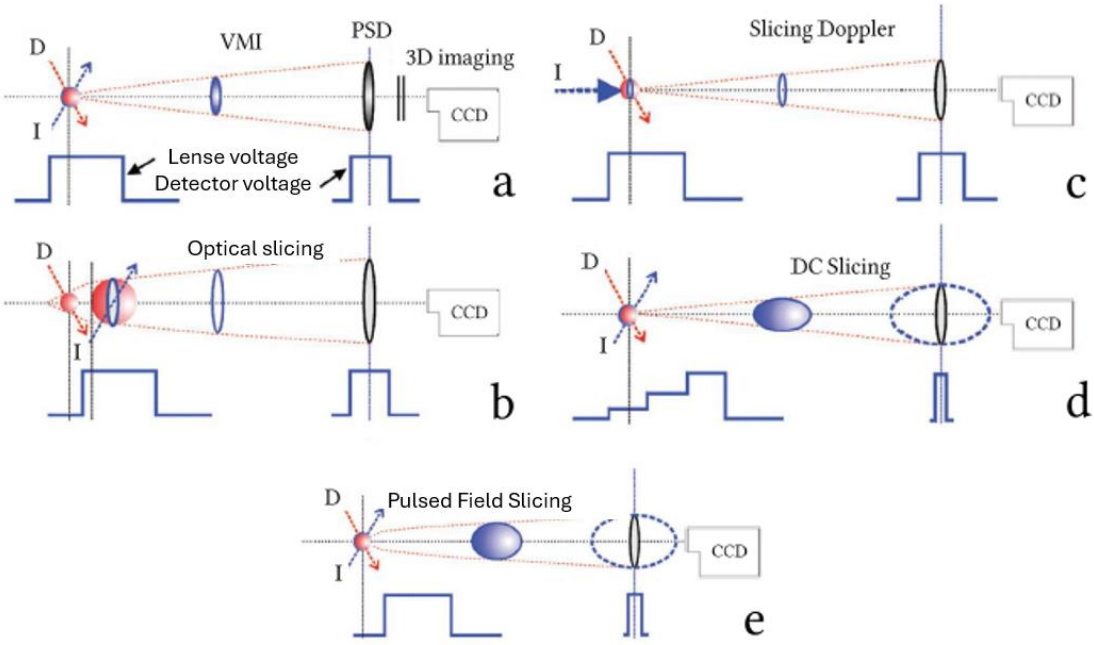

FIGURE 2.11: *COMPARATIVE FIGURE OF DIFFERENT EXPERIMENTAL SLICE IMAGING (SLICING) METHODS. IN ALL CASES, THE SOLID BLUE LINES REPRESENT THE DURATION AND INTENSITY OF THE VOLTAGES APPLIED TO THE EXTRACTOR LENSES AND THE TEMPORAL GATE OF THE DETECTOR. IN THE EXTRACTION PULSE REGION, THE*

TEMPORAL POSITION OF THE DISSOCIATION (D) AND IONIZATION (I) LASER PULSES IS SHOWN RELATIVE TO THE EXTRACTION PULSE ITSELF. (A) NORMAL VMI TECHNIQUE. (B) OPTICAL TOMOGRAPHY OR OPTICAL SLICING. (C) DOPPLER TOMOGRAPHY OR DOPPLER SLICING. (D) CONTINUOUS FIELD TOMOGRAPHY OR DC SLICING. (E) PULSED FIELD TOMOGRAPHY OR PULSED FIELD SLICING. FIGURE ADAPTED FROM REFERENCE [42].

Figure 2.11(b) shows the *Optical Tomography* or *Optical Slicing*. Here, the voltage used for extraction is not applied until the fragments have been ionized by the ionization laser (I). Following the creation of fragments by the dissociation laser (D) a delay of several tens of nanoseconds permitting the 3D distribution to expand, the ionization laser then targets only the central section of the 3D distribution for ionization, which is subsequently extracted by an applied electric field. Initially, Suzuki and his team [43] suggested the use of cylindrical lenses to focus the laser pulse into a linear shape that is perpendicular to the molecular beam. Subsequent approaches introduced the use of spherical lenses for implementing this tomographic technique [42]. Thanks to the employment of these focusing techniques, the method achieves a high degree of precision in isolating the central slice of the distribution. This precision significantly enhances the resolution of the velocity distributions derived from the tomographic process. The fine focus lines required, approximately 50 µm thick, allows for an improved resolution in the results when compared to earlier VMI techniques. However, it is important to note that achieving such focused laser beams requires precise optical alignment and uniform laser illumination.

Doppler map imaging is another method of the family of slicing techniques (Figure 2.11(c)). Here, a narrow-band laser selectively ionizes molecules whose speed in the direction of the beam's propagation is zero. For this to be accomplished, both the laser and the molecular beam must propagate in the same direction. This requirement makes Doppler tomography challenging to apply in molecular photodissociation experiments, where the pulsed valve and detector are aligned, making it very difficult to, on top of that, introduce the laser. Nonetheless, Arikawa and his team [44] successfully applied this technique to investigate HBr photodissociation. Conversely, this technique proves highly beneficial for reactive scattering studies involving crossed molecular beams [45], where the molecular beam's direction aligns parallel to the detector plane.

As mentioned earlier, both Optical and Doppler Tomography methods focus on ionizing the central slice of the initial 3D distribution. Therefore, a standard gate featuring a temporal width around 100 ns is typically employed. On the other hand, techniques like *Pulsed Field Slicing* and *DC slicing* (Figure 2.11(d-e)), which target the ionization of the entire 3D distribution, need a significantly narrower gate, approximately 20 ns in duration. These techniques force the expansion of the 3D ion distribution over several hundred nanoseconds, allowing for the isolation of the central slice through a narrowly timed gate. The key distinction between these methods lies in their respective mechanisms for achieving such expansion. In the case of DC slicing (Figure 2.11(d)), the expansion is a result of gradually accelerating the ion sphere, a process made possible by an extraction system devised by Suits and his team (Figure 2.12). Within this four-lens setup system, the ion sphere initially expands between the repeller plate and the L1 lens. The voltage of this lens is set to roughly 0.88 of the repeller plate's voltage. The L2 lens then adjusts the size of the projection on the detector, with its voltage at about 0.72 of the repeller plate's voltage. The L3 lens subsequently reinstates the velocity tomography conditions. A significant challenge of this approach is that a lower repeller plate voltage leads to more extensive ion sphere expansion, adversely affecting the detector's ion impact sensitivity. For this reason, Suits and his team established a minimum voltage threshold for the repeller plate at 500 V.

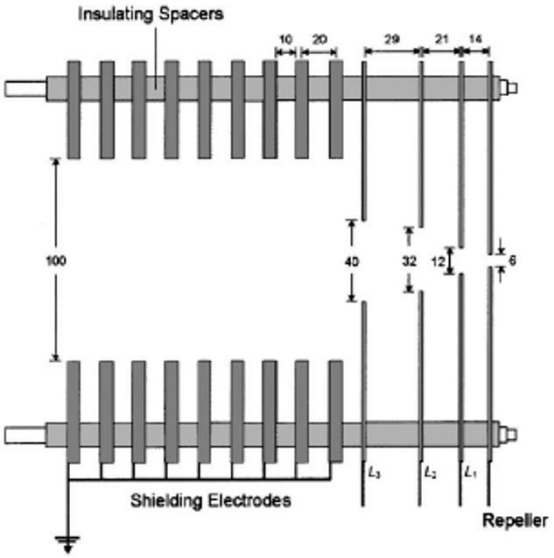

FIGURE 2.12: *SCHEMATIC REPRESENTATION OF THE EXTRACTION SYSTEM DESIGNED BY SUITS AND COLLABORATORS* [40] *FOR PERFORMING CONTINUOUS FIELD (DC) VELOCITY MAP IMAGING. THE DIAGRAM SHOWS THE FOUR LENSES USED (REPELLER, L1, L2, AND L3) TO PROGRESSIVELY ACCELERATE THE ION SPHERE. FOLLOWING THE LENSES ARE SHIELDING ELECTRODES THAT ISOLATE THE ION CLOUD FROM POTENTIAL DISTURBANCES.*

2.3 VMI Setup in Madrid

2.3.1. Vacuum chambers

Most of the experiments detailed in this PhD Thesis were conducted using the VMI machine installed at CLUR (UCM, Madrid), as shown in Figure 2.13. The apparatus consists of three distinct vacuum chambers: an initial expansion chamber for generating the molecular beam, a subsequent ionization chamber where the molecular beam encounters and interacts with the laser beams, and finally, a detection chamber where ions formed in the ionization chamber are detected.

To carry out these experiments, it's critical to keep the stainless steel chambers under high vacuum conditions, so any other molecule or atom external to the experiment interfere with the measurement. This is achieved using a combination of turbomolecular, rotary, and dry pumps to create a differential vacuum across the machine's various sections. For instance, in the expansion chamber, the largest and under highest gas pressure, an Agilent Turbo-V Twistorr turbomolecular pump with a 2000 L s^{-1} pumping capacity is connected to an Agilent TriScroll 600 dry pump with a 30 $m^3 h^{-1}$ pumping capacity (blue arrow in Figure 2.13), to ensure the chamber's pressure stays between 10^{-7} and 10^{-8} mbar under non-working conditions, and between 10^{-5} and 10^{-6} mbar during operation. The ionization chamber, separated from the expansion chamber by a conical boron-nitrite skimmer (Beam Dynamics Standard model 2) with an orifice of 0.6 mm diameter, makes use of a Pfeifer TMU 261 turbomolecular pump (210 L s^{-1} pumping speed) linked to a Ecodry 25 plus pump (25 $m^3 h^{-1}$ pumping speed), maintaining a pressure in the realm of 10^{-7}-10^{-8} mbar, which shifts to 10^{-6}-10^{-7} mbar during active experiments. Finally, the detection

chamber employs a Pfeifer HiPace 300 turbomolecular pump with a 255 L s^{-1} capacity, paired with another dry pump like that used in the ionization chamber, keeping its pressure in the range 10^{-8}-10^{-7} mbar under working conditions. Pressures across all chambers are measured by Penning-type pressure gauges (Pfeifer Vacuum PKR 251 and 250), capable of measuring pressures from atmospheric levels down to 10^{-9} mbar, making them incredibly versatile for the wide range of pressures encountered.

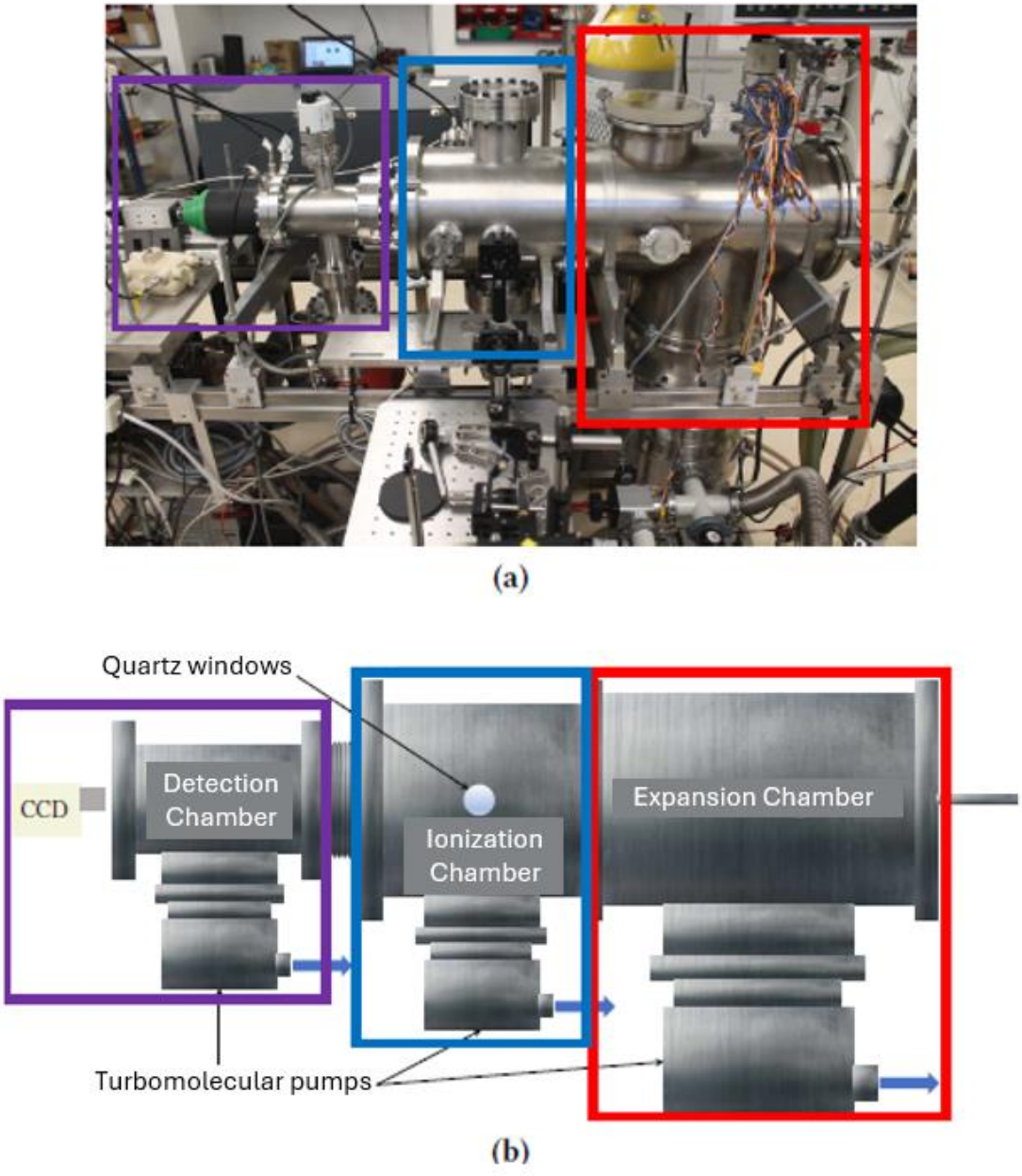

FIGURE 2.13: *(A) PHOTOGRAPH OF THE VELOCITY MAPPING MACHINE WITH ION IMAGING AT CLUR, UCM, MADRID. (B) SCHEMATIC REPRESENTATION OF THE THREE CHAMBERS THAT FORM THE APPARATUS. FROM RIGHT TO LEFT, THEY ARE THE EXPANSION CHAMBER, OUTLINED BY THE RED RECTANGLE, THE IONIZATION CHAMBER, BY THE BLUE RECTANGLE, AND THE DETECTION CHAMBER, BY THE PURPLE RECTANGLE.*

The experimental process is divided into three distinct stages. First, a supersonic expansion is generated *via* a pulsed valve within the expansion chamber. In the second stage, a molecular beam is generated, and it undergoes interaction at a perpendicular angle with both, the pump laser (responsible for exciting and breaking apart the molecules) and the probe laser (which serve to ionize the generated fragments). In the final stage, the ions that are created in the ionization chamber are then collected and guided to the detector for identification. Detailed explanations of each phase are provided in the sections that follow.

2.3.2. Molecular beam generation system

A molecular beam consists of a directed stream of molecules that have been cooled down in terms of both internal and translational energy. The molecules are cooled by a process known as supersonic adiabatic expansion, which happens when they pass through a small orifice and experience a rapid change in pressure. On the valve's reservoir side, the molecular pressure is significantly higher, often several atmospheres, but drops to about 10^{-5} to 10^{-6} mbar in the expansion chamber. This process is depicted in Figure 2.14, illustrating the various stages of the expansion. As the valve opens, molecules move from a high-pressure region to a much lower-pressure one, undergoing numerous collisions that generate phenomena like the Mach disk and shock barrier. This phase of expansion and the resulting molecular cooling continue until the collisions stop. The region where collisions no longer occur, and the molecular jet cools down is known as the silence zone. Here, the shock barrier and the Mach disk act as barriers, preventing the cooler molecules within this zone from interacting with those in the remainder of the expansion chamber.

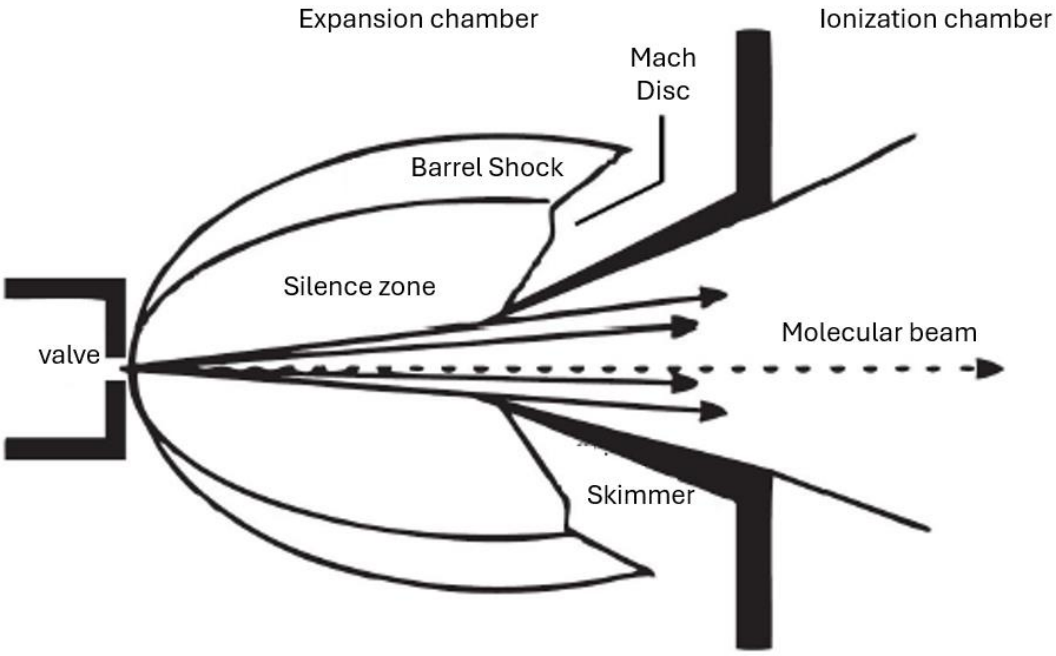

FIGURE 2.14: *DIAGRAM OF A SUPERSONIC JET FROM A CAMPARGUE STYLE MOLECULAR BEAM* [46].

After undergoing expansion, the molecular jet continues to a conical collimator, commonly referred to as skimmer, which orifice can have different diameters depending on the size of the beam you want to create, the one used in this Thesis has an orifice diameter of 0.6 mm. This skimmer functions as a spatial filter, selectively permitting only molecules from the axial region of the jet—those within the silence zone—to pass through. Consequently, this process results in the formation of a molecular beam where the molecules travel in parallel paths without colliding, although with a slight spread in their trajectories.

Molecular beams can either be pulsed, delivering molecules in short bursts, or continuous, providing a steady stream. The VMI machine at CLUR, utilizes a pulsed molecular beam for its experiments. To create a pulse molecular beam, a General Valve Series 9 is used. The valve is a solenoid-type capable of operating in either continuous or pulsed modes. The controller can set the frequency of its pulses to align with the lasers' repetition rate at 10 Hz, as well as the pulse's duration. A schematic of the valve, as depicted in its manual, is presented in Figure 2.15. The solenoid and a cylindrical magnet are combined to open the valve; an electric current through the solenoid draws the magnet towards it, pulling open the sealing joint, or poppet (which is conical for the valve in use), and thus the orifice opens allowing for the molecules to go through. Cutting the current allows the magnet to revert to its original position, sealing the orifice back. A damping spring is incorporated to ease the magnet's return, mitigating any potential for damage or wear. The poppet, essential for the valve operation, can be crafted from a variety of materials, including polytetrafluoroethylene (PTFE), as for the experiments described here. To prevent leaks, an O-ring seals the valve interior from its external environment within the expansion chamber. After the molecular beam travels through the skimmer, it goes to the ionization chamber, where it interacts with both pump and probe laser pulses, marking the next phase of the experiment.

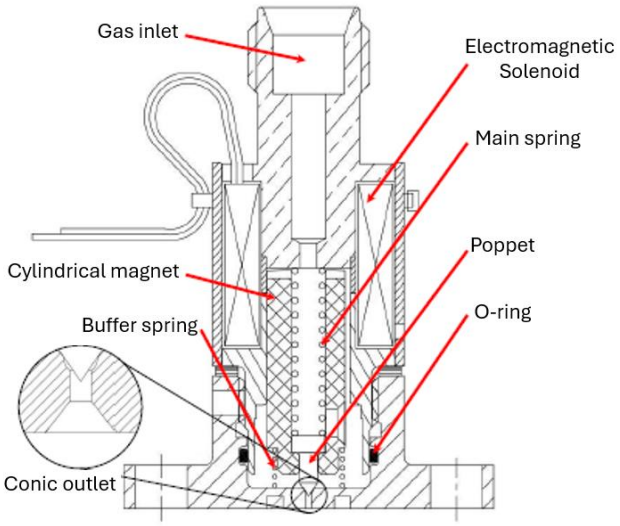

FIGURE 2.15: *DIAGRAM OF A SERIES 9 GENERAL PULSED VALVE TAKEN FROM ITS OWN MANUAL.*

2.3.3. Continuous and pulsed ion extraction system

After the photodissociation, the Newtons spheres expand in all directions of the space, however, the detector is placed further away for the interaction region between the molecular

and lasers beams. To be able to measure the ions produced, they must be extracted and send to the detector. This is achieved using a plate system (illustrated in Figure 2.16), which is based on a design by Papadakis and Kitsopoulos [47] (refer to Figure 2.9) but has been modified for compatibility with the velocity mapping system used in the Madrid setup.

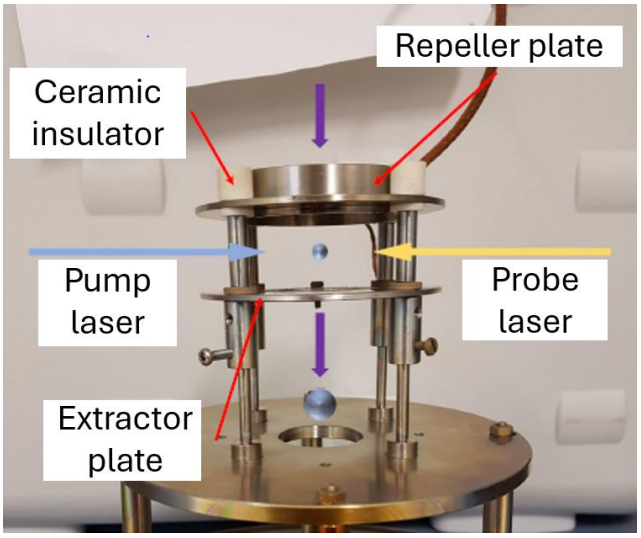

FIGURE 2.16: *PLATE SYSTEM OF THE VELOCITY MAPPING SYSTEM IN MADRID FOR EXTRACTING IONS FORMED AFTER DISSOCIATION. IN THE IMAGE, IT CAN BE DISTINGUISHED THE EXTRACTOR AND REPELLER PLATES, AS WELL AS THE CERAMIC INSULATORS RESPONSIBLE FOR ISOLATING THE HIGH VOLTAGE APPLIED TO THE REPELLER PLATE. THE PURPLE ARROWS INDICATE THE PROPAGATION OF THE MOLECULAR BEAM AND THE EXTRACTION DIRECTION OF THE NEWTON'S SPHERE.*

This setup, which includes a repeller plate and an extractor plate, simplifies the ion extraction process by requiring only a positive voltage to be applied to the repeller plate, propelling the ions towards the detector, while the extractor plate is grounded. Ceramic insulators are incorporated to ensure the high voltage on the repeller plate is isolated from the rest of the extraction system. Thanks to this innovative design, the system can operate in both VMI and Slicing modes when working with ion images. In order to work with the VMI, the system conditions previously defined must be applied.

In this Thesis, a single-field configuration with two plates, the repeller plate and the extractor plate, has been employed. Unlike configurations requiring specific voltage ratios for velocity mapping, this setup achieves the desired conditions by adjusting the position of the laser-molecular beam interaction region relative to the repeller plate. Applying voltage only to the repeller plate simplifies control, as the flight time of particles, and thus the image size, depends mainly on this parameter. The VMI (velocity map imaging) conditions are determined by the initial ion position along the time-of-flight axis relative to the repeller plate, with the self-focusing point set by the lens geometry rather than the electric field.

When working with the Slicing technique, the machine needs to change to Slicing mode. For that, first it is necessary to be in VMI conditions. Once the conditions are met, the repeller voltage is switched from continuous to pulsed signal, and a delay between ionization and extraction of, typically, 400-500 ns is employed, which generates a difference in the arrival times of the ion distribution of the same mass of approximately 200 ns. The time gate applied to the

detector has a width of approximately 20 ns, allowing the ion cloud, ellipsoidal in shape, to be sliced in sections of 10%. The selection of the central part of the distribution, which is the area containing the complete distribution information, is done by defining the rings or structures present and their radius. The central section will have a larger size and higher resolution due to the lower curvature of the ellipsoid. The selection of the central slice is hard, as it involves a series of image acquisitions at different delays in the time gate and subsequent comparison of the images taken in this way.

Figure 2.17 shows the images corresponding to the $CH_3(v = 0)$ fragment formed in the photodissociation of CH_3I at 333.45 nm, obtained at different time delays in the detector's time gate. The delay used in the extraction of these images was 400 ns, which gives us a total distribution of the cloud with a temporal width of approximately 200 ns. Each of the images in Figure 2.17 corresponds to sections of the distribution of 20 ns, spaced 20 ns apart.

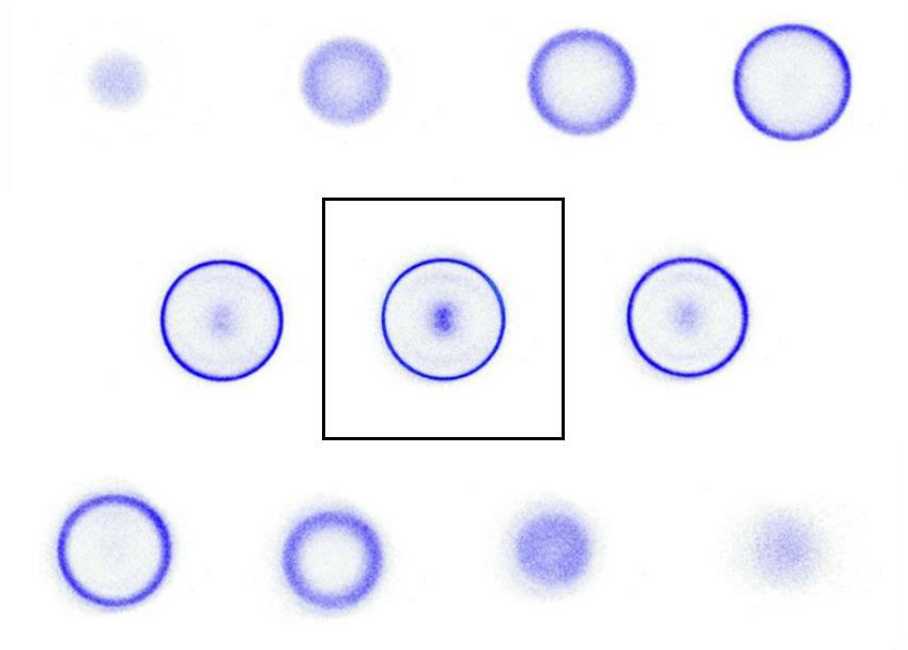

FIGURE 2.17: *SLICING STUDY OF THE DIFFERENT CONSTITUENT SECTIONS OF THE NEWTON SPHERES OF $CH_3(v = 0)$ OBTAINED IN THE PHOTODISSOCIATION OF CH_3I AT 333.45 NM. THE CENTRAL IMAGE FRAMED IN BLACK CORRESPONDS TO THE CENTRAL SECTION OF THE CLOUD, WHICH CONTAINS DIRECTLY ALL THE INFORMATION RELATED TO ANGULAR AND VELOCITY DISTRIBUTIONS.*

If we perform the same experiment using VMI and compare the results between the two techniques Figure 2.18, we observe that the VMI shows greater intensity due to the detection of the entire sphere. The tomographic image, however, shows greater sharpness (higher resolution), allowing us to observe photodissociation features that are not clearly visible in the VMI image, even after inversion of the VMI images.

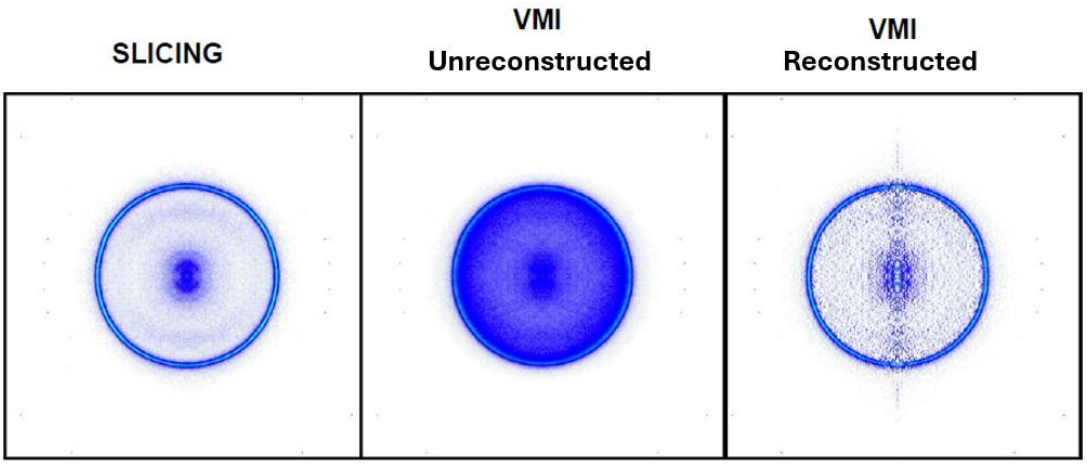

FIGURE 2.18: *COMPARISON BETWEEN THE $CH_3(v = 0)$ IMAGES OBTAINED USING THE INVERTED AND NON-INVERTED VMI IMAGES, AND THAT OBTAINED BY PULSED FIELD SLICING, CORRESPONDING TO THE PHOTODISSOCIATION OF CH_3I AT 333.45 NM. IN THE RECONSTRUCTED VMI IMAGE, WE CAN OBSERVE THE NOISE GENERATED BY USING RECONSTRUCTION METHOD, WHICH APPEARS VERTICALLY IN THE CENTRAL PART OF THE IMAGE.*

2.3.4. Detection system

To observe the Newton's sphere produced by the interaction of the molecular beam and laser pulses, a flat detector sensitive to the position of charged particles (such as ions and electrons) is required. This detector consists of a pair of electron-multiplying microchannel plates (MCPs) and a phosphor screen located inside the detection vacuum chamber. Following that, a Charged Coupled Device (CCD) camera is positioned externally at a suitable distance to clearly capture the images from the phosphor screen. This arrangement enables precise measurement and analysis of the ions' positions and trajectories following photodissociation.

In Figure 2.19 both the frontal and lateral perspectives of the detector employed within the Madrid VMI apparatus can be seen, detailing the components that comprise it. Meanwhile, Figure 2.20 provides a diagram illustrating the setup of the charged particle detector alongside the CCD camera, offering insight into the arrangement and function of each part within the system.

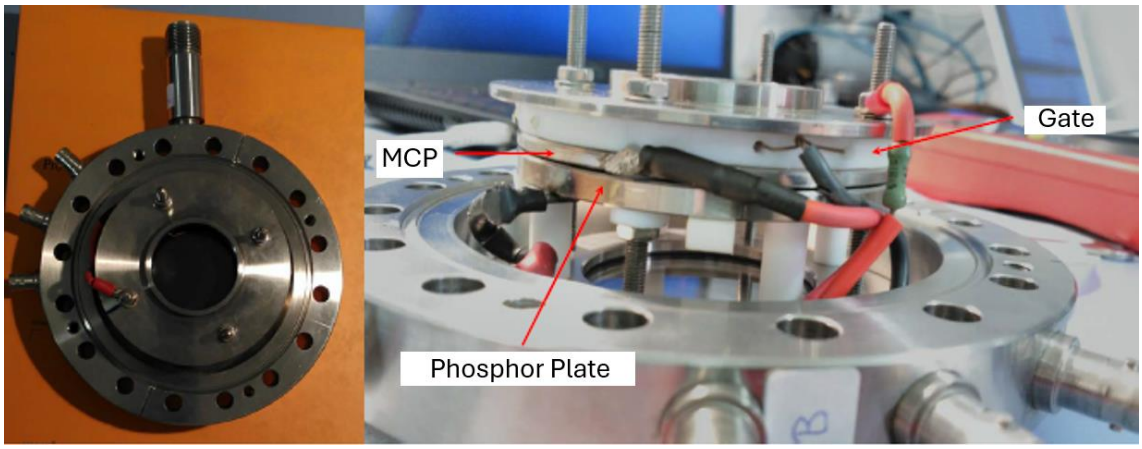

FIGURE 2.19: *POSITION SENSITIVE CHARGED PARTICLES DETECTOR (TOP VIEW ON THE RIGHT AND SIDE VIEW IN THE LEFT). THE DETECTOR CONSISTS OF TWO MCP PLATES AND A PHOSPHOR SCREEN.*

When striking the detector, ions first encounter the microchannel plates (MCPs), which consist of electron-multiplying channels, each 10 µm wide, set at an angle of about 5-9 degrees, as specified by the manufacturer Baspik, distributed by Topag. Arranged in series in a V-shaped Chevron configuration, these MCPs are designed to amplify the initial ion impact by generating an electron cascade when a differential voltage is applied across them. This amplification process results in the creation of approximately one million electrons for every ion that hits the MCPs. Exiting the second MCP, these electrons strike a phosphor-coated screen provided by PROXIVISION, where the energy of the electron avalanche is enough to trigger a phosphorescent glow, translating the physical impact into a visible signal. This glow is then captured by the CCD camera, and the image analyzed to extract all the information of the photodissociation process. Thus, an ion's collision with the detector yields two outcomes: an electrical pulse monitored by a digital oscilloscope, providing mass spectrum data based on the ions' time-of-flight, and a visual representation, the two-dimensional projection of the ions' Newton's spheres, captured as an image by the CCD camera. This dual-signal generation allows for a comprehensive analysis of the ions' characteristics and behavior upon impact.

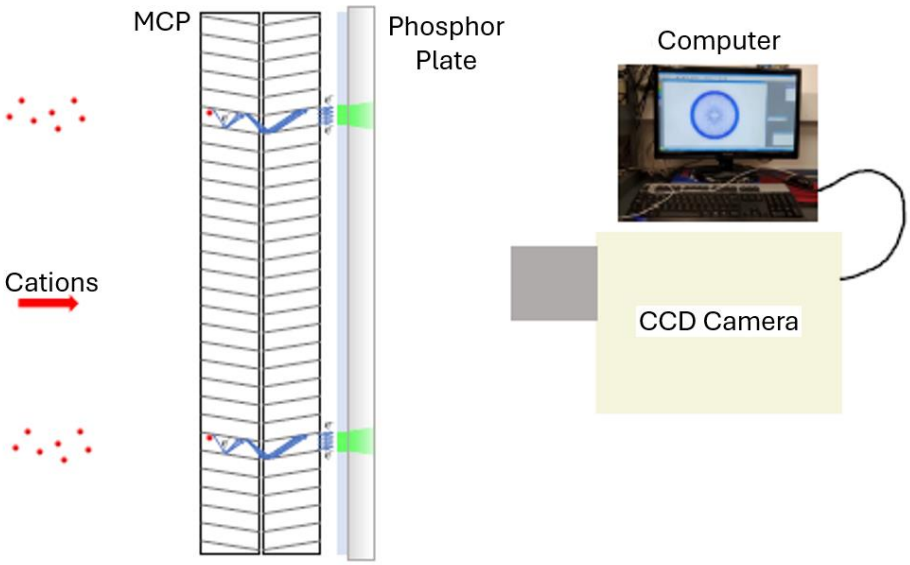

FIGURE 2.20: *SCHEMATIC REPRESENTATION OF THE SETUP COMPRISING THE CHARGED PARTICLE DETECTOR (IONS, ELECTRONS) AND THE CCD CAMERA. WHEN THE CATIONS, EXTRACTED AFTER DISSOCIATION, HIT THE MCPS, THEY PRODUCE AN ELECTRON CASCADE WITH A GAIN OF* $\sim 10^6$. *THE ELECTRON AVALANCHE STRIKES THE PHOSPHOR SCREEN, CAUSING GREEN PHOSPHORESCENT EMISSION, WHICH IS RECORDED BY THE CCD CAMERA.*

In a standard experiment, the CCD camera captures images that represent the ion spheres of each ionized fragment resulting from the photodissociation process. To isolate the image of a specific fragment, the detector's sensitivity, or gain, is reduced except when the desired ion or central slice of the Newton sphere arrives at the detector. This procedure, known as gating, involves applying a +500 V constant voltage on the front surface of the first MCP. Then, at a moment that correlates with the unique time-of-flight of the desired ionic fragment, a very short pulse (about 20 ns) of zero voltage is applied. As a result, the detector's sensitivity to ions arriving at times other than that of the targeted fragment is significantly reduced, enabling the capture of images for each type of fragment. This method ensures that ion images can be individually obtained for detailed study.

2.3.5. Experiment synchronization

All the different parts described above that are involved in the experiment must be synchronized. This synchronization is crucial so laser radiation arrives at the interaction region when the molecule is passing through, therefore, the gas and laser pulses must have the same frequency, 10 Hz for the experiments presented in this Thesis. It is also important that the temporal gate controlling which ion is detected must open at the specific time that the ion arrived, and not before or after. A digital pulse generator (DPG, Berkeley Nucleonics Corporation - BNC) is used for this purpose. This apparatus generates TTL pulses with a variable delay based on a reference time, t_0, that can be internal or external. For the experiments described in this Thesis and performed in the laboratory of Madrid, the reference time is internal. By setting different time delays between the firing lamps of both Nd:YAG lasers we can control the delay between the pump and probe lasers as well as the delay with the opening of the valve. In this

way, we can assure that the laser pulses interact with the pulse of molecules. In addition, the DPG controls the pulse extraction field to elongate the ion cloud when using the slicing technique. This is achieved by adding a high voltage (HV) switch to the repeller voltage. Moreover, another delay is set for the gate switch that selects the ions of interest, so the detector gain is low only when the desired ion, or slice of the Newton sphere, arrives at the detector. Figure 2.21 shows a schematic representation of how all the equipment and apparatuses of the experiment are connected, including the DPG controller and the HV sources to the experimental chamber.

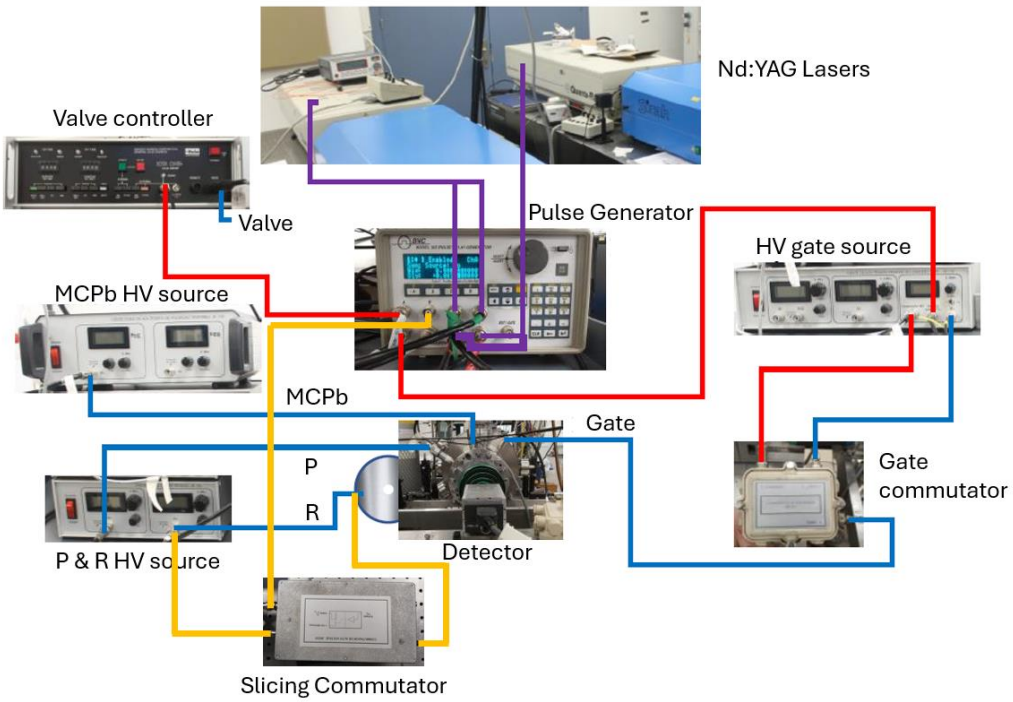

FIGURE 2.21: *SYNCHRONIZATION DIAGRAM OF THE VARIOUS COMPONENTS OF THE EXPERIMENTAL SYSTEM. THE BNC PULSE GENERATOR UNIT ACTS AS A TRIGGER PULSE GENERATOR AND DEFINES A TIME T_0 FROM WHICH THE REST OF THE ELEMENTS ARE SYNCHRONIZED. THE ENTIRE SYSTEM IS SYNCHRONIZED AT A REPETITION RATE OF 10 HZ. THE RED LINES SHOW THE PULSES THAT CONTROL THE VALVE AND THE GATE, WHILE THE PURPLE LINES SHOW THE PULSES THAT CONTROL THE FIRING OF THE ND:YAG LASERS. ADDITIONALLY, THE BLUE LINES REPRESENT THE HIGH-VOLTAGE (HV) CONNECTIONS FROM THE POWER SUPPLIES TO THE VARIOUS COMPONENTS. "P" AND "R" REFER TO THE PHOSPHOR SCREEN AND THE REPELLER PLATE, RESPECTIVELY.*

2.3.6. Calibration of the speed distribution

Given the detector's sensitivity to the spatial positioning of fragments in molecular photodissociation experiments, calibration is crucial to correlate the exact pixel on the CCD camera where a specific fragment (ion) is detected with its speed. This calibration involves performing a photodissociation experiment using a reference molecule with well-documented photodissociation characteristics. Methyl iodide, CH_3I, is typically chosen for this purpose due to the extensive research detailing its photodissociation pathways [48], [49], [50]. This allows for

accurate calibration, ensuring that the speed of a fragment can be precisely determined based on its observed position within the camera's field of view.

The primary distinction in the photodissociation paths of CH_3I lies in the spin-orbit splitting of the iodine atom photoproduct, with a value of 0.943 eV. In this Thesis, the calibration process was done using a single laser at 333.45 nm to excite CH_3I and detecting (ionizing) the $CH_3(\nu = 0)$ fragment through a REMPI (2+1) scheme within the same nanosecond pulse. At this specific wavelength, CH_3I predominantly dissociates *via* the channel:

$$\mathrm{CH_3} \rightarrow \mathrm{CH_3}(\nu = 0) + \mathrm{I}\left(^2P_{3/2}\right) \tag{2.15}$$

producing an image captured using the slice imaging technique with a 400 ns pulse delay, as illustrated in Figure 2.22(a). By performing angular integration on the image, the velocity distribution of the fragments is obtained (illustrated in Figure 2.22(a)), showcasing a prominent peak attributed to the $I(^2P_{3/2})$ channel at 151.75 pixels in this case. Given the $I(^2P_{1/2})$ channel's minor presence, almost imperceptible within the velocity distribution, calibration efforts are focused solely on the $I(^2P_{3/2})$ channel.

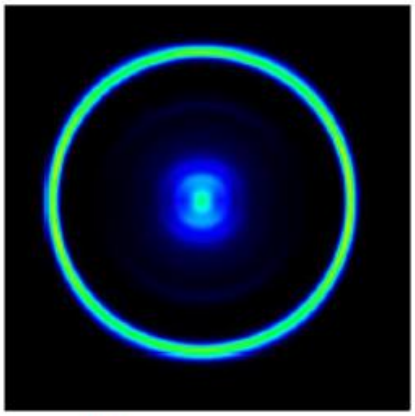

(a) Slicing image

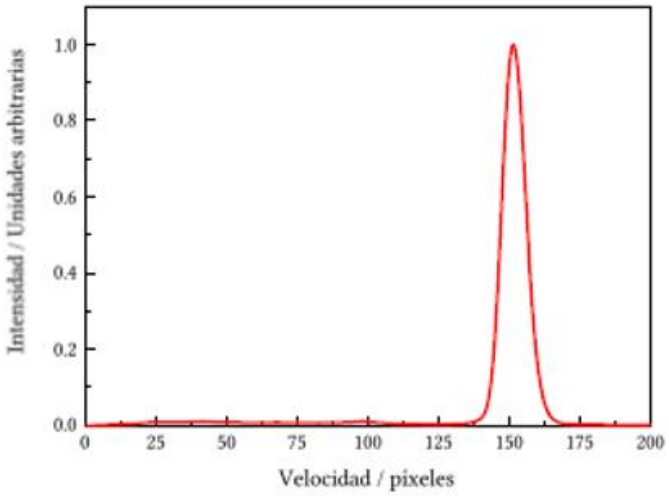

(b) Speed distribution

FIGURE 2.22: *(A) SLICE IMAGE OF THE $CH_3(\nu = 0)$ FRAGMENT FROM THE CH_3I PHOTODISSOCIATION AT 333.45 NM. (B) SPEED DISTRIBUTION, IN PIXELS OF THE CCD CAMERA, OBTAINED THROUGH THE ANGULAR INTEGRATION OF THE IMAGE.*

If the maximum translational energy associated with the $CH_3(\nu = 0)$ fragment corresponding to that channel is known, it is possible to determine the calibration constant which allows transforming the whole pixel into energy axis. The energy balance for this photodissociation channel is as follows:

$$E_T^{\mathrm{CH_3}(\nu=0)} = \frac{\mathrm{m_I}}{\mathrm{m_{CH_3I}}}\left[h\nu - D_0 + E_i(\mathrm{CH_3I}) - E_{SO}\left[\mathrm{I}\left(\,^2P_{j/2}\right)\right]\right] \qquad (2.16)$$

where $\mathrm{m_I}$ and $\mathrm{m_{CH_3I}}$ represent the masses of the Iodine fragment and methyl iodide respectably, $E_T^{\mathrm{CH_3}(v=0)}$ represents the maximum translational energy of the CH_3(ν=0) fragment at the system's center-of-mass (CM). The term *hv* refers to the photolysis laser energy. D_0 is the energy required to break the carbon-iodine bond, established at 2.410 ± 0.003 eV [21], $E_i(\mathrm{CH_3I})$ is the combined vibrational and rotational energy of the CH_3I molecule, which is considerable negligible since we are using a cold molecular beam. Finally, E_{SO} denotes the energy difference created by the spin-orbit interaction within the iodine atom's $^2P\left(E_{SO}\left[\mathrm{I}\left(^2P_{3/2}\right)\right] = 0\ eV, \mathrm{E}_{SO}\left[\mathrm{I}\left(^2P_{1/2}\right)\right] = 0.943\ \mathrm{eV}\right)$ [21].

From equation (2.16) and knowing the maximum kinetic energy of the transition, the calibration constant can be calculated as:

$$E_T = K \cdot Pix^2 \tag{2.17}$$

where *K* represents the calibration constant, and *Pix* is the pixel where the translational energy of the fragment should appear; as a reference number we used the maximum of the curve. Using this relationship, the distribution captured by the CCD camera in pixels is converted into the translational energy of the fragment. The calibration constant derived from this process applies universally to any singly charged ion and remains consistent across equal time-of-flight distances and under conditions of optimal spatial focus. However, equation (2.17) focuses solely on modifying the energy axis. To fully interpret the data, it is also necessary to consider the Jacobian's impact on the intensity axis of the distribution. This adjustment is crucial because transitioning from a velocity to a kinetic energy distribution needs a transformation that accounts for both axes to accurately reflect the change in energy parameters. Thus,

$$P(Pix)dPix = P(E_T)dE_T \tag{2.18}$$

and solving for $P(E_T)$:

$$P(E_T) = P(Pix)\frac{dPix}{dE_T} \tag{2.19}$$

since

$$dE_T = 2KPix \cdot dPix \tag{2.20}$$

Equation (2.20) yields to:

$$P(E_T) = \frac{P(Pix)}{2KPix} \tag{2.21}$$

Therefore, to apply the Jacobian, the intensity axis has to be divided by the pixel axis of the original distribution.

2.4. VMI System of FORTH (Crete, Greece)

As previously mentioned, some experiments of this PhD Thesis were conducted at the Ultraviolet Laser Facility in FORTH, Crete (Greece). The VMI apparatus equipped for ion imaging at FORTH, depicted in Figure 2.23, closely resembles the setup in Madrid. This apparatus also features a tri-chamber design, facilitating both velocity mapping and slice imaging.

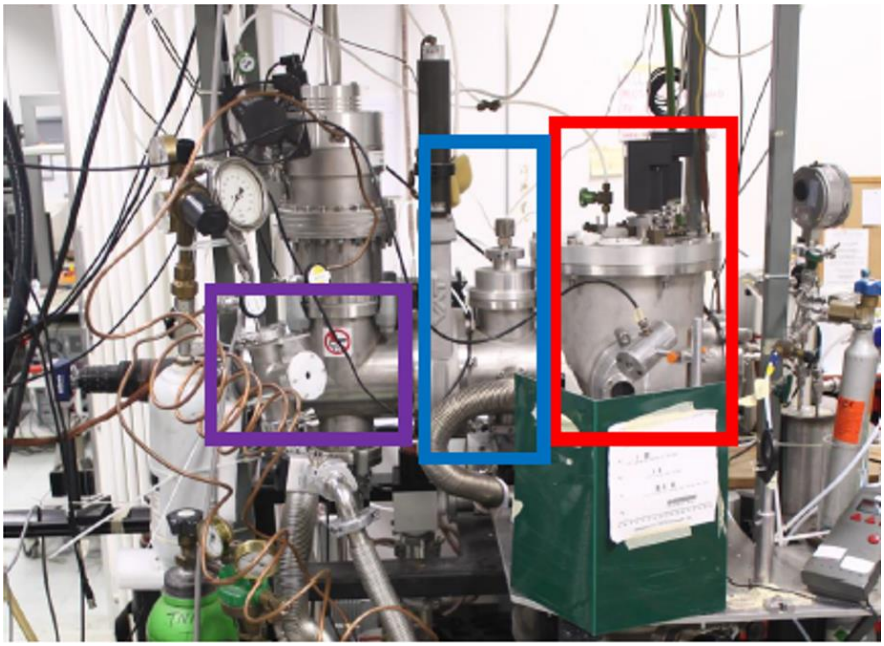

FIGURE 2.23: *VELOCITY MAP IMAGINE SYSTEM AT FORTH. THE EXPANSION CHAMBER IS MARKED WITH A RED RECTANGLE, THE IONIZATION CHAMBER WITH A BLUE RECTANGLE, AND THE DETECTION CHAMBER WITH A PURPLE RECTANGLE.*

Since the apparatus closely resembles the one in Madrid, only the main differences will be described. The main distinctions between this apparatus and the one in Madrid lie in the types of pulsed valves and extraction systems employed. Whereas the Madrid setup uses a solenoid valve, the FORTH equipment operates with a piezoelectric valve. This piezoelectric valve functions through a piezo plate that vibrates at specific frequencies when subjected to high voltage, thereby controlling the opening and closing of the valve's exit hole via a plunger mechanism. Additionally, the extraction system used at FORTH adheres to the original design crafted by Papadakis and Kitsopoulos, which was detailed earlier in Section 2.2.2. Apart from these two differences, the experimental system only differs in the lasers used.

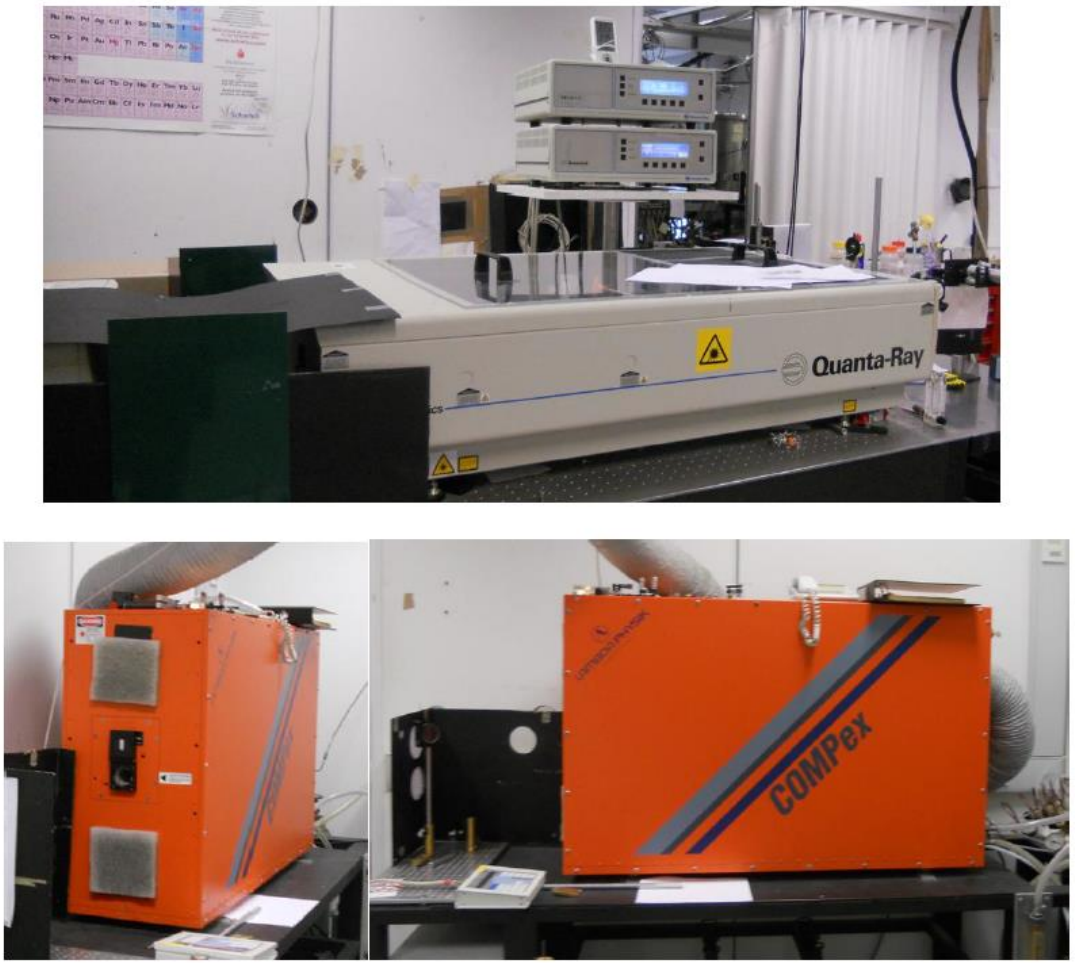

FIGURE 2.24: *PHOTOGRAPH OF THE NANOSECOND LASER SYSTEM USED AT FORTH IN CRETE TO PERFORM THE PHOTODISSOCIATION EXPERIMENTS OF CH_3NO_2 AND CH_3I AT 193 NM. THE UPPER PHOTOGRAPH CORRESPONDS TO A MOPO SYSTEM (SPECTRA-PHYSICS 730D10) PUMPED BY AN ND:YAG LASER (SPECTRA-PHYSICS PRO SERIES 450), AND THE LOWER PHOTOGRAPH SHOWS THE ARF EXCIMER LASER (LAMBDA PHYSIK COMPEX).*

In Figure 2.24, the nanosecond laser system from the Ultraviolet Laser Facility laboratory at FORTH (Crete) is shown. The upper photograph in Figure 2.24 shows the MOPO (Spectra-Physics 730D10) pumped by a Nd:YAG laser (Spectra-Physics Pro Series 450) at 532 nm. The lower photograph in Figure 2.24 shows the ArF excimer laser (Lambda Physik COMPEX). Excimer lasers are gas-phase lasers that use a mixture of a noble gas (Ar, Kr, or Xe) and a halogen gas (F_2 or Cl_2), which under suitable conditions of electrical excitation and high pressure, emit laser radiation in the ultraviolet range at fixed wavelengths depending on the gas mixture used. The argon-fluor (ArF) laser, used in this work, is a particular type of excimer laser with an emission of 193 nm.

In the ArF excimer laser, a discharge is generated over a high-pressure gas mixture, causing the Ar to react with F_2, producing the excimer monofluorinated argon (ArF), a temporary stable complex in an excited energy state. This generated complex can undergo spontaneous or stimulated emission, reducing its energy state to an unstable (highly repulsive) fundamental state. The fundamental state of the complex quickly dissociates. The result is an excimer laser that emits 193 nm, which is in the far ultraviolet region of the spectrum. The typical pulse duration for these lasers is of 10 ns and they can reach energies of up to 6 mJ.

Chapter 3 Study of the Photodissociation Pathways of Methylamine

3.1 Photodissociation dynamics of methylamine in the blue edge of the A-band. I. The H-atom elimination channel

Art. 1. *Photodissociation dynamics of methylamine in the blue edge of the A-band. I. The H-atom elimination channel*. Pedro Recio, Javier Cachón, Alexandre Zanchet, Sonia Marggi Poullain, and Luis Bañares. J. Chem. Phys. 158, 234304 (2023).

Methylamine (CH_3NH_2) has attracted significant attention due to its role as a prototypical molecule for studying photoinduced dynamics. This molecule has many industrial applications, such as in the production of pharmaceuticals, insecticides, and rubber chemicals. However, its fundamental appeal lies in its structural similarity to ammonia (NH_3), which has long been studied for its photodissociation dynamics. Both molecules share similar electronic structures and absorption spectra, but methylamine's photochemistry is more complex due to additional dissociation pathways.

The photodissociation of ammonia involves H-atom loss in the 190–220 nm wavelength range, which is controlled by an energy barrier in the first excited state, followed by a conical intersection (CI) between the excited state and the ground state. Methylamine behaves similarly, but its richer photochemistry arises because it has up to five different dissociation pathways, including:

- H-atom loss
- C–N bond cleavage
- Formation of NH and CH_4

The focus of this paper is on the H-atom elimination channel, a process in which one of the hydrogen atoms in methylamine is cleaved after absorbing light, particularly in the blue edge of the first absorption *A*-band (198–203 nm). This region of the absorption spectrum is significant because it corresponds to the $nN \rightarrow 3s$ electronic transition, where the nitrogen atom's lone-pair electrons are excited to a 3s Rydberg state.

Previous studies have focused on the first absorption *A*-band, where dissociation mechanisms involving H-atom loss and C–N bond fission were investigated. For example, Waschewsky et al. studied methylamine in the 203–240 nm range and showed that dissociation occurred through two major mechanisms: prompt dissociation leading directly to H + $CH_3NH(\tilde{X})$, and a statistical dissociation after internal conversion to the ground state. However, most previous studies did not cover the blue edge of the A-band (198–203 nm), which is the focus of this paper.

The geometrical change that occurs in the molecule upon excitation plays a critical role in these dynamics. Upon absorbing light, the C–NH_2 group of the molecule changes from a pyramidal configuration to a planar geometry, facilitating N–H bond cleavage. The molecule

then enters a CI seam, which acts as a junction between different potential energy surfaces and can lead to three possible outcomes:

1. Threshold dissociation into the second dissociation limit, forming H + $CH_3NH(\tilde{A})$.

2. Direct dissociation after passing through the CI, producing H + $CH_3NH(\tilde{X})$.

3. Internal conversion to the ground state, where the molecule remains in the ground state and later dissociates.

The goal of this study is to investigate the H-atom loss in methylamine in the 198–203 nm range (blue edge of the *A*-band) using pump-probe nanosecond laser pulses and velocity map imaging (VMI) to detect the H-atoms. The paper also utilizes high-level *ab initio* calculations to understand the potential energy surfaces and bond-breaking mechanisms involved, focusing on the N–H bond fission. Additionally, the study examines the role of the CI and exit barriers in these dissociation pathways, especially at shorter wavelengths than those previously studied (e.g., 203–240 nm).

The study's experimental and theoretical results clearly show that N–H bond cleavage is the dominant dissociation pathway in methylamine at the studied excitation wavelengths, while C–H bond fission is found to be energetically inaccessible under these conditions. The potential energy curves (PECs) calculated for both N–H and C–H bond dissociation show that the energy threshold for C–H bond fission is significantly higher than that of N–H fission. This means that the excitation energies used in this study (198–203 nm) are not sufficient to break the C–H bond. Additionally, a large energy barrier along the C–H dissociation pathway makes this process even less likely to occur.

In contrast, the N–H bond dissociation pathway is more accessible, with a lower energy barrier. This is consistent with the experimental results, where H-atom loss from the NH_2 group is observed as the primary dissociation channel. The study concludes that C–H bond cleavage does not contribute significantly to the observed H-atom elimination, despite some earlier reports suggesting its presence as a minor channel.

The presence of a conical intersection (CI) is central to understand the dynamics of the N–H bond cleavage. The paper explains that when methylamine is excited in the blue edge of the *A*-band (198–203 nm), the molecule undergoes a structural transformation from a pyramidal to a planar geometry. This change significantly lowers the energy barrier for N–H bond fission, allowing the molecule to access the CI seam.

Once the molecule reaches the CI, three possible dissociation pathways are identified:

1. Threshold dissociation into the excited state to form H + $CH_3NH(\tilde{A})$ (adiabatic channel). This pathway, labeled as contribution 'c' in the figures of the paper, leads to slow H-atoms and is energetically allowed only at the studied wavelengths (~200 nm). The branching ratio of this channel remains low (~5%).

2. Fast direct dissociation through the CI, leading to ground-state products H + $CH_3NH(\tilde{X})$ (non-adiabatic channel). This pathway, labeled as contribution 'a' in the figures of the paper, results in a prompt H-atom loss and shows a significant anisotropy parameter ($\beta \sim -0.3$), consistent with a perpendicular transition. The presence of a CI facilitates this fast dissociation mechanism.

3. Indirect dissociation where the molecule passes through the CI and relaxes back into the ground state before dissociating. This process, labeled as contribution 'b' in the figures of the paper, involves slower dissociation and exhibits more isotropic angular distributions. The reduced anisotropy parameter (β ~ -0.2) reflects the fact that the molecule spends more time in the excited state before dissociating, allowing some internal vibrational energy redistribution (IVR).

The study reveals that the dissociation mechanisms vary depending on the excitation wavelength. At shorter wavelengths (~200 nm), the molecule has enough energy to overcome the N–H bond cleavage barrier and directly access the CI. This leads to prompt dissociation, as observed in contribution 'a', with a high degree of anisotropy and narrow translational energy distributions (TEDs). The fast dissociation observed at shorter wavelengths can be attributed to the molecule not having time to fully redistribute the available energy before breaking the N–H bond.

At longer wavelengths (>210 nm), the molecule does not have enough energy to overcome the barrier directly and instead undergoes tunneling through the barrier. This results in a slower dissociation process, characterized by contribution 'b'. In this case, the molecule spends more time near the CI, allowing for more IVR, which leads to broader TEDs and more isotropic angular distributions.

The branching ratios for each pathway are influenced by the excitation wavelength:

- Contribution 'a' dominates at shorter wavelengths (~200 nm) but becomes less significant at longer wavelengths.
- Contribution 'b' remains the main pathway at all wavelengths but becomes more prominent at lower excitation energies.

One of the significant findings of the study is the identification of the threshold dissociation channel leading to H + $CH_3NH(\tilde{A})$ (contribution 'c'). This pathway had not been observed in previous studies due to the limitations of the experimental techniques used, which could not detect very low kinetic energy fragments. It is suggested that this channel becomes accessible only at higher excitation energies corresponding to excitation wavelengths <203 nm and contributes a small (~5%) but measurable portion of the overall H-atom yield.

The results of this study are largely consistent with previous works, but it also provides new insights into the dissociation dynamics of methylamine. For instance, while earlier studies identified two main pathways (prompt dissociation and statistical dissociation), this study adds a third channel involving adiabatic dissociation into the excited state of the CH_3NH fragment.

In conclusion, the study provides a comprehensive analysis of the H-atom elimination in methylamine following excitation in the blue edge of the *A*-band. The results confirm that N–H bond cleavage is the primary dissociation pathway, and the presence of conical intersections plays a crucial role in determining the dissociation dynamics. The findings also emphasize the importance of excitation energy in dictating whether the molecule undergoes prompt dissociation or statistical dissociation with IVR.

The Journal of Chemical Physics ARTICLE scitation.org/journal/jcp

Photodissociation dynamics of methylamine in the blue edge of the *A*-band. I. The H-atom elimination channel

Cite as: J. Chem. Phys. 158, 234304 (2023); doi: 10.1063/5.0152993
Submitted: 3 April 2023 • Accepted: 30 May 2023 •
Published Online: 16 June 2023

Pedro Recio,[1] Javier Cachón,[1] Alexandre Zanchet,[2] Sonia Marggi Poullain,[1] and Luis Bañares[1,3,a)]

AFFILIATIONS

[1] Departamento de Química Física (Unidad Asociada I+D+i al CSIC), Facultad de Ciencias Químicas, Universidad Complutense de Madrid, 28040 Madrid, Spain
[2] Instituto de Física Fundamental, Consejo Superior de Investigaciones Científicas, Serrano 123, 28006 Madrid, Spain
[3] Instituto Madrileño de Estudios Avanzados en Nanociencia (IMDEA-Nanoscience), Cantoblanco, 28049 Madrid, Spain

[a)] **Author to whom correspondence should be addressed:** lbanares@ucm.es

ABSTRACT

The photodissociation dynamics of methylamine (CH_3NH_2) upon excitation in the blue edge of the first absorption *A*-band, in the 198–203 nm range, are investigated by means of nanosecond pump–probe laser pulses and velocity map imaging combined with $H(^2S)$-atom detection through resonance enhanced multiphoton ionization. The images and corresponding translational energy distributions for the H-atoms produced show three different contributions associated with three reaction pathways. The experimental results are complemented by high-level *ab initio* calculations. The potential energy curves computed as a function of the N–H and C–H bond distances allow us to draw a picture of the different mechanisms. Major dissociation occurs through N–H bond cleavage and it is triggered by an initial geometrical change, i.e., from a pyramidal configuration of the $C–NH_2$ with respect to the N atom to a planar geometry. The molecule is then driven into a conical intersection (CI) seam where three outcomes can take place: first, threshold dissociation into the second dissociation limit, associated with the formation of $CH_3NH(\widetilde{A})$, is observed; second, direct dissociation after passage through the CI leading to the formation of ground state products; and third, internal conversion into the ground state well in advance to dissociation. While the two last pathways were previously reported at a variety of wavelengths in the 203–240 nm range, the former had not been observed before to the best of our knowledge. The role of the CI and the presence of an exit barrier in the excited state, which modify the dynamics leading the two last mechanisms, are discussed considering the different excitation energies used.

I. INTRODUCTION

Besides its relevant role in industry, from pharmaceuticals and insecticides to paint removers and rubber chemicals,[1] methylamine (CH_3NH_2) has attracted considerable interest as a prototypical system for photoinduced dynamics.[2] It is the simplest derivative of ammonia (NH_3), a textbook example of photodissociation dynamics. The H-atom loss in ammonia upon photoexcitation in the ~190–220 nm range is controlled by an energy barrier in the first excited state followed by a conical intersection with the ground state in the exit channel.[2,3] Although similar electronic structure and absorption spectrum characterize both methylamine and ammonia, the former presents a richer photochemistry. Up to five dissociation pathways have been reported experimentally,[4] involving the H-atom loss, the C–N bond cleavage, as well as NH and H_2 formation. Regarding the two former channels, a similar picture to ammonia has been drawn, involving an energy barrier in the excited state that drives the molecule into a conical intersection seam before dissociation. The aim of this work is to investigate the photodissociation dynamics of methylamine in the blue edge of its first absorption *A*-band focusing on the H-atom loss. Complementary results on the C–N bond cleavage upon one-photon absorption at the same excitation wavelengths are reported subsequently in a separated article.[5]

The photochemistry of CH_3NH_2 has been extensively investigated both experimentally[2,4,6–17] and theoretically.[18–27] Experimental results at a variety of wavelengths in the 203–240 nm range within the first absorption band have been reported, focusing in particu-

The Journal of Chemical Physics ARTICLE scitation.org/journal/jcp

lar in the H-atom loss.[2,6–8,10,11,16] The first absorption band lying between 190 and 240 nm arises from the $n_N \rightarrow 3s$ transition, from the lone pair orbital of the nitrogen atom to the 3*s* Rydberg state. This band corresponds to the electronic excitation $\widetilde{X}\,^1A' \rightarrow \widetilde{A}\,^1A'$, and it is characterized by a broadband continuum presenting some structure, which reflects vibrational activity in the ν_9 NH_2 wagging and the ν_7 CH_3 rocking vibrational modes and their combinations.[28]

Upon excitation in the $\widetilde{A}\,^1A'$ excited state, the photodynamics is characterized by a significant energy barrier. As suggested in the work of Waschewsky *et al.*[7] as well as Dunn and Morokuma,[19] the initial vibrational activity in the ν_9 NH_2 wagging mode triggers a structural change from a pyramidal configuration of the C–NH_2 with respect to the N atom into a planar one. This allows considerable reduction in the energy barrier associated with the N–H bond cleavage. Further dynamics involves tunneling through the barrier into the conical intersection seam governing the dissociation channels.

Ashfold and co-workers[2,8] used H-atom Rydberg tagging photofragment translational spectroscopy (HRT-PTS) to study methylamine photodissociation over a range of wavelengths spanning the first absorption band (203–240 nm). A bimodal translational energy distribution was observed suggesting at least two mechanisms leading to the formation of H-atoms, in agreement with earlier experiments performed in the work of Waschewsky *et al.*[7] They argued that the fast component was consistent with prompt dissociation via the exit channel conical intersection (CI), leading directly to H + $CH_3NH(\widetilde{X})$. The slow component was assigned to a statistical dissociation in the ground state after internal conversion through the CI. Reported Rice–Ramspergger–Kassel–Marcus (RRKM) theory modeling indicated indeed that internal conversion from the $\widetilde{A}$ state into the $\widetilde{X}$ ground state is highly unlikely. It was then proposed that the molecule could fail to pass the CI the first time, bouncing back into the potential well while transfer into the ground state occurs at a later time. This proposed scheme allows for intramolecular vibrational energy redistribution (IVR) in both the excited and ground states, explaining the slow component reported. However, the HRT-PTS technique used by Ashfold and co-workers[2,8] presents a clear limitation since it cannot detect any signal at low fragment kinetic energies, resulting in loss of information at threshold kinetic energies.

In 2008, in the work of Ahn *et al.*,[10] the photodissociation of CH_3NH_2 was studied in the 232–240 nm range using the velocity map ion imaging technique probing the H-atom fragment by 2 + 1 REMPI at 243.1 nm. They also observed two velocity components, where the component with high velocity was ascribed to N–H fragmentation via the coupling of two excited states. In contrast, the slow component was assigned to dissociation on the ground state prepared by nonadiabatic dynamics at the CI. More recently, Bar and co-workers[16] detected the H-atom photofragment by two-color reduced Doppler ion imaging upon excitation in the wavelength range of 227.50–239.95 nm. The H-atom fragment detected was attributed to the N–H bond cleavage and two different dissociation pathways were recovered. These two pathways exhibited anomalous branching ratio and anisotropy parameters depending on the excited vibronic band and it was attributed to the sensitivity of the nonadiabatic dynamics to the energy difference between the initially prepared vibrational states and the energy of the conical intersections.

In this work, we present a combined experimental and theoretical investigation on the photodissociation dynamics of methylamine (CH_3NH_2) producing H-atom fragments following excitation in the wavelength range 198–203 nm. This range was chosen to be continuous to the measurements reported by Ashfold and co-workers[2,8] at the blue edge of the first absorption band. On one hand, the higher excitation energy initially prepares the molecule in the $\widetilde{A}$ excited state above the energy barrier, which can modify the observed dissociation channels. On the other hand, the use of velocity map imaging with respect to HRT-PTS allows us to measure the low kinetic energy region and thus to obtain somehow improved results on possible threshold dissociation.

In Sec. II, the experimental and theoretical methods employed here are presented. In Sec. III A, the measured velocity map images along with the translational energy distributions for the H-atom fragments are shown while potential energy curves computed considering the N–H and C–H bond fissions are presented in Sec. III B. Finally, the results are discussed in Sec. IV in order to present a complete picture of the different reaction pathways leading the H-atom loss as a function of the excitation wavelength.

II. METHODS

A. Experimental

The main characteristics of the experimental setup have been described in detail elsewhere.[29,30] Briefly, a molecular beam is created by expanding a 10% gas mixture of CH_3NH_2 (Sigma-Aldrich ≥99.0%) in He (1 bar backing pressure) into vacuum using a pulse nozzle valve (General Valve Series 9, 0.5 mm orifice). The gas pulse passes through a skimmer (Beam Dynamics, Standard Model 2, 0.5 mm diameter orifice), entering into the reaction chamber, where it is intersected, at right angles, by the photolysis and probe laser pulses, which are focused and counter-propagated to each other. The interaction region is located between the electrical plates of a time-of-flight (TOF) mass spectrometer. The whole experiment runs at a repetition rate of 10 Hz.

A Nd:YAG (Quanta Ray Pro 230) laser pumping a dye (Sirah Cobra-Stretch) laser is employed to generate the photolysis laser. A sum-frequency mixing nonlinear crystal combines the fundamental and second harmonic radiation of the dye laser to produce the 198–203 nm wavelength range. In particular, we measure the photodissociation of methylamine at 198.42, 201.33, and 203.95 nm, which correspond to the one-photon vibronic transitions 9_0^{13}, 9_0^{12}, and 9_0^{11}, respectively, where ν_9 is the amino wagging mode.[28] The probe laser, which arrives 10 ns later, was generated using a Nd:YAG (Quanta Ray Pro 190) pumped frequency-doubled dye laser (Sirah Cobra-Stretch). The hydrogen atoms $H(^2S)$ produced are resonantly ionized through a (3 + 1) REMPI scheme at 364.8 nm via the $2p(^2P_J) \leftarrow 1s(^2S_{1/2})$ transition. The resulting photolysis and probe laser pulses, of typically 2.4 and 1.8 mJ/pulse, respectively, are focused into the reaction chamber with two lenses of 25 cm focal length each.

The generated H^+ ions in the interaction region between the gas pulse and the pump and probe laser pulses are detected using the spectrometer in the single-field configuration. The ions are accelerated toward the detector by applying a constant electric potential of 3.5 kV to the repeller plate, while the extractor plate is connected to ground.[31,32] The ions travel through a field-free TOF region (45 cm)

The Journal of Chemical Physics ARTICLE scitation.org/journal/jcp

before hitting independent matched microchannel plates (MCPs, Chevron configuration, 40 mm diameter).[32] The resulting electron avalanche strikes a phosphor screen (P47), creating the velocity map ion images. The images are recorded by a CCD camera (SONY 1024 × 768 pixel) controlled using National Instrument (NI) LabView 7.1 and IMAQ VISION software. Before extracting the kinetic energy and angular distributions, all the velocity map images (VMIs) are symmetrized and inverted by the Hankel inversion method. A resolution of about 1% in velocity is achieved without further software manipulation such as event counting.

The images have been recorded using a parallel polarization configuration with respect to the detector plane of both pulse lasers. However, in order to corroborate a good laser alignment, images employing a perpendicular polarization of both lasers are recorded. Independent velocity–radius calibration of the apparatus was done with a single laser pulse exciting CH_3I and detecting the $CH_3(v = 0)$ fragments through a (2 + 1) REMPI scheme at $\lambda = 333.45$ nm (one color pump–probe experiment), taking advantage of the well-known cold vibrational distribution for the $CH_3 + I(^2P_{3/2})$ channel at this photolysis wavelength.[29]

B. Theoretical

The elimination of H-atoms coming from the N- and C-atoms of methylamine has been calculated at the multi reference configuration interaction (MRCI) level to provide insight on the possible N–H and C–H fragmentation mechanisms. The strategy used to compute the potential energy curves (PECs) is the following. First, a relaxed scan along one of the X–H coordinates (X = C, N) has been performed at CASPT2[33] level for the ground state of CH_3NH_2. Then, the procedure has been repeated—but this time considering the first excited state. The obtained PECs correspond to the most favorable direct dissociation pathways on the ground and excited states, respectively. Finally, for all the optimized geometries along the obtained dissociation pathways, MRCI[34] calculations were performed to compute the two first electronic states with higher accuracy. The harmonic frequencies for both ground and excited states at their respective equilibrium geometries have been computed at CASPT2 level for an estimate of their zero point energies (ZPEs).

The MOLPRO package[35] was used for all the *ab initio* calculations and the basis set aug-cc-pVTZ of Dunning was employed.[36] For both the N–H and C–H coordinates, the active space considered at CASSCF level[37] consists of four electrons in six orbitals, while seven orbitals are considered closed. The obtained orbitals and references where then employed in the MRCI calculations. The only difference between the two cases is that no symmetry was considered for the N–H coordinate, while C_s symmetry was considered for the C–H coordinate.

III. RESULTS

A. Experimental results

Figure 1 depicts the inverted symmetrized H^+ velocity map images measured from the photodissociation of CH_3NH_2 at the excitation wavelengths 198.42, 201.33, and 203.95 nm in the blue edge of the absorption spectrum and at 239.95 nm, which corresponds to the 0_0^0 transition. The former excitation wavelengths correspond to excitation to the 9_0^{13}, 9_0^{12} and 9_0^{11} vibronic bands, respectively, of the $\widetilde{A}\,^1A'$ excited state.[28] The three first images (from left to right in Fig. 1) are very similar to each other, suggesting that the dissociation mechanism does not change significantly as a function of excitation wavelength in the range studied. The main difference regards the relative intensity between the different contributions, as it will be shown below in the H-atom translational energy and speed distributions.

The left panels of Fig. 2 show the center-of-mass (CM) H-atom translational energy distributions (TEDs) obtained by angular integration of the images of Fig. 1 at the excitation wavelengths 198.42, 201.33, and 203.95 nm.[28] All the VMIs present a main perpendicular ring, which translates into a prominent peak in the TEDs (black line). In addition, a smaller ring is observed closer to the center of mass (CM). This ring is represented in the speed and TEDs as a shoulder of the main peak located at threshold translational energies. A third, diffuse structure is observed at higher radius leading to a sort of a tail in the TEDs that extends until ~1.50 eV.

The experimental TEDs (black lines in the left panels of Fig. 2) were deconvoluted by fitting the experimental data to two Gaussian functions (green and pink lines) and to a Muckerman distribution (blue line)[38] described as

$$I(E_t) = BE_t^i(1 - E_t)^j, \tag{1}$$

where E_t is the fragment translational energy and B, i, and j are fitting parameters that do not contain a specific physical meaning.[38] This function, especially convenient for fitting Boltzmann-type distributions (see, for instance, Refs. 39 and 40), has been chosen for consistency reasons, allowing a more detailed comparison of the

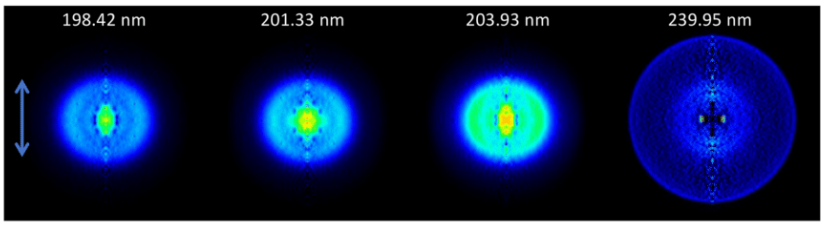

FIG. 1. Inverted symmetrized ion images for the H-atom fragment detected by (3 + 1) REMPI at 364.8 nm from the CH_3NH_2 photodissociation at 198.42, 201.33, and 203.95 nm in the blue edge of the absorption band, corresponding to the 9_0^{13}, 9_0^{12}, and 9_0^{11} vibronic bands, and at 239.95 nm, corresponding to the 0_0^0 transition (from left to right as indicated). The double arrow denotes the polarization direction of the laser pulses.

The Journal of Chemical Physics ARTICLE scitation.org/journal/jcp

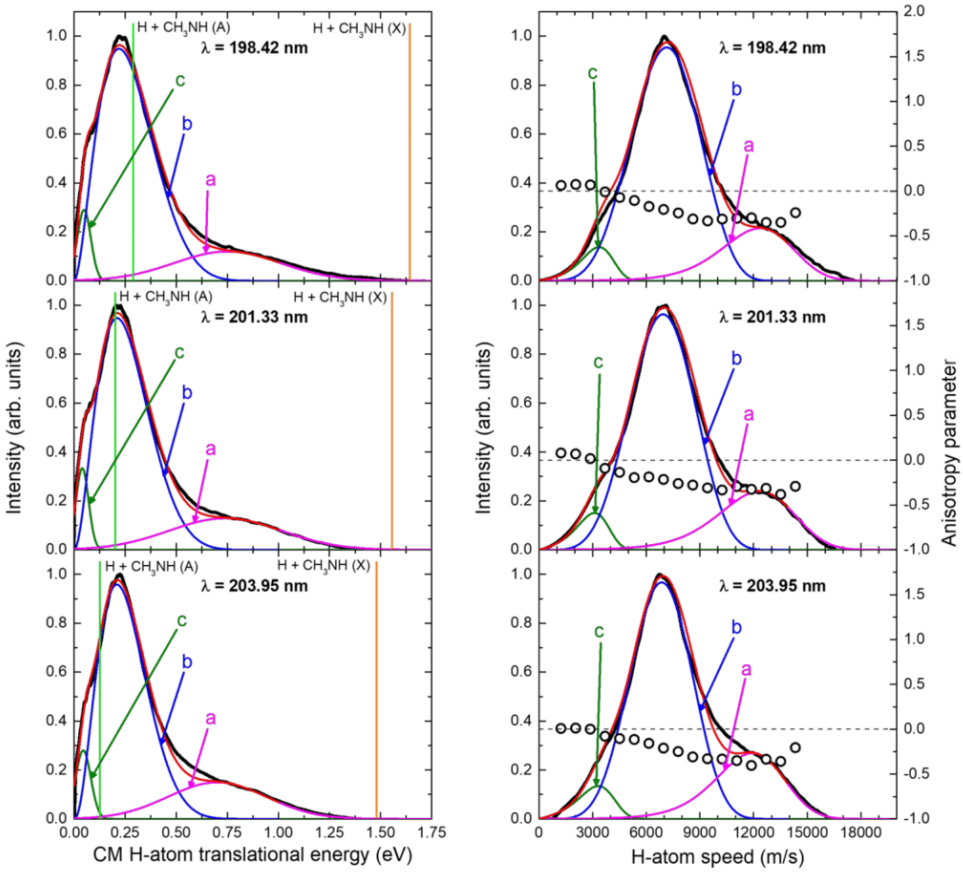

FIG. 2. (Left panels) Center-of-mass H-atom fragment translational energy distributions (TEDs, black line) obtained by angular integration of the images measured at excitation wavelengths 198.42, 201.33, and 203.95 nm. The two vertical lines (orange and light-green) correspond to the maximum translational energy for the two possible dissociation pathways, $H(^2S) + CH_3NH(\widetilde{X})$ and $H(^2S) + CH_3NH(\widetilde{A})$, respectively. The solid colored lines (green, blue, and pink) represent the fit to the three contributions distinguished in the TEDs (contributions *a*, *b*, and *c*, respectively), while the red line represents the overall fit. See the text for more details. (Right panels) H-atom fragment speed distributions. The solid colored lines are as in the TEDs of the left panels. Circles correspond to the anisotropy parameter β extracted pixel-to-pixel in the speed distribution.

results obtained at different excitation wavelengths. We note that similar results are obtained if a Gaussian function would be used instead to fit this contribution. The overall fit is represented by a red curve, which is the sum of the pink, blue, and green curves, labeled as *a*, *b*, and *c*, respectively, in Fig. 2.

In order to assign the contributions observed to different reaction pathways, maximum translational energies, E_T^{max}, for the C–H and N–H bond cleavages were estimated considering the corresponding co-fragment CH_3NH in the ground $(\widetilde{X})$ and first excited $(\widetilde{A})$ states,

$$E_T^{max} = \frac{m_{CH_3NH}}{m_{CH_3NH_2}}[h\nu - D_0 - E_{elec} - E_{int}(CH_3NH_2)], \quad (2)$$

where m_{CH_3NH} and $m_{CH_3NH_2}$ are the masses of CH_3NH and CH_3NH_2, respectively, $h\nu$ is the energy of the excitation photon, D_0 and E_{elec} are the dissociation energy and the energy between the ground and first excited states obtained from the theoretical calculations (4.55 and 1.38 eV, respectively), and $E_{int}(CH_3NH_2)$ is the internal energy of methylamine in the molecular beam, which is considered negligible under supersonic expansion conditions. We note that the dissociation energies obtained here for the first and second limits (4.55 and 5.93 eV, respectively) are in good agreement with the experimental values (4.45 and 5.89 eV) obtained from Ref. 41 and with the theoretical values (4.25 and 5.82 eV) obtained from the work of Ahn *et al.*[10]

The maximum translational energies for the elimination of H-atoms from the methyl moiety are remarkably large and do not fit in the energy scale in Fig. 2. Therefore, we only consider and display the ones associated with the N–H bond cleavage. Taking into account the position of the maximum translational energies, the two faster structures, contributions *a* and *b*, can be assigned to the formation of $CH_3NH(\widetilde{X})$ (pink and blue lines), while the threshold peak (green line, contribution *c*) corresponds to the formation of $CH_3NH(\widetilde{A})$.

The right panels of Fig. 2 represent the H-atom speed distributions, which include the same fitted contributions as in the left panels (labeled *a*, *b*, and *c*), along with the anisotropy parameters,

The Journal of Chemical Physics ARTICLE scitation.org/journal/jcp

β, calculated by fitting the angular distributions obtained by radial integration of the images pixel-by-pixel to

$$I(\theta) = 1 + \sum_{i=0}^{n} \beta_{2i} P_{2i}(\cos\theta), \quad (3)$$

where θ represents the angle between the photolysis laser polarization and the fragment recoil velocity, n is the number of absorbed photons, $P_{2i}(\cos\theta)$ is the $2i$th order Legendre polynomial, and β_{2i} the anisotropy parameters. In the present case, a single β parameter was used since a one-photon excitation is considered for the three contributions and no fragment alignment is possible for the $H(^2S)$ atom.

In addition, the angular distributions were obtained for each contribution observed in the speed distribution (a, b, and c) by radial integration of the images by sections. The anisotropy parameters β obtained for each contribution (a, b, and c) at each excitation wavelength are summarized in Table I along with the corresponding branching ratios. Average β parameters per contribution show negative values in agreement with the perpendicular character of the rings observed in the images. The negative values reported here are comparable to previous angular distributions characterized by $\beta \approx -0.3$ measured at the excitation wavelength of 222 nm reported in the work of Waschewsky *et al.*[7] While the anisotropy does not vary significantly as a function of the excitation wavelength, the measured β parameters show considerably lower values for lower translational energies. Contribution c lies at particularly low translational energies and the deduced β parameters likely reflect a lower angular resolution due to the limited number of pixels associated with this structure.

The branching ratios (BRs) have been estimated independently for each excitation wavelength as the area of the contribution with respect to the sum of the three areas. As already observed in Fig. 2, contribution b represents the main pathway for the generation of H-atoms, as reflected by the BR of ~70%, while BRs for contributions a and c are significantly lower. In addition, the BR for contribution c appears practically constant as a function of the excitation wavelength, while the BR for contribution b increases and the relative intensity of a decreases. Contribution b is nevertheless dominant for the three excitation wavelengths, representing more than 70%.

TABLE I. Anisotropy parameters (β) and branching ratios (BRs) for each contribution—a, b, and c in Fig. 2—and the three excitation wavelengths (λ_{exc}). The error bars for the reported β values are estimated around ±0.05 for contributions a and b and around ±0.1 for contribution c.

Contributions	Excitation wavelength (λ_{exc})	Anisotropy parameter (β)	BR (%)
	198.42	−0.33	18.5
a	201.33	−0.31	21.8
	203.93	−0.34	23.0
	198.42	−0.20	75.9
b	201.33	−0.21	72.6
	203.93	−0.21	71.6
	198.42	−0.10	5.6
c	201.33	−0.12	5.5
	203.93	−0.09	5.4

In order to make a direct comparison with previous experiments,[10,16] we have revisited the H-atom loss when exciting methylamine at the origin of the absorption band (0_0^0 transition) at the excitation wavelength of 239.95 nm. The measured H-atom image is shown in Fig. 1 and the corresponding TED is depicted in Fig. 3. The image in Fig. 1 features two main components: an inner diffuse structure and a sharper external ring. The translational energy distribution is indeed characterized by a fast peak around ~0.9 eV and a broader Boltzmann-type structure lying at lower energies. We have deconvoluted the experimental data into two contributions, labeled a and b. Equation (1) is used to fit contribution b and an asymmetric Gaussian function is used for contribution a. The overall fit is represented by a red line (see Fig. 3).

The results obtained here at the origin of the band are in good agreement with the ones previously reported in the work of Bar and co-workers[16] and of Ahn *et al.*[10] The TED is characterized by a bimodal structure with a similar relative intensity between the two components. The major difference observed with respect to the TEDs measured at the shorter excitation wavelengths in the blue edge of the absorption band lies in the presence of only two contributions here (see Fig. 3) while three contributions are observed at excitation wavelengths ~200 nm (see Fig. 2). The two contributions observed at the origin of the band have been previously assigned[10,16] to the production of $H(^2S) + CH_3NH(\widetilde{X})$, similar to contributions a and b observed at ~200 nm in Fig. 2 while $H(^2S) + CH_3NH(\widetilde{A})$, associated with contribution c, is not energetically opened at this wavelength. The branching ratio between contributions a and b is remarkably dependent on the excitation wavelength, i.e., at longer wavelengths, contribution a shows a much higher intensity, 44%, while contribution b is strongly favored at ~200 nm excitation, representing 56% at $\lambda(0_0^0) = 239.95$ nm. The anisotropy parameters are similarly obtained by fitting the angular distributions obtained by radial integration of the image in Fig. 1 to Eq. (3). As observed in the image, the slower component (contribution a) presents an almost isotropic distribution with $\beta = 0.07$. In contrast, the inner ring (contribution b) presents a slightly parallel anisotropy with $\beta = 0.18$. As discussed below, the electronic transition associated with the absorption step ($\widetilde{A}\ ^1A' \leftarrow \widetilde{X}\ ^1A'$) is characterized by a dipole moment

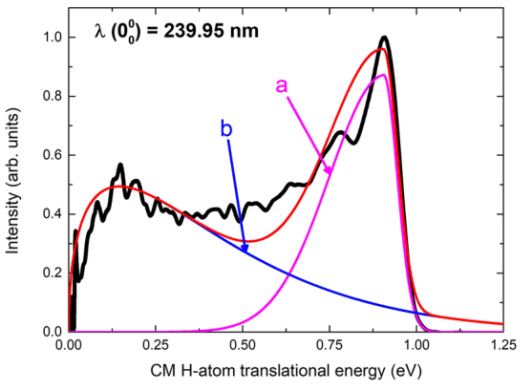

FIG. 3. CM H-atom translational energy distribution for excitation of methylamine at the origin (0_0^0 transition) of the absorption band at 239.95 nm (black line). The blue and pink lines represent the two dissociation pathways (contributions a and b), while the red line represents the overall fit.

The Journal of Chemical Physics ARTICLE scitation.org/journal/jcp

oriented perpendicularly to the C–N bond. Taking into account the geometry of the molecule in conjunction with the proposed reaction pathways and the literature, negative values of β would be expected for a prompt dissociation. Both values obtained here at the origin of the band could therefore highlight a somehow long reaction time, allowing some rotation of the molecule before bond cleavage. There are some discrepancies in the literature regarding the anisotropy parameters measured at this excitation wavelength. While Bar and co-workers[16] obtained values of ~−0.5 and 0.1 for contributions *a* and *b*, respectively, in the work of Ahn *et al.*,[10] positive values have been reported. The extremely low mass of the H-atom fragment can easily lead to somehow distorted images. This problem might explain some of these discrepancies since the angular distributions are extremely sensitive to any defect, even a small one. We note that in the present experiments, H-atom images were also recorded using a perpendicular polarization with respect to the detection plane of both the pump and probe lasers. This allowed us to check for the quality of the images since completely isotropic images were indeed obtained.

B. Theoretical results

The potential energy curves (PECs) calculated for the N–H and C–H direct dissociation pathways are shown in Figs. 4 and 5, respectively. The left panels [Figs. 4(a) and 5(a)] correspond to the minimum energy reaction paths when the ground state is relaxed and provide information on the dissociation energy and vertical excitation. The right panels [Figs. 4(b) and 5(b)] correspond to the minimum energy pathways when the first excited state is relaxed and provide information about the threshold energy for dissociation in the $\widetilde{A}$ state as well as about the energy of the relaxed structure associated with the origin of the absorption band. It is necessary to consider both optimizations since there is an important structural change of the equilibrium geometry between the ground and the first excited states. Methylamine presents a tetrahedral geometry—with respect to the carbon atom—and in the ground state, the two H-atoms attached to the nitrogen atom are out-of-plane, in a pyramidal geometry. In contrast, in the $\widetilde{A}$ state the two H-atoms (from the NH_2 moiety) along with the nitrogen atom are co-planar with the carbon atom.

The equilibrium geometry of methylamine in the $\widetilde{A}$ state lies at 5.31 eV above the ground state. Considering the zero point energy (ZPE) of 1.61 eV in the harmonic approximation, the first vibrational level of the $\widetilde{A}$ state should appear at 6.92 eV above the ground state equilibrium energy. In the ground electronic state, the harmonic ZPE, which corresponds to the energy of the ground vibrational state, is found to be 1.76 eV, which is slightly larger than that of the $\widetilde{A}$ state. The theoretical value of the origin of the absorption band can be considered taking into account the difference between the two last values and is estimated to be 5.16 eV, in good agreement with the experimental value of 5.18 eV,[28] highlighting the accuracy of the *ab initio* calculations. The vertical excitation from the ground state equilibrium geometry into the excited $\widetilde{A}$ state is estimated to be 5.92 eV, corresponding to ~209.4 nm, which is close to the maximum of the absorption band (~215 nm).

As observed in the left panels of Figs. 4 and 5, the ground state of methylamine presents a pronounced potential well characterized by dissociation energies of 4.58 and 4.30 eV for the N–H and C–H bond cleavages, respectively. Based on these values, the N–H bond appears to be slightly stronger than the C–H one. The $\widetilde{A}$ state shows a similar bound shape when the geometry is optimized in the ground state [Figs. 4(a) and 5(a)] while a second well is observed at longer C–H distances [Fig. 5(a)]. No direct dissociation is expected at this point. The available energy is lower than the dissociation energy of the $\widetilde{A}$ state, and any internal conversion into the ground state seems unlikely.

Turning now to the PECs of the relaxed geometry at the $\widetilde{A}$ state [Figs. 4(b) and 5(b)], it seems clear that dissociation in the $\widetilde{A}$ state is more favorable for the N–H bond cleavage than along the C–H bond. The threshold for the formation of CH_3NH from dissociation

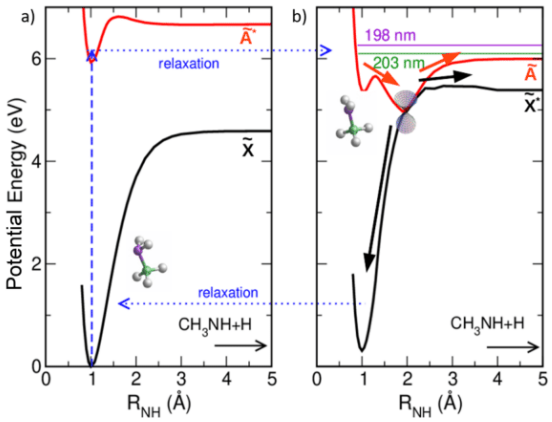

FIG. 4. Potential energy curves along the N–H coordinate. (a) Reaction path optimized for the ground state. (b) Reaction path optimized for the excited state. The purple and green vertical lines on panel (b) correspond to the higher and lower excitation wavelengths use in this work. The asterisks in the $\widetilde{A}$ state [panel (a)] and in the $\widetilde{X}$ state [panel (b)] indicate the state which has not been relaxed in each case.

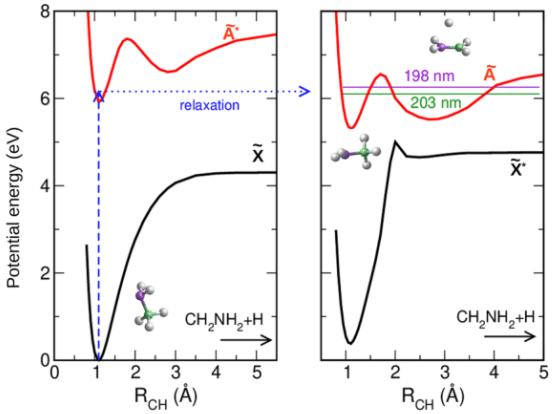

FIG. 5. Potential energy curves along the C–H coordinate. (a) Reaction path optimized for the ground state. (b) Reaction path optimized for the first excited state. The purple and green horizontal lines on panel (b) correspond to the energies of the higher and lower excitation wavelengths used in this work. The asterisks in the $\widetilde{A}$ state [panel (a)] and in the $\widetilde{X}$ state [panel (b)] indicate the state that has not been relaxed in each case.

The Journal of Chemical Physics ARTICLE scitation.org/journal/jcp

in the $\widetilde{A}$ state is indeed around 6 eV, while that for CH_2NH_2 appears above 6.5 eV, clearly above the photon energies used here. This preferred N–H bond breaking is in agreement with the measured TED depicted in Fig. 2 and with the literature.[6]

The second well observed in Fig. 5(a) reflects the presence of a stable isomer in the $\widetilde{A}$ state, where one H-atom from the methyl group migrates to form a bridge geometry, as depicted in Fig. 5(b). A relatively large barrier, higher than the excitation energies used here, separates the two isomers. As will be discussed in Sec. IV, the probability of tunneling through this barrier is expected to be significantly small, especially in comparison with the dynamics along the N–H coordinate. In contrast, the observed energy barrier along the N–H dissociation pathway, which is associated with a change in the electronic character from a 3*s* Rydberg state into a $n\sigma^*$ state, is lower than the photon energies used in the present experiments. The height of this barrier is estimated at ≈0.3 eV, intermediate between the values reported in the work of Wang *et al.*[26] (≈0.08 eV) and Xiao *et al.*[25] (≈0.8 eV). After the energy barrier, a conical intersection in the exit channel is found to connect the $\widetilde{A}$ state to the ground state, with the energy minimum lying at 4.98 eV, in good agreement with the value reported in the work of Wang *et al.*[26] This CI opens different reaction pathways, including dissociation in the excited state, prompt dissociation in the ground state after passage through the CI, or transfer into the ground state well followed by dissociation. These three outcomes are pictured as red and black arrows in Fig. 4(b). The mechanisms will be further discussed in Sec. IV along with the experimental results.

IV. DISCUSSION

The experimental and theoretical results presented above allow us to get a deeper insight into the reaction pathways involved in the H-atom elimination channels of the photodissociation of methylamine following its excitation in the blue edge of the first absorption band.

By one-photon absorption at ≈200 nm, the molecule is initially excited into the $\widetilde{A}$ state. According to the present experimental and theoretical results, N–H cleavage is favored while the C–H dissociation channel seems to be closed. First, as observed in Fig. 5 the photon energies used here are below the threshold for formation of CH_2NH_2 in its first excited state through C–H bond fission. The height of the barrier, which is considerably high to be overcome, is an additional restriction for the exploration of this reaction coordinate. One could imagine, however, that the H-atom, being so light, could tunnel through the barrier to form a bridge complex between the carbon and nitrogen atoms [see Fig. 5(b)]. However, even in this case, the available energy is not enough to reach the threshold and eliminate an H-atom from the methyl moiety in the $\widetilde{A}$ state. Moreover, no crossing with the ground state has been found in the computed PECs, so that no prompt relaxation into the ground state is expected. Therefore, once the isomer is formed by tunneling through the barrier, the molecule can remain in this second well a while before either tunneling back or relaxing through internal conversion. In the latter case, taking into account the excess of energy, further dynamics on the ground state would potentially allow to break one C–H bond. Such a mechanism would nevertheless be very slow, giving time to redistribute statistically the excess of energy, and would thus contribute to a Boltzmann distribution. Although Michael and Noyes[6] observed this C–H bond fission as a minor channel, the results presented here support that the H-atom elimination in methylamine occurs only from the NH_2 moiety, in agreement with the literature.

Focusing now on the N–H bond cleavage, the presence of a conical intersection [see Fig. 4(b)] makes the dissociation dynamics more complex. Once the parent molecule is excited into the $\widetilde{A}$ state by the absorption of one photon, an important structural change in the molecule is expected according to the computed equilibrium structures and in agreement with previous work.[7,19] The NH_2 group will switch from a pyramidal geometry—of the C–NH_2 with respect to the N atom—to a planar one likely triggered by the vibrational excitation in the NH_2 wagging mode (ν_9) characterizing the absorption step.[28] The selected excitation wavelengths correspond indeed to the 9_0^{13}, 9_0^{12} and 9_0^{11} vibronic bands. This geometrical change has a tremendous effect on the potential energy profile along the N–H coordinate, lowering drastically the barrier for dissociation. As clearly observed in Fig. 4(b), in this modified geometry, the molecule can overcome the barrier and find a direct way toward the conical intersection (CI). Interestingly, once the molecule has reached the CI, several pathways are accessible.

A first pathway consists of direct dissociation into the upper channel yielding $CH_3NH(\widetilde{A})$ + H. As observed in Fig. 4, the excitation energies used here are always just above the energy barrier associated with this dissociation limit. This process results in threshold dissociation leading to the small contribution *c* in Fig. 2. Although, to the best of our knowledge, this diabatic dissociation pathway has not been reported previously, the methyl formation upon excitation in the 222–240 nm range was suggested in the work of Thomas *et al.*[4] to arise from an initial motion into this dissociation limit but frustrated by the inadequate available energy leading to a re-sampling and a final C–N bond cleavage. In addition, previous studies have employed lower photon energies below the dissociation limit, leading to CH_3NH in its first excited state. In the work of Reed *et al.*,[8] the photodissociation of methylamine has been investigated at the close excitation wavelength of 203 nm. However, as mentioned above, the use of the HRA-PTS technique did not allow measurements at very low H-atom translational energies and thus this channel remained undetected. As observed in Table I, the branching ratio for contribution *c*, around 5%, seems to remain constant with the photon energy.

A second pathway can be associated with a transfer of population into the electronic ground state through the CI, followed by direct dissociation to ground state $CH_3NH(\widetilde{X})$ fragments. This pathway should lead to a fast contribution and it is indeed consistent with contribution *a* observed in the TEDs depicted in Fig. 2. This reaction pathway was previously proposed by Ashfold and co-workers,[2,8] Ahn *et al.*,[10] and Bar and co-workers.[16] The anisotropy of this contribution, characterized by a $\beta \sim -0.3$, is consistent with a dipole transition moment oriented perpendicular to the H-atom recoil direction in agreement with the reported value of −0.3 following excitation at 222 nm.[7] At Franck–Condon vertical excitation, the $\widetilde{A}\ ^1A'$ excited state is associated with a dipole moment in the plane of symmetry, but perpendicular to the C–N bond, while the planar equilibrium geometry of the excited state, $\widetilde{A}\ ^1A''$, is expected to be characterized by a transition dipole moment perpendicular to the plane of symmetry containing the C–NH_2. In the work of Waschewsky *et al.*, the expected anisotropy parameters were

The Journal of Chemical Physics ARTICLE scitation.org/journal/jcp

computed considering the H-atom loss from the amino group in the two geometries.[7] In the former, an anisotropy parameter between −0.35 and −0.55 is expected, while in the latter, β could reach the limiting value of −1 for a perpendicular transition. Taking into account that direct dissociation from the ground state equilibrium geometry is not possible, the measured β parameter must therefore reflect either (i) a less than prompt dissociation from the planar geometry or (ii) the contribution of different H-atom recoil directions due to the vibrational activity of the NH_2 wagging mode. In the first case, the molecule would stay trapped for some time in the CI seam before passing it and dissociating. This would explain the reduced anisotropy parameter as well as the relatively broad distribution observed in Fig. 2. The longer reaction time will allow for some transfer of energy between translational and internal degrees of freedom. In the second case, the low measured β values would reflect the sum of different values of the anisotropy parameter depending on the rovibrational state of the co-fragment. This phenomenon was reported for the H-atom produced from N–H bond cleavage in ammonia.[42] A total isotropic angular distribution was found to mask β values ranging from −1 to +2 for increasing values of N, the rotational level of the NH_2 co-fragment. It was assigned to the dynamics at the CI: a different torque, reflected by a different β value, leads to the NH_2 co-fragment in a different quantum state. This was supported by a detailed analysis using a model based on an impact parameter characterizing the torque force at the point of intersection. In the present case, since the rovibrational states of the CH_3NH co-fragment cannot be resolved in the TEDs, a similar detailed analysis cannot be carried out. The initial NH_2 wagging mode excited in the absorption spectrum could lead to a N–H bond cleavage from different geometries of the NH_2 with respect to the transition dipole moment, leading thus to different values of β.

Once the molecule reaches the CI seam, a third pathway can be involved. Instead of dissociating directly, the molecule relaxes downstream in the $\widetilde{X}$ state back to the well, although with an important excess of energy, followed by further dissociation in the ground state. This would lead to a situation somehow similar to an internal conversion in the sense that the molecule could redistribute the excess of energy among the different vibrational modes. However, in contrast to a standard internal conversion, going through the CI can be seen somehow equivalent to a collision with an energetic H-atom. The CI is indeed located at a large internuclear distance and thus the H-atom has already acquired by then a non-negligible amount of translational energy. The energy distribution will therefore be biased by the reaction dynamics resulting in a somehow distorted distribution, as observed for contribution b in Fig. 2. Even though this mechanism can directly compete with standard internal conversion, the time to reach the CI in the former should be considerably faster so that the internal conversion should not be favored. RRKM modeling carried out in the work of Ashfold *et al.*[2] showed indeed that ground state dissociation following internal conversion from the $\widetilde{A}$ state is rather unlikely. We note that C–H bond cleavage in the ground state could also contribute to this pathway, although based on previous work[6,8] only a minor contribution is expected.

A similar mechanism leading to the two latter fragmentation pathways was previously reported based on experimental results at a variety of excitation wavelengths lying between 239.95 and 203 nm.[2,8,10,16] In the work of Ashfold *et al.*[2] and Bar and co-workers,[16] it has been suggested that while direct dissociation through the CI into the ground state products will lead to a fast contribution, the molecule could fail to pass through the CI on its first attempt. The molecule would then bounce back into the potential well and revisit the CI several times before an effective $\widetilde{A} \rightarrow \widetilde{X}$ transfer occurs. This would allow for efficient intramolecular vibrational energy redistribution (IVR) in both electronic states, leading to a higher internal energy and a slower translational energy distribution.

The TED reported here at the onset of the absorption band ($\lambda(0_0^0)$ = 239.95 nm) depicted in Fig. 3 shows significant differences compared to those measured at the shorter excitation wavelengths of ≈200 nm. The branching ratio between contributions a and b changes completely, i.e., contribution a represents ~44% at the band origin while it accounts only for ~20% of the total H-atom yield at ≈200 nm. In addition, for the shorter excitation wavelengths, contribution a is characterized by a larger full-width-at-half-maximum (FWHM) while contribution b becomes considerably narrower. These changes were previously reported in the work of Reed *et al.*[8] Similar TEDs to those shown in Fig. 2 were measured for excitation wavelengths shorter than 210 nm. This excitation energy range would correspond to the energy needed to overcome the barrier observed in Fig. 4(b). For $\lambda \geq 210$ nm, tunneling through the barrier has been established as the first step in the N–H bond cleavage, supported by the lifetime of ~0.4 ps reported for the $\widetilde{A}$ state at the origin of the band,[43] while for $\lambda \leq 210$ nm and in particular at ≈200 nm, the molecule has enough energy to directly overcome the barrier. The higher excitation energy used here leads to a highly vibrational excited state. The larger FWHM characterizing contribution a arising from direct dissociation into ground state products through the CI is directly reflecting this initial internal energy acquired during the absorption step.

Previous experiments reported in the work of Ahn *et al.*[10] and Bar and co-workers[16] following excitation into the 9_0^1 vibronic band showed remarkable enhancement of contribution b, which was not observed for excitation in the 9_0^2. In the work of Ahn *et al.*,[10] this finding was rationalized using a qualitative picture of the CI seam simplified as a one-dimensional problem. In contrast to ν_9 = 0 or 2, the wave function for ν_9 = 1 is characterized by a node at the point of crossing, diminishing the probability of crossing and hence of direct dissociation related with contribution a. The molecule will have a higher probability of staying trapped in the upper cone and later leaked into the ground state of the molecule. A similar argument based on the presence of a node at the crossing seam cannot explain the present results. The branching ratios are similar for the three vibronic bands excited here, 9_0^{11}, 9_0^{12}, and 9_0^{13}, i.e., 203.95, 201.33, and 198.42 nm, respectively. The central node is however characteristic of a wave function with an odd value of n while a local maximum is expected for ν_9 = 12. In contrast, branching ratios show a smooth tendency where contribution b slightly increases for shorter wavelengths. The differences observed as a function of the excitation energy must therefore be ascribed to the mechanism before the CI through the energy barrier. Two different scenarios can be considered. At shorter wavelengths ($\lambda \leq 210$ nm), upon excitation the system has enough energy to overcome the barrier and directly accesses the CI. Taking into account the position of the CI in the exit channel, the two nascent fragments will have acquired some non-negligible translational energy before reaching the CI.

The Journal of Chemical Physics ARTICLE scitation.org/journal/jcp

This seems to favor a rather prompt transfer through the CI into the ground state—contribution *b*. The acquired energy and the location of the CI close to the asymptotic limit will facilitate dissociation into ground state products. The molecule will not explore the whole space, avoiding complete randomization of the available energy. This rather prompt mechanism was also reported in the work of Wang *et al.*[26] at an excitation wavelength of 205 nm shown by a representative trajectory. For longer wavelengths ($\lambda \geq 210$ nm), the available energy is significantly lower. Following tunneling through the barrier, the molecule would then have acquired considerably less translational energy. As previously suggested,[2,16] the molecule will stay trapped in the upper cone of the CI for some time before leaking into the ground state, followed by statistical dissociation. Therefore, the available energy can be shared into the different degrees of freedom during this slower process. IVR in both electronic states leads to a broader energy distribution. The anisotropy parameters measured here support these two mechanisms. The negative value around −0.2 (see Table I) obtained at around 200 nm, i.e., above the barrier, reflects a somehow more prompt dissociation with respect to the origin of the band characterized by a completely isotropic distribution. Experiments at shorter wavelengths, below 198 nm, could be interesting to further investigate direct dissociation in the $\widetilde{A}$ state.

V. CONCLUSIONS

In this work, we have presented velocity map imaging results on the photodissociation of methylamine (CH_3NH_2) upon excitation at three excitation wavelengths (198.42, 201.33, and 203.93 nm) detecting ground state hydrogen atoms, $H(^2S)$. For all the excitation energies, three different contributions are observed in the H-atom translational energy distributions, labeled as contributions *a*, *b*, and *c*. The potential energy curves computed as a function of the N–H and C–H bond distances confirm a major N–H bond fission. Based on the reported experimental and theoretical results, different reaction pathways as a function of the excitation energy are discussed. Contribution *a* is attributed to direct dissociation through the $\widetilde{A}$ state via a conical intersection (CI) to form ground state products, $H + CH_3NH(\widetilde{X})$. Contribution *b*, also leads $CH_3NH(\widetilde{X})$ although the mechanism is more complex. Instead of dissociating directly, as in contribution *a*, the molecule goes back to the $\widetilde{X}$ state prior to dissociation. The differences observed in the measured structures are rationalized in terms of the available energy. For higher excitation energies ($\lambda \leq 210$ nm), above the energy barrier found theoretically, the molecule acquires a considerable translational energy before reaching the CI. This seems to enhance a rather prompt passage through the CI into the ground state and, at the same time, prevents the molecule from exploring the whole space, avoiding complete randomization of the available energy before dissociation. At lower excitation energies ($\lambda \geq 210$ nm), the molecule tunnels through the barrier before arriving at the CI and can then fail to pass through it in a first attempt, spending more time in the excited state before a transfer into the ground state occurs. Intramolecular vibrational redistribution can then occur in both the excited state and the ground state, leading to the Boltzmann-type distribution measured. Finally, contribution *c*, which had not been observed before, is assigned to direct threshold adiabatic dissociation into $H + CH_3NH(\widetilde{A})$.

ACKNOWLEDGMENTS

P.R. is grateful to Universidad Complutense de Madrid (UCM) for a Margarita Salas postdoctoral contract. J.C. acknowledges financial support from the Spanish Ministry of Science and Innovation under the FPI predoctoral program. This research has been carried out within the Unidad Asociada Química Física Molecular between the Departamento de Química Física of Universidad Complutense de Madrid and CSIC. This work has been financed by the Grant Nos. PGC2018-096444-B-I00, PID2019-107115GB-C21, PID2021-122839NB-I00, and PID2021-122549NB-C21 from the Spanish Ministry of Science and Innovation. Financial support (Grant No. PR27/21-010) by the Madrid Government (Comunidad de Madrid Spain) under the Multiannual Agreement with Universidad Complutense de Madrid in the line Research Incentive for Young Ph.D.'s, in the context of the V PRICIT (Regional Program of Research and Technological Innovation) is also acknowledged. The facilities provided by the Centro de Láseres Ultrarrápidos at Universidad Complutense de Madrid are gratefully acknowledged.

AUTHOR DECLARATIONS

Conflict of Interest

The authors have no conflicts to disclose.

Author Contributions

P.R. and J.C. contributed equally to this work.

Pedro Recio: Data curation (equal); Formal analysis (equal); Investigation (equal); Writing – original draft (equal). **Javier Cachón**: Data curation (equal); Formal analysis (equal); Investigation (equal). **Alexandre Zanchet**: Data curation (equal); Formal analysis (equal); Investigation (equal); Methodology (equal); Writing – original draft (equal). **Sonia Marggi Poullain**: Conceptualization (equal); Data curation (equal); Investigation (equal); Writing – original draft (equal). **Luis Bañares**: Conceptualization (lead); Funding acquisition (lead); Supervision (lead); Writing – review & editing (lead).

DATA AVAILABILITY

The data that support the findings of this study are available from the corresponding author upon reasonable request.

REFERENCES

[1] P. Roose, K. Eller, E. Henkes, R. Rossbacher, and H. Höke, "Amines, aliphatic," in *Ullmann's Encyclopedia of Industrial Chemistry* (Wiley-VCH Verlag GmbH & Co. KGaA, Weinheim, 2015), pp. 1–55.

[2] M. N. R. Ashfold, R. N. Dixon, M. Kono, D. H. Mordaunty, and C. L. Reed, Philos. Trans. R. Soc. London, Ser. A **355**, 1659 (1997).

[3] H. Yu, N. L. Evans, A. S. Chatterley, G. M. Roberts, V. G. Stavros, and S. Ullrich, J. Phys. Chem. A **118**, 9438 (2014).

[4] J. O. Thomas, K. E. Lower, and C. Murray, J. Phys. Chem. A **118**, 9844 (2014).

[5] J. Cachón, P. Recio, A. Zanchet, S. M. Poullain, and L. Bañares, "Photodissociation dynamics of methylamine in the blue edge of the A-band. II: The $NH_2 + CH_3$ channel," J. Chem. Phys. (submitted) (2022).

The Journal of Chemical Physics ARTICLE scitation.org/journal/jcp

[6]J. V. Michael and W. A. Noyes, J. Am. Chem. Soc. **85**, 1228 (1963).
[7]G. C. G. Waschewsky, D. C. Kitchen, P. W. Browning, and L. J. Butler, J. Phys. Chem. **99**, 2635 (1995).
[8]C. L. Reed, M. Kono, and M. N. R. Ashfold, J. Chem. Soc., Faraday Trans. **92**, 4897 (1996).
[9]A. Golan, S. Rosenwaks, and I. Bar, J. Chem. Phys. **125**, 151103 (2006).
[10]D.-S. Ahn, J. Lee, J.-M. Choi, K.-S. Lee, S. J. Baeck, K. Lee, K. K. Baeck, and S. K. Kim, J. Chem. Phys. **128**, 224305 (2008).
[11]D.-S. Ahn, J. Lee, Y. C. Perk, Y. S. Lee, and S. K. Kim, J. Chem. Phys. **136**, 024306 (2012).
[12]J. O. Thomas, K. E. Lower, and C. Murray, J. Phys. Chem. Lett. **3**, 1341 (2012).
[13]R. Marom, U. Zecharia, S. Rosenwaks, and I. Bar, J. Chem. Phys. **128**, 154319 (2008).
[14]R. Marom, T. Weiss, S. Rosenwaks, and I. Bar, J. Chem. Phys. **130**, 164312 (2009).
[15]R. Marom, C. Levi, T. Weiss, S. Rosenwaks, Y. Zeiri, R. Kosloff, and I. Bar, J. Phys. Chem. A **114**, 9623–9627 (2010).
[16]M. Epshtein, A. Portnov, and I. Bar, Phys. Chem. Chem. Phys. **17**, 19607 (2015).
[17]Y. Onitsuka, K. Yamasaki, H. Goto, and H. Kohguchi, J. Phys. Chem. A **120**, 8584 (2016).
[18]E. Kassab, J. T. Gleghorn, and E. M. Evleth, J. Am. Chem. Soc. **105**, 1746 (1983).
[19]K. M. Dunn and K. Morokuma, J. Phys. Chem. **100**, 123 (1996).
[20]M. H. Park, K.-W. Choi, S. Choi, S. K. Kim, and Y. S. Choi, J. Chem. Phys. **125**, 084311 (2006).
[21]C. Levi, G. J. Halász, Á. Vibók, I. Bar, Y. Zeiri, R. Kosloff, and M. Baer, J. Phys. Chem. **128**, 244302 (2008).
[22]C. Levi, G. J. Halász, Á. Vibók, I. Bar, Y. Zeiri, R. Kosloff, and M. Baer, Int. J. Quantum Chem. **109**, 2482 (2009).
[23]C. Levi, R. Kosloff, Y. Zeiri, and I. Bar, J. Chem. Phys. **131**, 064302 (2009).
[24]C. Levi, G. J. Halasz, A. Vibok, I. Bar, Y. Zeiri, R. Kosloff, and M. Baer, J. Phys. Chem. A **113**, 6756 (2009).
[25]H. Xiao, S. Maeda, and K. Morokuma, J. Phys. Chem. A **117**, 5757 (2013).
[26]Y. Wang, C. Xie, H. Guo, and D. R. Yarkony, J. Phys. Chem. A **123**, 5231 (2019).
[27]K. A. Parker and D. G. Truhlar, J. Chem. Phys. **152**, 244309 (2020).
[28]M.-J. Hubin-Franskin, J. Delwiche, A. Giuliani, M.-P. Ska, F. Motte-Tollet, I. C. Walker, N. J. Mason, J. M. Gingell, and N. C. Jones, J. Chem. Phys. **116**, 9261 (2002).
[29]L. Rubio-Lago, A. García-Vela, A. Arregui, G. A. Amaral, and L. Bañares, J. Chem. Phys. **131**, 174309 (2009).
[30]M. G. González, J. D. Rodríguez, L. Rubio-Lago, A. García-Vela, and L. Bañares, Phys. Chem. Chem. Phys. **13**, 16404–16415 (2011).
[31]L. Rubio-Lago, G. A. Amaral, A. N. Oldani, J. D. Rodríguez, M. G. González, G. A. Pino, and L. Bañares, Phys. Chem. Chem. Phys. **13**, 1082–1091 (2011).
[32]V. Papadakis and T. N. Kitsopoulos, Rev. Sci. Instrum. **77**, 083101 (2006).
[33]H.-J. Werner, Mol. Phys. **89**, 645 (1996).
[34]P. J. Knowles and H.-J. Werner, Theor. Chim. Acta **84**, 95 (1992).
[35]H.-J. Werner, P. J. Knowles, G. Knizia, F. R. Manby, M. Schütz, P. Celani, W. Györffy, D. Kats, T. Korona, R. Lindh, A. Mitrushenkov, G. Rauhut, K. R. Shamasundar, T. B. Adler, R. D. Amos, S. J. Bennie, A. Bernhardsson, A. Berning, D. L. Cooper, M. J. O. Deegan, A. J. Dobbyn, F. Eckert, E. Goll, C. Hampel, A. Hesselmann, G. Hetzer, T. Hrenar, G. Jansen, C. Köppl, S. J. R. Lee, Y. Liu, A. W. Lloyd, Q. Ma, R. A. Mata, A. J. May, S. J. McNicholas, W. Meyer, T. F. Miller III, M. E. Mura, A. Nicklass, D. P. O'Neill, P. Palmieri, D. Peng, K. Pflüger, R. Pitzer, M. Reiher, T. Shiozaki, H. Stoll, A. J. Stone, R. Tarroni, T. Thorsteinsson, M. Wang, and M. Welborn, MOLPRO, version 2015.1, a package of *ab initio* programs, 2015, see http://www.molpro.net.
[36]J. T. H. Dunning, J. Chem. Phys. **90**, 1007–1023 (1989).
[37]H. J. Werner and P. J. Knowles, J. Chem. Phys. **82**, 5053 (1985).
[38]J. T. Muckerman, J. Phys. Chem. **93**, 179 (1989).
[39]V. Goncharov, N. Herath, and A. G. Suits, J. Phys. Chem. A **112**, 9423 (2008).
[40]S. M. Poullain, D. V. Chicharro, A. Zanchet, L. Rubio-Lago, A. García-Vela, and L. Bañares, Phys. Chem. Chem. Phys. **21**, 23017 (2019).
[41]S. P. Sander, J. P. D. Abbatt, J. R. Barker, J. Burkholder, R. R. Friedl, D. M. Golden, R. Huie, C. E. Kolb, M. J. Kurlyo, G. K. Moortgat, V. L. Orkin, and P. H. Wine, "Chemical kinetics and photochemical data for use in atmospheric studies: Evaluation No. 17," Technical Report No. 17 (JPL Publication 10-6, Jet Propulsion Laboratory, 2011).
[42]D. H. Mordaunt, M. N. R. Ashfold, and R. N. Dixon, J. Chem. Phys. **104**, 6460 (1996).
[43]S. J. Baek, K.-W. Choi, Y. S. Choi, and S. K. Kim, J. Chem. Phys. **118**, 11026 (2003).

3.2 Photodissociation dynamics of methylamine in the blue edge of the *A*-band. II. The NH_2 + CH_3 channel

Art. 2. *Photodissociation dynamics of methylamine in the blue edge of the A-band. II. The NH_2 + CH_3 channel.*, Javier Cachón, Pedro Recio, Alexandre Zanchet, Sonia Marggi Poullain, and Luis Bañares. J. Chem. Phys. 159, 064302 (2023).

The study of the photodissociation dynamics of molecules like ammonia (NH_3) and its derivatives, particularly primary amines ($R–NH_2$), has attracted considerable attention due to their increasing concentration in the atmosphere and their role in various chemical and biological processes. Amines, being bases, help stabilize small atmospheric particles and enhance aerosol nucleation rates, which in turn impacts cloud formation and atmospheric chemistry. Moreover, amines play a critical role in the biochemical processes essential for life, serving as precursors to amino acids, the fundamental building blocks of proteins and other biomolecules.

Among these amines, methylamine (CH_3NH_2) stands out due to its dual relevance in atmospheric chemistry, astrochemistry, and astrobiology. Methylamine has been detected in the interstellar medium, which has led to its study as a representative model molecule for better understanding both photodissociation dynamics and molecular evolution in space. Furthermore, being the simplest derivative of ammonia, methylamine is often studied as a model system for spectroscopic analysis and photodissociation processes. It has a relatively simple molecular structure, which makes it ideal for probing the photoinduced dynamics that are relevant to more complex organic molecules.

In terms of photodissociation, ammonia and methylamine share several similarities, especially in their UV-induced photodynamics. Ammonia (NH_3) is considered a prototype system where dissociation dynamics are governed by an energy barrier that must be overcome. After excitation to the first excited electronic state, NH_3 undergoes H-atom loss, which occurs through a conical intersection (CI) between the excited and ground states. A CI is a point where potential energy surfaces of different electronic states intersect, facilitating transitions between these states and driving the dissociation process. The energy barrier and the CI are key features in the dissociation pathways.

Methylamine, which shares a similar UV absorption spectrum and electronic structure to ammonia, exhibits analogous dynamics but opens a wider range of dissociation pathways due to the increased molecular complexity (additional hydrogen atoms and possible bond cleavages). This makes the photodissociation of methylamine more intricate than that of ammonia. A variety of theoretical and experimental studies have been conducted to investigate these dynamics, especially using deuterated isotopologues of methylamine. These have provided a deeper understanding of the mechanisms behind its photoinduced dissociation.

The first absorption band of methylamine, lying between 240 and 190 nm, is attributed to a $n_N \rightarrow 3s$ Rydberg transition. This transition moves an electron from the nitrogen atom's lone pair orbital into a Rydberg orbital. This corresponds to an $\tilde{A}\ ^1A' \rightarrow \tilde{X}\ ^1A'$ electronic transition, leading to a broad absorption spectrum. Several vibrational progressions are observed in this

band, with the most prominent one associated with the ν_9 amine wagging mode. The dissociation channels that are typically observed after excitation in this band include:

$CH_3NH_2 \rightarrow H + CH_3NH$ $\Delta H = 4.332$ eV (3.1)

$CH_3NH_2 \rightarrow H + CH_2NH_2$ $\Delta H = 4.046$ eV (3.2)

$CH_3NH_2 \rightarrow CH_3 + NH_2$ $\Delta H = 3.690$ eV (3.3)

$CH_3NH_2 \rightarrow H_2 + CH_2NH$ $\Delta H = 1.787$ eV (3.4)

$CH_3NH_2 \rightarrow CH_4 + NH$ $\Delta H = 3.191$ eV (3.5)

The reaction enthalpies (ΔH) provided here are based on the standard enthalpies of formation at 298 K as tabulated in NASA-JPL's evaluation [51]. Previous studies, particularly focusing on H-atom loss, have demonstrated that H-atom elimination occurs primarily from the NH_2 moiety in methylamine after excitation. This is similar to the photodynamics of ammonia, where a conical intersection governs the dissociation pathway. After photoexcitation to the first excited state, methylamine follows an analogous path, with an energy barrier that must be overcome before the molecule dissociates through a conical intersection defining the adiabatic and non-adiabatic channels.

One of the less studied channels is the C–N bond fission leading to the formation of methyl radicals (CH_3) and amino radicals (NH_2). While early experiments, such as those by Michael and Noyes [52], had detected this channel using mass spectrometry, it was considered a minor dissociation pathway, with a quantum yield (Φ) less than 0.05, compared to the dominant H-atom elimination channel (Φ ≈ 0.75). Early *ab initio* electronic structure calculations revealed the presence of an energy barrier along the C–N bond cleavage coordinate, which rationalized the low yield of this channel. Despite the C–N bond being weaker than the N–H bond, the higher energy barrier for C–N bond dissociation results in the predominance of H-atom loss.

The aim of the present study is to investigate the C–N bond cleavage upon excitation of methylamine in the 198–204 nm range, which corresponds to the blue edge of the first absorption *A*-band. The focus is on understanding the methyl radical formation from the C–N bond fission and providing new insights into this process by combining both experimental techniques, such as velocity map imaging (VMI), and high-level *ab initio* calculations of potential energy curves (PECs). This work builds on previous studies, particularly focusing on the H-atom loss channel, while expanding the investigation to the C–N bond fission dynamics.

Upon photoexcitation of methylamine in the 198–204 nm range, the molecule is excited from the ground electronic state ($\tilde{X}\ ^1A'$) to the first excited state ($\tilde{A}\ ^1A'$). This absorption leads to significant changes in the molecule's geometry. In the ground state, the C–NH_2 group exhibits a pyramidal structure, with the two H atoms from the NH_2 moiety arranged out-of-plane. However, upon excitation to the $\tilde{A}$ state, the geometry of the molecule changes, becoming more planar. This drastic geometric transformation likely results from vibrational activity in the NH_2 wagging mode (ν_9), which characterizes the absorption step. The transitions probed in the experiments correspond to the vibronic bands 9_{11}^0 (203.95 nm), 9_{12}^0 (201.33 nm), and 9_{13}^0 (198.42 nm), all of which are part of this vibrational progression.

This structural change in the excited state plays a crucial role in lowering the energy barrier for C–N bond dissociation, making the barrier more accessible for dissociation upon excitation at wavelengths below 204 nm. This transformation also leads the molecule toward a conical

intersection (CI) between the excited and ground states. Once the molecule reaches the CI, it can follow different dissociation pathways:

1. Direct dissociation along the excited Ã state, leading to the formation of CH_3 and $NH_2(\tilde{A})$ fragments.

2. Crossing the CI and dissociating directly into ground-state products (CH_3 and NH_2 in their ground electronic states).

3. Returning to the ground state in a highly excited rovibrational state, followed by slow dissociation.

The translational energy distributions (TEDs) measured for the vibrationally-state resolved CH_3 fragments in this study show a single Boltzmann-type distribution, which indicates that the major dissociation pathway is a slow dissociation from a highly excited state. This result contrasts with previous findings for the H-atom loss channel, where multiple contributions to the TEDs were observed (e.g., Gaussian and Boltzmann-like distributions) indicating the presence of different dissociation mechanisms. In the case of the C–N bond cleavage, however, a single Boltzmann-type contribution dominates, suggesting that slow dissociation is the primary mechanism.

Further insights into the dissociation mechanisms are provided by the analysis of the angular distributions of the photofragments. The anisotropy parameter (β), which characterizes the angular dependence of the fragment recoil velocities, reveals the presence of two dissociation mechanisms:

- At low CH_3 fragment velocities, the angular distribution is isotropic ($\beta \approx 0$), suggesting a slow dissociation mechanism. This would be consistent with a reaction time longer than the rotational period of the molecule, indicating that the molecule has time to rotate before dissociation.
- At higher CH_3 velocities, the angular distribution becomes anisotropic ($\beta \approx -0.3$), indicating a prompt dissociation pathway. In this case, the anisotropy parameter suggests that the dissociation occurs rapidly after excitation, with a transition dipole moment that is perpendicular to the C–N bond. A β value of -1 would be expected for a purely direct dissociation pathway, but the smaller value ($\beta \approx -0.3$) observed in this study suggests that the prompt and slow dissociation mechanisms may overlap.

Although the TEDs are dominated by a Boltzmann-type distribution reflecting slow dissociation, the presence of a prompt dissociation pathway cannot be ruled out. The PEC calculations show that after excitation, the molecule may reach the CI and follow different paths depending on the internal energy distribution and molecular geometry. The prompt dissociation mechanism, although minor, likely involves dissociation through the CI into ground-state products. The isotropic angular distribution at low velocities suggests that most of the dissociation occurs through a slow process, where the molecule relaxes into the ground state before breaking the C–N bond.

These findings can be compared with previous studies, particularly those of Thomas et al. (2014), who investigated the C–N bond cleavage of methylamine at longer wavelengths (222-240 nm). In that study, the C–N bond dissociation was observed but only occurred through frustrated N–H bond cleavage because the photon energies were not high enough to overcome

the energy barrier for direct dissociation. The current study, by contrast, uses photon energies above the barrier, making direct dissociation through the CI accessible.

The frustrated N–H bond cleavage mechanism proposed by Thomas et al. offers a plausible explanation for the slow dissociation observed in the present study. After excitation, the molecule preferentially evolves along the N–H bond elongation pathway toward the CI. Upon reaching the CI, the molecule may return to the ground state in a highly excited rovibrational state. This results in a slow C–N bond dissociation, which dominates the TEDs observed in this experiment.

The current findings are consistent with the low quantum yield of the C–N bond cleavage reported in earlier studies. The N–H bond dissociation channel is energetically more favorable and dominates the overall dissociation dynamics, while the C–N bond cleavage remains a minor channel. Nevertheless, the present study provides valuable new insights into the mechanisms of this dissociation, including the presence of both prompt and slow dissociation pathways, and the role of the conical intersection in driving the dissociation dynamics.

The Journal of Chemical Physics ARTICLE pubs.aip.org/aip/jcp

Photodissociation dynamics of methylamine in the blue edge of the *A*-band. II. The $NH_2 + CH_3$ channel

Cite as: J. Chem. Phys. 159, 064302 (2023); doi: 10.1063/5.0159855
Submitted: 27 May 2023 • Accepted: 20 July 2023 •
Published Online: 9 August 2023

Javier Cachón,[1] Pedro Recio,[1] Alexandre Zanchet,[2] Sonia Marggi Poullain,[1] and Luis Bañares[1,3,a]

AFFILIATIONS

[1] Departamento de Química Física (Unidad Asociada I+D+i al CSIC), Facultad de Ciencias Químicas, Universidad Complutense de Madrid, 28040 Madrid, Spain
[2] Instituto de Física Fundamental, Consejo Superior de Investigaciones Científicas, Serrano 123, 28006 Madrid, Spain
[3] Instituto Madrileño de Estudios Avanzados en Nanociencia (IMDEA-Nanoscience), Cantoblanco, 28049 Madrid, Spain

[a] Author to whom correspondence should be addressed: lbanares@ucm.es

ABSTRACT

The photodissociation dynamics leading to the C–N bond cleavage in methylamine (CH_3NH_2) are investigated upon photoexcitation in the blue edge of the first absorption *A*-band, in the 198–204 nm range. Velocity map images of the generated methyl (CH_3) fragment detected in specific vibrational modes, i.e., $v = 0$, $\nu_1 = 1$, and $\nu_2 = 1$, through resonance enhanced multiphoton ionization, are presented along with the corresponding translational energy distributions and the angular analysis. The experimental results are complemented by high-level *ab initio* calculations of potential energy curves as a function of the C–N bond distance. While a similar single Boltzmann-type contribution is observed in all the translational energy distributions measured, the speed-dependent anisotropy parameter obtained through the angular analysis reveals the presence of two different mechanisms. Prompt dissociation through the conical intersection between the $\tilde{A}\ ^1A'$ first excited state and the ground state located in the exit channel is, indeed, revealed as a minor channel. In contrast, slow dissociation on the ground state, presumably from frustrated N–H bond cleavage trajectories, constitutes the major reaction pathway leading to the methyl formation.

I. INTRODUCTION

The interest on the photodissociation dynamics of ammonia (NH_3) derivates, the so-called amines ($R–NH_2$), has risen in the last few years as a result of their increase in the atmosphere. In addition, amines can act as base molecules and stabilize small particles enhancing aerosol nucleation rates.[1] They also play a crucial role in the survival of life as precursors of amino acids, the building blocks of proteins and, hence, of life itself. Among the wide range of primary amines, methylamine (CH_3NH_2) has attracted a lot of interest due to its relevance in atmospheric chemistry,[2–4] astrochemistry, and astrobiology and due to its presence in the interstellar medium.[5,6] Methylamine, as the simplest derivative of ammonia, also serves as a model system for spectroscopy and photoinduced dynamics, particularly related to predissociation mechanisms.

The UV photodynamics of ammonia and methylamine show a large number of similarities. Ammonia is considered a prototype for photodissociation dynamics governed by an energy barrier.[7–10] Following excitation into the first excited state, at around 190–220 nm, H-atom loss takes place, after an energy barrier, through a conical intersection (CI) located in the exit channel. Methylamine presents a similar absorption spectrum and electronic structure, leading to analogous photodynamics. A higher number of dissociation channels are, nevertheless, opened, and theoretical and experimental investigations reveal a more complex photochemistry.[9,11–30] Besides the variety of techniques used, experiments employing deuterated methylamine isotopologues have considerably contributed to a deeper understanding of their photoinduced dynamics.[11,13,15,17,18,26,31]

The first absorption band of methylamine lying between 240 and 190 nm is assigned to an $n_N \rightarrow 3s$ transition, from the lone pair orbital of the nitrogen atom into the 3*s* Rydberg state. It corresponds to the $\tilde{A}\ ^1A' \leftarrow \tilde{X}\ ^1A'$ electronic transition leading to a broadband spectrum showing several vibrational progressions, the most prominent one assigned to the ν_9 amine wagging mode.[17,31,32] Although there has been some controversy over the assignment of the spectral

The Journal of Chemical Physics ARTICLE pubs.aip.org/aip/jcp

origin and vibrational bands, the ν_7 methyl rocking mode seems to also contribute to the vibrational structure observed.

The following channels have been observed following photoexcitation in its first absorption band:

	$\rightarrow$ H + CH_3NH	ΔH = 4.332 eV	(1)
	$\rightarrow$ H + CH_2NH_2	ΔH = 4.046 eV	(2)
$CH_3NH_2 + h\nu$	$\rightarrow$ CH_3 + NH_2	ΔH = 3.690 eV	(3)
	$\rightarrow$ H_2 + CH_2NH	ΔH = 1.787 eV	(4)
	$\rightarrow$ CH_4 + NH	ΔH = 3.191 eV	(5)

Note that the given reaction enthalpies are derived from standard enthalpies of formation at 298 K tabulated in the NASA-JPL evaluation.[33]

The two first channels, related to H-atom loss, have been investigated in detail earlier[11,13,15,16,18,26,29] and are, indeed, associated with photodynamics similar to that of ammonia. The experimental and theoretical work demonstrated that the C–H bond fission is particularly unfavorable, and a major H-atom loss takes place from the NH_2 moiety. Following photoexcitation into the first excited state $\widetilde{A}\ ^1A'$, an energy barrier controls the subsequent dissociation. Once it is overcome, a CI located at large N–H bond distances between the first excited and the ground electronic states governs the dissociation dynamics. Theoretical and experimental investigations on the C–N bond cleavage, labeled channel (3), highlighted analogous dynamics also characterized by an energy barrier and a CI in the exit channel. The aim of the present work is to investigate its photodissociation dynamics following excitation in the blue edge of the first absorption band, in the 198–203 nm range. A first publication[34] has focused on the H-atom loss, while here we investigate the formation of methyl radicals by the C–N bond cleavage.

The photoinduced C–N bond fission was first detected by Michael and Noyes[11] using mass spectrometry along with broadband radiation (194–244 nm) as a minor dissociation channel (quantum yield $\Phi < 0.05$), in contrast to the high-yield H-atom elimination channel ($\Phi = 0.75$). Early *ab initio* calculations of potential energy curves (PECs) by Kassab *et al.*[12] and Dunn and Morokuma[14] confirmed the presence of an energy barrier and a conical intersection in the exit channel. The small energy barriers found along both the C–N and N–H bond coordinates result from a Rydberg–valence avoided crossing and provide direct pathways for dissociation. The small quantum yield of the C–N channel was then rationalized in terms of the height of the barrier. Despite the fact that the C–N bond is weaker, a higher energy barrier in the C–N bond coordinate would favor the H-atom loss. A thorough experimental study on the photodynamics upon excitation at 222 nm was reported by Waschewsky *et al.*[13] using photofragment translational spectroscopy and emission spectroscopy. Four dissociation channels were discussed, including the H-atom loss from both C–H and N–H bond fissions and the C–N bond cleavage as well as the H_2 elimination. In particular, the C–N channel was shown to result from rather prompt dissociation along the excited state, yielding electronically excited $NH_2(\widetilde{A})$. Xiao *et al.*[26] later reported a theoretical study of the photodissociation pathways. Critical points between the ground state, the $\widetilde{A}\ ^1A'$ excited state, and the first triplet state, i.e., minima, transition states, minimum-energy CIs, and minima on the seam of crossing, were explored. The results confirmed the previous findings concerning the dynamics leading to the H-atom loss and the C–N bond fission.

Thomas *et al.*[28] investigated the photodissociation dynamics of methylamine following excitation in the 222–240 nm range using the (2 + 1) resonance enhanced multiphoton ionization (REMPI) detection of methyl fragments in conjunction with time-of-flight mass spectrometry (TOFMS). The experiments were complemented with *ab initio* calculations of relevant stationary points, such as minima and transition states. The results confirmed the presence of an energy barrier along the C–N bond coordinate, insurmountable at the excitation energies used. The authors proposed an alternative dissociation pathway through the frustrated N–H bond cleavage. Once at the CI mediating the H-atom loss, the molecule will come back into the ground electronic state and dissociate into CH_3 + NH_2 in their respective ground electronic states. This alternative pathway explained the high vibrational content characterizing the methyl fragments produced while consistent with the *ab initio* calculations. This mechanism was later supported by Onitsuka *et al.*'s[30] results from ion imaging and dispersed fluorescence spectroscopy upon excitation in the 205–213 nm range. Bimodal translational energy distributions were measured for CH_3 ($v = 0$), and the contribution at lower energies was assigned to the formation of $NH_2(\widetilde{A})$.

In this work, we investigate the C–N bond cleavage upon methylamine photoexcitation in the 198–204 nm range. These excitation wavelengths correspond to total energies higher than the energy barrier controlling the dissociation. In contrast to previous experiments in the literature, the direct dissociation in the excited electronic state, through the CI in the exit channel, is, therefore, accessible. Velocity map images (VMI) of the methyl fragment detected by the (2 + 1) REMPI along with *ab initio* calculations of the PECs are presented. While the translational energy distributions show a single Boltzmann-type distribution, reflecting a slow reaction pathway, the angular analysis based on the anisotropy parameter reveals the presence beneath of a prompt direct dissociation mechanism. The experimental and theoretical methods are summarized in Sec. II, while in Sec. III, the results are presented, including the methyl fragment VMI and the PECs as a function of the C–N bond distance. The two dissociation mechanisms revealed by the experimental results are discussed, based on the calculations carried out along with the existing literature, in Sec. IV, while Sec. V details the most relevant conclusions of this work.

II. METHODS

A. Experimental methods

The experimental setup has been described in detail earlier,[35,36] and only a brief summary will be given here. A molecular beam is created by expanding a gas mixture of CH_3NH_2 in He (10%, 1 atm backing pressure) into vacuum using a pulsed nozzle (General Valve Series 9, 0.5 mm orifice) synchronized with the laser system to operate at 10 Hz. The gas beam passes through a skimmer (Beam Dynamics Standard Model 2, 0.5 mm orifice), forming a molecular beam that travels into the reaction chamber where it is intersected, at right angles, by the photolysis and the probe laser pulses. The interaction region is located between the electrical plates of a TOFMS. The whole experiment runs at a repetition rate of 10 Hz.

The Journal of Chemical Physics ARTICLE pubs.aip.org/aip/jcp

The photolysis laser was generated by an Nd:YAG (Quanta-Ray Pro 230) pumped frequency-doubled dye laser (Sirah Cobra-Stretch). A sum-frequency mixing nonlinear crystal combines the fundamental and second harmonic radiation of the dye laser to produce the desired wavelengths; in particular, we use λ_{exc} = 198.42, 201.33, and 203.95 nm, which correspond in methylamine to the one-photon transitions 9_0^{13}, 9_0^{12}, and 9_0^{11}, respectively.[17,31,32] The resulting radiation, of typically 1.7 mJ per pulse, was focused into the reaction chamber with a lens of 25 cm focal length. The produced CH_3 fragments were ionized 10 ns later with the focused counter-propagated probe pulse of ≈2 mJ, generated by a frequency-doubled dye laser (Sirah Cobra-Stretch) pumped by another Nd:YAG laser (Quanta-Ray Pro 190). The CH_3 fragments in the selected vibrational states $v = 0$, $v_1 = 1$, and $v_2 = 1$ were resonantly ionized at λ = 333.45, 329.50, and 333.90 nm, respectively, using a (2 + 1) REMPI scheme through the $3p_z(^2A_2'' \leftarrow {}^2A_2'')$ transition.[37]

The produced ions are accelerated by an electric field generated between two electrodes: a repeller set at 3 kV and a grounded extractor.[36,38] In a field-free time-of-flight (TOF) region (40 cm), the ions are separated by their different charge/mass ratios before hitting the impedance matched microchannel plates (MCPs) (chevron configuration, 40 mm diameter). The gain of the MCPs is gated with a narrow-width (20 ns) high voltage (500 V) pulse to selectively detect the ion of interest. The resulting electron avalanche strikes a phosphor screen (P47), thereby creating the ion image, which is recorded using a charge-coupled device (CCD) camera [Sony 1024 × 768 pixels, controlled using the National Instruments (NI) LabVIEW 7.1 and IMAQ VISION software] and analyzed with a commercial software application (DaVis).[39] The final image is obtained as the sum of around 40 000–100 000 laser shots depending on the quality of the signal. The obtained VMI were symmetrized and then inverted with the Hankel transformation method so that the 3D distribution of the Newton sphere is recovered. The images presented here were recorded using a parallel polarization configuration with respect to the detector plane of both pump and probe lasers. However, in order to corroborate a good laser alignment, images employing a perpendicular polarization of both lasers are always recorded as well.

In order to obtain a velocity–radius calibration of the apparatus, additional images of $CH_3(v = 0)$ fragments were measured. The CH_3 $(v = 0)$ photofragments were produced in a single color pump-and-probe experiment exciting CH_3I at λ = 333.45 nm, taking advantage of the well-known cold vibrational distribution for the $CH_3 + I(^2P_{3/2})$ channel at this photolysis wavelength.[34]

B. Theoretical methods

The C–N bond cleavage has been considered at the multireference configuration interaction (MRCI) level to provide insight into the possible mechanisms. The MOLPRO package[40] was used for all the calculations, and the basis set aug-cc-pVTZ of Dunning has been employed.[41] The active space considered at the complete active space self-consistent field (CASSCF) level[42] consists of four electrons in six orbitals, while seven orbitals are considered closed. The obtained orbitals and references were then employed in the MRCI calculations. The strategy used to compute the PECs is the following: First, a relaxed scan along one of the C–N coordinates has been performed at the CASPT2[43] level for the ground state of CH_3NH_2. Second, the procedure has been repeated but for the first excited state. The obtained PECs correspond to the most favorable direct dissociation pathways on the ground and excited states, respectively. Finally, for all the optimized geometries along the obtained dissociation pathway, MRCI[44] calculations were performed to compute the two first electronic states with higher accuracy. The harmonic frequencies for both the ground and excited states at their respective equilibrium geometries have been computed at the CASPT2 level for a first estimation of their zero-point energies (ZPEs).

III. RESULTS

A. Experimental results

Figure 1 presents the VMI of the CH_3 fragment along with the corresponding total translational energy distributions (TEDs) obtained by angular integration of the image. The images and TEDs were measured following photoexcitation at λ_{exc} = 203.95, 201.33, and 198.42 nm, corresponding to the 9_0^{11}, 9_0^{12}, and 9_0^{13} vibronic bands, respectively, at the blue edge of the first absorption band.[17,31,32] The notation X_m^n will be used here, with m and n being the initial and final vibrational states, respectively, while X denoting the corresponding vibrational mode. For each excitation wavelength, the vibrational activity in the generated CH_3 radical was explored by tuning the probe laser wavelength to the center of the two-photon $3p_z(^2A_2'' \leftarrow {}^2A_2'')$ transition in CH_3 in its 0_0^0, 1_1^1, and 2_1^1 bands, located at 333.45, 333.90, and 329.50 nm, respectively. A large pump–probe signal was obtained at all detection wavelengths reflecting a high vibrational activity characterizing this channel. In all cases, the images show a similar unstructured blot, leading to a Boltzmann-type distribution in the TEDs. We note that with increasing excitation photon energy, the distribution becomes slightly broader, regardless of the vibrational state of the methyl fragment detected.

The available energy (E_{av}) for the $CH_3 + NH_2(\widetilde{X})$ and $CH_3 + NH_2(\widetilde{A})$ dissociation channels, shown in Fig. 1 as blue and green vertical bars, respectively, corresponds to[45]

$$E_{av} = h\nu - D_0 - E_{elec} - E_{\mathrm{int}}(CH_3), \quad (1)$$

where $h\nu$ is the excitation photon energy, D_0 is the C–N dissociation energy of methylamine, i.e., 3.727 eV (from Ref. 46), and E_{elec} is the electronic energy characterizing the NH_2 co-fragment, i.e., 0 eV for $NH_2(\widetilde{X})$ and 1.379 eV for the first excited state $NH_2(\widetilde{A})$.[46] $E_{\mathrm{int}}(CH_3)$ represents the internal energy of the CH_3 fragment, which was determined as the vibrational energy corresponding to each methyl vibronic band selected in the experiment—by tuning the probe laser wavelength—0_0^0, 1_1^1, and 2_1^1 bands. For the 0_0^0 band, $E_{\mathrm{int}}(CH_3)$ = 0 eV, while for the 1_1^1 and 2_1^1 bands, $E_{\mathrm{int}}(CH_3)$ is 0.37 and 0.08 eV, respectively, which correspond to the CH_3 photofragment vibrational frequency in the symmetric stretch mode (ν_1) and the umbrella mode (ν_2),[45] respectively. In addition, the combs depicted in Fig. 1 represent the possible excitation of the co-fragment NH_2 in its bending mode ν_2, extracted from the high resolution work of Ashfold and co-workers.[7] This vibrational mode has been selected to reflect the high rovibrational content of the co-fragment since NH_2 produced in the photodissociation of ammonia is characterized by well-defined rovibrational progressions in this mode.[10,48] The possible corresponding rotational levels are not taken into account here. As observed in the TEDs, we cannot distinguish the two dissociation

The Journal of Chemical Physics ARTICLE pubs.aip.org/aip/jcp

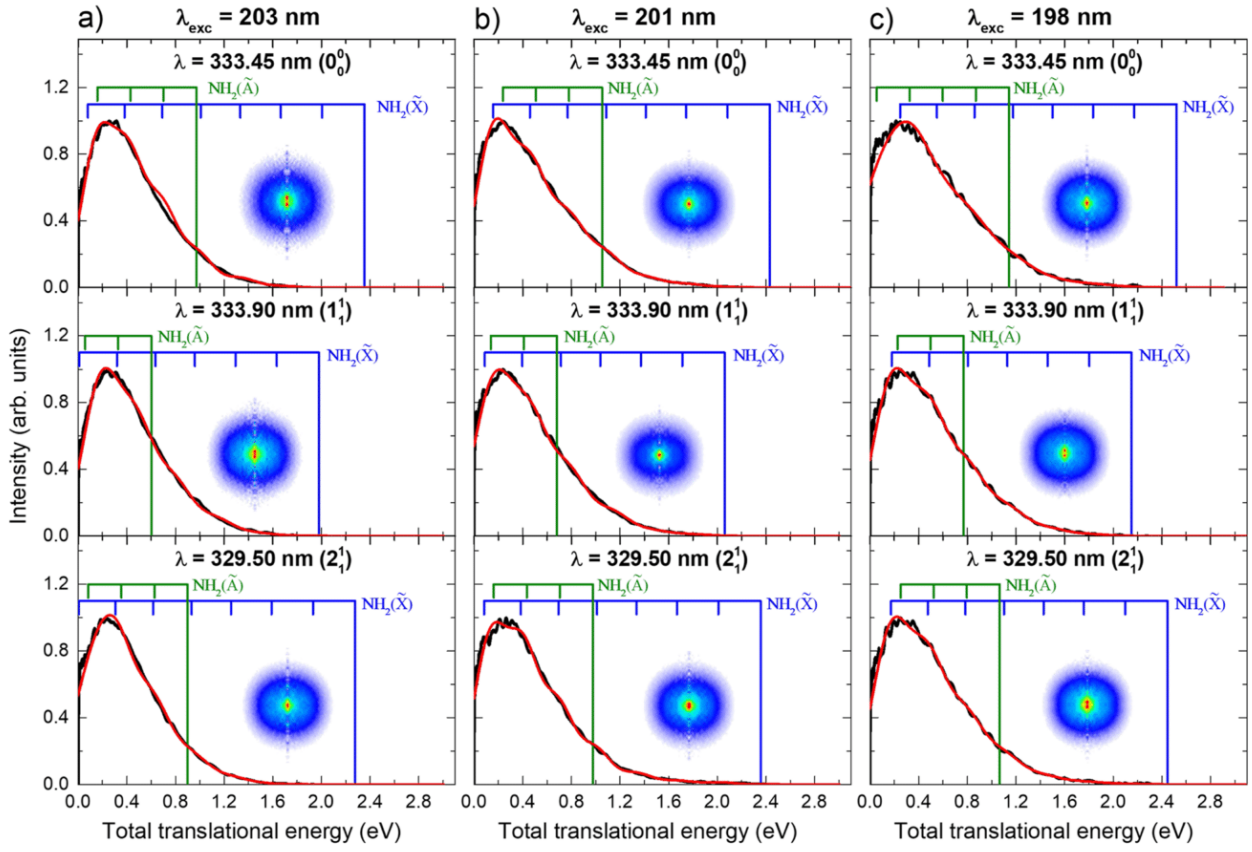

FIG. 1. Abel-inverted velocity map images of the CH_3 radical arising from the photodissociation of methylamine upon excitation at (a) λ_{exc} = 203.95 nm, (b) 201.33 nm, and (c) 198.42 nm. Three probe wavelengths are used to detect the CH_3 fragments in the 0_0^0, 1_1^1, and 2_1^1 vibronic bands. Each image is depicted inside its corresponding total translational energy distribution panel (black line). The blue combs correspond to the ν_2 vibrational levels for the $CH_3 + NH_2(\tilde{X}, \nu_2)$ channel, while the green combs correspond to the ν_2 vibrational levels of the $CH_3 + NH_2(\tilde{A}, \nu_2)$ channel (the vibrational quantum numbers increase from left to right; $\nu_2 = 0$ coincides with the vertical bars). The red line represents the overall fit (see the text). In the images, the polarization axis for both pump and probe lasers is set along the vertical axis.

channels associated with the formation of NH_2 in its ground and first excited states.

The TEDs represented in Fig. 1 have been fitted using one Gaussian function for each channel, i.e., for each $NH_2(\tilde{X}, \nu_2)$ and each $NH_2(\tilde{A}, \nu_2)$. The overall fit is depicted as a red line in all TEDs, although no information on the respective population can be extracted from this fit. First, as observed, a high number of Gaussian functions are included in the fit since several ν_2 levels can be populated for each dissociation channel. Second, some $NH_2(\tilde{X}, \nu_2)$ levels almost overlap in energy with some $NH_2(\tilde{A}, \nu_2)$ levels, making specially difficult any deconvolution. We additionally note that the rotational structure characterizing the NH_2 fragment has not been taken into account here. The overall fit is, indeed, shown only for illustrative purposes in order to highlight the high rovibrational energy content of the co-fragment NH_2.

Measurements were also performed as a reference at 239.95 nm, which corresponds to the origin of the band (0_0^0 transition). The CH_3 fragment was similarly detected in the three vibronic bands. The recorded VMI along with the TEDs obtained by angular integration are depicted in Fig. 2. An unstructured blot is also observed in the image, which leads to a Boltzmann-type distribution in the corresponding TED. The vertical bar shows the available energy for the $CH_3 + NH_2(\tilde{X})$ channel, while the combs similarly represent the possible excitation of the $NH_2(\tilde{X})$ co-fragment in the ν_2 vibrational mode. We note that at this excitation wavelength, the $CH_3 + NH_2(\tilde{A})$ channel is only energetically opened for the formation of CH_3 in $\nu = 0$ with an available energy of only 0.064 eV. No threshold signal is observed in Fig. 2(a) so that the contribution in the three TEDs can be fully assigned to the formation of ground-state $NH_2(\tilde{X})$ products. While the results obtained may seem to be very similar for all excitation wavelengths, i.e., in the 198–204 nm range as well as at 239.95 nm, a close inspection of the TEDs reveals some differences. While all TEDs obtained above the energy barrier (excitation wavelengths 198–204 nm) peak at around ~0.3 eV, the distributions recorded upon excitation at 239.95 nm (0_0^0 band) show a maximum at around ~0.15 eV. In addition, the TEDs shown in Fig. 2 measured at 239.95 nm are also considerably narrower compared to the distributions measured at higher excitation energies (Fig. 1).

The Journal of Chemical Physics ARTICLE pubs.aip.org/aip/jcp

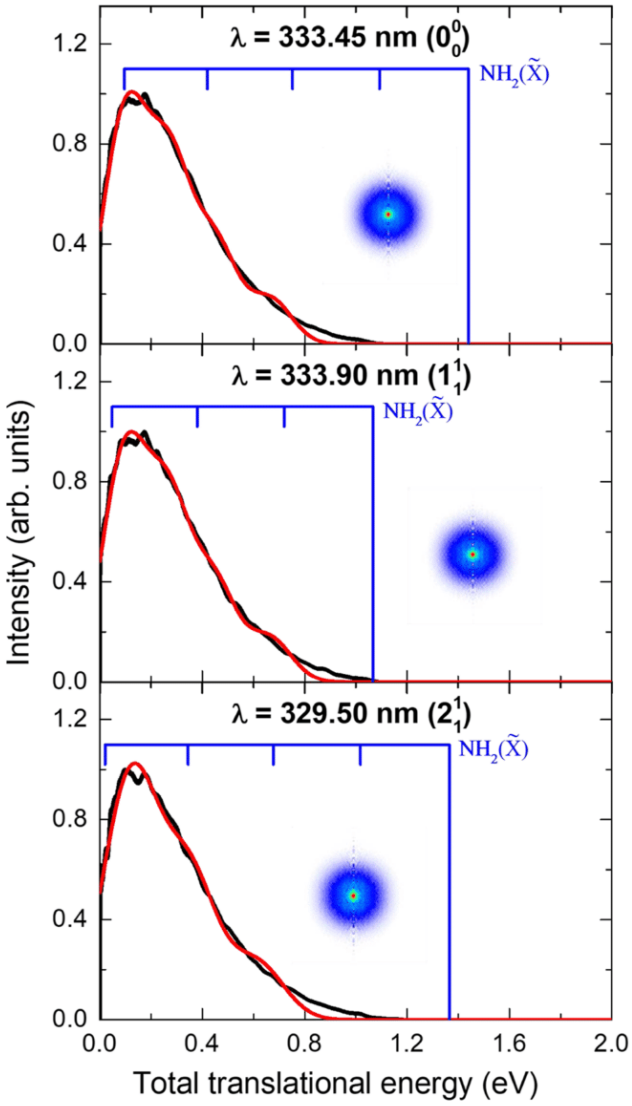

FIG. 2. Abel-inverted velocity map images of the CH_3 radical arising from the photodissociation of methylamine upon excitation at the origin of the *A*-band of methylamine [$\lambda_{exc}(0_0^0)$ = 239.95 nm], for the 0_0^0, 1_1^1, and 2_1^1 detection wavelengths. Each image is depicted inside its corresponding total translational energy distribution panel (black line). The blue vertical bar and combs correspond to the $CH_3 + NH_2(\tilde{X}, v_2)$ channel (the vibrational quantum numbers increase from left to right; $v_2 = 0$ coincides with the vertical bars). The red line represents an estimated fit based on the position of vibrational levels as performed in Fig. 1. In the images, the polarization axis for both pump and probe lasers is set along the vertical axis.

The speed-dependent angular distributions are obtained by the radial integration of slices of about 20 pixels of the methyl images and are fitted to[46,48]

$$I(\theta) = 1 + \sum_{k=0}^{n} \beta_{2k} P_{2k}(\cos\,\theta), \qquad (2)$$

where θ represents the angle between the photolysis laser polarization and the fragment recoil velocity, n is the number of absorbed photons, $P_{2k}(\cos\theta)$ is the $2k$th order Legendre polynomial, and β_{2k} are the anisotropy parameters. The angular distributions extracted as a function of the CH_3 velocity are all characterized by a single β parameter. The obtained anisotropy parameters β are depicted along with the corresponding CH_3 velocity distribution in Fig. 3, following photodissociation at 201.33 and 239.95 nm. The results are shown for the detection of the CH_3 fragment in its vibrational ground state, although similar results are obtained for vibrationally excited CH_3. As observed in Fig. 3, a completely isotropic distribution associated with $\beta \approx 0$ characterizes the photodissociation at the origin of the band, while at λ_{exc} = 201.33 nm, the anisotropy parameter decreases for increasing CH_3 velocities. At higher velocities, a negative value of around −0.3 is obtained, while at lower velocities, i.e., threshold energies, the angular distribution is almost isotropic. A similar behavior is recovered for all excitation wavelengths in the 198–204 nm range. We note that these results are also visible in a close inspection of the images. While perfectly isotropic images are recovered at 239.95 nm in Fig. 2, the images in Fig. 1 present a certain elongation along the horizontal axis, reflecting the anisotropy of the angular distributions. The transition dipole moment associated with the excitation into $CH_3NH_2(\tilde{A}\ ^1A')$ is located perpendicular to the C–N bond, and β values close to −1 were predicted.[13] The completely isotropic angular distributions measured could reflect a long reaction time—longer than the rotational period of the parent molecule—thus leading to an isotropic distribution. Isotropic angular distributions are typically obtained when fragments are produced from a statistical dissociation in the ground state. The anisotropic angular distributions, obtained here at higher velocities following excitation in the 198–204 nm range, characterized by $\beta \sim -0.3$ are in agreement with the value of $\beta = -0.4$ following photodissociation at 222 nm reported by Waschewsky *et al.*[13] This reduced anisotropy with respect to the predicted value was then attributed to some molecular rotations prior to dissociation. The trend observed in Fig. 3 seems to indicate the presence of two dissociation pathways

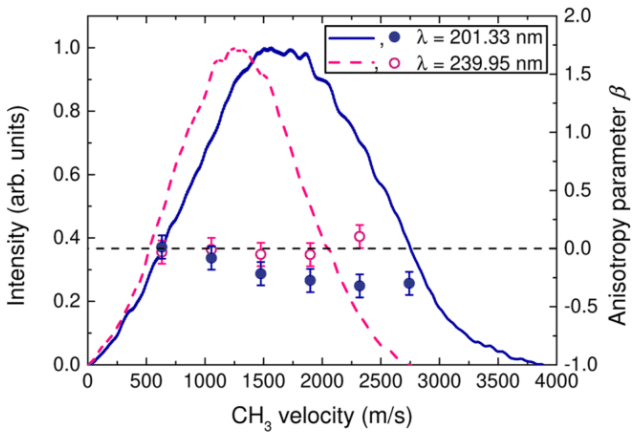

FIG. 3. Anisotropy parameter β (circles) as a function of the CH_3 fragment velocity along with the corresponding velocity distribution (line), following photodissociation at 201.33 nm (full blue line and circles) and at 239.95 nm (0_0^0) (pink dashed line and circles), for the detection of CH_3 in its 0_0^0 band.

The Journal of Chemical Physics ARTICLE pubs.aip.org/aip/jcp

following excitation in the 198–204 nm range, in contrast to the results obtained at the origin of the band. A major indirect pathway characterized by a long reaction time, such as a statistical dissociation, is characterized by an isotropic distribution and dominates the measured TEDs. A second dissociation pathway associated with a somehow faster reaction time is characterized by a negative value of the anisotropy parameter reflecting the perpendicular transition from the ground to the excited state. This pathway would be characterized by a CH_3 energy distribution peaking at higher values, hidden underneath the global Boltzmann-type distribution.

B. Theoretical results

Figure 4 shows the PECs for the ground ($\widetilde{X}$) and the first excited ($\widetilde{A}$) states of methylamine obtained as a function of the C–N distance, while the rest of the molecules are relaxed at each point in either its ground state (left panel) or its first excited state (right panel). Therefore, the left panel of Fig. 4 provides information on the dissociation energy—on the ground state—and the vertical excitation, while the right panel of Fig. 4 properly describes the threshold energy for dissociation in the $\widetilde{A}$ excited state as well as the energy of the relaxed structure associated with the origin of the absorption band. A dissociation energy of 3.82 eV for the formation of ground-state products is found, while the threshold for the formation of $NH_2(\widetilde{A})$ is located at 5.20 eV, in good agreement with the experimental values of 3.727 and 5.106 eV, respectively, from Ref. 46. We note that the theoretical values do not take into account any correction based on the zero-point energy (ZPE).

One-photon absorption in the Franck–Condon region leads the molecule into a bound $\widetilde{A}$ state where a high barrier appears to prevent dissociation. Relaxation on this state can, nevertheless, significantly modify the subsequent dynamics. As observed in Fig. 4, the molecule of tetrahedral geometry (with respect to the carbon atom) is characterized in the ground state by the two H-atoms from the NH_2 moiety being out-of-plane in a pyramidal geometry of C–NH_2 with respect to the N atom. In contrast, these two atoms are co-planar with the nitrogen and carbon atoms if we consider the relaxed geometry in the excited state. This striking change in molecular geometry, previously reported by Morokuma *et al.*,[14,27] characterizes the dynamics in the excited state leading to other reaction pathways, including the major H-atom loss.[34] Similarly, this geometrical change lowers the barrier significantly and a CI appears between the $\widetilde{A}$ and $\widetilde{X}$ states. The minimum energy of this CI is found at ~4.4 eV in very good agreement with the values published by Wang *et al.*[49] According to the right panel of Fig. 4, the barrier is located at an energy of ~6.04 eV, slightly higher than previously reported values.[27,28,49] Xiao *et al.*[27] carried out a CASPT2 reaction path search and obtained a transition state at 5.59 eV, while Thomas *et al.*[28] performed *ab initio* calculations of stationary points retrieving a value of 5.86 eV. More recently, Wang *et al.* have built a set of quasi-diabatic potential energy surfaces fitted over 7700 points and obtained a barrier lying at 5.81 eV. Further optimization at the MRCI level of the geometry at the top of the barrier [Fig. 4(b)] would, indeed, lower its energy. Once at the CI, three different pathways would be possible: the molecule can either go back to the ground state in highly excited rovibrational states, directly dissociate into the second dissociation limit [$NH_2(\widetilde{A})$ + $CH_3(\widetilde{X})$], or rapidly dissociate through the CI into the first dissociation limit [$NH_2(\widetilde{X})$ + $CH_3(\widetilde{X})$].

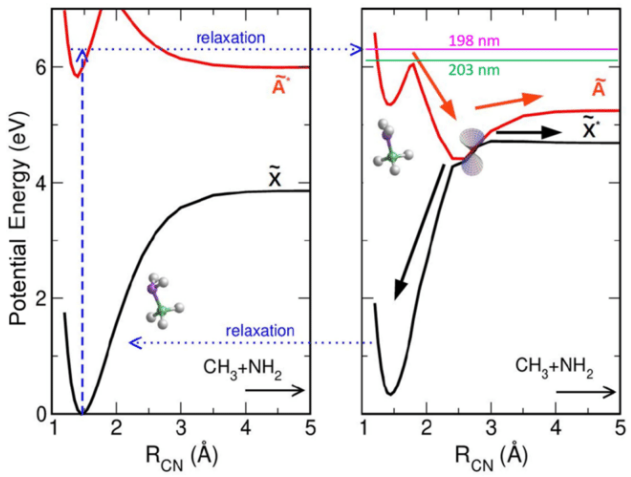

FIG. 4. Potential energy curves along the C–N coordinate. (Left panel) Reaction path optimized for the $\widetilde{X}$ ground state. (Right panel) Reaction path optimized for the $\widetilde{A}$ excited state. The purple and green horizontal lines in the right panel correspond to the higher and lower excitation wavelengths used in this work. The asterisk appears in the state label that is not optimized.

IV. DISCUSSION

One-photon absorption in the blue edge of the first absorption band (in the 198–204 nm range) excites methylamine into the electronically excited $\widetilde{A}$ state. There, the molecule suffers an important structural change, i.e., the C–NH_2 group switches from a pyramidal geometry into a planar one. In agreement with previous studies,[13,14] this geometric transformation upon electronic excitation is likely triggered by the initial vibrational activity in the NH_2 wagging mode, which characterizes the absorption step. A vibrational progression in the ν_9 mode is, indeed, well observed in the absorption spectrum, and the excitation wavelengths used here are associated with the vibronic transitions 9_0^{11} (203.95 nm), 9_0^{12} (201.33 nm), and 9_0^{13} (198.42 nm).

This geometrical change drastically lowers the energy of the barrier, which can be easily overcome upon excitation at wavelengths below 204 nm, as those used in the present work. In addition, this change in molecular configuration also favors the pathway to the CI between the excited and ground states. Based on the PECs shown in Fig. 4, once at the CI, the molecule can follow several pathways: (i) direct dissociation into the $\widetilde{A}$ state, leading to CH_3 + $NH_2(\widetilde{A})$; (ii) crossing the CI to directly dissociate into ground-state products, or (iii) going back into the ground state well in highly excited rovibrational states and then slowly dissociate. These dynamics are similar to those reported for the H-atom elimination channel of methylamine photodissociation at the same excitation wavelengths, i.e., the blue edge of the first absorption band.[34] However, the present experimental results are substantially different as all TEDs measured for the CH_3 fragment show single Boltzmann-type contributions, whereas the corresponding TEDs measured for the H-atom were deconvoluted into three contributions described by Gaussian and Boltzmann-like distributions, which were assigned to the different reaction pathways.[34]

The Journal of Chemical Physics ARTICLE pubs.aip.org/aip/jcp

The anisotropy analysis of the images presented here reflects, however, the presence of two different reaction pathways overlapped behind the Boltzmann-type distributions. At low CH_3 velocities, an isotropic angular distribution with $\beta \sim 0$ is found, similarly to the results obtained at the origin of the band. This would reflect a slow dissociation mechanism characterized by a reaction time longer than the rotational period of the molecule. In contrast, at higher CH_3 velocities, an anisotropic distribution with $\beta \sim -0.3$ is obtained, reflecting a prompt dissociation pathway. The transition dipole moment associated with the vertical excitation into the $\widetilde{A}$ excited state is expected to be located perpendicular to the C–N bond—in both the equilibrium ground geometry and the planar geometry of the excited state—so that a β close to −1 would be expected for any direct dissociation. The measured anisotropic distribution could, therefore, reflect a direct dissociation through the CI, likely into ground-state products. Based on the available energy for each dissociation channel shown by the vertical bars in Fig. 1, we cannot assign a particular exit channel. The first dissociation limit seems, nevertheless, more favorable for a direct and fast dissociation process due to the energetics. The smaller β value measured, −0.3 compared to the maximum value of −1 for a pure perpendicular transition, could simply reflect the overlap between the two dissociation mechanisms. The TEDs are, indeed, completely governed by a global Boltzmann-type distribution, highlighting the slow dissociation mechanism and the high rovibrational excitation of the NH_2 co-fragment. A Gaussian contribution from this prompt dissociation could be well-hidden behind. However, the role of a small amount of rotation cannot be ruled out. The molecule could stay trapped in the seam of the CI for some time before dissociating. This would explain a somehow reduced β value and high rovibrational excitation of the fragments due to the redistribution of the available energy.

Thomas *et al.*[28] investigated the C–N bond cleavage following photoexcitation in the 222–240 nm range by measuring the (2 + 1) REMPI spectra of the nascent methyl fragment. The results were consistent with dissociation, leading to rovibrationally excited fragments in their respective ground states. Since all the photon energies used in that experiment were selected below the energy barrier, direct dissociation through the CI was not opened. The authors evaluated the possible alternate reaction pathways, including the intersystem crossing to the triplet T_1 state, which was ruled out. Taking into account the low branching ratio of the C–N bond cleavage on the overall dissociation channels of methylamine, slow dissociation on the ground state from the frustrated N–H cleavage was proposed and later supported by surface-hopping trajectory calculations.[49] The N–H bond dissociation is, indeed, the major channel, and following photoexcitation into the $\widetilde{A}$ excited state, the molecule would preferentially go tunneling through the barrier into the CI located at larger N–H bond distances. As previously discussed elsewhere,[16,34] besides the direct dissociation through the CI leading to the H-atom loss, the molecule could go back into the ground-state well in highly excited rovibrational states. The sampling of the phase space would be limited due to the location of the CI in the exit channel along with the acquired translational energy. Therefore, only a small portion would lead to the C–N bond cleavage with a major branching going into the H-atom loss.

The reaction pathway proposed by Thomas *et al.*[28] would also explain the Boltzmann-type distribution obtained here at photon energies above the barrier. Only a small part of trajectories would directly go into longer C–N bond distances reaching the CI, leading mainly to a prompt dissociation. In contrast, the molecule would preferentially evolve through the N–H bond elongation into the CI. As discussed in our complementary work on the H-atom formation,[34] the position of the CI in the exit channel along with the presence of an energy barrier controls the photodissociation. At the photon energies considered here, above the energy barrier associated with the N–H coordinate, the passage through the CI into the highly excited ground state is highly efficient. The nascent H-atom and co-fragment have acquired a considerable amount of translational energy, favoring a prompt dissociation since the molecule will not explore the whole space. A small number of frustrated N–H cleavage trajectories will lead to slow C–N bond dissociation, contributing to the TEDs presented in the present work. We cannot, however, rule out the slow dissociation from the highly rovibrationally excited ground state populated directly from the CI observed in Fig. 4, associated with the C–N bond cleavage. Although the present experiment does not provide branching ratios between the different fragments—H-atom loss vs CH_3 fragment, the mechanism proposed by Thomas *et al.* would explain the low branching ratio reported elsewhere. The N–H bond dissociation channel described above appears, indeed, to be highly favorable compared to the two supplementary minor channels reported for the H-atom loss[34] and to the C–N bond cleavage reported here. On-the-fly trajectories following excitation around 200 nm would be particularly interesting in order to support and further unravel the reaction pathways proposed.

V. CONCLUSIONS

In this work, a joint experimental and theoretical study of the C–N bond cleavage from the photodissociation of methylamine in the blue edge of the first absorption band (198–204 nm wavelength range) is presented. Velocity map imaging is employed in conjunction with resonance enhanced multiphoton ionization detection of vibrationally state selected CH_3 fragments, in particular, in $v = 0$, $v_1 = 1$, and $v_2 = 1$. The recorded images show in all cases a similar unstructured blot, leading to a Boltzmann-type distribution characterizing the corresponding translational energy distributions. The speed-dependent anisotropy parameters from the obtained angular distributions reveal, however, the presence of two dissociation mechanisms. The computed potential energy curves along the C–N distance reveal a similar landscape to the major H-atom loss dissociation channel characterized by an energy barrier and a conical intersection in the exit channel. Upon excitation in the 198–204 nm wavelength range, well above the energy barrier, direct dissociation of the C–N bond through the conical intersection is proposed as a minor channel. In contrast, the observed Boltzmann-type distributions reflect a major slow dissociation mechanism in the ground state. This slow dissociation pathway could arise from a frustrated N–H bond cleavage and from passage through the CI associated with the C–N bond elongation into a vibrationally hot ground state.

The Journal of Chemical Physics ARTICLE pubs.aip.org/aip/jcp

ACKNOWLEDGMENTS

P.R. is grateful to Universidad Complutense de Madrid (UCM) for a Margarita Salas postdoctoral contract. J.C. acknowledges the financial support from the Spanish Ministry of Science and Innovation under the FPI predoctoral program. This research was carried out within the Unidad Asociada Química Física Molecular between the Departamento de Química Física of Universidad Complutense de Madrid and CSIC. This work was funded by Grant Nos. PGC2018-096444-B-I00, PID2019-107115GB-C21, PID2021-122839NB-I00, and PID2021-122549NB-C21 from the Spanish Ministry of Science and Innovation. The financial support (Grant No. PR27/21-010) provided by the Madrid Government (Comunidad de Madrid, Spain) under the Multiannual Agreement with Universidad Complutense de Madrid in the line Research Incentive for Young Ph.D.s, in the context of the V PRICIT (Regional Programme of Research and Technological Innovation), is also acknowledged. The facilities provided by the Centro de Láseres Ultrarrápidos at Universidad Complutense de Madrid are gratefully acknowledged.

AUTHOR DECLARATIONS

Conflict of Interest

The authors have no conflicts to disclose.

Author Contributions

Javier Cachón: Data curation (equal); Formal analysis (equal); Methodology (equal); Writing – original draft (equal). **Pedro Recio**: Data curation (equal); Formal analysis (equal); Investigation (equal); Methodology (equal); Writing – original draft (equal). **Alexandre Zanchet**: Data curation (equal); Methodology (equal); Software (equal); Writing – original draft (equal). **Sonia Marggi Poullain**: Investigation (equal); Methodology (equal); Supervision (equal); Writing – original draft (equal); Writing – review & editing (equal). **Luis Bañares**: Conceptualization (lead); Project administration (lead); Resources (lead); Supervision (lead); Writing – review & editing (lead).

DATA AVAILABILITY

The data that support the findings of this study are available from the corresponding author upon reasonable request.

REFERENCES

[1] J. Kirkby, J. Curtius, J. Almeida, E. Dunne, J. Duplissy, S. Ehrhart, A. Franchin, S. Gagné, L. Ickes, A. Kürten *et al.*, "Role of sulphuric acid, ammonia and galactic cosmic rays in atmospheric aerosol nucleation," Nature **476**, 429–433 (2011).
[2] S.-S. Lv, S.-K. Miao, Y. Ma, M.-M. Zhang, Y. Wen, C.-Y. Wang, Y.-P. Zhu, and W. Huang, "Properties and atmospheric implication of methylamine–sulfuric acid–water clusters," J. Phys. Chem. A **119**, 8657–8666 (2015).
[3] F. Yu and G. Luo, "Modeling of gaseous dimethylamine in the global atmosphere: Impacts of oxidation and aerosol uptake," Atmos. Chem. Phys. **14**, 12455 (2014).
[4] J. Mao, F. Yu, Y. Zhang, J. An, L. Wang, J. Zheng, L. Yao, G. Luo, W. Ma, Q. Yu, C. Huang, L. Li, and L. Chen, "High-resolution modeling of gaseous methylamines over a polluted region in China: Source-dependent emissions and implications of spatial variations," Atmos. Chem. Phys. **18**, 7933–7950 (2018).
[5] N. Kaifu, M. Morimoto, K. Nagane, K. Akabane, T. Iguchi, and K. Takagi, "Detection of interstellar methylamine," Astrophys. J. **191**, L135–L137 (1974).
[6] N. Fourikis, K. Takagi, and M. Morimoto, "Detection of interstellar methylamine by its $2_{02} \rightarrow 1_{10}$ a_a- state transition," Astrophys. J. **191**, L139–L141 (1974).
[7] J. Biesner, L. Schnieder, G. Ahlers, X. Xie, K. H. Welge, M. N. R. Ashfold, and R. N. Dixon, "State selective photodissociation dynamics of $\tilde{A}$ state ammonia. II," J. Chem. Phys. **91**, 2901–2911 (1989).
[8] J. Biesner, L. Schnieder, J. Schmeer, G. Ahlers, X. Xie, K. H. Welge, M. N. R. Ashfold, and R. N. Dixon, "State selective photodissociation dynamics of $\tilde{A}$ state ammonia. I," J. Chem. Phys. **88**, 3607–3616 (1988).
[9] M. N. R. Ashfold, R. N. Dixon, M. Kono, D. H. Mordaunty, and C. L. Reed, "Near ultraviolet photolysis of ammonia and methylamine studied by H Rydberg atom photofragment translational spectroscopy," Philos. Trans. R. Soc. London, Ser. A **355**, 1659–1676 (1997).
[10] J. D. Rodríguez, M. G. González, L. Rubio-Lago, and L. Bañares, "A velocity map imaging study of the photodissociation of the $\tilde{A}$ state of ammonia," Phys. Chem. Chem. Phys. **16**, 406–413 (2014).
[11] J. V. Michael and W. A. Noyes, "The photochemistry of methylamine," J. Am. Chem. Soc. **85**, 1228–1233 (1963).
[12] E. Kassab, J. T. Gleghorn, and E. M. Evleth, "Theoretical aspects of the photochemistry of methanol, methylamine, and related materials," J. Am. Chem. Soc. **105**, 1746–1753 (1983).
[13] G. C. G. Waschewsky, D. C. Kitchen, P. W. Browning, and L. J. Butler, "Competing bond fission and molecular elimination channels in the photodissociation of CH_3NH_2 at 222 nm," J. Phys. Chem. **99**, 2635–2645 (1995).
[14] K. M. Dunn and K. Morokuma, "*Ab initio* study of the photochemical dissociation of methylamine," J. Phys. Chem. **100**, 123–129 (1996).
[15] C. L. Reed, M. Kono, and M. N. R. Ashfold, "Near-UV photolysis of methylamine studied by H-atom photofragment translational spectroscopy," J. Chem. Soc., Faraday Trans. **92**, 4897–4904 (1996).
[16] A. Golan, S. Rosenwaks, and I. Bar, "Mode-dependent enhancement of photodissociation and photoionization in a seven atom molecule," J. Chem. Phys. **125**, 151103–151104 (2006).
[17] M. H. Park, K.-W. Choi, S. Choi, S. K. Kim, and Y. S. Choi, "Vibrational structures of methylamine isotopomers in the predissociative $\tilde{A}$ states: CH_3NHD, CD_3NH_2, CD_3NHD, and CD_3ND_2," J. Chem. Phys. **125**, 084311 (2006).
[18] D.-S. Ahn, J. Lee, J.-M. Choi, K.-S. Lee, S. J. Baek, K. Lee, K.-K. Baeck, and S. K. Kim, "State-selective predissociation dynamics of methylamines: The vibronic and H/D effects on the conical intersection dynamics," J. Chem. Phys. **128**, 224305–224307 (2008).
[19] C. Levi, G. J. Halasz, Á. Vibók, I. Bar, Y. Zeiri, R. Kosloff, and M. Baer, "An intraline of conical intersections for methylamine," J. Chem. Phys. **128**, 244302–244306 (2008).
[20] R. Marom, U. Zecharia, S. Rosenwaks, and I. Bar, "Vibrational overtone spectra of N–H stretches and intramolecular dynamics on the ground and electronically excited states of methylamine," J. Chem. Phys. **128**, 154319 (2008).
[21] R. Marom, T. Weiss, S. Rosenwaks, and I. Bar, "Site-dependent photodissociation of vibrationally excited CH_3NH_2," J. Chem. Phys. **130**, 164312–164317 (2009).
[22] C. Levi, G. J. Halasz, Á. Vibók, I. Bar, Y. Zeiri, R. Kosloff, and M. Baer, "A novel intraline of conical intersections for methylamine: A theoretical study," Int. J. Quantum Chem. **109**, 2482–2489 (2009).
[23] C. Levi, R. Kosloff, Y. Zeiri, and I. Bar, "Time-dependent quantum wave-packet description of H and D atom tunneling in N–H and N–D photodissociation of methylamine and methylamine-d_2," J. Chem. Phys. **131**, 064302–064307 (2009).
[24] R. Marom, C. Levi, T. Weiss, S. Rosenwaks, Y. Zeiri, R. Kosloff, and I. Bar, "Quantum tunneling of hydrogen atom in dissociation of photoexcited methylamine," J. Phys. Chem. A **114**, 9623–9627 (2010).
[25] C. Levi, G. J. Halasz, Á. Vibók, I. Bar, Y. Zeiri, R. Kosloff, and M. Baer, "Intralines of quasi-conical intersections on torsion planes: Methylamine as a case study," J. Phys. Chem. A **113**, 6756–6762 (2009).
[26] D.-S. Ahn, J. Lee, Y. C. Perk, Y. S. Lee, and S. K. Kim, "Nuclear motion captured by the slow electron velocity imaging technique in the tunneling predissociation of the S_1 methylamine," J. Chem. Phys. **136**, 024306 (2012).

The Journal of Chemical Physics ARTICLE pubs.aip.org/aip/jcp

[27]H. Xiao, S. Maeda, and K. Morokuma, "Theoretical study on the photodissociation of methylamine involving S_1, T_1, and S_0 states," J. Phys. Chem. A **117**, 5757–5764 (2013).
[28]J. O. Thomas, K. E. Lower, and C. Murray, "Formation of vibrationally excited methyl radicals following state-specific excitation of methylamine," J. Phys. Chem. A **118**, 9844–9852 (2014).
[29]M. Epshtein, A. Portnov, and I. Bar, "Evidence for quantum effects in the predissociation of methylamine isotopologues," Phys. Chem. Chem. Phys. **17**, 19607–19615 (2015).
[30]Y. Onitsuka, K. Yamasaki, H. Goto, and H. Kohguchi, "Detection of the excited-state NH_2 ($\tilde{A}\ ^2A_1$) in the ultraviolet photodissociation of methylamine," J. Phys. Chem. A **120**, 8584–8589 (2016).
[31]S. J. Baek, K.-W. Choi, Y. S. Choi, and S. K. Kim, "Spectroscopy and dynamics of methylamine. I. Rotational and vibrational structures of CH_3NH_2 and CH_3ND_2 in $\tilde{A}$ states," J. Chem. Phys. **118**, 11026–11039 (2003).
[32]M.-J. Hubin-Franskin, J. Delwiche, A. Giuliani, M.-P. Ska, F. Motte-Tollet, I. C. Walker, N. J. Mason, J. M. Gingell, and N. C. Jones, "Electronic excitation and optical cross sections of methylamine and ethylamine in the UV–VUV spectral region," J. Chem. Phys. **116**, 9261–9268 (2002).
[33]S. P. Sander, J. Abbatt, J. R. Barker, J. B. Burkholder, R. R. Friedl, D. M. Golden, R. E. Huie, C. E. Kolb, M. J. Kurylo, G. K. Moortgat, V. L. Orkin, and P. H. Wine, "Chemical kinetics and photochemical data for use in atmospheric studies," Evaluation No. 17, NASA JPL Publication 10-6, Jet Propulsion Laboratory, Pasadena, CA, 2011.
[34]P. Recio, J. Cachón, A. Zanchet, S. Marggi Poullain, and L. Bañares, "Photodissociation dynamics of methylamine in the blue edge of the *A* band. I. The H-atom channel," J. Chem. Phys. **158**, 234304 (2023).
[35]L. Rubio-Lago, A. García-Vela, A. Arregui, G. A. Amaral, and L. Bañares, "The photodissociation of CH_3I in the red edge of the *A*-band: Comparison between slice imaging experiments and multisurface wave packet calculations," J. Chem. Phys. **131**, 174309 (2009).
[36]L. Rubio-Lago, J. D. Rodríguez, A. García-Vela, M. G. González, G. A. Amaral, and L. Bañares, "A slice imaging and multisurface wave packet study of the photodissociation of CH_3I at 304 nm," Phys. Chem. Chem. Phys. **13**, 8186–8194 (2011).
[37]B. Zhang, J. Zhang, and K. Liu, "Imaging the 'missing' bands in the resonance-enhanced multiphoton ionization detection of methyl radical," J. Chem. Phys. **122**, 104310 (2005).
[38]V. Papadakis and T. N. Kitsopoulos, "Slice imaging and velocity mapping using a single field," Rev. Sci. Instrum. **77**, 083101 (2006).
[39]L. GmbH, Davis 6.2.
[40]H.-J. Werner, P. J. Knowles, G. Knizia, F. R. Manby, M. Schütz, P. Celani, W. Györffy, D. Kats, T. Korona, R. Lindh, A. Mitrushenkov, G. Rauhut, K. R. Shamasundar, T. B. Adler, R. D. Amos, S. J. Bennie, A. Bernhardsson, A. Berning, D. L. Cooper, M. J. O. Deegan, A. J. Dobbyn, F. Eckert, E. Goll, C. Hampel, A. Hesselmann, G. Hetzer, T. Hrenar, G. Jansen, C. Köppl, S. J. R. Lee, Y. Liu, A. W. Lloyd, Q. Ma, R. A. Mata, A. J. May, S. J. McNicholas, W. Meyer, T. F. Miller III, M. E. Mura, A. Nicklass, D. P. O'Neill, P. Palmieri, D. Peng, K. Pflüger, R. Pitzer, M. Reiher, T. Shiozaki, H. Stoll, A. J. Stone, R. Tarroni, T. Thorsteinsson, M. Wang, and M. Welborn, MOLPRO, version 2015.1, a package of *ab initio* programs, 2015, see http://www.molpro.net.
[41]T. H. Dunning, "Gaussian basis sets for use in correlated molecular calculations. I. The atoms boron through neon and hydrogen," J. Chem. Phys. **90**, 1007 (1988).
[42]H.-J. Werner and P. J. Knowles, "A second order multiconfiguration SCF procedure with optimum convergence," J. Chem. Phys. **82**, 5053 (1985).
[43]H.-J. Werner, "Third-order multireference perturbation theory the CASPT3 method," Mol. Phys. **89**, 645–661 (1996).
[44]P. J. Knowles and H.-J. Werner, "Internally contracted multiconfiguration-reference configuration interaction calculations for excited states," Theor. Chim. Acta **84**, 95–103 (1992).
[45]A. T. J. B. Eppink and D. H. Parker, "Methyl iodide *A*-band decomposition study by photofragment velocity imaging," J. Chem. Phys. **109**, 4758 (1998).
[46]*NIST Chemistry Webbook: NIST Standard Reference Database Number 69*, edited by P. J. Linstrom and W. G. Mallard (National Institute of Standards and Technology, Gaithersburg, MD, 2022).
[47]R. N. Zare and W. G. Harter, *Angular Momentum: Understanding Spatial Aspects in Chemistry and Physics* (Wiley, New York, 1988), p. 120.
[48]R. N. Dixon, "The determination of the vector correlation between photofragment rotational and translational motions from the analysis of Doppler-broadened spectral line profiles," J. Chem. Phys. **85**, 1866–1879 (1986).
[49]Y. Wang, C. Xie, H. Guo, and D. R. Yarkony, "A quasi-diabatic representation of the $1,2^1A$ states of methylamine," J. Phys. Chem. A **123**, 5231–5241 (2019).

3.3 Photodissociation dynamics of methylamine in the blue edge of the *A*-band. III. The NH + CH_4 channel

Art. 3. *Photodissociation dynamics of methylamine in the blue edge of the A-band. III. The NH + CH_4 channel*., Javier Cachón, Pedro Recio, Alexandre Zanchet, Sonia Marggi Poullain, and Luis Bañares. To be submitted (2024).

Abstract

The formation of NH($\tilde{X}^3\Sigma^-, \mathrm{v} = 0\ \mathrm{J} = 2$) from the photodissociation of methylamine (CH_3NH_2) is investigated by using resonance-enhanced multiphoton ionization (REMPI) detection combined with velocity map imaging (VMI). Three excitation wavelengths were selected: 198.42 and 201.33 nm, in the blue edge of the first absorption band and 239.95 nm associated with the 0_0^0 transition. The experimental results, consisting of NH translational energy distributions as well as angular distributions, are complemented by *ab initio* calculations consisting of relevant potential energy curves. The experimental results are complemented by *ab initio* calculations of the potential energy curves. The results are consistent with the formation of NH through a roaming-mediated intersystem crossing (ISC) mechanism, which involves the initial cleavage of C – N bond into CH_3 and NH_2 fragments, followed by the migration of a hydrogen atom to form NH and methane (CH_4).

Introduction

The NH radical has long been recognized as a cornerstone in molecular dynamics and spectroscopy due to its importance in various chemical and physical processes. As a fundamental species, the NH radical plays a vital role in atmospheric, combustion, and astrochemical systems, which makes it the subject of both experimental and theoretical research. Its relatively simple electronic structure and reactivity offer a lot of insights into molecular dissociation dynamics, reaction mechanisms, and energy transfer. As a diatomic radical, its open-shell structure provides an ideal system for studying intricate processes like intersystem crossing, photodissociation, and roaming dynamics, making NH indispensable in spectroscopic studies and kinetic modeling [52], [53].

The NH radical ($\tilde{X}^3\Sigma^-$) plays an important role in understanding photodissociation dynamics, given their electronic structure [54], [55]. An important molecule in the astrochemical and atmospheric chemistry [56] that has received a great attention in recent years is methylamine (CH_3NH_2). Methylamine photodissociation in the first absorption band (A-band) has garnered considerable attention due to the complexity of its dissociation pathways. This A-band, between 240 and 190 nm, is assign to the transition from the long pair orbital of the N-atom into the $3s$ Rydberg state, correspond to the $\tilde{A}^1A' \leftarrow \tilde{X}^1A'$ electronic transition. The absorption band is characterized by a well-defined vibrational structure, which has been assigned to several vibration propagation, specially to the ν_7, CH_3 rocking, and ν_9, NH_2 wagging, vibrational modes.

In 1962, Michael and Noyes [57] published a study on the photodissociation of methylamine, where they describe four possible dissociation pathways. These were the elimination of H-atoms, from both the nitrogen and carbon moieties, the breaking of the C-N bond to produce

the radicals CH_3 and NH_2, and the formation of H_2. After this, the main dissociation channels of methylamine have been deeply studied. For instance, recently, Recio *et al.* [53] study the H-atom elimination using velocity map imagine (VMI) and resonant enhanced multiphoton ionization (REMPI) techniques in the blue edge of the A-band (198-204 nm). The experimental results were explained in combination of *ab initio* calculation of the potential energy curves (PECs). They observed an important structural change upon excitation of the parent molecule, where the pyramidal geometry around the nitrogen atom (C-NH_2) transformed into a planar structure. This geometry change causes the barrier present in the excited state to lower considerably resulting in the appearance of a conical intersection (CI). Thanks to the presence of the CI, three dissociation pathways could explained the experimental results that they obtained, as CH_3NH_2 it could dissociate in the first excited state producing H + $CH_3NH(\tilde{A})$ or in the ground state, after crossing the CI. The third possible pathway was suggested to be a frustrated crossing of the CI going back to the well with enough energy to break the N-H bond. The probability of crossing the CI or not was rationalized in terms of the excitation energy.

A follow up publication was made from the same group, where the C-N bond cleavage channel [54] was studied. The theoretical calculations performed in for the PECs presented a very similar landscape to the H-atom elimination channel [53], where a conical intersection in the exit channel characterized the dissociation. In contrast, experimentally the results, measured in the same wavelength range (198-204 nm), were not that clear, as Boltzmann-type distributions were obtained in all cases. However, the angular analysis of the CH_3 fragments suggests the presence of a minor prompt dissociation mechanism that operates through a CI in the exit channel. Although, the angular analysis of the CH_3 fragments suggests the presence of a minor prompt dissociation mechanism that operates through a CI in the exit channel, the main dissociation process was suggested to arise from the frustrated N-H bond cleavage and passing through the CI. This results in the elongation of the C-N bond generating vibrationally excited fragments.

For the $NH(\tilde{X}^3\Sigma^-)$ radical formation after the dissociation of methylamine, only Thomas *et al.* [58] have reported experimental evidence based on measured REMPI spectra of their formation as primary products following state-specific excitation to the S_1 state. The experimental results were complemented by *ab initio* calculations of relevant stationary points. The results seem to indicate that the formation of $NH(\tilde{X}^3\Sigma^-)$, which requires populating the first triplet excited electronic state, could take place through a roaming-mediated intersystem crossing (ISC). The roaming dynamics bypassing the conventional tight transition states typically required for dissociation, could offer an alternative route for NH formation on the T_1 surface.

Apart from the work of Thomas *et al.* [58], there has not been any more work regarding the $NH(\tilde{X}^3\Sigma^-)$ + CH_4 dissociation channel from methylamine, to the best of our knowledge. Moreover, no ion-imagine experiment has been reported for this channel. For this reason, we have performed a velocity map imagine experiment using REMPI spectroscopy to detect $NH(\tilde{X}^3\Sigma^-)$ radicals upon photodissociation of CH_3NH_2. These techniques allow us to study the translational energy and angular distributions of the generated photofragments, creating a complete picture of the mechanism. By comparing measurements at the beginning and at the blue edge of the first absorption band we can understand the processes that generate this dissociation channel in the A-band. In addition, the experimental finding, are complemented by the complete potential energy curves for the formation of $NH(\tilde{X}^3\Sigma^-)$ radicals and CH_4 of the ground and first electronic singlet and triplet states as a function of the C-N distance and of the distance to the transferred H-atoms between the carbon and nitrogen atom.

Experimental Methodology

The experimental setup used in this study has been described in detail previously [68], [69], and only a summary is provided here. The molecular beam is created by expanding a gas mixture of CH_3NH_2 in helium (10%, 1 atm backing pressure) into vacuum using a pulsed nozzle (General Valve Series 9 with a 0.5 mm orifice). The nozzle is synchronized with the nanosecond pulsed laser system, which operates at 10 Hz. The gas beam passes through a skimmer with an orifice of 0.5 mm (Beam Dynamics Standard Model 2) before entering the reaction chamber. Here, the molecular beam is intersected, at right angles, by the photolysis and probe laser in counter propagation. The interaction occurs between the electrical plates of a time-of-flight mass spectrometer (TOFMS) with velocity map imaging capabilities. The entire experiment was conducted at a repetition rate of 10 Hz.

The photolysis laser is generated using a Nd:YAG laser (Quanta-Ray Pro 230) pumped frequency-doubled dye laser (Sirah Cobra-Stretch). By combining the fundamental and second harmonic radiation of the dye laser with a sum-frequency mixing nonlinear crystal, the desired wavelengths are produced. Specifically, three wavelengths are used for this experiment: 198.42, 201.33, and 239.95 nm, corresponding to one-photon vibronic transitions 9_0^{13}, 9_0^{12}, and 0_0^0 in methylamine [70], [71], [72]. The resulting radiation, typically 1.7 mJ per pulse, is focused into the reaction chamber with a 25 cm focal length lens. After a delay of 10 ns, NH fragments were ionized by a counter-propagating probe pulse of about 2 mJ, generated by a frequency-doubled dye laser (Sirah Cobra-Stretch), pumped by another Nd:YAG laser (Quanta-Ray Pro 190). The NH($\tilde{X}^3\Sigma^-$) fragments in $\mathrm{v} = 0$ $\mathrm{J} = 2$ were resonantly ionized at 336.14 nm, using a (3 + 1) resonance-enhanced multiphoton ionization (REMPI) scheme. Since NH and methyl radicals have the same mass and cannot be separated, images measured off-resonance, at $\lambda = 335.53$ nm, were subtracted to the NH images recorded at 336.14 nm in order to eliminate any possible methyl contamination.

The ions produced are accelerated by an electric field generated between two electrodes: a 3 kV repeller and a grounded extractor and go through a field-free region of 40 cm where they are separated based on their mass-to-charge ratio before striking impedance-matched microchannel plates (MCPs) arranged in a chevron configuration. A 20 ns high-voltage pulse (500 V) was applied to gate the gain of the MCPs, ensuring selective detection of the ions of interest. The resulting electron avalanche hit a phosphor screen, generating an image recorded by a CCD camera (Sony 1024 × 768 pixels) controlled by National Instruments (NI) LabVIEW 7.1 and IMAQ VISION software. The final image, obtained from approximately 40,000 to 100,000 laser shots, is symmetrized and then inverted using the Hankel transformation method to reconstruct the three-dimensional distribution of the Newton sphere [68], [73]. In order to transform the pixel position of the CCD camera into translational energy, independent velocity-radius calibration of the apparatus was done. For this calibration, one-color laser, at 333.45 nm, pump-probe technique was used to excited the CH_3I and detect the $CH_3(v = 0)$ fragment through the well-known cold vibrational distribution for the CH_3 + I($^2P_{3/2}$) channel at this photolysis wavelength.[55]

Theoretical Methodology

The NH formation in the photodissociation of methylamine has been considered at the multireference configuration interaction (MRCI) level to provide insight into the possible mechanisms. For all the calculations, the MOLPRO package with a basis set aug-cc-pVQZ of Dunning [74] has been employed. Assuming that no direct mechanisms can lead to the formation of methane, here we explore the possibility of a roaming mechanism in which C-N bond cleavage is frustrated and the methyl radical strip an H atom of the NH_2 fragment to lead to NH+CH_4. The calculations relative to the NH_2 + CH_3 fragmentation channel are already detailed in Ref. [75]. Since the ground state of NH is a triplet state, in contrast to our previous works, MRCI calculations along the C-N bond are carried out following the minimum fragmentation path of the lower triplet state. The active space employed for this calculation is the same as in Ref. [75], four electrons in six orbitals, while seven orbitals are considered closed, at the complete active space self-consistent field (CASSCF) level [56].

In a second step, the reaction path leading from CH_3 + NH_2 to CH_4 + NH is then obtained as follows: first we define the reaction coordinate as $s = R_{NH} - R_{CH}$, such as a value of $s = 0$ indicate that an H-atom is at the same distance from the NH and CH_3 moieties. Then, following the strategy of our previous work, the geometries to build the potential energy curves (PECs) associated to this reaction path are obtained for several imposed distances of *s* between -4.0 and 3.5 Å, with a step of 0.2 Å, while relaxing the remaining coordinates of the system at a CASPT2 [76] level. As for the C-N bond cleavage, all the relaxations were performed on the ^{3}A' state. Finally, for all the optimized geometries along the obtained reaction path, MRCI [77] calculations are performed to compute the two first singlet and the first triplet electronic states of the parent molecule with higher accuracy. In order to generate orbitals suitable for MRCI calculations, the complete active space self-consistent field (CASSCF) method[74] employed considers an active space of 14 electrons in 13 orbitals with the two 1s orbitals kept closed. In order to obtained a energy scale referenced to the minimum in the CH_3NH_2 ground state, since everything else was optimized in the triplet, the energy in this point was also computed at same level.

Results and discussion

The inverted velocity map images recorded for the NH ($\tilde{X}^3\Sigma^-, v = 0\, J = 2$) fragments produced in the photodissociation of methylamine at the three selected excitation energies, 198.42, 201.33, and 239.95 nm, corresponding to 9_0^{13}, 9_0^{12}, and 0_0^0 transitions, respectively, are depicted in Figure 3.1. Since methyl ions produced by multiphoton ionization could contaminate the NH signal of interest, images were recorded in each case using a 335.53 nm probe and subtracted to the NH images recorded using the (3+1) REMPI scheme. The translational energy distributions (TEDs) obtained by angular integration of the inverted images are also shown in Figure 3.1. An unstructured blot is observed in the images at all excitation wavelengths leading to Boltzmann-type distributions in the TEDs. As observed, the image obtained at the 0_0^0 transition is considerably small leading to smaller translational energies. The widths, *w*, characterizing each distribution, measured at half intensity, are summarized in Table 3.1. As observed, *w* increases as the excitation energy increases, *i.e.* for shorter wavelengths. *w* is indeed particularly lower at the origin of the band. The reported TEDs reflect the formation of

NH in conjunction with the methane (CH_4) co-fragment in a broad distribution of ro-vibrational states.

The red vertical line represents the maximum translational energy that the fragment can obtained (E_{av}) calculated as:

$$E_{av} = \frac{m_{CH_4}}{m_{CH_3NH_2}}[hv - D_0 - E_{int}(NH) + E_{\text{int}}(CH_3NH_2)] \quad (1)$$

where hv is the photon energy used for exciting the molecule, D_0 is the dissociation energy of methylamine, 2.95 eV (extracted from ref [78]) and $E_{int}(NH)$ the internal energy of the NH fragment detected which consist in vibrational and rotational energies ($E_{\text{int}}(NH) = E_{vib} + E_{rot}$). Since NH is detected at $v = 0$, $E_{vib} = 0$ eV, while the rotation energy is calculated for $J = 2$ as $E_{rot} = B \cdot J(J+1)$, where B is the rotation constant ($B = 16.34\ cm^{-1}$ [57]). $E_{\text{int}}(CH_3NH_2)$ represents the internal energy of the methylamine parent molecule which can be considered negligible since a molecular beam is used.

The fraction of the available energy transferred to internal energy of the co-fragment, f_{int} is determined using:

$$f_{int} = \frac{E_{int}}{E_{av}} = \frac{E_{peak} - E_{av}}{E_{av}} \quad (2)$$

where E_{int} denotes the internal energy and E_{peak} the energy position at the maximum of the distribution. Significantly high values of f_{int} are found at all excitation wavelengths, reflecting an efficient transfer of most available energy into internal energy. These values are consistent with a slow dissociation leading to the formation of methane in highly excited ro-vibrational states.

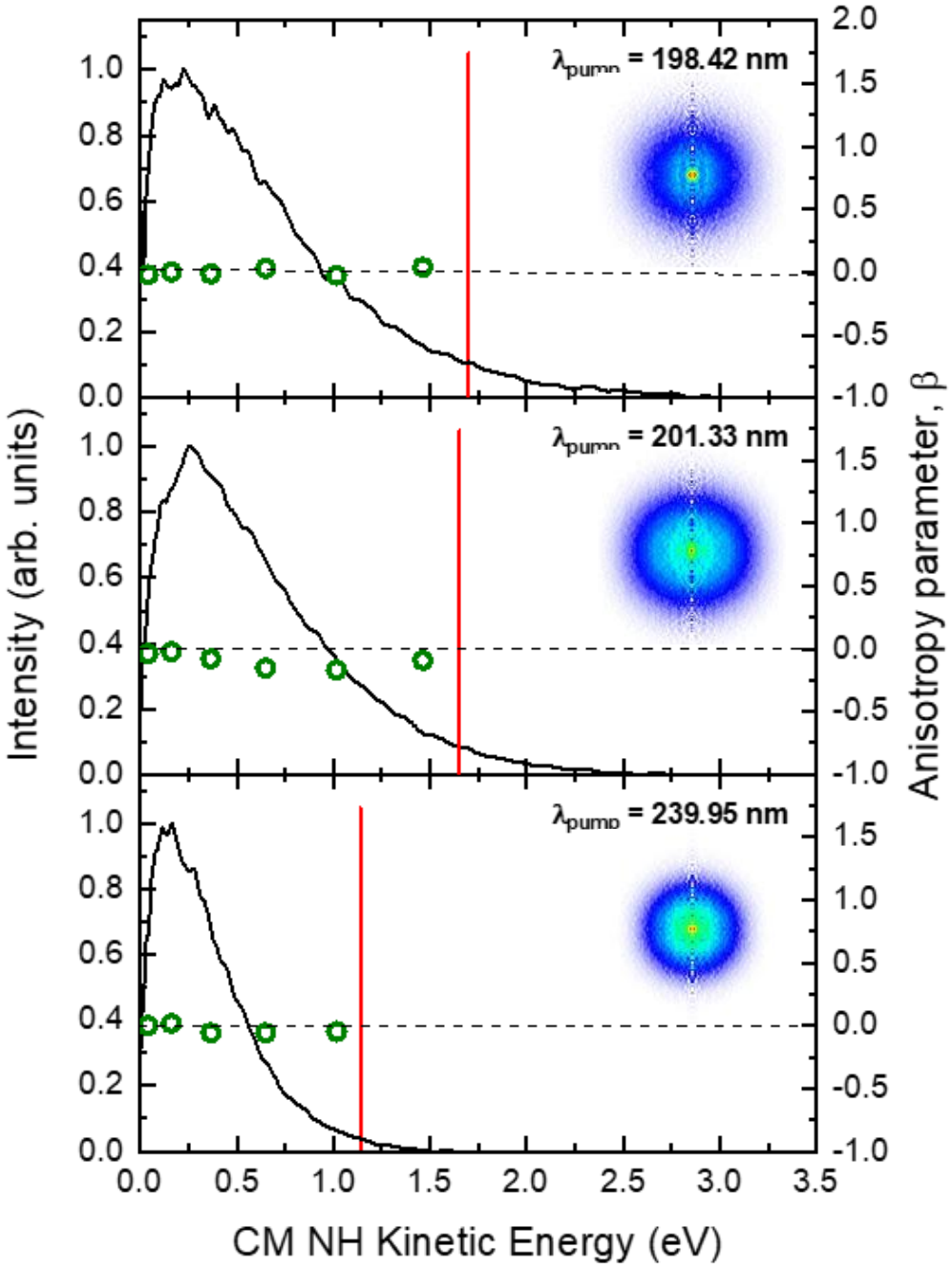

FIGURE 3.31: *CENTER-OF-MASS (CM) TRANSLATIONAL ENERGY DISTRIBUTIONS OF NH FRAGMENTS FROM THE PHOTODISSOCIATION OF METHYLAMINE AT THREE EXCITATION WAVELENGTHS, FROM TOP TO BOTTOM 198.42, 201.33 AND 239.95 NM. THE TRANSLATIONAL ENERGY, BLACK LINE, IS PLOTTED WITH THE LEFT Y-AXIS, WHILE THE ANISOTROPY PARAMETER (Β), GREEN CIRCLES, IN THE RIGHT AXIS. THE PROBE WAVELENGTH USED IN ALL CASES IS 336.14 NM. THE RED VERTICAL LINE REPRESENT THE MAXIMUM TRANSLATIONAL ENERGY OF THE FRAGMENT.*

Table 3.1: widths estimated at the TEDs half intensity, fraction of the available energy that appears as the co-fragment internal energy, and average anisotropy parameter (β) obtained with eq 2. All values have an error of 2%.

λ_{exc}	width (eV)	f_{int}	β
198.42	0.92	0.87	0.00
201.33	0.88	0.84	-0.06
239.95	0.50	0.85	0.02

The speed-dependent angular distributions were obtained by the radial integration of the images and fitted to the following equation [13]:

$$I(\theta) = 1 + \beta P_2(cos\theta) \quad (3)$$

where θ represents the angle between the photolysis laser polarization and the fragment recoil velocity, $P_2(cos\theta)$ is the 2nd order Legendre polynomial, and β is the anisotropy parameter. Anisotropy parameter (β) is plotted as a function of the NH CM translational energy in Fig. 3.1 (green circles) while the value obtained for the whole image is presented in Table 3.1. In all cases, the values of β are close to zero, reflecting an isotropic distribution, typical of a slow dissociation process during which the molecule can rotate and the initial anisotropy is lost. These results, along with the Boltzmann-type TEDs, are consistent with the roaming mechanism proposed by Murray and coworkers [58].

The formation of NH($\tilde{X}^3\Sigma^-$) radicals from a direct dissociation will require an H-atom migration while the C-N bond dissociates. Taking into account that the umbrella vibrational mode is the one activated by excitation into the first singlet electronic state, it seems unlikely to promote such nuclear rearrangement, even if an intersystem crossing (ISC) can occur at some point. In addition, a three-body dissociation into CH_3 + H + NH could be considered. The dissociation energy for this path is higher than the one-photon excitation energy and experiments detecting methyl radicals [54] show no evidence of this path as a result of the one-photon excitation. Moreover, NH cannot be produced as a result of the secondary dissociation of NH_2 following a second photon absorption, since NH_2 does not absorb in the wavelength range employed in the present work. NH fragments were considered by Murray and co-workers to be produced from an initial N-H bond cleavage. A huge barrier was found to characterize the follow up C-N bond cleavage. Hence, we also discard this pathway and explore the more likely mechanism taking place through an initial C-N bond cleavage follow by a H-atom transfer.

In Figure 3.32, the potential energy curves (PECs) for the generation of NH radicals through this mechanism are presented in two panels. The PECs as a function of the C-N bond distance are depicted in the left panel of Fig. 3.2 for the ground state (black line) and two excited states, the first singlet (red line) and the first triplet (blue line) state of CH_3NH_2. These PECs are equivalent to those published by our group previously where the C-N bond dissociation mechanisms of methylamine were discussed [54], although including now geometries optimized considering also the triplet state.

In the right panel of Fig. 3.32, the PECs are shown for the same three states but as a function of the reaction coordinate describing an H-atom transfer from NH_2 to CH_3 fragments. The reaction coordinate is defined as $s = R_{NH} - R_{CH}$, where R_{NH} and R_{CH} are the intramolecular

distances of the nitrogen and carbon atoms with their corresponding H-atoms. Therefore, $s = 0$ corresponds by definition to a situation where the transferred H-atom is located at the same distance of C and N, and, thus, is located close to the transition state of the reaction. At negative s values, the transferred H-atom is close to the N-atom and far from the C-atom. For s = -4, it directly corresponds to the NH_2 + CH_3 dissociation and the energies can be directly compared to the asymptotic values of the C-N bond cleavage potential energy curves. In contrast, at positive values, the H-atom is close to the C-atom and the asymptote corresponds to the formation of methane. In this way, the right panel can be seen as a continuation of the left one to follow the energetics into the NH formation.

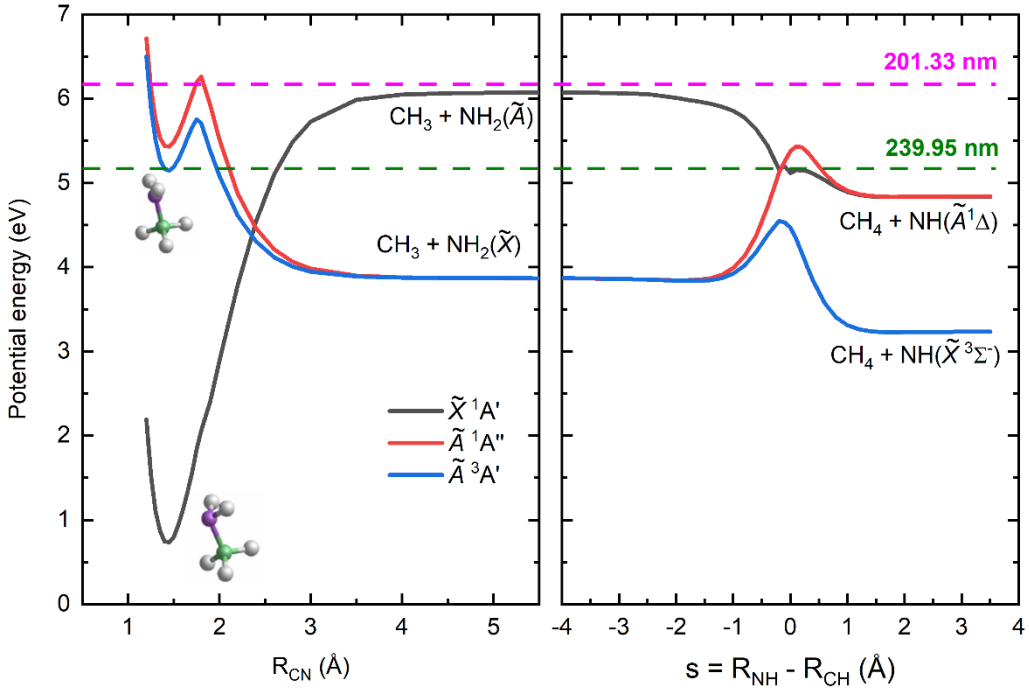

FIGURE 3.32: *POTENTIAL ENERGY CURVES FOR CH_3NH_2 DISSOCIATION AS A FUNCTION OF THE C–N BOND DISTANCE (LEFT PANEL) AND AS A FUNCTION OF THE H-ATOM TRANSFERRED BETWEEN THE NH AND CH_3 MOIETIES (RIGHT PANEL). THREE ELECTRONIC STATES HAVE BEEN CONSIDERED: THE GROUND STATE ($\tilde{X}^1A'$), THE FIRST SINGLET EXCITED STATE ($\tilde{A}^1A''$), AND THE TRIPLET EXCITED STATE ($\tilde{A}^3A'$), REPRESENTED AS BLACK, RED AND BLUE LINES, RESPECTIVELY. TWO HORIZONTAL DASHED LINES ARE DEPICTED INDICATING THE EXPERIMENTAL EXCITATION ENERGY AT 239.95 NM (GREEN) AND AT 201.33 NM (PINK).*

The production of NH($\tilde{X}^3\Sigma^-$) radicals starts by exciting CH_3NH_2, producing CH_3 and NH_2 fragments. Upon one-photon excitation, a strong structural change happens. The two H-atoms of the NH_2 moiety move from a pyramidal geometry with respect to the N-atom (C-NH_2) in the ground state, to a planar structure in the excited state where the two H-atoms are in the plane formed by the nitrogen and carbon atoms. As a result, the barrier lowers and a conical intersection (CI) between the ground and first singlet excited electronic states appears. Several outcomes are possible there. The molecule could dissociate directly in the first excited state or cross the CI and dissociate in the ground state. The experiments reported in our recent work [54] show however that a major slow dissociation in a vibrationally hot ground state of the molecule leads to the methyl formation in the ground state. The PECs reported in Figure 3.2 correspond to the planar geometry of the molecule, and the three pathways leading to CH_3 +

NH_2 asymptotes can be observed in the left panel. While the triplet state was discarded by Thomas *et al.[58]* from being responsible to the formation of the CH_3 + NH_2 channel, it needs to be taken into account here as, experimentally, the NH($\tilde{X}^3\Sigma^-$) has been detected, showing that an intersystem crossing (ISC) has to occur. Then, the question that arises is where the ISC from the singlet to the triplet surface can take place.

The calculated potential energy curves actually show that ISC can take place in three regions and does not need to be mediated by roaming, in contrast to Murray and co-workers results. The first possibility is inside the well of the excited singlet states in the Franck-Condon region, just after the molecule has been excited to the $\tilde{A}^1A''$. It is clear that the well of the singlet state is embedded in the well of the triplet state. As it was demonstrated recently, ISC can be favored in this kind of situation[59]. For excitation energies lower than the barrier, this mechanism is expected to be quite efficient as the system will remain in the well for a long time. For higher excitation energies, this mechanism is expected to lose efficiency, because if the system has enough energy to overcome the barrier, it will not remain long enough in the well to undergo an ISC. In any case, if the molecules remain in the $\tilde{A}^1A''$ state and arrives to the CI, the minimum energy crossing point (MECPs) between singlet and triplet lies very close. It can also undergo an ISC in this region, as MECP are also known to greatly favor ISC. Finally, a change of spin state could also occur if the CH_3 and $NH_2(\tilde{X})$ asymptote finally end up recombining, as two doublet fragments can give rise either to a singlet state or a triplet.

In a roaming mechanism, the two fragments depart from one to another, if they do not possess enough translational energy to reach products or by some constraints imposed by the conservation of the total angular momentum, both fragments are attracted and come close again. In the second case, it is conceptually similar to a secondary reaction in which the fragments collide with a given energy. For the hydrogen transfer to happen during this collision, the NH_2 fragment, must be facing the CH_3 with the H-atoms. This can simply be explained by the rotation of the NH_2 fragment as it gets away and close again. Of course, only few collisions are expected to be reactive to produce this exit channel, as the methylamine can form again without any barrier, as it can be seen in the left panel of Fig. 3.32 and also described in our previous work. Nevertheless, since the total energy is conserved, even if the geometrical factor may be unfavorable, the fragments have enough energy for a H-atom transfer from the NH_2 to the CH_3, producing CH_4 + NH. This appears clearly in the right panel of Fig. 3.32. Another possibility, although minimal as it has been explained in ref. [54] it could be that the C-N bond breakage generates $NH_2(\tilde{A})$ fragments, leading preferentially to NH in its excited state.

At the shorter excitation wavelengths used in this work, 198.95 nm and 201.33 nm, the dissociation pathway leading to CH_4 + NH($\tilde{A}^1\Delta$) is also open and can be reached from either $NH_2(\tilde{A})$ or $NH_2(\tilde{X})$ dissociated limits. Since this channel correlates directly with the $^1A''$ excited state of methylamine, no ISC is required to reach these products. However, this pathway is expected to be closed near the origin of the absorption band (around 239.95 nm), as there is an important barrier in the that cannot be overcome by the energy received by the system at this wavelength. Experiments detecting NH($\tilde{A}^1\Delta$) fragments are currently in progress.

Conclusions

This study investigates the photodissociation dynamics of methylamine (CH_3NH_2), focusing on the formation of NH radicals when the molecule is excited at specific wavelengths in the blue

edge of the first absorption band (198.42 and 201.33 nm) or at the origin of that band (239.95 nm). Velocity map imaging in conjunction with resonance enhanced multiphoton ionization detection of NH($\tilde{X}^3\Sigma^-, v = 0, J = 2$) has been used. The NH ion images present in all cases a *bulk* signal with no clear structure, which is translated in the translational energy distributions as a Boltzmann-type distribution, characteristic of a statistical dissociation process. The anisotropy parameter (β) suggest a slow dissociation process, in agreement with a roaming mediated mechanism as proposed by other authors [60]. Potential energy curves have been performed in the possibility of a roaming dissociation process to explain the mechanism.

The formation of NH($\tilde{X}^3\Sigma^-$) radicals involves exciting CH_3NH_2, leading to CH_3 and NH_2 fragment production. After excitation, a structural transformation of CH_3NH_2 from a pyramidal to planar shape reduces an energy barrier, creating a conical intersection (CI) where dissociation paths diverge. The most likely path, consistent with observed slow reaction rates, suggests a frustrated N–H bond break before crossing the CI, producing vibrationally excited ground state products. Additionally, an intersystem crossing (ISC) allows the molecule to transition from singlet to triplet states, primarily in the Franck-Condon region. The NH($\tilde{X}^3\Sigma^-$) radicals will arise from secondary collisions between CH_3 and NH_2 fragments, where the NH_2 is facing the CH_3 with the H-atoms.

Chapter 4 Stereodynamics Study of the Photodissociation of Halocarbons in the UV: Atomic Photofragment Alignment

4.1 Structural effects on the energy disposal and atomic photofragment alignment for the photodissociation of alkyl iodides at the excitation wavelengths 254 and 268 nm

Art. 4. *Structural effects on the energy disposal and atomic photofragment alignment for the photodissociation of alkyl iodides at the excitation wavelengths 254 and 268 nm*, Javier Cachón, Pedro Recio, David Sorribes, Sonia Marggi Poullain, Luis Rubio-Lago, and Luis Bañares. J. Phys. Chem. A, 128, 8312-8321 (2024).

This study begins by explaining the historical significance of alkyl iodides as model systems for investigating photodissociation dynamics in the ultraviolet (UV) region. This class of molecules shows a strong absorption band, known as the *A*-band, in the wavelength range of 220–320 nm, peaking around 260 nm. According to Mulliken's theory, this absorption is due to a transition from the nonbonding lone pair on the iodine atom to an antibonding orbital along the carbon-iodine (C-I) bond ($n \rightarrow \sigma^*$ transition). The *A*-band is particularly interesting because it involves spin-orbit (SO) coupling, which leads to complex electronic dynamics.

Three key spin-orbit electronic states are involved in alkyl iodides photodissociation, each connected to distinct iodine atom products:

1. $^3Q_1$ and $^1Q_1$ correlate with $I(\,^2P_{3/2})$, the ground state iodine fragment.
2. $^3Q_0$ correlates with $I^*(\,^2P_{1/2})$, the excited state iodine fragment.

The $^3Q_0$ state is accessed through a parallel transition, while the $^3Q_1$ and $^1Q_1$ states are accessed *via* perpendicular transitions. The nonadiabatic coupling between the $^3Q_0$ and $^1Q_1$ states is particularly important for understanding the non-adiabatic dynamics that result in ground-state iodine formation after excitation to the $^3Q_0$.

Therefore, the presence of the heavy iodine atom enhances spin-orbit coupling, making this family of molecules ideal for probing non-adiabatic transitions through conical intersections or avoided crossings. While molecules with C_{3v} symmetry (such as methyl iodide, CH_3I, or tert-butyl iodide, *t*-C_4H_9I) closely follow the $^3Q_0$, $^3Q_1$, and $^1Q_1$ state behavior, molecules with lower symmetry, like iso-propyl iodide (*i*-C_3H_7I), exhibit more complex splitting of these states.

This work aims to explore how the structure of alkyl iodides —linear versus branched—affects the photodissociation dynamics and stereodynamics. Specially, how energy is distributed between translational, rotational, and vibrational modes of the fragments, and how the

anisotropy and alignment parameters provide a description of the role played by the molecular structure in adiabatic and, especially, non-adiabatic photodissociation dynamics through conical intersections or avoided crossings.

The total translational energy distributions (TEDs) measured for both iodine states, ground-state $I(\,^2P_{3/2})$ and spin-orbit excited-state $I^*(\,^2P_{1/2})$, reveal significant differences between linear and branched alkyl iodides. For linear iodides, such as methyl iodide (CH_3I) and ethyl iodide (C_2H_5I), a large proportion of the available energy is released as translational energy, indicating that less energy is being transferred into internal (rotational and vibrational) modes. The energy distribution for these simpler molecules suggests a prompt dissociation mechanism, with minimal interaction between the C-I stretch and other vibrational modes.

In contrast, branched alkyl iodides, such as tert-butyl iodide (*t*-C_4H_9I), exhibit broader energy distributions with a larger proportion of the energy transferred to internal modes of the alkyl fragment. The greater internal energy disposal observed in branched molecules is attributed to the coupling between the C-I bond dissociation and the bending modes of the carbon chain, leading to a more complex multidimensional dissociation dynamics. This is particularly evident in t-C_4H_9I, where a significant amount of energy is partitioned into the vibrational modes of the co-fragment, resulting in lower translational energy for the iodine photofragments.

The internal energy fraction (f_{int}), which quantifies the proportion of the available energy transferred to internal modes of the alkyl fragment, increases as the alkyl chain length increases in the linear series (e.g., from CH_3I to *n*-butyl iodide (*n*-C_4H_9I)). This trend is reversed for the branched alkyl iodides, where f_{int} is smaller, indicating that less energy is transferred into internal modes for branched structures compared to their linear counterparts. The multidimensional character of dissociation becomes more pronounced for branched structures due to increased coupling of the reaction coordinate with vibrational modes, leading to more complex energy redistribution.

The alignment of the spin-orbit ground-state iodine fragments is another key focus of the results of this work. The anisotropy parameter (β), which reflects the angular distribution of the fragments relative to the laser polarization, indicates that most of the alkyl iodides dissociate through a parallel transition to the $^3Q_0$ state. This is consistent with high β values (close to 2), especially for CH_3I and C_2H_5I, where the dissociation is relatively direct, and most energy is released into translational motion. The alignment of the iodine fragment is particularly strong in these smaller molecules, indicating that the photodissociation involves minimal energy transfer to internal rotational or vibrational modes of the alkyl co-fragment.

However, as the alkyl chain becomes longer (e.g., *n*-propyl iodide (*n*-C_3H_7I) and *n*-butyl iodide (*n*-C_4H_9I)), the degree of alignment decreases, reflecting increased energy transfer into internal degrees of freedom of the alkyl fragment. This results in a reduction of alignment along the recoil axis, suggesting that the C-I bond no longer serves as the dominant axis for dissociation as the molecule becomes more complex.

For branched iodides, such as *t*-C_4H_9I, the alignment is reduced even further, indicating significant rotational excitation of the alkyl fragment. Interestingly, *t*-C_4H_9I exhibits a higher alignment at 254 nm than expected, possibly due to the higher symmetry of the molecule (C_{3v} symmetry), which allows for more constrained rotational motion despite its branched structure. This observation suggests that even in more complex molecules, certain structural features, such as symmetry, can preserve a degree of alignment in the photofragments.

The effect of the two excitation wavelengths (254 nm and 268 nm) on the photodissociation dynamics is also discussed. Although the two wavelengths are close to each other and to the *A*-band maximum, there are subtle differences in the energy distribution and alignment of the fragments. At 268 nm, which is somewhat to the red of the absorption band, the translational energy distributions show slightly higher peak energies, and the anisotropy is generally stronger compared to 254 nm, which corresponds precisely to the maximum of the band, especially for the smaller linear iodides. These differences may be due to non-adiabatic coupling effects that vary with excitation wavelength, influencing the partitioning of energy between translational and internal modes.

For branched alkyl iodides, such as *iso*-propyl iodide (*i*-C_3H_7I) and *t*-C_4H_9I, the differences between the two wavelengths are less pronounced. Both wavelengths favor dissociation pathways that predominantly yield ground-state iodine $I\left(\,^2P_{3/2}\right)$, with minimal formation of excited-state iodine $I^*\left(\,^2P_{1/2}\right)$. The lack of excited-state iodine suggests that these molecules favor non-adiabatic pathways that bypass the $^3Q_0$ state once the conical intersection or avoided crossing is reached, instead dissociating through the $^1Q_1$and $^3Q_1$ states.

THE JOURNAL OF PHYSICAL CHEMISTRY A
A JOURNAL OF THE AMERICAN CHEMICAL SOCIETY

pubs.acs.org/JPCA Article

Structural Effects on the Energy Disposal and Atomic Photofragment Alignment for the Photodissociation of Alkyl Iodides at Excitation Wavelengths of 254 and 268 nm

Published as part of The Journal of Physical Chemistry A special issue "Xueming Yang Festschrift".

Javier Cachón, Pedro Recio, David Sorribes, Sonia Marggi Poullain, Luis Rubio-Lago,* and Luis Bañares*

Cite This: J. Phys. Chem. A 2024, 128, 8312−8321 Read Online

ACCESS | Metrics & More | Article Recommendations

ABSTRACT: This work represents a step forward in the understanding of the widely studied photodynamics of alkyl iodides in the first absorption band. Ultraviolet (UV) photodissociation of several alkyl iodides (RI), specifically, a series of linear and ramified molecules with R = C_nH_{2n+1}, n = 1−4, at excitation wavelengths of 254 and 268 nm, which correspond to the maximum of the first absorption A-band, has been studied by combining resonance-enhanced multiphoton ionization (REMPI) detection of atomic photofragments I($^2P_{3/2}$) and I*($^2P_{1/2}$) and of pulsed slice imaging. Detailed examination of the total translational energy distributions of both atomic photofragments has been combined with stereodynamical information on the process obtained from the anisotropy β and alignment $a_0^2(\|)$ and Re$[a_1^2(\|, \perp)]$ parameters to provide a description of the role played by the molecular structure of alkyl iodides in adiabatic and, especially, in nonadiabatic photodissociation dynamics through conical intersections or avoided crossings. The present results suggest that the linear structures couple more efficiently with the pure C−I reaction coordinate, whereas for the branched structures, the coupling with additional vibrational (bending) modes gains importance, showing the dissociation process a multidimensional character. In addition, a large degree of cofragment rotational alignment has been found for the small linear CH_3I and C_2H_5I and, unexpectedly, for the branched t-C_4H_9I (C_{3v} symmetry), whereas the rest of the alkyl iodides show low alignment parameters.

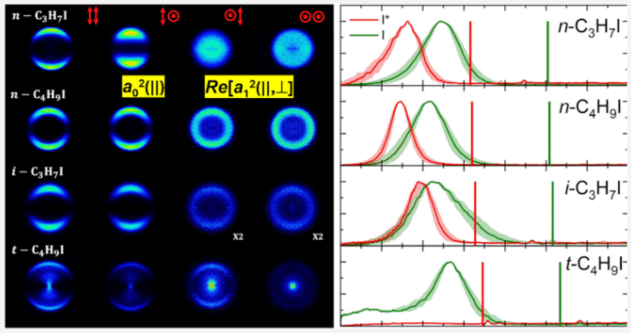

INTRODUCTION

Alkyl iodides have been considered over the years as model systems for photodissociation dynamics in UV.[1−10] This family of molecules shows a first absorption band in the wavelength range of 220−320 nm with a maximum at 260 nm,[11] which is termed the A-band. According to Mulliken,[1,2] this A-band is assigned to a $n \rightarrow \sigma^*$ transition from the I atom lone-pair orbital to an orbital centered on C−I of σ^* antibonding character. The presence of the heavy I atom in the molecule implies strong spin−orbit (SO) coupling.[12] There are three spin−orbit states that can be accessed by dipole-allowed transitions from the electronic ground state in C_{3v} symmetry. In the notation proposed by Mulliken,[1] there are two states, $^3Q_1$ and $^1Q_1$, which are accessible through perpendicular transitions, and one state, $^3Q_0$, which can be accessed by a parallel transition.[13] Interestingly, the $^3Q_0$ state correlates with the R + I*($^2P_{1/2}$) fragments in an adiabatic way, while the former states correlate with R + I($^2P_{3/2}$) fragments also adiabatically. In addition, there exists nonadiabatic coupling between the $^3Q_0$ and $^1Q_1$ states, which provides an additional means to produce I($^2P_{3/2}$) products nonadiabatically.[4] At the center of the absorption band, the parallel transition to the $^3Q_0$ state dominates the absorption spectrum;[14] at higher and lower wavelengths, respective perpendicular transitions to the $^3Q_1$ and $^1Q_1$ states gain importance.

The proposed picture is strictly valid for symmetric-top alkyl iodides (C_{3v} symmetry), such as CH_3I or t-C_4H_9I. For molecules of lower symmetry, as for instance i-C_3H_7I, the $^3Q_1$ and $^1Q_1$ states are split into two states of A' and A'' symmetries, and the $^3Q_0$ state changes symmetry to A'. This

Received: April 4, 2024
Revised: September 4, 2024
Accepted: September 5, 2024
Published: September 19, 2024

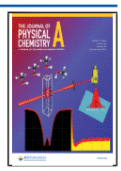

https://doi.org/10.1021/acs.jpca.4c02217
J. Phys. Chem. A 2024, 128, 8312−8321

way, the $^3Q_0$ state changes to the $3A'$ state in C_s symmetry, while the $^1Q_1$ and $^3Q_1$ states split into $2A''$ and $4A'$ states, and $1A''$ and $2A'$ states, respectively. The correlation diagrams for alkyl iodides with C_{3v} and C_s symmetries[15] are shown in Figure 1. In the case of C_s symmetry, the conical intersection that

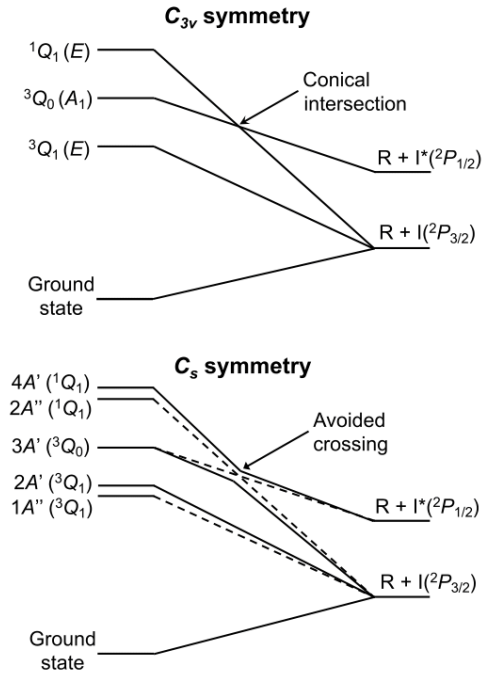

Figure 1. Diagrams showing the correlation of Mulliken's $^3Q_1$, $^3Q_0$, and $^1Q_1$ states of alkyl iodides along the reaction (C−I bond) coordinate for symmetries (top) C_{3v} and (bottom) C_s.[15]

appears for C_{3v} symmetry is replaced by an avoided crossing between the $4A'$ and $3A'$ states. The former correlates adiabatically with the R + I*($^2P_{1/2}$) fragments, while the latter is adiabatically correlated with the R + I($^2P_{3/2}$) fragments. Importantly, nonadiabatic passage through this curve crossing retains a significant role in the photodissociation dynamics. Despite the symmetry loss, neither the calculated absorption spectra for the RI, nor the calculated ab initio potential energy curves show a significant dependence of the carbon-chain structure[16,17] and thus, in all of the literature on the topic, the electronic states corresponding to the C_{3v} symmetry, i.e., $^3Q_0$, $^3Q_1$, and $^1Q_1$, are used for convenience independently of the alkyl iodide under consideration.

In this work, the photodissociation of several saturated linear (CH_3I, C_2H_5I, n-C_3H_7I, and n-C_4H_9I) and branched (i-C_3H_7I and t-C_4H_9I) alkyl iodides have been excited and dissociated at 254 and 268 nm close to the maximum of the first absorption A-band. The I*($^2P_{1/2}$) and I($^2P_{3/2}$) photoproducts are detected using the slice imaging technique in combination with (2 + 1) resonance-enhanced multiphoton ionization (REMPI) detection. The recorded iodine-atom images at different polarization directions of pump and probe lasers, and specifically the angular and translational energy distributions, are analyzed to provide information about the energy disposal into different degrees of freedom of the products as well as the dissociation atomic photofragment anisotropy. In the following sections, we will show how a direct comparison between sets of data taken at the two close excitation wavelengths challenges the traditional interpretation of the dissociation dynamics accepted for these molecular systems.

The maximum of the first A absorption band for different alkyl iodides found in the literature is as follows: CH_3I at 258 nm,[18] C_2H_5I at 258 nm,[19] n-C_3H_7I at 256 nm,[11] n-C_4H_9I at 257 nm,[20] i-C_3H_7I at 260 nm,[11] and t-C_4H_9I at 268 nm.[21] We have chosen the excitation wavelength 268 nm to compare the present results with those obtained from femtosecond time-resolved experiments by Corrales et al.[17] and 254 nm to compare with femtosecond time-resolved experiments by Warne et al.[22] and Downes-Ward et al.[23] In particular, Warne et al.[22] used time-resolved UV-pump (269 and 255 nm) and UV-probe (395 nm) multiphoton ionization photoelectron spectroscopy to study the photodissociation of CH_3I close to the maximum of the A-band. They observed different reaction times associated with distinct dynamical structures at the two wavelengths studied. These surprising results were assigned to an unexpected contribution of the dynamics of the $^1Q_1$ state at 255 nm, reflecting a more complex dissociation path occurring on the $^1Q_1$ potential surface. Later, Downes-Ward et al.[23] confirmed the same results at 254 nm by time-resolved measurements using an extreme ultraviolet probe in photoelectron spectroscopy experiments.

The paper is structured as follows. The experimental apparatus and a description of the analytical tools employed to extract the stereodynamical information are summarized in the Experimental Section. The results are presented and discussed in the corresponding sections.

EXPERIMENTAL SECTION

The main specifications of the experimental apparatus and method have been widely described elsewhere.[24,25] Here, only a brief description of the setup and experimental conditions will be given. All of the molecules used in this work have been obtained from Sigma-Aldrich with purities of 99%, except for t-C_4H_9I that was 95% pure. A molecular beam is created by expanding the vapor pressure of the studied molecule at room temperature using a pulse nozzle valve (General Valve Series 9, 0.5 mm orifice) with He (1 bar). The pulse gas traverses a 0.5 mm diameter skimmer (Beam Dynamics, Standard Model 2) and the resulting molecular beam enters into the ionization chamber, where it interacts with the photolysis and detection lasers. The two lasers are counter-propagated and focused with 25 cm focal lenses into a time-of-flight mass spectrometer (TOFMS). The pulse valve and lasers run with a repetition rate of 10 Hz.

To generate the photolysis laser radiation at the wavelengths used in this work, λ = 254 and 268 nm (located in the vicinity of the A-band maximum of the RI), a Nd:YAG (Quanta Ray Pro 230) pumped dye (Sirah Cobra-Stretch) laser is used, producing 2.2 mJ/pulse. With a delay time of 10 ns with respect of the photolysis pulse, the detection laser pulse (1.7 mJ/pulse, Nd:YAG (Quanta Ray Pro 190) pumped, frequency-doubled dye (Sirah Cobra-Stretch)) arrives at the interaction region. The two iodine atoms, I($^2P_{3/2}$) and I*($^2P_{1/2}$), are resonantly ionized through (2 + 1) REMPI schemes at 304.63 and 305.56 nm, respectively, which correspond to ($^3P_2$)-$6p[3]_{5/2} \leftarrow 5p(^2P_{3/2})$ and $(^3P_1)6p[1]_{3/2} \leftarrow 5p(^2P_{3/2})$ transitions.

Slice images were acquired with a delayed-pulse extraction slicing setup using a single-field configuration.[24,26,27] The delayed-pulse extraction permits the velocity spreading of the ion cloud in such a way that the arrival time of the cloud at the

https://doi.org/10.1021/acs.jpca.4c02217
J. Phys. Chem. A 2024, 128, 8312−8321

detector extends for hundreds of nanoseconds. Then, a narrow time gate is used in the detector, and thus, only the central slice of the expanded ion cloud was selected. The temporal width set for the gate must be as short as possible and in any case in the order of a few tens of nanoseconds, to ensure that the slice width corresponds only to the central portion of the sphere and any signal outside this central portion has been excluded. In the present case, the same temporal width was selected for all of the measurements. A 400 ns delay was applied on the repeller plate to measure $I(^2P_{3/2})$ and $I^*(^2P_{1/2})$ images. The fragment ions were then accelerated to the detector by using a constant electric potential of 3.0 kV to the repeller plate.[24,27] The ions then fly through a field-free time-of-flight region of 45 cm length before impacting impedance-matched microchannel plates (MCPs, Chevron configuration, 40 mm diameter). The resulting avalanche of electrons arrives at a phosphor screen (P47), generating a slice ion image. The image is acquired by a CCD camera (SONY 1024 × 768 pixels) driven by National Instrument (NI) LabView 7.1 and IMAQ VISION software. All raw slice images were symmetrized before extracting the kinetic energy and angular distributions from them. The resolution in velocity achieved was of about 1%.[26,27]

In order to study the stereodynamics of the photodissociation of different alkyl iodides studied, and due to the use of the slicing technique, the images for $I(^2P_{3/2})$, where atomic alignment effects are expected, have been recorded employing four linear pump−probe laser polarization configurations: *XX*, *XZ*, *ZX*, and *ZZ*. Here, *X* indicates a direction perpendicular to the laser propagation axis (which is *Y*), and *Z* stands for a direction parallel to the molecular beam axis. However, since the $I^*(^2P_{1/2})$ fragment has total angular momentum $J = 1/2$ (and cannot show angular alignment), the corresponding $I^*(^2P_{1/2})$ fragment images were acquired only for the case of pump and probe lasers parallel to the detector (i.e., *XX*).

For the calibration of the spectrometer, independent measurements were carried out using a single laser pulse experiment in which CH_3I was excited, and $CH_3(\nu = 0)$ fragments were detected by REMPI (2 + 1) at a wavelength of 333.45 nm, considering the well-known energetics for the $CH_3 + I(^2P_{3/2})$ channel at this photolysis wavelength.

Atomic Alignment Analysis. The slice imaging or slicing technique provides a useful tool to study the angular momentum alignment of photodissociation products.[28] The slicing name refers to the possibility of detecting those photofragments localized in a narrow section—slice—of the photofragment 3D distribution. In particular, when the central slice is recorded, the consequent analysis does not require any mathematical transformation. The technique allows us to measure sliced images in different configurations of photolysis and detection laser polarization. The analysis of the photofragment polarization requires four pump−probe linear polarization configurations, namely, *XX*, *XZ*, *ZX*, and *ZZ*. Here, the *XYZ* axis system indicates the laboratory frame, with counter-propagating laser beams along the *Y*-axis. The molecular beam propagates along the *Z*-axis, which is the time-of-flight axis.

This way, the *XX* images contain the stereodynamic data: dissociation anisotropy and photoproduct alignment. In the case of *XZ* images, the polarization vector of the probe beam is perpendicular to the plane of the detector and the remaining β_2^{XZ} parameter is associated with both the dissociation anisotropy and the photofragment polarization. In a similar way, the *ZX* images do not contain information related to the dissociation anisotropy. Finally, the *ZZ* images do not contain any dynamical information and are used as a reference to avoid systematic errors.

In the following paragraphs, the equations employed to perform a concerted analysis of the four images to provide different polarization parameters are presented.

The angular distributions extracted from the images are usually written as linear combinations of Legendre polynomials. If linearly polarized pump and probe laser pulses are used, then the linear combination is made of only even-order polynomials, and the polynomial expansion is limited by the number of pump and probe photons involved. For a one-photon dissociation process using linearly polarized light and a (2 + 1) REMPI detection, as used in the present work, a maximum rank of 6 results in a complete expression for the angular intensity[15]

$$I(\theta)^{FG} = 1 + \beta_2^{FG} P_2(\cos\theta) + \beta_4^{FG} P_4(\cos\theta) + \beta_6^{FG} P_6(\cos\theta) \quad (1)$$

where θ is the angle describing the photofragment distribution within the image plane. Here, *F* and *G* indicate the directions of the photolysis and probe lasers, respectively, with respect to *XY* (the slicing plane, which is perpendicular to time-of-flight axis *Z*). $P_k(\cos\theta)$ is the *k*th Legendre polynomial and β_k^{FG} are the *k*th anisotropy parameters in the laboratory frame.

Equation 1 provides a convenient and directly measured set of β_k^{FG} coefficients where all vector correlations are expressed in a standard way. Rakitzis and Zare[29,30] proposed an ensemble of parameters, the $a_q^k(p)$ molecular frame polarization parameters, and established general relationships with the laboratory frame anisotropy parameters, β_k^{FG}. For the particular case of pure perpendicular transitions, specific equations connecting β_k^{FG} and $a_q^k(\perp)$ were developed. A similar set of equations for parallel transitions have been developed recently by Recio et al.,[31] involving the matching $a_q^k(\parallel)$ parameters as well as the $\mathrm{Re}[a_q^k(\parallel, \perp)]$ parameter, which accounts for the interference between parallel and perpendicular transitions. We will have $q = 0$ for a one-photon parallel transition ($\beta = 2$) and thus only $a_0^k(\parallel)$ parameters. For angular distributions fitted to eq 1 with $\beta_6 = 0$, $k = 2$, which results in the following expressions:

$$\beta_2^{XX} = \frac{\beta + \frac{s_2}{7}\left\{11a_0^2(\parallel) + \sqrt{\frac{8}{3}}\mathrm{Re}[a_1^2(\parallel, \perp)]\right\}}{1 + \frac{s_2}{5}\left\{2a_0^2(\parallel) + \sqrt{\frac{8}{3}}\mathrm{Re}[a_1^2(\parallel, \perp)]\right\}} \quad (2a)$$

$$\beta_4^{XX} = \frac{12s_2\left\{\frac{3}{35}a_0^2(\parallel) + \sqrt{\frac{8}{3}}\mathrm{Re}[a_1^2(\parallel, \perp)]\right\}}{1 + \frac{s_2}{5}\left\{2a_0^2(\parallel) + \sqrt{\frac{8}{3}}\mathrm{Re}[a_1^2(\parallel, \perp)]\right\}} \quad (2b)$$

$$\beta_2^{XZ} = \frac{\beta + s_2 a_0^2(\parallel)}{1 + \frac{1}{2}s_2 a_0^2(\parallel)} \quad (2c)$$

$$\beta_2^{ZX} = s_2 a_0^2(\parallel) \quad (2d)$$

It should be noted that for $k = 2$, the β_4^{ZX} and β_4^{XZ} parameters are identically zero. The s_2 coefficient is a sensitivity factor, which can be obtained from Table 1 of ref 30. According to ref 32, the s_2 coefficient shows a value of 80/333 for the $I(^2P_{3/2})$

https://doi.org/10.1021/acs.jpca.4c02217
J. Phys. Chem. A 2024, 128, 8312−8321

photofragment when using a hyperfine depolarization coefficient of 10/37.

Limit values for the $a_0^2(\|)$ parameter of the $I(^2P_{3/2})$ photofragment are in the range $(-0.8, +0.8)$.[33] Here, the higher values, positive and negative, correspond to the population in $m_J = \pm 1/2$ and $m_J = \pm 3/2$ states, with respect to the quantization of the I atom recoil direction.

In the case of a parallel transition, no net change in the projection of the total angular momentum on the bond axis is expected. For a diatomic molecule, the determination of the $a_0^2(\|)$ parameter for one of the fragments provides similarly indirect information about the other, due to preservation of the angular momentum. However, if the coproduct of the atom is a polyatomic fragment, then the angular momenta of both photoproducts are conditioned by the rotation of the latter and no preferential population is expected for the atomic species. Any divergence from such an expectation would imply significant dynamical information.

RESULTS AND DISCUSSION

Figures 2 and 3 show a series of slice images recorded for the $I(^2P_{3/2})$ and $I^*(^2P_{1/2})$ fragments, respectively, after dissociation

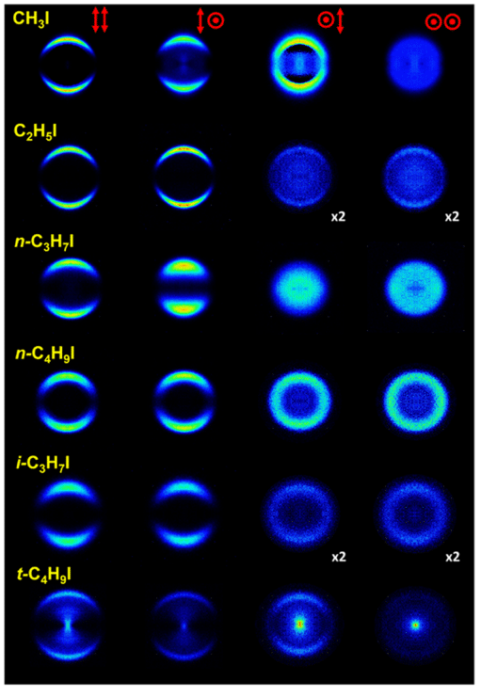

Figure 2. $I(^2P_{3/2})$ symmetrized slice images for the pump−probe polarizations *XX*, *XZ*, *ZX*, and *ZZ* (represented by vertical double arrows (*X* polarization) and circles (*Z* polarization)), measured at an excitation wavelength of 254 nm, and (2 + 1) REMPI probe wavelength 304.63 nm, for the six species studied in this work. The contrast in those figures marked with x2 has been enhanced by a factor of 2.

of the corresponding alkyl iodides at the excitation wavelength of 254 nm, precisely at roughly the maximum of the A-band absorption spectra of the RI with the exception of branched *i*-C_3H_7I and *t*-C_4H_9I, for which the maximum is broader and shifted toward longer wavelengths, i.e., 260 and 268 nm, respectively.

Images of the $I(^2P_{3/2})$ fragment at the four polarization configurations were recorded for each species, CH_3I, C_2H_5I, *n*-C_3H_7I, *n*-C_4H_9I, *i*-C_3H_7I, and *t*-C_4H_9I. The polarization configurations are indicated by red arrows (*X* polarization) and circles (*Z* polarization) at the top of Figure 2. The *XX* images, which gather the information on the dissociation event and all possible polarization effects, show (with the exception of *t*-C_4H_9I) a single feature, i.e., a highly anisotropic ring that can be ascribed to the formation of I fragments by absorption through a parallel transition and further R−I bond excision in a highly repulsive potential energy surface.[17] The width of the ring increases as the carbon chain gains complexity, with the exception, once more, of *t*-C_4H_9I, which surprisingly shows a substantially narrower ring than its linear equivalent (*n*-C_4H_9I). The $I(^2P_{3/2})$ image arising from photodissociation of *t*-C_4H_9I shows, additionally, a feature at lower recoil energies (inside the ring), which can be associated with multiphoton ionization and subsequent dissociation.[17]

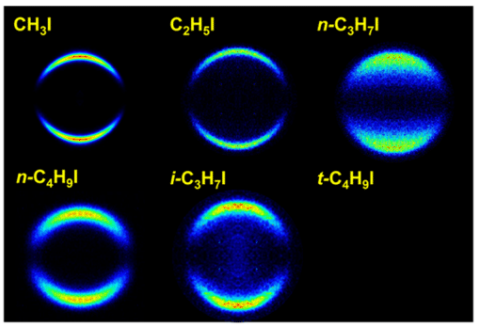

Figure 3. $I^*(^2P_{1/2})$ symmetrized slice images (only for *XX* polarization configuration) measured at an excitation wavelength of 254 nm and (2 + 1) REMPI probe wavelength 305.56 nm, for five of the six species studied in this work. The *t*-C_4H_9I image is not shown since no signal was observed.

Comparison between the images taken at the four polarizations would shed some light on the $I(^2P_{3/2})$ photofragment alignment. Differences between the *XX*, *XZ*, and *ZX* images are attributable to photofragment polarization effects. In particular, similar intensity distributions of *XX* and *XZ* images might suggest that the stereodynamics is governed by the dissociation process and that the polarization effects, if present, would contribute mildly. Such could be the case for C_2H_5I, *n*-C_4H_9I, *i*-C_3H_7I, and *t*-C_4H_9I species. The CH_3I and *n*-C_3H_7I species show, however, large variations in the intensity distributions of the *XX*, *XZ*, and *ZX* images, which suggests a significant photofragment alignment for those molecules.

Since no alignment can be observed for the $I^*(^2P_{1/2})$ fragment, Figure 3 shows only *XX* images for each molecule. In this case, all of the recorded images can be described by a single feature, a highly anisotropic ring corresponding to a parallel transition, that has been assigned to prompt dissociation in a highly repulsive surface.[17] Clearly, the width of the ring depends strongly on the structure of the molecule, although in general terms it can be linked to the number of carbon atoms in the chain and the complexity of the species. No signal attributed to the $I^*(^2P_{1/2})$ fragment was detected in the photodissociation of *t*-C_4H_9I.

Total Translational Energy Distributions. Angular integration of *XX* images shown in Figures 2 and 3 for both fragments $I(^2P_{3/2})$ and $I^*(^2P_{1/2})$ renders the total translational energy distributions (TEDs) shown in Figure 4. The reference (vertical line) represents the total available energy for the dissociation products after C−I bond cleavage for each channel

https://doi.org/10.1021/acs.jpca.4c02217
J. Phys. Chem. A 2024, 128, 8312−8321

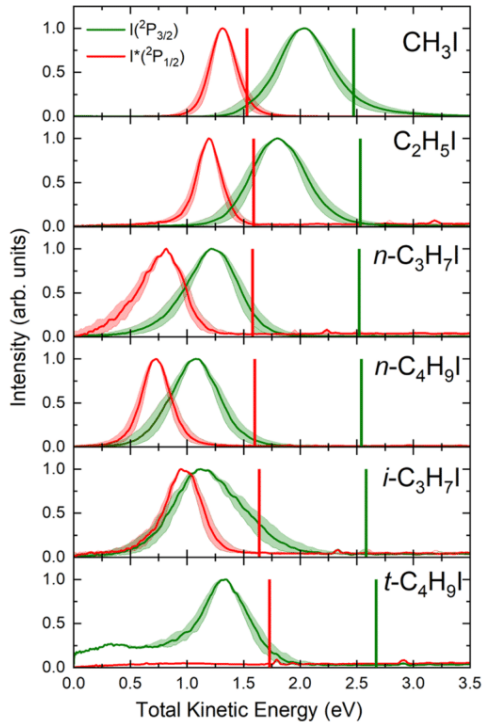

Figure 4. Comparison between $I(^2P_{3/2})$ (green) and $I^*(^2P_{1/2})$ (red) total translational energy distributions (TEDs) after the photodissociation of different alkyl iodides at an excitation wavelength of 254 nm. The vertical green and red lines indicate the maximum total energy available for both dissociation channels yielding $I(^2P_{3/2})$ and $I^*(^2P_{1/2})$ in correlation with *R*, respectively. The shadowed areas indicate the energy profile of the slice of the sphere measured.

for different alkyl iodides RI, which has been calculated as follows

$$E_{av} = \frac{m_R}{m_{RI}}[h\nu - D_0 - E_{SO} + E_{int}] \quad (3)$$

where m_R and m_{RI} are the masses of the R cofragment and the parent molecule RI, respectively, $h\nu$ represents the photon energy, i.e., the excitation energy transferred to the molecule, E_{SO} corresponds to the $I(^2P)$ spin−orbit splitting (i.e., 0 and 0.943 eV for $I(^2P_{3/2})$ and $I^*(^2P_{1/2})$, respectively), and E_{int} is the internal energy of the RI, to be considered negligible in a supersonic expansion. The term D_0 denotes the C−I bond dissociation energy for each RI. The D_0 values have been reported in the literature and are collected in Table 1. With the exception of *t*-C_4H_9I, the distributions display a simple Gaussian-like shape, suggesting a single dissociation mechanism in every case. The $I^*(^2P_{1/2})$ distribution is absent in the panel corresponding to *t*-C_4H_9I photodissociation, and the $I(^2P_{3/2})$ distribution shows, in addition, a broad feature at low total translational energies, corresponding to the above-mentioned MPI process.[17]

A striking feature in Figure 4 is the shift of the distributions toward lower-energy values as the linear carbon chain increases in size, while the opposite trend is observed for the branched species, *i*-C_3H_7I and *t*-C_4H_9I. The displacement of the distribution from the available energy vertical mark (taking the peak of the distribution as a reference) is associated with the amount of available energy transferred to internal degrees of freedom (rotation and vibration) of R cofragments. A peak of the distribution that is close to the maximum available energy indicates a photodissociation where most of the energy available for the C−I bond cleavage is transformed into fragment kinetic energy. In contrast, a distribution shifted downward from the available energy reference indicates that a certain amount of the available energy has been transferred to rotational and vibrational (internal) energy of the cofragments, E'_{int}. The described energy distribution can be quantified by the fraction of the available energy that appears as cofragment internal energy, f_{int}, which can be obtained as

$$f_{int} = \frac{E_{peak} - E_{av}}{E_{av}} = \frac{E'_{int}}{E_{av}} \quad (4)$$

The f_{int} values determined from the TEDs for different RIs are collected in Table 1 along with the areas of the Gaussian-like curves describing the total TEDs. The area of the TEDs correlates straightforwardly with the internal energy of the R cofragment if, in addition, its molecular structure is considered. As the number of carbon atoms in the R chain increases or if the structure changes from linear to branched, the number of vibrational degrees of freedom (normal modes) with a variety of frequencies increases as well. Larger areas would indicate R radicals of increasing complexity, recoiling with higher rotational and/or vibrational excitation in an increasing number of vibrational normal modes. On the other hand, lower areas would indicate R radicals with a simpler structure, with fewer vibrational degrees of freedom, and which barely rotate or vibrate when recoiling. Intramolecular vibrational

Table 1. Experimental Dissociation Energy (D_0) Taken from Refs 34 and 37 (in eV), Fraction of the Available Energy That Appears as R Cofragment Internal Energy (f_{int}), and Area Under the Curve of the Total Translational Energy Distributions (TEDs) (in Arbitrary Units) for Both Photodissociation Channels Yielding $I(^2P_{3/2})$ and $I^*(^2P_{1/2})$ at Excitation Wavelengths of 254 and 268 nm for the Alkyl Iodides Studied in This Work[a]

		$I^*(^2P_{1/2})$				$I(^2P_{3/2})$			
		254 nm		268 nm		254 nm		268 nm	
	D_0	f_{int}	area	f_{int}	area	f_{int}	area	f_{int}	area
CH_3I	2.41[34]	0.13	0.29	0.08	0.24	0.17	0.59	0.03	0.45
C_2H_5I	2.35[36]	0.25	0.28	0.19	0.47	0.29	0.59	0.30	0.80
n-C_3H_7I	2.36[37]	0.48	0.47	0.37	0.28	0.52	0.56	0.47	0.55
n-C_4H_9I	2.34[35]	0.54	0.32	0.54	0.32	0.58	0.52	0.58	0.52
i-C_3H_7I	2.30[37]	0.42	0.42	0.61	0.11	0.56	0.72	0.59	0.77
t-C_4H_9I	2.21[35]					0.43	0.41	0.46	0.43

[a]The experimental error is estimated to be about 15% for each parameter.

https://doi.org/10.1021/acs.jpca.4c02217
J. Phys. Chem. A 2024, 128, 8312−8321

energy redistribution (IVR) should have an increasing role as the number of vibrational normal modes increase in the R cofragment, especially in the nonadiabatic photodissociation dynamics mediated by the conical intersection (C_{3v} symmetry) or the avoided crossing (C_s symmetry).

The trends observed for the f_{int} values and the areas of the curves in the TEDs measured at 254 nm for both dissociation channels and for different linear and branched RI clearly indicate the distinct internal energy content of the R cofragment resulting from the photodissociation depending on the molecular structure and the effect of molecular complexity on the nonadiabatic dynamics characteristic of the photodissociation mechanism associated with alkyl iodides.

In particular, at 254 nm excitation energy and for the R + I($^2P_{3/2}$) channel, f_{int} values increase almost linearly for the linear RI, from zero for CH_3I up to 0.58 for n-C_4H_9I. Conversely, the areas of the TED curves slightly decrease along the series of linear RI. For the R + I*($^2P_{1/2}$) channel, f_{int} values increase also linearly for the linear RI, from zero for CH_3I up to 0.54 for n-C_4H_9I, and the areas of the TED curves barely increase or level off. The trend is quite different for the R + I($^2P_{3/2}$) channel of the branched RI (i-C_3H_7I and t-C_4H_9I), i.e., the f_{int} values decrease and the areas of the TEDs also decrease strongly.

The measurements described above were also carried out at an excitation wavelength of 268 nm, which is shifted to red with respect to the maximum of the A-band absorption spectra of the RI with the exception of t-C_4H_9I for which the maximum of the absorption band is precisely at 268 nm.[21]

The images recorded for the I($^2P_{3/2}$) fragment at the four polarization configurations for different RI studied upon excitation at 268 nm are shown in Figure 5, while the I*($^2P_{1/2}$) images are shown (only for the XX polarization configuration) in Figure 6. The corresponding total TEDs for both fragments are displayed in Figure 7. Taking into consideration that the two excitation wavelengths employed in this study are close to each other and to the absorption maximum of the A-band of different RI, similar images would be rather expected. Certainly, for both excitation wavelengths, an anisotropic ring, whose width and radius depend strongly on the molecular structure and photodissociation channel (adiabatic or nonadiabatic), constitutes the single feature of most of the slice images. The differences in the width and size of the rings can be clearly detected in the total TEDs of Figures 4 and 7. Interestingly, the most striking difference is found actually in the ring anisotropy. A simple visual inspection of Figures 2 and 5, on the one hand, and of Figures 3 and 6, on the other hand, indicates that the anisotropy of the I($^2P_{3/2}$) rings is lower at 268 nm than at 254 nm, while the opposite occurs for the I*($^2P_{1/2}$) fragment. Specific values of the dissociation anisotropy parameter will be presented and discussed in the next section.

At 268 nm, the f_{int} values shown in Table 1, reflecting the shift of the total TED maximum with respect to the available energy reference, increase for both dissociation channels (I*($^2P_{1/2}$) and I($^2P_{3/2}$)) when the complexity of the linear RI increases, in a similar fashion as at 254 nm. Therefore, for both 254 and 268 nm excitation wavelengths, the internal energy of the R cofragment increases as the chain increases in the series of linear RI. As commented on above, more energy is released as internal energy and less as translational energy of the fragments as the vibrational degrees of freedom and size of the linear R cofragment increase. Moreover, this effect is stronger

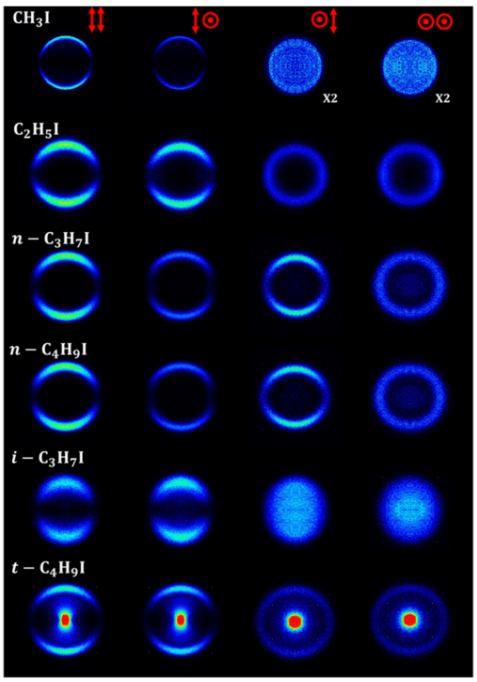

Figure 5. I($^2P_{3/2}$) symmetrized slice images for the pump−probe polarizations XX, XZ, ZX, and ZZ (represented by vertical double arrows (X polarization) and circles (Z polarization)) measured at an excitation wavelength of 268 nm and (2 + 1) REMPI probe wavelength of 304.63 nm, for the six species studied in this work. The contrast in those figures marked with x2 has been enhanced by a factor of 2.

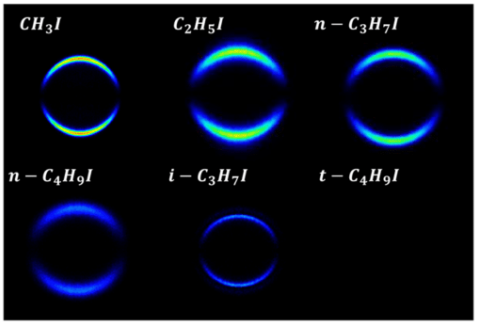

Figure 6. I*($^2P_{1/2}$) symmetrized slice images (only for XX polarization configuration) measured at an excitation wavelength of 268 nm and (2 + 1) REMPI probe wavelength of 305.56 nm for five of the six species studied in this work. The t-C_4H_9I image is not shown since no signal was observed.

for the nonadiabatic R + I($^2P_{3/2}$) channel, and this explains why for the largest linear molecule n-C_4H_9I, the two channels overlap for both 254 and 268 nm excitation wavelengths. This result also explains why the rings in the images become broader as the size and complexity of the R cofragment increase.

As in the case of a 254 nm excitation wavelength, the branched molecules show a different trend in comparison with the linear ones. Now, f_{int} values stabilize (i-C_3H_7I) or even decrease (t-C_4H_9I).[17] Thus, the amount of total energy released as fragment translational energy increases for the branched molecules, which may correspond to a less efficient energy flux into the internal degrees of freedom of the branched radicals. These results perfectly match those

https://doi.org/10.1021/acs.jpca.4c02217
J. Phys. Chem. A 2024, 128, 8312−8321

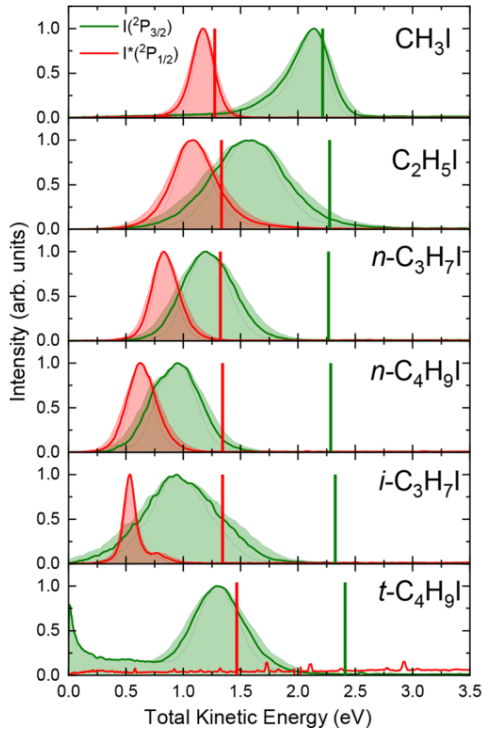

Figure 7. Comparison between the $I(^2P_{3/2})$ (green) and $I^*(^2P_{1/2})$ (red) total translational energy distributions (TEDs) after the photodissociation of different alkyl iodides at an excitation wavelength of 268 nm. The vertical green and red lines indicate the maximum total energy available for both dissociation channels yielding $I(^2P_{3/2})$ and $I^*(^2P_{1/2})$ in correlation with R, respectively. The shadowed areas indicate the energy profile of the slice of the sphere measured.

obtained previously in femtosecond time-resolved experiments at 268 nm.[17]

Similar trends for the areas of the curves in the TEDs are observed for both dissociation channels at 268 nm in comparison with the 254 nm excitation wavelength.

The alkyl iodides studied in this work might be vibrationally characterized by four main vibrational modes. The stretching mode of the C−I bond is primarily excited in the absorption step, leading to fast C−I dissociation. The transition to the $^3Q_0/3A'$ state implies, however, a geometrical change that would reflect in the bending C−I mode.[21] The internal energy accumulated in these two main vibrational modes is, in addition, partially transferred to the carbonated chain through intramolecular vibrational energy redistribution (IVR). The vibrational activity in the carbonated chain might be visualized in terms of two major modes (or group of modes), which we will call, for conciseness, the C−C stretching mode, responsible for the propagation of the vibrational excitation through the R moiety, and the C−C bending mode, which would include the C−H motion as well. The amount of internal energy transferred to the dissociation products will strongly depend on the interplay of the four vibrational modes, which, in turn, is plainly related to the length and structure of the molecule under scrutiny.

As the molecule gets heavier and branched, the amount of internal energy transferred from the stretching C−I to the bending C−I increases, a fact that surfaces as an increasing shift in the corresponding translational energy distributions. One intriguing aspect of the photodissociation dynamics is that the energy transferred from the C−I coordinate to the C−C stretching and bending modes is not just accumulated as vibrational activity of different internal modes, but it does contribute as well to the dissociation process, providing to the dissociation a multidimensional character.[21]

The observed trend for f_{int} and for the areas of the curves in the TEDs at both wavelengths informs us about the coupling between the C−I modes and the C−C and C−H internal modes. For the linear molecules, the increase of f_{int} along the series of linear molecules indicates an efficient transfer of energy along the C−C chain and the pertinent redistribution among the low-energy vibrational modes, which will result, as will be discussed later, in a progressive scrambling of the R-fragment along the recoil axis. Remarkably, there are no significant differences between the adiabatic and nonadiabatic channels, which indicates that the IVR takes place primarily prior to the adiabatic passing through the conical intersection. For the branched molecules, the f_{int} measured for i-C_3H_7I is similar to that of its linear counterpart and larger than that of t-C_4H_9I. These values suggest that the redistribution of the internal energy along the carbonated chain affects mostly the skeleton C−C bending modes (and probably, in the case of i-C_3H_7I, the lower-energy C−H vibrational modes), which are straightforwardly excited through the C−I stretching motion.

Dissociation Anisotropy and Alignment Parameters. The angular distributions of the $I(^2P_{3/2})/I^*(^2P_{1/2})$ photofragments obtained from the radial integration of the slice images depicted in Figures 2, 3, 5, and 6 have been fitted to eq 1, which is valid for a one-photon dissociation process and (2 + 1) REMPI photofragment detection.

The least-squares fit generates a set of anisotropy parameters (β_2, β_4, and β_6) for each image. In the case of the $I^*(^2P_{1/2})$ fragment, the total angular momentum is $J = 1/2$, and no alignment is present. Thus, only the XX images were acquired, which were consequently fitted using a single β_2 parameter in

Table 2. β_2 and β_4 Anisotropy Parameters Obtained from the Fits of the XX, XZ, and ZX Slice Images for $I(^2P_{3/2})$ Measured at Excitation Wavelengths of 254 and 268 nm for the Series of Alkyl Iodides Studied in This Work[a]

	254 nm				268 nm			
	β_2^{XX}	β_4^{XX}	β_2^{XZ}	β_2^{ZX}	β_2^{XX}	β_4^{XX}	β_2^{XZ}	β_2^{ZX}
CH_3I	2.34	0.41	1.93	0.56	1.75	−0.19	1.65	−0.05
C_2H_5I	1.89	−0.23	1.78	0.00	1.71	−0.17	1.57	−0.29
n-C_3H_7I	1.95	−0.13	2.31	0.21	1.82	−0.07	1.57	0.75
n-C_4H_9I	1.83	−0.01	1.85	0.17	1.79	−0.08	1.82	0.08
i-C_3H_7I	2.04	0.09	2.03	0.06	1.76	−0.04	1.78	0.58
t-C_4H_9I	2.00	0.10	1.86	0.44	2.05	0.40	2.00	0.50

[a]The uncertainties for the βi parameters are estimated to be within ±0.2 for CH_3I and ±0.05 for all of the other species.

https://doi.org/10.1021/acs.jpca.4c02217
J. Phys. Chem. A 2024, 128, 8312−8321

The Journal of Physical Chemistry A pubs.acs.org/JPCA Article

Table 3. Anisotropy Parameter (β) for Both Iodine Fragments, I*($^2P_{1/2}$) and I($^2P_{3/2}$), and Alignment Parameters ($a_0^2(\|)$, Re[$a_1^2(\|, \perp)$]) Derived from the I($^2P_{3/2}$) Images for Each of the Studied Alkyl Iodides Measured at Excitation Wavelengths of 254 and 268 nm[a]

	I*($^2P_{1/2}$)		I($^2P_{3/2}$)					
	254 nm	268 nm	254 nm			268 nm		
	β	β	β	$a_0^2(\|)$	Re[$a_1^2(\|, \perp)$]	β	$a_0^2(\|)$	Re[$a_1^2(\|, \perp)$]
CH_3I	2.38	1.97	2.17	1.07	−0.04	1.56	0.45	0.08
C_2H_5I	1.64	2.18	1.79	0.53	0.08	1.60	0.15	0.02
n-C_3H_7I	1.87	2.00	1.90	0.05	−0.01	1.64	0.27	0.02
n-C_4H_9I	1.68	1.75	1.85	−0.09	0.00	1.80	−0.04	0.00
i-C_3H_7I	2.12	1.90	2.03	0.05	−0.02	1.71	0.13	0.02
t-C_4H_9I			1.87	0.70	0.01	2.00	0.53	−0.06

[a]The uncertainties for the β and $a_0^2(\|)$ and Re[$a_1^2(\|, \perp)$] parameters are estimated to be within ±0.2 for CH_3I and ±0.05 for all other species.

eq 1 (i.e., the sum is truncated to the second term). However, for total angular momentum $J = 3/2$, as for the I($^2P_{3/2}$) fragment, J can be produced preferentially in the $m_J = \pm 1/2$ and $\pm 3/2$ states. Accordingly, the angular distributions extracted from the XX images were fitted to the β_i terms of eq 1. Only one β_2 parameter was needed for the XZ and ZX images, whereas the β_6 parameter was found to be close to zero in all cases. The β_2 and β_4 anisotropy parameters obtained from the fits of the XX, XZ, and ZX slice images for the I($^2P_{3/2}$) fragment at the two excitation wavelengths and for the series of alkyl iodides studied are listed in Table 2.

Table 3 shows the dissociation anisotropy parameter β for the I*($^2P_{1/2}$) fragment, and β and the polarization parameters $a_0^2(\|)$ and Re[$a_1^2(\|, \perp)$], extracted from the phenomenological β_i parameters of Table 2 using eq 2, for the I($^2P_{3/2}$) fragment. At first glance, the values obtained for β agree, in all cases, with a fast prompt photodissociation mechanism occurring from the $^3Q_0$ or $3A'$ states for C_{3v} or C_s symmetries, respectively, for both R + I($^2P_{3/2}$) and R + I*($^2P_{1/2}$) channels.[16,34] The large positive values, close to the maximum $\beta = 2$ corresponding to a pure parallel transition, prove that at the two excitation wavelengths employed in this work and for all of the alkyl iodides studied, the absorption step is produced almost exclusively to the $^3Q_0/3A'$ state.

It must be noticed, however, that the anisotropy parameter associated with iodine images measured from CH_3I photodissociation is over the limiting value for a parallel transition. The iodine images that correspond to the photodissociation of CH_3I at 254 nm excitation wavelength, shown in Figures 2 and 3, are affected by an unavoidable nonnegligible space charge. This space charge effect has been considered in the data analysis, but, in any case, it entails an overestimation of the anisotropy parameters for a parallel transition.

The differences between the various RIs have been traditionally attributed to the length and structure of the radical R moiety. In the present case, general trends are observed for the β parameter as a function of the linear and branched RI molecules irrespective of the excitation wavelength. In particular, a shallow decrease of β from the limiting value of +2 toward values between +1.5 and +1.8—reflecting the interplay of the conical intersection (or avoided crossing) that connects the $^3Q_0$-like state with the R + I($^2P_{3/2}$) channel—occurs as the length of the carbon chain for the linear RI increases, irrespective of the dissociation channel and excitation wavelength. Interestingly, for the branched RI, the β values tend to increase (with respect to their linear counterpart), reaching values close to or equal to the limiting value of +2.

The $a_0^2(\|)$ alignment parameters for the I($^2P_{3/2}$) photofragment shown in Table 3 vary from +0.56, close to the limiting value of +0.8, for CH_3I, down to around zero for the longer linear RI, n-C_3H_7I and n-C_4H_9I, at the excitation wavelength of 254 nm. At 268 nm, $a_0^2(\|)$ also decreases for the same sequence of linear RIs. Interestingly, the $a_0^2(\|)$ values for the branched i-C_3H_7I are comparable to those of its linear counterpart n-C_3H_7I. For the branched t-C_4H_9I, the $a_0^2(\|)$ value at 254 nm is close to the limit (+0.7), and it is significantly large (+0.53) at 268 nm. At both excitation wavelengths, the large $a_0^2(\|)$ values, which are in the same trend as for CH_3I, would indicate that a high alignment is recovered when there is a higher symmetry in the molecule (C_{3v} vs C_s) irrespective of the length and structure of the R radical.

A reduction of $a_0^2(\|)$ with respect to asymptotic values (±0.8) in a polyatomic system would imply an increase of the population of internal (vibrational) states in the photodissociation process by an increase of IVR of the available energy. The increase of IVR would entail a quality loss of the C−I bond as a quantization axis. In other words, low $a_0^2(\|)$ values would correspond to scrambling of the R moiety along the recoil direction.

As seen in Table 3, the $a_0^2(\|)$ parameter decreases along the series of linear RI molecules. For CH_3I and C_2H_5I, the $a_0^2(\|)$ parameter takes large positive values at both excitation wavelengths, indicating a preference for the $m_J = \pm 3/2$ states of the I($^2P_{3/2}$) fragment. Taking into account the limiting values of ±0.8 for this parameter, the $a_0^2(\|)$ obtained for CH_3I and C_2H_5I imply a high degree of alignment in the corresponding coproducts in each case. Such a result turns out to be exceptional if we consider the polyatomic nature of both CH_3 and C_2H_5 fragments. The alignment of the I($^2P_{3/2}$) atom implies that the projection of the CH_3 and C_2H_5 rotational angular momentum is greatly constrained along the recoil direction. This constraint implies that those fragments do not isotropically mix, and the rotational angular momentum shows instead a narrow distribution of rotational states, which are aligned along the recoil direction. As the linear chain increases, the alignment decreases and it is totally lost for n-C_4H_9I at both excitation wavelengths. The dependence of $a_0^2(\|)$ with the length of the carbonated chain is in excellent agreement with the values measured for f_{int} discussed in the preceding section and suggests that the C−I

https://doi.org/10.1021/acs.jpca.4c02217
J. Phys. Chem. A 2024, 128, 8312−8321

coordinate is mainly coupled with the normal skeleton C−C vibrational modes.

Strikingly, a large $a_0^2(\|)$ value is obtained for t-C_4H_9I at both excitation wavelengths, which indicates a large degree of alignment along the recoil direction. With similar f_{int} values than its linear counterpart, the presence of an extra methyl moiety in the central carbon atom of the t-C_4H_9 fragment prevents efficient excitation of C−C bending modes and, therefore, the vibrational excitation initially located in the C−I bond is transferred toward the C−H modes with little deformation of the chain.

The $\mathrm{Re}[a_1^2(\|, \perp)]$ parameter has been measured as well and the corresponding values are gathered in Table 3. In all cases, the $\mathrm{Re}[a_1^2(\|, \perp)]$ values are close to zero, although those numbers might not reflect necessarily valuable information. The $\mathrm{Re}[a_1^2(\|, \perp)]$ parameter provides information about coherent contributions from the interference between parallel and perpendicular transitions. Such interference might indeed exist and be present in the molecules studied in this work yet not show up at the studied excitation wavelengths. As reported by Rakitzis et al.,[38] while a_0^k is practically independent of the excitation wavelength, the $\mathrm{Re}[a_1^2(\|, \perp)]$ interference parameter displays an oscillatory behavior with the excitation wavelength. Without more data at different excitation wavelengths to validate the present results, we cannot extract any valid conclusion from the $\mathrm{Re}[a_1^2(\|, \perp)]$ values shown in Table 3.

■ CONCLUSIONS

The photodissociation of linear and branched alkyl iodides in the A-band has been studied by slice imaging and resonance-enhanced multiphoton ionization of the iodine fragments at the two excitation wavelengths of 254 and 268 nm in the vicinity of the maximum of the absorption band. The results presented in this work highlight the effect of the carbonated chain (R) length and structure on the photofragment energy distribution and anisotropy. It has been shown how the vibrational modes of the carbon chain distribute efficiently the energy deposited in the C−I bond after absorption of the excitation photon by the molecules. For the linear species, the increase of the fraction of the available energy that is transferred to internal degrees of freedom of the molecule, f_{int}, increases along the series, while the R cofragment rotational alignment, represented by the $a_0^2(\|)$ parameter, decreases accordingly. Remarkably, the smaller CH_3I and C_2H_5I species show a large degree of cofragment rotational alignment along the recoil direction. This alignment is lost for the longer molecules as the content of the fragment's internal energy increases. The f_{int} values for the branched species, on the other hand, show a mild decrease with the size of the molecule and a certain stabilization with respect to their linear counterparts, indicating that the energy redistribution is not favored when the C−I stretch mode is normal to the carbon chain. In this sense, the case of t-C_4H_9I at 254 nm is particularly interesting, showing the largest alignment of the ensemble.

■ AUTHOR INFORMATION

Corresponding Authors

Luis Rubio-Lago − *Departamento de Química Física, Facultad de Ciencias Químicas, Universidad Complutense de Madrid, 28040 Madrid, Spain*; Email: luis.rubio@ucm.es

Luis Bañares − *Departamento de Química Física, Facultad de Ciencias Químicas, Universidad Complutense de Madrid, 28040 Madrid, Spain; Instituto Madrileño de Estudios Avanzados en Nanociencia (IMDEA Nanoscience), 28049 Madrid, Spain*; orcid.org/0000-0002-0777-2375; Email: lbanares@ucm.es

Authors

Javier Cachón − *Departamento de Química Física, Facultad de Ciencias Químicas, Universidad Complutense de Madrid, 28040 Madrid, Spain*

Pedro Recio − *Departamento de Química Física, Facultad de Ciencias Químicas, Universidad Complutense de Madrid, 28040 Madrid, Spain*; orcid.org/0000-0002-4867-2872

David Sorribes − *Departamento de Química Física, Facultad de Ciencias Químicas, Universidad Complutense de Madrid, 28040 Madrid, Spain*

Sonia Marggi Poullain − *Departamento de Química Física, Facultad de Ciencias Químicas, Universidad Complutense de Madrid, 28040 Madrid, Spain*; orcid.org/0000-0001-6712-3628

Complete contact information is available at: https://pubs.acs.org/10.1021/acs.jpca.4c02217

Notes

The authors declare no competing financial interest.

■ ACKNOWLEDGMENTS

P.R. gratefully acknowledges Universidad Complutense de Madrid (UCM) for a Margarita Salas postdoctoral contract and for a Juan de la Cierva postdoctoral contract funded by MCIN/AEI/10.13039/501100011033 and by the European Union "NextGenerationEU"/PRTR. J.C. and D.S. thank the financial support from the Spanish Ministry of Science and Innovation under the FPI predoctoral program. This work was funded by Grant No. PID2021-122839NB-I00 from the Spanish Ministry of Science and Innovation. The financial support (Grant No. PR27/21-010) provided by the Madrid Government (Comunidad de Madrid, Spain) under the Multiannual Agreement with Universidad Complutense de Madrid in the line Research Incentive for Young PhDs, in the context of the V PRICIT (Regional Programme of Research and Technological Innovation), is also acknowledged. The facilities provided by the Center for Ultrafast Lasers (CLUR) of Universidad Complutense de Madrid are gratefully acknowledged.

■ REFERENCES

(1) Mulliken, R. S. Intensities in Molecular Electronic Spectra X. Calculations on Mixed-Halogen, Hydrogen Halide, Alkyl Halide, and Hydroxyl Spectra. *J. Chem. Phys.* **1940**, *8*, 382.

(2) Mulliken, R. S.; Teller, E. Interpretation of the methyl iodide absorption bands near λ 2000. *Phys. Rev.* **1942**, *61*, 283.

(3) Donohue, T.; Wiesenfeld, J. R. Photodissociation of alkyl iodides. *J. Chem. Phys.* **1975**, *63*, 3130.

(4) Riley, S. J.; Wilson, K. R. Excited fragments from excited molecules: energy partitioning in the photodissociation of alkyl iodides. *Faraday Discuss. Chem. Soc.* **1972**, *53*, 132.

(5) Guo, H.; Schatz, G. C. Time-dependent dynamics of methyl iodide photodissociation in the first continuum. *J. Chem. Phys.* **1990**, *93*, 393.

(6) Guo, H.; Lao, K. Q.; Schatz, G. C.; Hammerich, A. D. Quantum nonadiabatic effects in the photodissociation of vibrationally excited CH_3I. *J. Chem. Phys.* **1991**, *94*, 6562.

(7) Rist, C.; Alexander, M. H. Adiabatic representations for the study of flux redistribution during photodissociation involving coupled

https://doi.org/10.1021/acs.jpca.4c02217
J. Phys. Chem. A 2024, 128, 8312−8321

electronic states: The effect of vibrational excitation on the photofragmentation of CH_3I. *J. Chem. Phys.* **1993**, *98*, 6196.
(8) Schinke, R. *Photodissociation Dynamics*; Cambridge University Press: N.Y., 1993.
(9) Amatatsu, Y.; Morokuma, K.; Yabushita, S. Ab initio potential energy surfaces and trajectory studies of A-band photodissociation dynamics: $CH_3I^* \rightarrow CH_3 + I$ and $CH_3 + I^*$. *J. Chem. Phys.* **1991**, *94*, 4858.
(10) Amatatsu, Y.; Yabushita, S.; Morokuma, K. Full nine-dimensional ab initio potential energy surfaces and trajectory studies of A-band photodissociation dynamics: $CH_3I^* \rightarrow CH_3 + I$, $CH_3 + I^*$, and $CD_3I^* \rightarrow CD_3 + I$, $CD_3 + I^*$. *J. Chem. Phys.* **1996**, *104*, 9783.
(11) Roehl, C. M.; Burkholder, J. B.; Moortgat, G. K.; Ravishankara, A. R.; Crutzen, P. J. Temperature dependence of UV absorption cross sections and atmospheric implications of several alkyl iodides. *J. Geophys. Res.: Atmos.* **1997**, *102*, 12819.
(12) Herzberg, G. *Molecular Spectra and Molecular Structure*; Van Nostrand Company, 1996.
(13) Mulliken, R. S. The Low Electronic States of Simple Heteropolar Diatomic Molecules. I. General Survey. *Phys. Rev.* **1936**, *50*, 1017.
(14) Riley, S. J.; Wilson, K. R. Magnetic circular dichroism spectra of the methyl halides. Resolution of the n→ σ^* continuum. *Chem. Phys. Lett.* **1975**, *34*, 39.
(15) McGivern, W. S.; Li, R.; Zou, P.; North, S. W. Photodissociation dynamics of CH_2BrCl studied using resonance enhanced multiphoton ionization (REMPI) with time-of-flight mass spectrometry. *J. Chem. Phys.* **1999**, *111*, 5771.
(16) Shubert, V. A.; Rednic, M.; Pratt, S. T. Photodissociation of i-C_3H_7I within the A band and anisotropy-based decomposition of the translational energy distributions. *J. Chem. Phys.* **2009**, *130*, 134306.
(17) Corrales, M. E.; Loriot, V.; Balerdi, G.; González-Vázquez, J.; de Nalda, R.; Bañares, L.; Zewail, A. H. Structural dynamics effects on the ultrafast chemical bond cleavage of a photodissociation reaction. *Phys. Chem. Chem. Phys.* **2014**, *16*, 8812−8818.
(18) Atkinson, R.; Baulch, D. L.; Cox, R. A.; R F Hampson, J.; Kerr, J. A.; Rossi, M. J.; Troe, J. Evaluated kinetic, photochemical and heterogeneous data for atmospheric chemistry: Supplement V. IUPAC subcommittee on gas kinetic data evaluation for atmospheric chemistry. *J. Phys. Chem. Ref. Data* **1997**, *26*, 521.
(19) Young, C. J.; Hurley, M. D.; Wallington, T. J.; Mabury, S. A. Atmospheric chemistry of 4:2 fluorotelomer iodide (n-$C_4F_9CH_2CH_2I$): Kinetics and products of photolysis and reaction with OH radicals and Cl atoms. *J. Phys. Chem. A* **2008**, *112*, 13542.
(20) Boschi, R. A.; Salahub, D. R. The far ultra-violet spectra of some 1-iodoalkanes. *Mol. Phys.* **1972**, *24*, 289.
(21) Phillips, D. L.; Myers, A. B.; Valentini, J. J. Investigation of solvation effects on short-time photodissociation dynamics of alkyl iodides. *J. Chem. Phys.* **1992**, *96*, 2039.
(22) Warne, E. M.; Downes-Ward, B.; Woodhouse, J.; Parkes, M. A.; Bellshaw, D.; Springate, E.; Majchrzak, P.; Zhang, Y.; Karras, G.; Wyatt, A. S.; et al. Photodissociation dynamics of CH_3I probed via multiphoton ionisation photoelectron spectroscopy. *Phys. Chem. Chem. Phys.* **2019**, *21*, 11142.
(23) Downes-Ward, B.; Warne, E. M.; Woodhouse, J.; Parkes, M. A.; Springate, E.; Pearcy, P. A. J.; Zhang, Y.; Karras, G.; Wyatt, A. S.; Chapman, R. T.; Minns, R. S. Photodissociation dynamics of methyl iodide across the A-band probed by femtosecond extreme ultraviolet photoelectron spectroscopy. *J. Phys. B: Atom. Mol. Opt. Phys.* **2021**, *54*, 134003.
(24) Rubio-Lago, L.; Garcıa-Vela, A.; Arregui, A.; Amaral, G. A.; Bañares, L. The photodissociation of CH_3I in the red edge of the A-band: Comparison between slice imaging experiments and multisurface wave packet calculations. *J. Chem. Phys.* **2009**, *131*, 174309.
(25) González, M. G.; Rodrıguez, J. D.; Rubio-Lago, L.; Garcıa-Vela, A.; Bañares, L. Slice imaging and wave packet study of the photodissociation of CH_3I in the blue edge of the A-band: evidence of reverse $^3Q_0 \leftarrow^1 Q_1$ non-adiabatic dynamics. *Phys. Chem. Chem. Phys.* **2011**, *13*, 16404−16415.
(26) Papadakis, V.; Kitsopoulos, T. N. Slice imaging and velocity mapping using a single field. *Rev. Sci. Instrum.* **2006**, *77*, 083101.
(27) Rubio-Lago, L.; Amaral, G. A.; Oldani, A. N.; Rodrıguez, J. D.; González, M. G.; Pino, G. A.; Bañares, L. Photodissociation of pyrrole−ammonia clusters by velocity map imaging: mechanism for the H-atom transfer reaction. *Phys. Chem. Chem. Phys.* **2011**, *13*, 1082−1091.
(28) Suits, A. G. Invited Review Article: Photofragment imaging. *Rev. Sci. Instrum.* **2018**, *89*, 111101.
(29) Rakitzis, T. P.; Zare, R. N. Photofragment angular momentum distributions in the molecular frame: Determination and interpretation. *J. Chem. Phys.* **1999**, *110*, 3341.
(30) Rakitzis, T. P. Direct measurements of photofragment alignment from unnormalized Abel-inverted images. *Chem. Phys. Lett.* **2001**, *342*, 121−126.
(31) Recio, P.; Cachón, J.; Rubio-Lago, L.; Chicharro, D. V.; Zanchet, A.; Limão-Vieira, P.; Oliveira, N.; Samartzis, P. C.; Poullain, S. M.; Bañares, L. Imaging the Photodissociation Dynamics and Fragment Alignment of CH_2BrI at 193 nm. *J. Phys. Chem. A* **2022**, *126*, 8404−8422.
(32) Orr-Ewing, A. J.; Zare, R. N. Orientation and Alignment of Reaction Products. *Annu. Rev. Phys. Chem.* **1994**, *45*, 315−366.
(33) Samartzis, P. C.; Bakker, B. L. G.; Rakitzis, T. P.; Parker, D. H.; Kitsopoulos, T. N. Spin-orbit branching ratios for the Cl atom photofragments following the excitation of Cl_2 from 310 to 470 nm. *J. Chem. Phys.* **1999**, *110*, 5201.
(34) Eppink, A. T. J. B.; Parker, D. H. Energy partitioning following photodissociation of methyl iodide in the A band: A velocity mapping study. *J. Chem. Phys.* **1999**, *110*, 832.
(35) Kim, Y. S.; Kang, W. K.; Kim, D.-C.; Jung, K.-H. Photodissociation of tert-Butyl Iodide at 277 and 304 nm: Evidence for Direct and Indirect Dissociation in A-Band Photolysis of Alkyl Iodide. *J. Phys. Chem. A* **1997**, *101*, 7576.
(36) Paterson, C.; Godwin, F.; Gorry, P. Photofragmentation dynamics of C_2H_5I and CF_3CH_2I at 248 nm. *Mol. Phys.* **1987**, *60*, 729−747.
(37) Godwin, F.; Paterson, C.; Gorry, P. Photofragmentation dynamics of *n*-C_3H_7I and *i*-C_3H_7I at 248 nm. *Mol. Phys.* **1987**, *61*, 827−848.
(38) Rakitzis, T. P.; Kandel, S. A.; Alexander, A. J.; Kim, Z. H.; Zare, R. N. Measurements of Cl-atom photofragment angular momentum distributions in the photodissociation of Cl_2 and ICl. *J. Chem. Phys.* **1999**, *110*, 3351.

https://doi.org/10.1021/acs.jpca.4c02217
J. Phys. Chem. A 2024, 128, 8312−8321

4.2 Imaging the photodissociation dynamics and fragment alignment of CH_2BrI at 193 nm

Art. 5. *Imaging the photodissociation dynamics and fragment alignment of CH_2BrI at 193 nm*, Pedro Recio, Javier Cachón, Luis Rubio-Lago, David V. Chicharro, Alexandre Zanchet, Paulo Limão-Vieira, Nelson de Oliveira, Petros C. Samartzis, Sonia Marggi Poullain, and Luis Bañares. J. Phys. Chem. A, 126, 8404-8422 (2022).

Halocarbons (R−X, where R is an alkyl radical and X is a halogen atom like Cl, Br, or I) are of great importance in atmospheric chemistry, specifically due to their significant role in tropospheric chemistry and ozone depletion. Halocarbons are notable because when they undergo photolysis (breakdown by light excitation), they produce reactive atomic halogens, which can then participate in further chemical reactions in the atmosphere. These reactions contribute to the formation of pollutants and have a notable effect on the depletion of the ozone layer, one of the key environmental concerns over recent decades.

Dihalocarbons, such as bromoiodomethane (CH_2BrI), are particularly interesting to researchers because they contain two different halogen atoms (Br and I, in this case), which complicate their photochemistry. The structure of their excited states is complex, leading to intricate dissociation pathways when these molecules are exposed to light. Because of this complexity, dihalocarbons like CH_2BrI serve as useful prototypes for studying bond-selective electronic excitations and dissociations in molecules with multiple halogens.

Previous studies on halocarbons have established that they exhibit bond-selective dissociation depending on the wavelength of light used for excitation. In the case of CH_2BrI, earlier research highlighted that the molecule has three main absorption bands:

1. The *A* band, at around 268 nm, where the C−I bond is selectively dissociated due to the excitation of the σ^*(C−I) ← *n*(I) transition.

2. The *A'* band, at around 210 nm, where the C−Br bond is broken due to excitation to the σ^*(C−Br) ← *n*(Br) transition.

3. A third band, starting around 200 nm, attributed to a Rydberg transition on the iodine atom.

Past work by researchers such as Lee and Bersohn (1982) and Butler *et al*. (1984) investigated the photodissociation of CH_2BrI at various wavelengths (248, 210, and 193 nm), confirming the bond-selective photochemistry behavior of the molecule. At 193 nm, the wavelength of interest in this work, previous studies showed the presence of multiple dissociation pathways, including both C−I and C−Br bond fission, and a third pathway involving the formation of IBr through concerted elimination. In particular, the work of Butler and co-workers found that both iodine and bromine atoms are produced in their excited spin-orbit states (I* and Br*).

The current study aims to build on this foundation by exploring the photodissociation dynamics and atomic fragment alignment of CH_2BrI at 193 nm in greater detail. The experimental approach employs slice imaging and resonance-enhanced multiphoton ionization

(REMPI) detection techniques to capture the behavior of the bromine (Br) and iodine (I) photofragments. The high-resolution ultraviolet (UV)-vacuum ultraviolet (VUV) absorption spectrum of gas phase CH_2BrI was measured in the photon energy range of 5−11 eV using the VUV Fourier transform spectrometer (FTS) at the VUV beamline DESIRS of the synchrotron SOLEIL. The spectrum was fully assigned to electronic states and vibronic transitions, and the electronic transition corresponding to the 193 nm excitation was fully assigned to the 2_0^1 vibronic band of the 13A' ← *X* A_1 transition. Additionally, *ab initio* electronic structure calculations are used to understand the vertical excitation energies and potential energy curves of the system.

The study aims to provide a comprehensive picture of the dissociation dynamics and stereodynamics at this specific excitation wavelength, where excitation into highly excited states and complex dissociation pathways are expected. The results of this work are crucial for improving the understanding of how halocarbons behave under ultraviolet (UV) light, which has important implications for atmospheric chemistry and environmental science.

The experimental results, particularly the translational energy distributions (TEDs) of the Br and I fragment, reveal key insights into how the available energy is partitioned among the fragments. The TEDs show three distinct energy components, suggesting that multiple dissociation pathways contribute to the overall dynamics:

- A low-energy Boltzmann-like peak, attributed to statistical processes and secondary dissociation.
- A mid-energy peak, which is sharp and attributed to prompt dissociation (single-photon absorption) of the parent molecule.
- A high-energy peak, which is most prominent in the case of Br fragments and indicates the presence of a secondary dissociation pathway, likely involving two-photon absorption.

The dissociation mechanisms of CH_2BrI at 193 nm are analyzed in terms of the competition between prompt dissociation (direct bond cleavage) and statistical dissociation following internal conversion. The results indicate that both the C−Br and C−I bonds can break, but the dynamics of the dissociation differ depending on which bond is being broken.

- C−Br Bond dissociation: The dissociation of the C−Br bond is primarily associated with excitation into the 13A' electronic state. Predissociation occurs via the 11A' or 11A" states, eventually leading to dissociation through the lower 10A' or 9A" states. This process is relatively direct, but it is also accompanied by internal conversion and energy redistribution among the different degrees of freedom (rotational and vibrational) of the fragments.
- C−I Bond dissociation: The C−I bond dissociation is somewhat more complex. While a direct dissociation pathway exists, involving predissociation through the 6A' or 6A" states, the process is dominated by a fast internal conversion mechanism that precedes the bond cleavage. This suggests that dissociation *via* the C−I bond is less favored in terms of direct dissociation at this wavelength compared to C−Br bond fission.

The alignment of the halogen atom photofragments is analyzed, which gives insight into the angular momentum distribution of the atomic fragments. The alignment parameters $a_q^k(p)$ reveal that the CH_2Br and CH_2I co-fragments exhibit strong alignment along the recoil direction, particularly in the case of Br fragments. This suggests that the rotational angular momentum of

the co-fragments is highly constrained, and the dissociation dynamics are strongly influenced by the geometry of the dissociating molecule.

The anisotropy parameter (β) further supports this interpretation. For the Br($^2P_{3/2}$) fragments, the β parameter evolves as a step function, indicating three distinct dynamical regions corresponding to the different energy components of the TED. These findings are consistent with a dissociation model where rotational excitation of the CH_2Br and CH_2I co-fragments plays a significant role in the energy redistribution process.

The study also identifies a secondary dissociation process, particularly for Br fragments, where a second photon absorption leads to further fragmentation. This secondary process is evidenced by the presence of high-energy Br fragments in the TED, as well as the distinct anisotropy observed in the fragment alignment measurements. It is suggested that this secondary dissociation likely occurs through a statistical mechanism, where the excess energy from the first photon is distributed into rotational and vibrational excitation, and a second photon provides the energy needed for further dissociation.

The results of this study are compared to previous research on the photodissociation of CH_2BrI at different wavelengths (particularly 248 and 210 nm). The findings at 193 nm confirm many of the earlier conclusions but also provide new insights into the role of secondary dissociation and the importance of rotational excitation in the dynamics. Notably, the present study provides a clearer picture of the branching ratios between different dissociation pathways and how they vary with excitation energy.

It can be concluded that the photodissociation of CH_2BrI at 193 nm is a highly complex process, involving multiple dissociation pathways, including both prompt, statistical and secondary processes. The dissociation dynamics are dominated by the energy distribution into the rotational and vibrational degrees of freedom of the co-fragments, and the soft impulsive model provides a good framework for understanding the observed behaviors. The study significantly advances the understanding of the CH_2BrI photochemistry and provides important insights into the environmental implications of halocarbon dissociation in the atmosphere.

THE JOURNAL OF PHYSICAL CHEMISTRY A
A JOURNAL OF THE AMERICAN CHEMICAL SOCIETY

pubs.acs.org/JPCA Article

Imaging the Photodissociation Dynamics and Fragment Alignment of CH_2BrI at 193 nm

Published as part of The Journal of Physical Chemistry virtual special issue "Paul L. Houston Festschrift".

Pedro Recio, Javier Cachón, Luis Rubio-Lago, David V. Chicharro, Alexandre Zanchet, Paulo Limão-Vieira, Nelson de Oliveira, Peter C. Samartzis, Sonia Marggi Poullain, and Luis Bañares*

Cite This: J. Phys. Chem. A 2022, 126, 8404−8422 Read Online

ACCESS | Metrics & More | Article Recommendations | Supporting Information

ABSTRACT: The photodissociation dynamics and photofragment alignment of bromoiodomethane (CH_2BrI) have been studied at 193 nm using a double experimental and theoretical approach. In addition, the ultraviolet (UV)-vacuum ultraviolet (VUV) absorption spectrum of gas phase CH_2BrI has been measured in the photon energy range of 5−11 eV using the VUV Fourier transform spectrometer (FTS) at the VUV beamline DESIRS of the synchrotron SOLEIL facility. The slice imaging technique in combination with resonance enhanced multiphoton ionization (REMPI) detection of the $Br(^2P_J)$ and $I(^2P_J)$ (with J = 3/2 and 1/2 for Br/I and Br*/I*, respectively) atomic photofragments have been used to produce experimental translational energy and angular distributions, which were analyzed to deliver, on one hand, the partitioning of the available energy among the different degrees-of-freedom of the photofragments and, on the other, the photofragment polarization in terms of $a_q^k(p)$ alignment parameters. The experimental measurements were rationalized in terms of high-level *ab initio* calculations of vertical excitation energies, transition dipole moments and potential energy curves (PECs) along different reaction coordinates to provide a complete picture of the photodissociation dynamics. The results indicate that for excitation at 193 nm, prompt C−X cleavage (with X being either halogen atom, Br or I) competes with fast internal conversion and consequent stochastic dissociation in lower electronic states. In the case of the $CH_2Br + I(^2P_{3/2})/I^*(^2P_{1/2})$ channels, the dynamics are greatly biased toward the stochastic dissociation process due to both the particular PECs landscape and the unfavored excitation of the CH_2BrI ensemble with respect to the C−I molecular axis at this excitation energy. The *ab initio* PECs provide a tentative path for the fast dissociation process in either case. For the C−Br bond breakage, excitation to the 13A' electronic state and predissociation through the 11A'/11A'' or 12A'/12A'' states, leading to direct dissociation through the 10A'/9A'' states, appear as the most consistent dynamics. For the C−I channel, predissociation does not become a reliable possibility and a fast internal conversion may precede dissociation through the repulsive 6A'/6A'' and 4A'/4A'' states. The large content of rotational and vibrational excitation of the polyatomic cofragments is justified through the soft impulsive model and the geometrical changes produced along the dissociation pathway. Strikingly, the $a_q^k(p)$ alignment parameters obtained for the $Br(^2P_{3/2})$ and $I(^2P_{3/2})$ photoproducts indicate that the rotational angular momentum of the CH_2X (X = I or Br) cofragment appears highly constrained along the recoil direction. Finally, this work presents a highly plausible explanation for the branching ratio of secondary dissociation processes in the photodynamics of CH_2BrI at 193 nm.

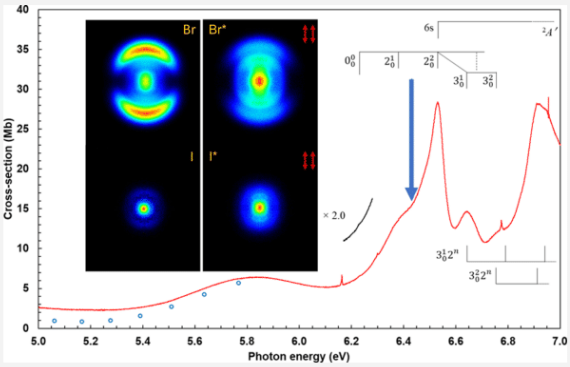

■ INTRODUCTION

Halocarbons (R−X, where R is an alkyl radical and X = Cl, Br, I) have revived significant attention in several chemistry areas due to their role in the troposphere chemistry. In particular, photolysis of halocarbons yields atomic halogen fragments, able to react with other particles of the atmosphere and produce pollutant species.[1,2] In addition, reactive halogen atoms have an important effect on ozone depletion, which constitutes one of the biggest atmospheric problems of the last century.[3−5] Dihalocarbons, as bromoiodomethane (CH_2BrI), become even more relevant due to the presence of two halogen atoms. Another characteristic of dihalocarbons that increases their interest is the intricate structure of the excited states involved in

Received: August 17, 2022
Revised: October 13, 2022
Published: November 2, 2022

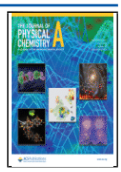

https://doi.org/10.1021/acs.jpca.2c05897
J. Phys. Chem. A 2022, 126, 8404−8422

their photochemistry. As such, they are amenable to be used as prototypes for bond-selective electronic excitation and dissociation.

The UV absorption spectrum of CH_2BrI is well-known to consist of three bands.[6] The first absorption band (A band), centered at 268 nm, has been attributed almost exclusively to the $\sigma^*(C-I) \leftarrow n(I)$ transition and C−I bond dissociation. In contrast, the second absorption band (that will be named here as A' band) is centered at 210 nm and has been assigned to the $\sigma^*(C-Br) \leftarrow n(Br)$ transition and C−Br bond breakage. The third band,[7,8] which starts around 200 nm, has been assigned to a Rydberg transition on the I atom.

Lee and Bersohn[9] published, in 1982, an investigation on the photodissociation of CH_2BrI at 258 nm using photofragment translational spectroscopy. A more detailed investigation using the same technique was published later by Butler et al.,[8] who measured the photodissociation from the three absorption bands by exciting the molecule at 248, 210, and 193 nm, and validated the bond selectivity photochemistry typical of dihalocarbons. In the A band (at 248 nm), dissociation of the C−I bond was confirmed to be the major decomposition process although a small contribution of C−Br bond fission was confirmed. In the A' band (at 210 nm), cleavage of C−Br bond was the only decomposition pathway observed for the title molecule. At higher excitation energies (at 193 nm), besides the C−Br and C−I bond fissions—with dominance of the former over the latter—the presence of a third dissociation channel was detected, specifically, IBr formation produced by concerted elimination. At such high excitation energies, both halogen atoms were mainly produced in the spin−orbit excited state, $^2P_{1/2}$, while the IBr fragment was concluded to be formed exclusively in high electronic excited states.[8] The photofragment polarization analysis performed in the same work was consistent with a mechanism where the excitation is produced to a Rydberg level of the iodine atom and consequent predissociation on a longer time scale than the rotational period of the parent molecule. The bond selectivity proposed by Butler et al.[8] was confirmed later on by the theoretical calculations of Liu et al.[10] and Lindh and co-workers,[11] who calculated the vertical excitation energies and oscillator strengths for the excited states comprising the A and A' bands and the potential energy curves (PECs), respectively, for both C−Br and C−I bond fission dissociation channels. Lindh and co-workers[11] also studied the isomerization process to *iso*-CH_2−Br−I and *iso*-CH_2−I−Br. Isomerization processes have been largely reported in experimental studies of CH_2BrI in solution.[7,12,13] Using different solvents and matrices, it was demonstrated the solvent-induced character of the isomerization process as well as the observed coupling between the $\sigma^*(C-I) \leftarrow n(I)$ and the $\sigma^*(C-Br) \leftarrow n(Br)$ transitions at specific wavelengths.

Further experimental studies on the photodissociation of CH_2BrI that delve into the electronic structure of the molecule have been carried out by different groups. Leone and co-workers,[14] for instance, performed experiments using femtosecond time-resolved extreme ultraviolet (XUV) transient absorption spectroscopy, following excitation at 266 nm. Similar results as those published by Butler et al.[8] were reported. In particular, dissociation in the A band was dominated by C−I dissociation (about 80%), and C−Br dissociation was observed as a minor pathway. The technique employed allows the transient characterization of the dissociation process and thus, a slow dissociation dynamics of the C−Br bond cleavage was determined, which was rationalized in terms of the difference between the repulsive slopes of the excited states and the relative internal energy deposited into the CH_2I radical.

Weinacht and co-workers,[15,16] using ultraviolet (UV)-pump, vacuum ultraviolet (VUV)-probe time-resolved photoelectron spectroscopy, velocity map imaging (VMI), and *ab initio* calculations, compared the photodissociation of CH_2I_2 and CH_2BrI at 267 nm. The photodissociation of CH_2BrI was described as a direct decomposition process along the C−I coordinate. However, C−I bond dissociation of CH_2I_2 should involve internal conversion and motion along multiple dimensions. These conflicts in the photodissociation mechanisms arise from differences in the nonadiabatic couplings between electronic states of the two molecules. Coulomb explosion imaging has been employed by Burt et al.[17] in a UV pump−IR probe scheme to observe the dissociation dynamics following excitation at 271.6 nm. The results, consistent with previous results from Butler and co-workers,[8] revealed in particular secondary dissociation of CH_2Br through a second UV-photon absorption. Köckert and co-workers[18] have recently published a work where UV pump−XUV probe pulses along with multimass ion imaging were used to study the photodissociation of CH_2BrI at 271 nm in the A band yielding the CH_2Br + I channel, where the influence of parent rotation on a charge transfer process was investigated. The results suggest that, in spite of the slow dissociation, the critical interatomic distance for charge transfer is rapidly reached.

Pan et al.[19] published a VMI study on the photodissociation of CH_2BrI centered on the first absorption A-band (280−310 nm) in which both spin−orbit $I(^2P_{3/2})$ and $I^*(^2P_{1/2})$ photofragments were detected by (2 + 1) resonance-enhanced multiphoton ionization (REMPI). The results concluded that most of the available energy was partitioned into internal energy of the CH_2Br radical, while only a small amount was imparted to the photofragments. The reported behavior was consistent with a simple impulsive model in agreement with Butler et al.[8] Finally, Lin and co-workers[20] studied the photodissociation of CH_2BrI at 243 nm by using cavity ring-down spectroscopy seeking for elimination of IBr. The ground state IBr fragment was observed and characterized by a vibrational population of 1:0.58:0.34 for the vibrational $v'' = 0, 1, 2$ levels, respectively. The quantum yield of this channel was determined as well, and the considerably low value of 0.044 found was consistent with what Butler et al.[8] predicted in the A' band (at 210 nm).

The aim of the present study is to investigate the photodissociation dynamics and the atomic photofragment alignment of CH_2BrI in the B-band excited at 193 nm through the detection of iodine, $I(^2P_{3/2})$ and $I^*(^2P_{1/2})$, and bromine, $Br(^2P_{3/2})$ and $Br^*(^2P_{1/2})$, photofragments by using pump−probe nanosecond lasers and the slice imaging technique coupled to (2 + 1) REMPI detection, in combination with *ab initio* electronic structure calculations of vertical excitation energies, transition dipole moments and potential energy curves up to 10 eV. In addition, we have measured the gas phase high-resolution UV−VUV absorption spectrum in order to assign the different electronic states accessed by UV−VUV one-photon excitation in this region. The present study is as an extension of a previous publication,[21] where the photodissociation of bromoiodomethane was investigated around the maximum of the first two absorption bands, the A and A' bands, at 266 and 210 nm, respectively. In a similar fashion than that of the present work, the formation of the $I(^2P_{3/2})$, $I^*(^2P_{1/2})$, $Br(^2P_{3/2})$, and $Br^*(^2P_{1/2})$ photoproducts was experimentally characterized by using the VMI and slice imaging (SI) techniques and

https://doi.org/10.1021/acs.jpca.2c05897
J. Phys. Chem. A 2022, 126, 8404−8422

rationalized with the aid of high level *ab initio* calculations. It was concluded in the said work that the I atoms were produced from the *A* band through direct dissociation in the $5A'$ excited state, while the formation of I* atoms involved the $5A' \rightarrow 4A'/4A''$ nonadiabatic crossing. Furthermore, the presence of a minor contribution of Br and Br* atoms in the photodissociation from the *A* band was attributed to indirect dissociation via a curve crossing between the $5A'$ state and an upper excited state. Dissociation in the A' band was characterized, in contrast, by a strong photoselectivity, since no I or I* atoms were observed. The dissociation leading to Br and Br* atoms was proposed to occur via the $9A'$, $8A''$, and $10A''$ excited states. In 2018, a complementary femtosecond time-resolved VMI experiment of bromoiodomethane and chloroiodomethane was published by some of the authors of the present work.[22] CH_2BrI was excited at 268 nm in the first *A* absorption band and the I/I* fragments were detected by (2 + 1) REMPI. Asymptotic images were measured, and the transients obtained permitted the determination of reaction times. In addition, high level *ab initio* electronic structure calculations and full dimension on-the-fly trajectory calculations including surface hopping were performed, yielding CH_2Br and I/I* products. The main finding of this work was an *anchor* effect due to the substituent Br atom in the parent molecule, which implies significant rotational motion of the dissociating molecule, and leads to a remarkable rotational energy of the CH_2Br radical cofragment. It was concluded that this energy flux into internal degrees of freedom of the molecule is the main key factor governing the real time photodissociation dynamics,[22] which was very much in agreement with the conclusions found by Köckert et al.[18]

The region of the VUV absorption spectrum of CH_2BrI in which the present work focuses has not received as much attention as the *A* and A' bands. As introduced in the previous paragraphs, only Butler et al.[8] studied thoroughly the photodissociation of the title molecule at 193 nm using photofragment translational spectroscopy. Hence, a deep investigation of the photodissociation dynamics of CH_2BrI at this excitation wavelength (193 nm) seemed very timely considering the complex excitation to a region congested with many excited states of Rydberg character and the complex dissociation mechanisms expected. We have included measurements of the stereodynamics of the photodissociation process by determining the atomic photofragment alignment parameters to give light into de different possible mechanisms at play. The support of high level *ab initio* electronic structure calculations including vertical excitation energies, transition dipole moments and potential energy curves for different internal coordinates is crucial to interpret the experimental results in an excitation region where different dissociation mechanisms compete.

The present work is divided in the following sections. The experimental and theoretical approaches are explained in the Methods section, as well as, the methodology employed to determine the stereodynamics of the process in the form of atomic photofragment alignment. In the Experimental Results and Theoretical Results sections the most relevant experimental and theoretical results are presented, respectively. In the Analysis and Discussion section both experimental and theoretical results are discussed jointly. Finally, the main conclusions of this work are presented in the Conclusions section.

METHODS

Experimental Setups. The high-resolution UV−VUV absorption spectrum of gas phase CH_2BrI was measured using the VUV Fourier transform spectrometer (FTS),[23] which is one of the permanent endstations of the VUV beamline DESIRS[24] at the synchrotron SOLEIL facility. The VUV FTS covers a large UV−VUV spectral range from 4 to 30 eV with a line width of 0.08 cm^{-1} on a large spectral window ($\Delta E/E$ = 7%),[25] over which all spectral features can be acquired in a multiplex way. The detailed description of the beamline and the VUV FTS instrument can be found in refs.[25,26] In brief, the FTS measurement implies a two steps procedure. A first absorption measurement covering the full VUV spectral range is completed using a windowless cell. A reservoir filled with the liquid sample is connected to the main sample environmental vacuum chamber. After a series of freeze, pump, and thaw purification steps of the sample, the sample in the gas phase controlled by a needle valve is allowed to flow through a 10 cm cylindrical windowless cell with two rectangular tubes at both ends. The synchrotron beam is going through the cell and is ultimately recorded by the FTS instrument. In order to calibrate the column density, another measurement at moderate spectral resolution is performed inside a 9 cm long MgF_2 windowed cell. This time, only a few spectral windows are recorded, providing absolute absorption cross sections. The windowless spectrum is scaled upon these reference points following the procedure detailed in ref 25. The VUV-FTS is extremely sensitive to external perturbation,[25] a statistical study gave an estimated uncertainty for the absolute cross-section of ±10%. Concerning the energy scale, no further calibration is required for this experiment since the accuracy is intrinsically referred to the indexation HeNe stabilized laser leading already to a relative error in the range of 10^{-6}.[23] The spectral resolution was set to 4.3 cm^{-1}, which is more than sufficient to depict the quite broad structures of CH_2BrI. Due to the high flux, we have noticed signatures of photolysis products of CH_2BrI in the spectrum, those are in general quite weak. Most of these signatures have been identified and are listed in Table S1 of the Supporting Information (SI).

The nanosecond laser pump−probe and slice imaging experimental setup at FORTH-IESL used in the present experiments has been already described in detail elsewhere[27−30] and only a brief description is presented here. A molecular beam is created by expanding a gas mixture of CH_2BrI in He (10%, 1 atm backing pressure) into vacuum using a piezoelectric pulsed valve working at a repetition rate of 10 Hz. The beam passes through a skimmer and is collimated to a diameter of 1 mm prior to intersect focused laser beams at right angles. Excitation of CH_2BrI was carried out at 193 nm using an excimer laser (Lambda Physik COMPEX, operating with ArF), linearly polarized using Brewster reflection. For the detection of the fragments a MOPO (Spectra-Physics 730D10) pumped by a Nd:YAG laser (Quanta Ray Pro 250) and delayed 10 ns with respect to the pump laser was used. (2 + 1) REMPI detection of $Br(^2P_{3/2})$ and $Br^*(^2P_{1/2})$ was carried out at 250.35 and 262.45 nm, respectively, through the transitions $(^3P)5p(^2S_{1/2}) \leftarrow 5p(^2P_{3/2})$ and $(^3P)5p(^2S_{1/2}) \leftarrow 5p(^2P_{1/2})$.[31] The $I(^2P_{3/2})$ and $I^*(^2P_{1/2})$ products were detected at 304.58 and 305.49 nm, respectively, for the $(^3P_2)6p[3]_{7/2} \leftarrow 5p(^2P_{3/2})$ and $(^3P_1)$-$6p[1]_{3/2} \leftarrow 5p(^2P_{1/2})$ transitions.[32] The generated Br^+ and I^+ ions are projected onto the position-sensitive detector system (two microchannel plates MCPs coupled to a phosphor screen).

https://doi.org/10.1021/acs.jpca.2c05897
J. Phys. Chem. A 2022, 126, 8404−8422

Slice images of Br^+ or I^+ are recorded using a 500 ns pulsed extraction delay applied on the repeller plate and an effective 10 ns detector gate on the front MCP. As Br presents two isotopes ^{79}Br and ^{81}Br with similar abundance, it is necessary to select an extraction delay allowing a complete separation of the ion clouds from both isotopes such that the imaged slice correspond to a single isotope, $^{79}Br^+$ in the present case. The images for $Br(^2P_{3/2})$ and $I(^2P_{3/2})$, where atomic alignment effects can be expected, were recorded using the three laser polarization configurations: X(pump)X(probe), XZ, and ZX, where X is perpendicular to the laser propagation axis and Z is parallel to the molecular beam. However, the images for the $Br^*(^2P_{1/2})$ and $I^*(^2P_{1/2})$ fragments were recorded only for both lasers parallel to the detector (XX) since these fragments cannot present any alignment effects.[a] The ZZ images, which do not contain any dynamical information, were obtained in all cases as a reference to avoid systematic errors, such as detector inhomogeneities.

The sliced images were quadrant symmetrized prior to extracting the kinetic energy and angular distributions. For all the two-color pump−probe measured images, the contribution of each laser alone was subtracted, so that the observed signal was only pump−probe.

Atomic Alignment Analysis. The slice imaging technique provides a direct measurement of the central slice of the 3D photofragment distribution produced in a photodissociation process. Such development constitutes one of the main advantages of the technique, since it that does not demand for any mathematical transformation to map the photofragment distribution. The slice images can be, therefore, straightforwardly interpreted to extract the relevant dynamical information.

The analysis process requires slice images acquired in four combinations of the pump and probe laser polarizations, namely, X(pump)X(probe), XZ, ZX, and ZZ configurations. The XYZ axis system denotes the laboratory frame, with both lasers counterpropagating along the Y axis, and the molecular beam propagating along the Z axis (the time-of-flight axis). In such fashion, the XX images comprise all the stereodynamical information, *i.e.*, the anisotropy of the dissociation process and the orientation and/or alignment of the photoproducts. For the XZ images, the probe polarization vector lies perpendicular to the detection plane and, therefore, all the information related to the angular momenta of the products is lost. Similarly, the ZX images have lost the information related to the anisotropy of the dissociation process. The ZZ images do not contain any dynamical information and are used as a reference to avoid systematic errors.

Among the relevant information that can be extracted from the images, photofragment alignment plays a key role to understand the underlying dynamics. The laboratory intensity distribution of a one-photon dissociation process and $(n + m)$ REMPI detection is given by the expression[33]

$$I(\theta_{pump}) \times I(\theta_{probe}) = [1 + \beta P_2(\cos\theta_{pump})] \times \sum_{k=2}^{2n+m} 1 + A_0^k P_k(\cos\theta_{probe}) \quad (1)$$

where $I(\theta_{pump})$ and $I(\theta_{probe})$ are the intensity distributions associated with the photolysis and detection processes, respectively, with θ_{pump} and θ_{probe} denoting the angle between the photolysis and probe polarization directions with respect to the recoil direction; β is the dissociation anisotropy parameter, A_0^k are the photofragment polarization parameters and $P_k(\cos\theta)$, the k-th Legendre polynomial.

When using linearly polarized pump and probe laser pulses, the experiment is not sensitive to photofragment orientation and the k index takes only even values. In addition, for $(2 + 1)$ REMPI detection, as used in this work, the expansion is truncated at $k = 4$ and eq 1 should be expressed as an expansion of Legendre polynomials up to $k = 6$[34,35]

$$I(\theta)^{FG} = 1 + \beta_2^{FG} P_2(\cos\theta) + \beta_4^{FG} P_4(\cos\theta) + \beta_6^{FG} P_6(\cos\theta) \quad (2)$$

where F and G denote the photolysis and probe polarization directions, respectively, with respect to the slicing plane XY (perpendicular to the time-of-flight axis Z), and β_k^{FG} are the anisotropy parameters in the laboratory frame. The phenomenological β_k^{FG} parameters comprise all the dynamical and geometrical information on the process. In order to extract the dynamical data, the β_k^{FG} must be transformed into a different set of parameters.

Rakitzis and Zare described the stereodynamics of molecular photodissociation in terms of a set of polarization parameters, the $a_q^k(p)$.[33] In a series of subsequent publications, Rakitzis established useful expressions for different laboratory geometries and dynamical problems;[34] among those, he established the relationship between the laboratory frame anisotropy parameters, β_k, and the molecular frame polarization parameters, $a_q^k(p)$, through the following expressions in terms of $A_q^k(p)$ coefficients

$$\beta_2 N = c\beta + s_2\left\{A_0^2(\text{iso}) + \frac{1}{7}[2A_0^2(\text{aniso}) + cA_1^2 - 2cA_2^2]\right\} + s_4\left\{\frac{1}{21}[6A_0^4(\text{aniso}) + \sqrt{30}\,cA_1^4 + \sqrt{15}\,cA_2^4]\right\} \quad (3a)$$

$$\beta_4 N = s_2\left\{\frac{1}{35}[18A_0^2(\text{aniso}) - 12cA_1^2 + 3cA_2^2]\right\} + s_4\left\{A_0^4(\text{iso}) + \frac{1}{77}[20A_0^4(\text{aniso}) + \sqrt{30}\,cA_1^4 + 6\sqrt{15}\,cA_2^4]\right\} \quad (3b)$$

$$\beta_6 N = s_4\left\{\frac{1}{35}[15A_0^4(\text{aniso}) - 2\sqrt{30}\,cA_1^4 + \sqrt{15}\,cA_2^4]\right\} \quad (3c)$$

where N, proportional to the population, is given by

$$N = 1 + s_2\left\{\frac{1}{5}[A_0^2(\text{aniso}) + cA_1^2 + cA_2^2]\right\} \quad (3d)$$

The s_k are the kth-order sensitivity factors (normalized so that $s_0 = 1$), and c is a constant that can take the values 1 or $-1/2$ for linear or circular polarization of the photolysis laser, respectively; for the work presented here $c = 1$, since only linear polarization of the photolysis laser has been employed. The

https://doi.org/10.1021/acs.jpca.2c05897
J. Phys. Chem. A 2022, 126, 8404−8422

Table 1. Theoretical Vertical Excitation Energies (VEE) at the Franck−Condon (FC) Geometry, Symmetry in C_s, and Transition Dipole Moments (TDM) for Each Axis *X*, *Y*, and *Z*, of the First 36 Spin-Orbit States[a]

state number	VEE (eV)	symmetry	TDM (Debye)	*X*	*Y*	*Z*
1	0	1*A*′	1.30986	0.00000	1.30410	0.12275
2	4.133	1*A*″	0.00613	0.00613	0.00000	0.00000
3	4.133	2*A*′	0.00600	0.00000	0.00108	0.00590
4	4.256	2*A*″	0.11184	0.11184	0.00000	0.00000
5	4.319	3*A*′	0.22751	0.00000	0.07456	0.21495
6	4.584	3*A*″	0.00457	0.00457	0.00000	0.00000
7	4.705	4*A*′	0.12771	0.00000	0.00440	0.12763
8	4.932	5*A*′	0.59943	0.00000	0.17768	0.57249
9	4.948	4*A*″	0.30256	0.30256	0.00000	0.00000
10	5.322	5*A*″	0.01374	0.01374	0.00000	0.00000
11	5.370	6*A*′	0.29829	0.00000	0.07993	0.28738
12	5.408	6*A*″	0.15374	0.15374	0.00000	0.00000
13	5.568	7*A*′	0.21505	0.00000	0.00908	0.21486
14	5.626	7*A*″	0.02479	0.02479	0.00000	0.00000
15	5.641	8*A*′	0.06915	0.00000	0.04068	0.05592
16	6.088	8*A*″	0.09765	0.09765	0.00000	0.00000
17	6.123	9*A*′	1.12145	0.00000	0.01733	1.12132
18	6.362	9*A*″	0.00291	0.00291	0.00000	0.00000
19	6.371	10*A*″	0.02094	0.02094	0.00000	0.00000
20	6.386	10*A*′	0.13551	0.00000	0.00859	0.13524
21	6.964	11*A*′	0.24789	0.00000	0.09803	0.22768
22	6.990	11*A*″	0.00676	0.00676	0.00000	0.00000
23	6.997	12*A*″	0.03406	0.03406	0.00000	0.00000
24	7.010	12*A*′	0.08612	0.00000	0.06370	0.05795
25	7.322	13*A*′	0.66826	0.00000	0.06924	0.66467
26	7.412	13*A*″	0.00253	0.00253	0.00000	0.00000
27	7.425	14*A*′	0.05863	0.00000	0.02062	0.05489
28	7.525	14*A*″	0.03169	0.03169	0.00000	0.00000
29	7.571	15*A*′	0.24548	0.00000	0.03467	0.24302
30	7.578	15*A*″	0.00353	0.00353	0.00000	0.00000
31	7.619	16*A*′	0.28788	0.00000	0.06907	0.27947
32	7.697	16*A*″	0.10122	0.10122	0.00000	0.00000
33	8.041	17*A*′	1.41181	0.00000	0.10479	1.40792
34	8.132	17*A*″	0.00279	0.00279	0.00000	0.00000
35	8.139	18*A*″	0.01123	0.01123	0.00000	0.00000
36	8.157	18*A*′	0.75683	0.00000	0.04372	0.75557

[a]The *X* axis is located perpendicular to the Br−C−I plane, while the *Y* and *Z* axis are in the plane, *Y* being perpendicular to C−Br and pointing roughly between Br and I, and *Z* being parallel to Br−I.

$A_q^k(p)$ coefficients in eqs 3a−3d) are related to the $a_q^k(p)$ parameters and are used to simplify the equations.[b]

Equations 3a−3d constitute the major result of Rakitzis' work[34] (presented as eqs 7a−7d in ref 34) since they lead to various sets of easy-to-handle expressions to analyze the experimental data.[34,36,37]

The $a_q^k(p)$ parameters can be classified into three different groups, i.e., $a_q^k(\parallel)$, $a_q^k(\perp)$, and $a_q^k(\parallel, \perp)$, according to the transition dipole moment of the one-photon excitation process. For a one-photon pure parallel transition (described by $\beta = 2$), $q = 0$, and we shall have only the $a_0^k(\parallel)$ parameters. For a one-photon pure perpendicular transition (described by $\beta = -1$), $q = 0, 2$, and the polarization is described by $a_q^k(\perp)$ parameters. The $a_q^k(\parallel, \perp)$ parameters represent contributions that arise from the interference between parallel and perpendicular transitions. Equations 3a−3d have been transformed by Rakitzis into straightforwardly implementable expressions for pure perpendicular transitions and even for the complicated interference case. To the best of our knowledge, such set of expressions have not been explicitly unraveled for a pure parallel transition, although the $a_q^k(p)$ formalism has been indeed used in several works.[36,37] In the following paragraphs, this gap is straightened out and the equivalent set of equations for parallel transitions (with and without the possibility of interferences from perpendicular transitions) are developed.

For a parallel transition, the $A_q^k(p)$ coefficients are expressed as

$$\begin{aligned} A_0^k(\text{iso}) &= a_0^k(\parallel) \\ A_0^k(\text{aniso}) &= 2a_0^k(\parallel) \\ A_1^k &= \sqrt{\frac{8}{3}}\, Re[a_1^k(\parallel, \perp)] \\ A_2^k &= 0 \end{aligned} \tag{4}$$

https://doi.org/10.1021/acs.jpca.2c05897
J. Phys. Chem. A 2022, 126, 8404−8422

Substitution of eq 4 into eqs 3a−3d results in the following equations

$$\beta_2 N = \beta + s_2\left\{\frac{11}{7}{a_0}^2(\|) + \frac{1}{7}\sqrt{\frac{8}{3}}Re[{a_1}^2(\|,\perp)]\right\} + s_4\left\{\frac{12}{21}{a_0}^4(\|) + 4\sqrt{5}Re[{a_1}^2(\|,\perp)]\right\} \quad (5a)$$

$$\beta_4 N = s_2\left\{\frac{36}{35}{a_0}^2(\|) - 12\sqrt{\frac{8}{3}}Re[{a_1}^2(\|,\perp)]\right\} + s_4\left\{\frac{117}{77}{a_0}^4(\|) + \frac{4}{77}\sqrt{5}Re[{a_1}^4(\|,\perp)]\right\} \quad (5b)$$

$$\beta_6 N = s_4\left\{\frac{10}{11}{a_0}^4(\|) - \frac{8}{33}\sqrt{\frac{8}{3}}Re[{a_1}^4(\|,\perp)]\right\} \quad (5c)$$

$$N = 1 + s_2\left\{\frac{1}{5}\left[2{a_0}^2(\|) + \sqrt{\frac{8}{3}}Re[{a_1}^2(\|,\perp)]\right]\right\} \quad (5d)$$

For experimental results that can be fitted to eq 2 with $\beta_6 = 0$ (as those acquired in the present work), the second order sensitivity parameter, s_4 is equal to 0; the relationship between the measured β_k^{FG} and the alignment parameters β, $a_0^k(\|)$, and $Re[a_1^k(\|,\perp)]$, for the three FG geometries, XX, XZ, and ZX, are given, therefore, by

$$\beta_2^{XX} = \frac{\beta + \frac{s_2}{7}\left\{11{a_0}^2(\|) + \sqrt{\frac{8}{3}}Re[{a_1}^2(\|,\perp)]\right\}}{1 + \frac{s_2}{5}\left\{2{a_0}^2(\|) + \sqrt{\frac{8}{3}}Re[{a_1}^2(\|,\perp)]\right\}} \quad (6a)$$

$$\beta_4^{XX} = \frac{12s_2\left\{\frac{3}{35}{a_0}^2(\|) + \sqrt{\frac{8}{3}}Re[{a_1}^2(\|,\perp)]\right\}}{1 + \frac{s_2}{5}\left\{2{a_0}^2(\|) + \sqrt{\frac{8}{3}}Re[{a_1}^2(\|,\perp)]\right\}} \quad (6b)$$

$$\beta_2^{XZ} = \frac{\beta + s_2{a_0}^2(\|)}{1 + \frac{1}{2}s_2{a_0}^2(\|)} \quad (6c)$$

$$\beta_2^{ZX} = s_2{a_0}^2(\|) \quad (6d)$$

The s_2 coefficient is calculated according to Table 1 in ref 34 (including the long-time-limit hyperfine depolarization coefficient[38] of 10/37) yielding values of −25/74 and 80/333 for $Br(^2P_{3/2})$ and $I(^2P_{3/2})$, respectively.

Description of the Polarization Parameters. The probability of absorption of a photolysis photon by the molecule is proportional to $|\vec{\mu}\cdot\vec{\epsilon}|$, where $\vec{\mu}$ is the transition dipole moment for excitation from the initial electronic state to the final excited state, and $\vec{\epsilon}$ is the polarization direction of the linearly polarized photolysis light. In the absorption step, only those molecules with the axis conveniently oriented with respect to the photolysis electric field are excited, and thus, the product ensemble is produced with a certain degree of alignment along the polarization of the photolysis pulse if the photodissociation process is fast enough. For diatomic or polyatomic molecules with a well-defined molecular axis, parallel or perpendicular transitions can be referred to as the alignment of the molecular axis with respect to the transition dipole moment. The transition dipole moment is aligned along the molecular axis in a parallel transition while in a perpendicular transition it is located perpendicular to the molecular axis. When dissociation is faster than the molecular rotational period—like in a prompt dissociation—the fragments will recoil along the molecular axis, and the dissociation will be well described by the axial recoil limit. In these cases, the parallel or perpendicular character of the electronic transition will be directly reflected by maximum values of the anisotropy parameter. However, in polyatomic molecules with more than one main molecular axis, the dissociating bond might not be completely aligned or antialigned along the polarization direction of the photolysis laser, even for prompt dissociation. This is the case of the CH_2BrI molecule since the presence of two well-defined molecular axes, C−Br and C−I bonds, forming a Br−C−I angle around 114°, leads to transition dipole moments located in the Br−C−I plane, but often at a certain angle of both the C−Br and C−I bonds.[30] Therefore, no correlation can be drawn *a priori* between the transition character and the molecular axis.

For both the $Br(^2P_{3/2})$ and $I(^2P_{3/2})$ atoms, the ${a_0}^2(\|)$ parameter ranges from −0.8 to +0.8,[39] where the maximal positive and negative values would correspond to population of the corresponding atom in exclusively $m_J = \pm 1/2$ and $m_J = \pm 3/2$ states, respectively, with respect to the quantization axes, given by the Br and I atom recoil directions.

For parallel transitions there is no net change in the projection of the total angular momentum onto the bond axis. In a diatomic AB molecule, the preservation of the angular momentum implies that $m_J(A) + m_J(B) = 0$. Determination of the ${a_0}^2(\|)$ polarization parameter for one of the fragments provides, therefore, indirect similar information for the other. On the contrary, in those cases where the coproduct of the atomic fragments is a polyatomic, the angular momentum of both products is conditioned by the rotation of the latest, and no preferential population (alignment) is expected for the atomic species. As discussed in the following sections, any divergence from such expectance would aport significant dynamical information.

Theoretical Method. To shed light into the possible fragmentation pathways of CH_2BrI, high level *ab initio* calculations were performed to compute 1D potential energy curves (PECs) that connect the Franck−Condon region to three possible fragmentation channels: CH_2I + Br, CH_2Br + I, and CH_2 + IBr. All calculations were performed with the MOLPRO package[40] and the ANO-RCC-VQZP basis set was considered. For iodine and bromine, core pseudopotentials of 28 and 10 electrons, respectively, were employed. To obtain the geometries to build the PECs, several relaxed scans have been performed on the ground state at CASPT2 level,[41] where the reaction coordinate is fixed at several distances while the remaining coordinates are optimized. In total, four relaxed scans were performed: one where CH_2Br is relaxed as a function of the C−I distance, R_{CI}, the counterpart where CH_2I is relaxed as a function of the C−Br distance, R_{CBr}, and a roaming mechanism where the Br atom dissociates and strip the I atom to form IBr. Finally, a direct mechanism where the C−X distance is considered as the reaction coordinate, X being the geometrical center between the I and Br atoms. Since CH_2 in its ground state is a triplet state, for the two channels leading to IBr, both singlet and triplet states have been explored at large distances and a progressive transition in the geometries was considered to obtain a smooth ground state PEC. For each fragmentation path, 9 singlet states ($5A'$ and $4A''$) and 9 triplet states ($5A'$ and $4A''$) have then been computed at CASSCF/MRCI level[42] for

https://doi.org/10.1021/acs.jpca.2c05897

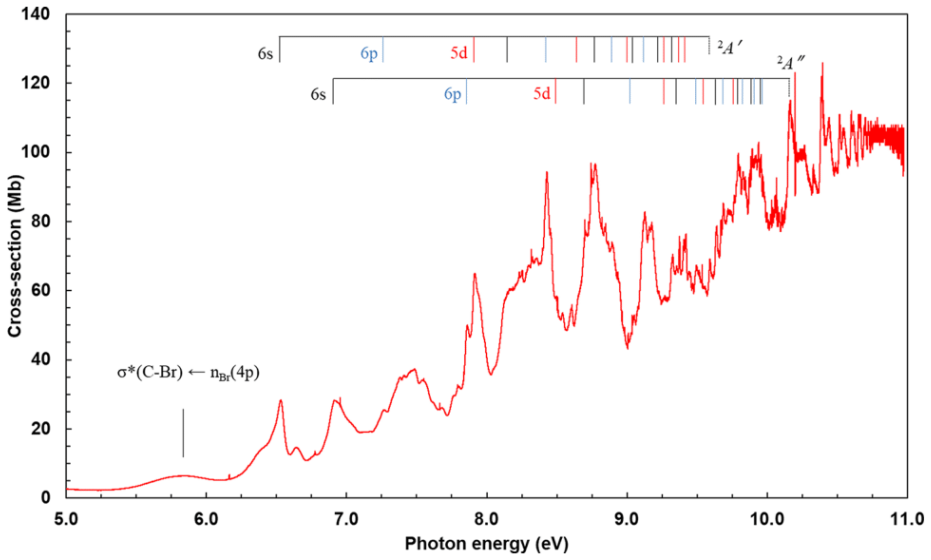

Figure 1. Gas-phase room-temperature high-resolution VUV photoabsorption spectrum of CH_2BrI (red line) in the 5−11 eV photon energy range. The spectrum presents tentative assignments of both valence and Rydberg states (see the text for more details).

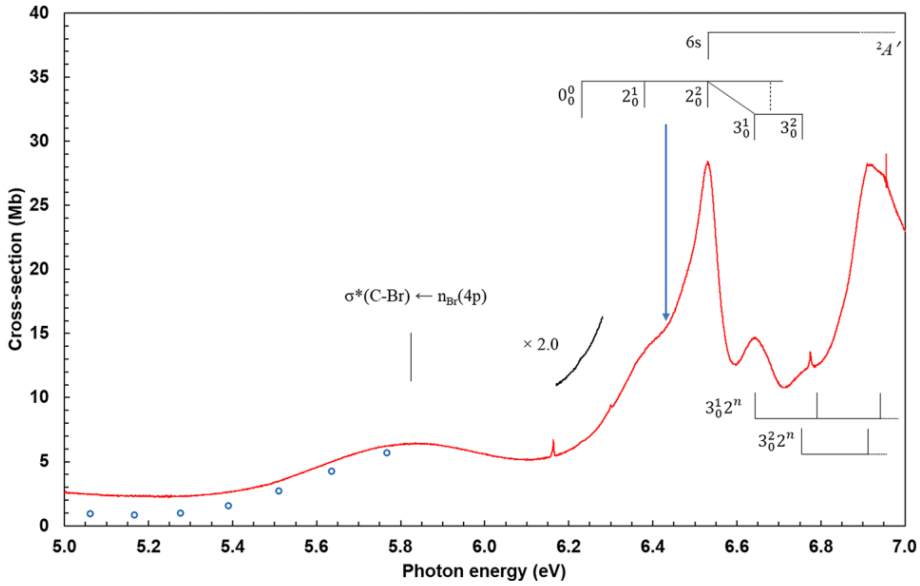

Figure 2. High-resolution VUV photoabsorption spectrum of CH_2BrI (red line) in the 5−7 eV photon energy range. The blue circles correspond to the VUV data of Mössinger et al.[6] The spectrum shows an assignment of both Rydberg states and vibrational levels. The vertical arrow indicates the excitation energy (wavelength), 6.424 eV (193 nm), used in the present photodissociation study. The narrow peaks at 6.163 and 6.774 eV correspond to methyl iodide, while the peak at 6.955 eV to atomic I from photolysis of the molecule (see SI).

approximately 30 geometries. The active space employed to generate the reference configurations consists of 20 electrons in 12 orbitals (9 a' and 3 a''), while 13 a' and 6 a'' orbitals where kept doubly occupied. Finally, spin−orbit matrix elements where calculated from the obtained MRCI electronic wave functions using the Breit−Pauli method implemented in MOLPRO,[43] and the 36 eigenvalues of the full spin−orbit matrix considered in this work were computed.

EXPERIMENTAL RESULTS

High-Resolution VUV Absorption Spectrum. The gas-phase room-temperature high-resolution VUV absorption spectrum of CH_2BrI (photoabsorption cross-section in units of Mb ≡ 10^{-18} cm^2), measured in the 5−11 eV photon energy range, is shown in Figure 1, while an expanded view of the energy region of interest in this work (5−7 eV) is depicted in Figure 2. More detailed sections corresponding to higher photon energies (7−11 eV) along with a detailed description of the identified features is included in the Supporting Information (SI) for the interested reader.

We have adopted the normal mode description and numbering from the vibrational analysis of Lee et al.[44] This includes, in particular, fine structure assignment to the CH_2 scissoring and wagging modes, ν_2' and ν_3', respectively, with ground state energies of 1374 cm^{-1} and 1150 cm^{-1},[7] along with the contribution of C−Br stretching ν_4', C−I stretching ν_5', and Br−C−I bending ν_6' modes, with ground state energies of 616 cm^{-1}, 517 cm^{-1}, and 144 cm^{-1}, respectively. The absorption bands are classified as excitations from the ground state to

https://doi.org/10.1021/acs.jpca.2c05897
J. Phys. Chem. A 2022, 126, 8404−8422

valence states, but mainly with Rydberg character. For the assignments of the vibronic structure, we use the notation X_m^n, with m and n being the initial and final vibrational states, respectively, while X denotes the particular geometric change the molecule undergoes in the photoabsorption process.

The 5−7 eV Photon Energy Range. The first absorption band, the so-called *A*-band, lying in the 4−5 eV energy range is assigned to the $\sigma^*(C-I) \leftarrow n_I(5p)$ transition (not shown in the spectra of Figures 1 and 2). A first weak structureless band peaking at 5.837 eV (~212 nm) is observed in Figures 1 and 2 and assigned to the $\sigma^*(C-Br) \leftarrow n_{Br}(4p)$ transition (*i.e.*, $9A' \leftarrow \tilde{X}^1A'$ based on the high-level *ab initio* calculations carried out in the present work—see below). As in our previous work,[21] this band is referred to as the A' band. This band has been previously reported[6,7,10,45−48] where a general agreement is noted for its maximum position, yet the absolute cross-section values in the wavelength range 215−250 nm (5.767−4.959 eV) of Mössinger et al.[6] are 9−35% lower than the present high-resolution data (see Figure 2). Additionally, this band has been also the subject of experimental[7,46,48] and theoretical[10,47,48] photodissociation dynamics studies, with relevant information about the energies of the activated vibrational modes.

The second feature observed peaking at 6.529 eV (~190 nm), with a local cross-section value of 28.2 Mb, can be assigned to the lowest lying 6s Rydberg transition from the iodine nonbonding $n_I(5p)$ lone pair converging to the lowest ionic−electronic ground state ($2A'$). In agreement with the present calculations (see below), a partially overlapped valence transition is observed with its vertical value tentatively placed also at 6.529 eV. We have assigned this to the $\sigma^*(C-Br) \leftarrow n_{Br}(4p)$ (*i.e.*, $13A' \leftarrow \tilde{X}^1A'$) transition. The 0_0^0 origin band is tentatively assigned at 6.23(2) eV. The modest fine structure observed is attributed to vibrational excitation as identified in Table S3 of the ESI. A 2_0^n (n = 0−3) progression of the CH_2 scissoring mode, ν_2', is identified with an average spacing of 0.154 eV (1242 cm^{-1}), although a contribution from the CH_2 wagging mode, ν_3', is also discernible. Notice that excitation in the present work is at 193 nm (6.424 eV), as indicated by the vertical arrow in Figure 2, therefore at about the 2_0^1 vibronic band of the $13A' \leftarrow \tilde{X}^1A'$ transition.

Above 7 eV Photon Energy Range. The photoabsorption spectrum above 7 eV displays prominent Rydberg features (see Figure 1), while based on the present calculations, a valence transition is predicted at 8.04 eV. The experimental vertical value is at 7.488 eV (with a cross-section of 37.2 Mb), in reasonable agreement with the calculation given the level of accuracy used (±0.5 eV), and is assigned to the $17A' \leftarrow \tilde{X}^1A'$ transition. Given the background contribution to the absorption band, the nature of this transition is reminiscent of a dissociative character. We are not aware of any other information in the literature to compare with the present finding. The lowest-lying Rydberg series is assigned to the promotion of iodine nonbonding $n_I(5p)$ lone pair electron to an *ns* Rydberg orbital, with the first member for n = 6 at 6.529 eV and an effective quantum number n^* = 2.11 while extending up to n = 11. Similar *np* and *nd* Rydberg series converging to the lowest cationic electronic state, $2A'$, lying at 9.5944 eV[44] are also identified, with the first members for n = 6 and n = 5, respectively, lying at 7.27(4) eV and 7.922 eV (with n^* = 2.42 and 2.85). The modest fine structure observed for the first members of the three Rydberg series can be assigned to different vibrational modes, i.e., CH_2 scissoring and wagging, ν_2' and ν_3', C−Br stretching ν_4' and C−I stretching ν_5' modes. More detailed information, including a full assignment, can be found in the SI. Also *ns*, *np*, and *nd* Rydberg series converging to the second ionization energy at 10.1644 eV,[49] corresponding to the $2A''$ ionic state, have been identified. The first members of these series are associated with features at 6.913 eV (n^* = 2.05), 7.866 eV (n^* = 2.43) and 8.49(9) eV (n^* = 2.86). The present Rydberg (tentative) assignments have been made up to n = 12 for the *ns* and *np* series (see the SI for detailed information). The observed fine structure in these absorption peaks has been similarly assigned to vibrational excitation involving the CH_2 scissoring ν_2', the CH_2 wagging ν_3', the C−Br stretching ν_4', the C−I stretching ν_5', and the Br−C−I bending ν_6' modes.

Photodissociation Dynamics and Atomic Photofragment Alignment. *Br*($^2P_{1/2}$) and I*($^2P_{1/2}$) Ion Images.* Figure 3 shows 2D slice ion images of Br*($^2P_{1/2}$) and I*($^2P_{1/2}$) produced in the photodissociation of CH_2BrI at 193 nm. Three different features can be distinguished in the Br*($^2P_{1/2}$) image, namely, a central intense oval-shaped disc, assigned to multiphoton ionization (MPI) and statistical decay, and two highly anisotropic rings of different radii. A careful inspection of the I*($^2P_{1/2}$) image, whose overall signal is significantly lower than that of Br*($^2P_{1/2}$), brings to light three features, quite similar to those observed for the Br* fragment. Since in the original I*($^2P_{1/2}$) image, the outermost contribution was highly obscured by the intense and unstructured central blot to obtain a good visualization of the rings, the intensity of the external feature has been amplified with respect to the central one by a factor of 2. The polarization of the pump and probe lasers were set mutually parallel and with respect to the detection plane, as indicated by the red arrows on the top right corner of the image (*XX* images).

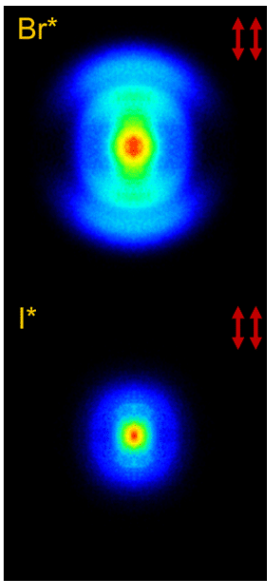

Figure 3. Symmetrized slice ion images of the Br*($^2P_{1/2}$) and I*($^2P_{1/2}$) fragments produced in the photodissociation of CH_2BrI at excitation wavelength λ = 193 nm, detected by (2 + 1) REMPI at 262.45 and 305.49 nm, respectively. The external ring in the I* image has been increased by a factor of 2 with respect to the central feature for better visualization. The red arrows show the polarization of the pump (left) and probe (right) lasers.

https://doi.org/10.1021/acs.jpca.2c05897
J. Phys. Chem. A 2022, 126, 8404−8422

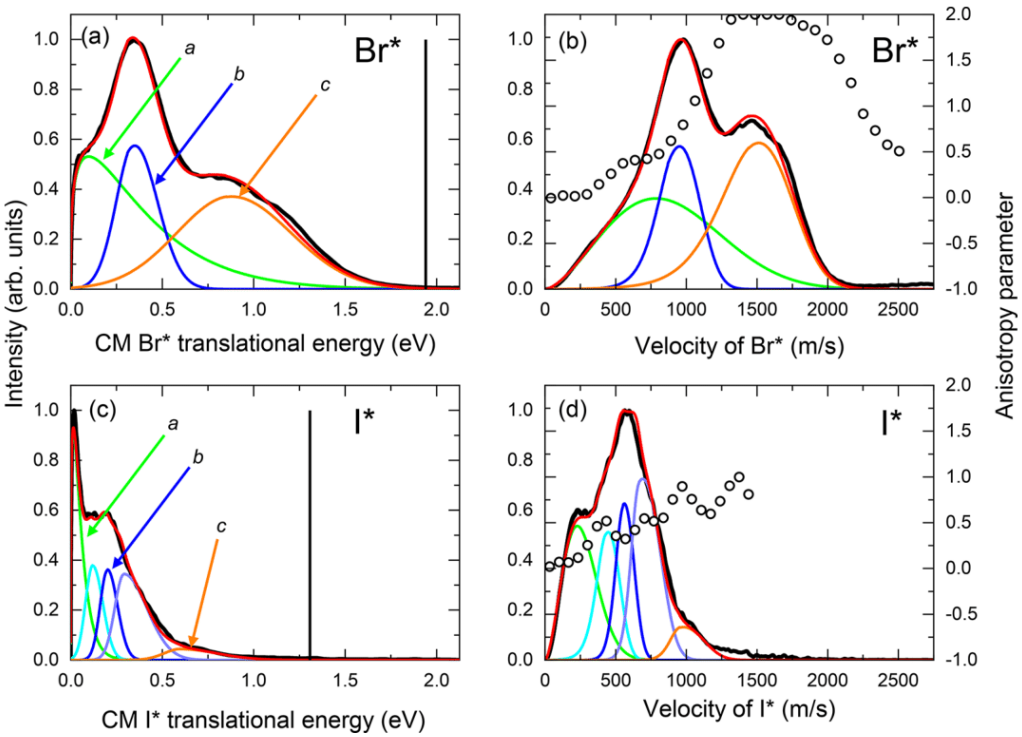

Figure 4. (a, b) Center-of-mass (CM) translational energy and velocity distributions for the Br*($^2P_{1/2}$) fragment, respectively, represented by the black curve. The color lines correspond to three contributions obtained in the deconvolution—labeled *a*, *b* and *c*—wherein the red curve comprises the overall fit. (c, d) The black curve corresponds to the experimental translational energy and velocity distributions for the I*($^2P_{1/2}$) fragment, while the green, blue-ish, and orange represent the different *a*, *b*, and *c* contributions. The black vertical lines in the energy distributions represent the available energy for the main dissociation process. The black circles in the velocity distributions correspond to the anisotropy β parameter.

The translational energy distributions (TEDs) obtained from the angular integration of the Br*($^2P_{1/2}$) and I*($^2P_{1/2}$) slice images are presented in Figure 4a and 4c. Both distributions depict reasonably well the features observed in the images, *i.e.*, a very low-recoil peak—a shoulder in the case of Br*—a central peak (which will be later on attributed to prompt C−X bond breaking) and a high kinetic energy contribution, the later one concealed in the tail of the I* TED. Despite the similarities between both distributions for the Br*($^2P_{1/2}$) and I*($^2P_{1/2}$) photofragments, the differences in intensity and in shape are evident. With the aim of identifying the possible channels and the underlying dynamics giving rise to the observed features, the experimental profiles have been fitted to a series of mathematical functions.

The low-recoil peak was fitted to a simplified Muckerman distribution[50]

$$I(E_k) = AE_k^i(1 - E_k)^j \quad (7)$$

represented by green lines in Figure 4a and 4c, where E_k is the translational (kinetic) energy of the fragment, and *A*, *i*, and *j* are fitting parameters that do not contain any specific physical meaning. Muckerman functions are widely used to reproduce Boltzmann-like profiles, *i.e.*, contributions from statistical processes.[50] Gaussian functions were used, on the other hand, to fit the other two contributions (blue-ish and orange lines in Figure 4a and 4c). The broad and unstructured peaks in the Br* TED (Figure 4a) were satisfactorily reproduced by two Gaussian distributions peaking at 0.31 eV (full-width-half-maximum, fwhm = 0.23 eV) and 0.88 eV (fwhm = 0.63 eV), respectively; the Muckerman function for the low-recoil contribution peaked at ∼0.1 eV.

Moreover, as in the case of Br*, a Muckerman and a Gaussian function were used to reproduce the low and high energy contributions of the I* TED (Figure 4c), located at <0.1 and 0.6 eV (fwhm = 0.29 eV), respectively, corresponding to the central and outermost contributions of the I* image (Figure 3). The central contribution in the TED of the I* product, however, appears as a plateau which shows a clear structure reminiscent of vibrational activity in the CH_2Br coproduct; a set of three Gaussians were tentatively used to reproduce the observed structure.

For the sake of clarity, the slow-recoil, the intense middle and the fast contributions were labeled *a*, *b*, and *c*, respectively. The deconvolution analysis of the Br* and I* distributions into three different components, as described above, is amply justified by three relevant arguments. First, the results depicted in Figure 4 are similarly reproduced when certain experimental conditions, such as the laser power and the temperature of the molecular beam, were varied; second, these three contributions have been previously reported at other excitation wavelengths by different authors, including our previous work on the CH_2BrI photodissociation from the *A* and *A*′ bands;[21] third, the measured photofragment polarization discussed hereafter supports the existence of the three contributions.

Through radial integration of the images shown in Figure 3, the corresponding angular distributions (not shown in this work) were obtained. The subsequent analysis using eq 1 produces the speed-dependent anisotropy β parameter shown in Figure 4b and 4d. From the evolution of the β parameter with the velocity (v) of the fragment, the existence of three dynamical regions can be presumed, corroborating the deconvolution analysis presented previously. For the Br* fragment, $\beta(v)$ can be

https://doi.org/10.1021/acs.jpca.2c05897
J. Phys. Chem. A 2022, 126, 8404−8422

visualized as a step function, showing quite clearly three dynamical regions. At low Br* velocities, the anisotropy parameter takes values close to zero; at velocities ∼500 m/s, β increases abruptly up to $\beta \simeq 0.5$. The second plateau lasts until v ∼ 1100 m/s where a second sudden change takes the anisotropy parameter to $\beta = 2$, the maximum value for a pure parallel transition. The following decay is due to the signal intensity decrease. It must be warned that neither the frontiers where the change is produced, nor the values obtained for the anisotropy parameter should be taken as absolute references. Clearly, the overlap between the three contributions to the overall process must alter both numerical results. A strong confirmation of three dynamical regions and relatable valuable information can be extracted nevertheless, as it will be discussed in following sections.

A similar, although somehow more complicated picture can be extracted from Figure 4d, corresponding to the I* fragment. Impressively, the differences in the behavior of the anisotropy parameter in Figure 4d with respect to that observed in Figure 4b can be straightforwardly related to the differences observed both in nature and ratio of the deconvolution analysis. In the velocity region dominated by the low-recoil component (a contribution), the β parameter takes values close to zero. At velocities ∼500 m/s, the value increases but, instead of reaching a plateau, the value oscillates between $\beta \sim 0.3$ and 0.6; it is not a coincidence that the velocity distribution—or the TED, by all means—in this region (b component) shows a vibrational-like structure and ought to be fitted using a set of three Gaussian functions. For velocities above ∼1000 m/s, the anisotropy parameter increases to a maximum value of $\beta \sim 1$, although the oscillatory behavior persists. Wether the reduced value of β should be related to the nature of contribution c or to the branching ratio between the b and c components, will be later on discussed in detail. It must be mentioned in this moment, however, that the results obtained for the $I(^2P_{3/2})$ species will cause a partial reinterpretation of the deconvolution analysis performed for the $I^*(^2P_{1/2})$ product.

Br($^2P_{3/2}$) and I($^2P_{3/2}$) Ion Images. Figures 5 and 6 show the 2D slice images and the corresponding translational energy distributions for the $Br(^2P_{3/2})$ and $I(^2P_{3/2})$ fragments produced in the photodissociation of CH_2BrI at 193 nm. Since the $Br(^2P_{3/2})$ and $I(^2P_{3/2})$ atoms may show polarization effects, as discussed later, images in the four *XX*, *XZ*, *ZX*, and *ZZ* configurations were acquired. The direction of the pump and probe laser polarizations is indicated in each image by red arrows (parallel polarization) and dots and circles (perpendicular polarization) on the top right corner.

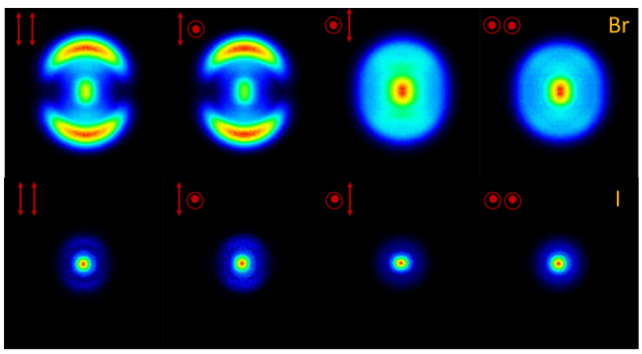

Figure 5. Symmetrized slice ion images of the $Br(^2P_{3/2})$ and $I(^2P_{3/2})$ fragments produced in the photodissociation of CH_2BrI at excitation wavelength λ = 193 nm, detected by (2 + 1) REMPI at 250.35 and 304.58 nm, respectively. The external ring in the I images has been increased by a factor of 3 with respect to the central feature. The red arrows show the polarization of the pump (left) and probe (right) lasers.

Only two different features can be distinguished in the $Br(^2P_{3/2})$ and $I(^2P_{3/2})$ images; specifically, a highly anisotropic ring and a central intense low-recoil disc assigned to MPI and statistical processes. As in the case of Br* and I*, the overall signal recorded for the iodine atom is significantly lower than that of the bromine atom. Despite the qualitative coincidences, the images of the I fragment differ strongly from those obtained for the Br atom both in size and in the intensity ratio of the two features. The color pattern in the $I(^2P_{3/2})$ images was altered, as before, to enhance the visualization of the external ring, whose intensity was multiplied by a factor of 3 with respect to the central feature. The ring displays parallel anisotropy, although not as strongly as in the bromine case.

The TEDs shown in Figure 6a and 6c reproduce the observed features in the images, although the existence of an additional contribution in both cases can be guessed. As in the case of Br* and I*, a deconvolution analysis was carried out to uncover all possible contributions to the experimental profile. The analysis provides, indeed, three contributions for both fragments. The slow-recoil contribution, peaking at less than 0.1 eV is clearly visible in both cases—constituting the dominant feature in the I TED—and is well reproduced by a Muckerman function. The intense and broad peak at 0.80 eV (fwhm = 0.48 eV), which dominates the TED of the Br atom shows a glimpse of a minor contribution at lower kinetic energy values. The analysis shows that the TED is well reproduced by two Gaussian functions (besides the mentioned Muckerman function), and allows us to locate the middle contribution at 0.35 eV with a fwhm of 0.38 eV. The I TED shows a hint as well of a third contribution, this time located at higher kinetic energy values than that of the main feature of the profile. The analysis shows, once more, that the TED profile is well reproduced by three contributions, the said Muckerman function (a contribution) and two Gaussian functions, that is to say, a middle one located at 0.26 with a fwhm of 0.24 eV (b contribution) and week higher-recoil peak located at 0.60 eV with a fwhm of 0.30 eV (c contribution).

According to eq 6a, the analysis of the photofragment polarization for the $Br(^2P_{3/2})$ and $I(^2P_{3/2})$ fragments requires the additional measurement of the *XZ* and *ZX* images. The images acquired at the various configurations of the pump and probe laser polarizations comprise different amount and type of information. The *XX* image, for instance, gathers all the data derived from both the dissociation and detection processes; the polarization of the probe laser in the *XZ* images is aligned perpendicular to the detection plane and, therefore, the information relative to the detection of the fragments is lost. The *ZX* image, on the other hand, cannot be related to the anisotropy of the dissociation step. A preliminary inspection of the images, might, therefore, shed some light onto the photofragment polarization in the form of atomic photofragment alignment.

The *XX* and *XZ* images recorded for the Br fragment present quite similar shapes with no observable differences between them. This fact suggests a minor photofragment alignment or, in other words, that the stereodynamics of the photodecomposition process is governed by the dissociation anisotropy. The differences between the *XX* and *ZX* images should inform on the photofragment polarization evinced by the detection process. In

https://doi.org/10.1021/acs.jpca.2c05897
J. Phys. Chem. A 2022, 126, 8404−8422

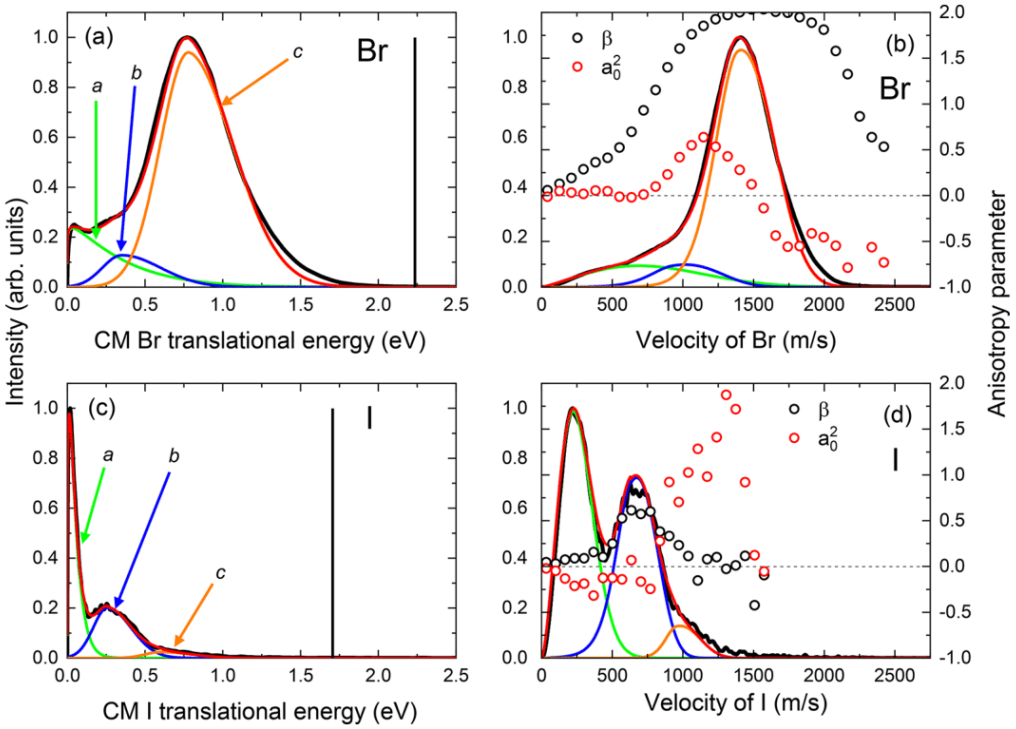

Figure 6. (a, c) Center-of-mass (CM) translational energy distributions for the Br($^2P_{3/2}$) and I($^2P_{3/2}$) fragments, respectively, represented by black curves. The green, blue, and orange lines correspond to three contributions obtained in the deconvolution analysis—labeled, respectively, *a*, *b*, and *c*—while the red curve is the overall fit. (b, d) Velocity distributions of the same fragments. The black circles correspond to the anisotropy β parameter, while the red circles correspond to the $a_0^2(\|)$ alignment parameter. The green, blue, and orange lines correspond to three different contributions in the photodissociation process, while the red curve is the overall fit.

those cases, such as the current one, where the dissociation anisotropy dominates the stereodynamics, the specificity of the *ZX* image becomes more evident when compared to the *ZZ* image. The *ZZ* image does not comprise any dynamical information, and therefore, any anisotropic deviation must be integrated in the apparatus function. Consequently, if no photofragment polarization were expected, the *ZX* and *ZZ* images should look alike. The differences observed, explicitly, a weak anisotropic feature between the central spot and the outer ring, suggest that minor but non-negligible photofragment polarization is manifested in the detection process.

As before, the comparison between the iodine *XX* and *XZ* images emphasizes the predominance of the dissociation process on the photofragment polarization. The strong similitude between the *ZX* and *ZZ* images suggests, on the other hand, that there are no polarization effects that could be brought to the surface by the detection process.

Through radial integration of the images shown in Figure 5, the corresponding angular distributions (not shown in this work) were obtained. The subsequent analysis using eq 6aresults in the speed-dependent anisotropy β and alignment $a_0^2(\|)$ parameters shown in Figure 6b and 6d. From the evolution of β with the velocity of the fragment, the existence of three dynamical regions is confirmed. It must be stated that the analysis included the $Re[a_1^2(\|, \perp)]$ parameter, but no deviations from $Re[a_1^2(\|, \perp)] \approx 0$ were found.

The behavior of the β parameter throughout the Br profile turns out to be highly conditioned by the predominant *c* contribution and obscures the anisotropy values anticipated for the other two contributions. On the light shed by the analysis performed for the Br* fragment, however, some information can be extracted. In the low recoil velocity region ($v \leq 500$ ms^{-1}), the β parameter increases almost linearly from zero to ~0.4. From 500 to 1500 ms^{-1}, the anisotropy increases up to $\beta = 2$, in coincidence with the maximum of the distribution. The wide overlap between the *a* and *b* contributions distorts the step-like behavior observed for the Br* fragment, but it might safely be concluded a $\beta \simeq 0$ for the low-recoil component and a β somewhat higher, closer to 0.5, for the *b* component. The *fast c* contribution shows, as before, the maximum value corresponding to a perpendicular transition.

The variations of the $a_0^2(\|)$ alignment parameter throughout the Br profile can be, on the other hand, clearly associated with the three dynamical regions. For the low-recoil contribution, $a_0^2(\|) = 0$; a maximum value of ~0.7 is obtained at $v \simeq 1250$ ms^{-1}, coincident with the maximum of the *b* contribution, from were, $a_0^2(\|)$ decreases down to ~−0.6. The strong overlap between the *b* and *c* curves suggests that the real value of the $a_0^2(\|)$ parameter corresponding to the *b* contribution must be larger by far than the observed maximum of ~0.7. In addition, the registered change of sign indicates two rather different dynamical sources for the *b* and *c* contributions.

The dependence of the β parameter on the velocity of the I($^2P_{3/2}$) fragment indicates that some similar conclusions are applicable to this case, which can be summarized as follows: At low recoil velocities, the TED is dominated by an isotropic contribution ($\beta = 0$), which is coherent with a stochastic dynamics; in the middle region, the predominant parallel contribution is characterized by a anisotropy value of ≃0.5−0.6. At higher velocities, however, a clear discrepancy with the previous cases reveals and forces, in addition, a partial

https://doi.org/10.1021/acs.jpca.2c05897
J. Phys. Chem. A 2022, 126, 8404−8422

reinterpretation of the analysis performed for the $I^*(^2P_{1/2})$ fragment (see above). The β parameter in the region corresponding to the c contribution of Figure 6d clearly decreases to zero. This fact points toward a different overall dynamics for the source of this component in the $I(^2P_J)$ TEDs than that behind the same component in the $Br(^2P_J)$ (with $J = 3/2$ and $1/2$ for Br/I and Br*/I*, respectively) distributions. Assuming a concomitant dynamics for formation of $I(^2P_{3/2})$ and $I^*(^2P_{1/2})$, the average values of $\beta \sim 0.8$ and the oscillatory behavior observed in the high energy region of Figure 4d suggest a wider b contribution than that originally assumed, which should include the orange Gaussian function, initially interpreted as the third, c contribution. An additional conclusion of this interpretation is a minor or negligible contribution to the I signal, in this case, of the process behind the c component of the TED.

The maximum translational energies—associated with the total available energy, E_{av}—for the dissociation products are represented in panels a and c of Figures 4 and 6 as black vertical bars. The E_{av} values were derived from the energy balance for the photodissociation of CH_2XY (where X and Y represent either halogen atom) in the following way:

$$E_{av} = h\nu - D_0(CH_2X - Y) - E_{SO}(Y) + E_{int}(CH_2XY) \quad (8)$$

where $h\nu$ represents the excitation photon energy; $D_0(CH_2X-Y)$ is the C−Y bond dissociation energy, which takes values of 2.936 and 2.389 eV[8] for $CH_2I(\tilde{X})$−Br and $CH_2Br(\tilde{X})$−I channels, respectively; $E_{SO}(Y)$ is the spin−orbit splitting of the $Br(^2P_J)$ and $I(^2P_J)$ atoms (for I and Br, $E_{SO} = 0$; and $E_{SO}(Br^*) = 0.460$ eV and $E_{SO}(I^*) = 0.943$ eV). The term $E_{int}(CH_2XY)$ corresponds to the internal energy of the parent molecule, which, under molecular beam conditions, might be considered negligible.

THEORETICAL RESULTS

The vertical excitation energies and respective total transition dipole moments (TDM) are presented in Table 1. The TDMs along each axis are also included. The X axis is located perpendicular to the Br−C−I plane, while the Y and Z axis are in the plane, Y being perpendicular to C−Br and pointing roughly between Br and I, and Z being parallel to Br−I. We note that A'' states are characterized as expected by a TDM along the X axis, *i.e.*, perpendicular to the Br−C−I plane, while A' states are associated with TDM components in the Y and Z axis, *i.e.*, in the plane.

The results are in good agreement with recent previous results,[21] although the vertical excitation energies obtained here are somewhat larger, around 0.4 eV above. The present calculations include a larger active space in order to properly describe higher excited states and, in particular, those absorbing around 193 nm, in the third absorption B-band.

The first excited states characterize the A band, where a major absorption into the $5A'$ state is expected along with some contribution of the $4A'$ and $4A''$ states. At higher energies, we note the noticeable excitation of the $9A'$ state, characteristic of the A' band lying around 210 nm. At the highest energies, in particular at 193 nm, major absorption into the $13A'$ state is expected, in agreement with the reported absorption spectrum (see Figure 2).

The potential energy curves (PECs) as a function of the C−Br and C−I distances are depicted in Figures 7 and 8, respectively. The first excited states, in particular the $4A'$, $4A''$, $5A'$, and $5A''$ states, present a highly repulsive shape along the C−I distance (see Figure 8), as expected for the A band, which is related to the C−I bond cleavage.

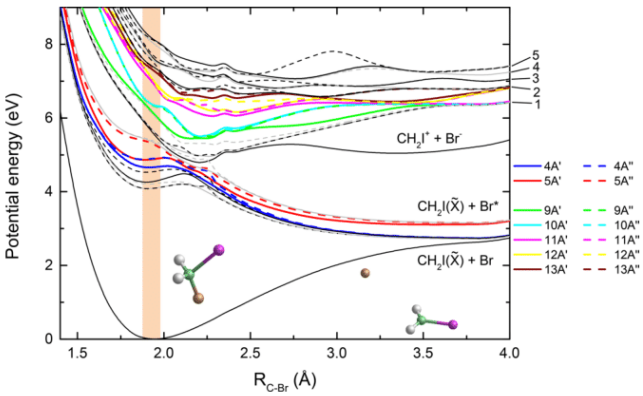

Figure 7. Computed CASSCF/MRCI potential energy curves for the CH_2I + Br channel of CH_2BrI relaxing the CH_2I moiety in the ground state using CASPT2. The solid lines correspond to the A' symmetry levels while the dotted lines correspond to the A'' symmetry. Colored curves correspond to the representative excited states. The shaded area indicates the Franck−Condon region. Numbered asymptotes are as follows: (1) $CH_2I(\tilde{A})$ + Br; (2) $CH_2I(\tilde{A})$ + Br*; (3) $CH_2I(\tilde{B})$ + Br; (4) $CH_2I(\tilde{C})$ + Br; (5) $CH_2I(\tilde{B})$ + Br*.

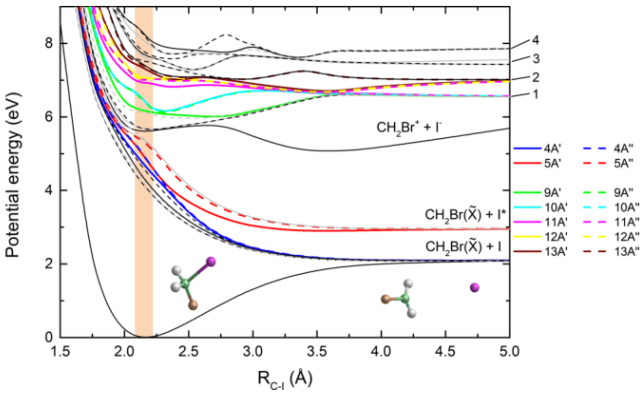

Figure 8. Computed CASSCF/MRCI potential energy curves for the CH_2Br + I/I* channels of CH_2BrI relaxing the CH_2Br moiety in the ground state using CASPT2. The solid lines correspond to the A' symmetry levels while the dotted lines correspond to the A'' symmetry. Colored curves correspond to the representative excited states. The shaded area indicates the Franck−Condon region. Numbered asymptotes are as follows: (1) $CH_2Br(\tilde{A})$ + I; (2) $CH_2Br(\tilde{B})$ + I; (3) $CH_2Br(\tilde{A})$ + I*; (4) $CH_2Br(\tilde{B})$ + I*.

We notice that the present PECs correspond to the adiabatic representation. In Figure 7, a clear avoided crossing is observed between these first excited states ($4A'$, $4A''$, $5A'$, and $5A''$) and higher excited states including the $9A'$. In the diabatic representation, the first excited states, associated with the A-band, are indeed characterized by a bound shape along the C−Br distance while higher excited states, in particular the $9A'$ state, present a purely repulsive shape along this coordinate. This is consistent with the structureless continuum observed in the absorption spectrum associated with the A'-band. At higher energies, the $13A'$ state presents a rather bound shape along both the C−I and C−Br distances, in agreement with the measured absorption spectrum, characterized by well-defined vibrational progressions. In Figure 7, two avoided crossings are clearly observed allowing dissociation: from $13A'$ to $11A'/11A''$

https://doi.org/10.1021/acs.jpca.2c05897
J. Phys. Chem. A 2022, 126, 8404−8422

or $12A'/12A''$ and then into $10A'/9A''$. In contrast, direct elimination of iodine seems unlikely since no avoided crossings are observed in the proximity of the Franck−Condon region.

Figures 9 and 10 show possible pathways to produce CH_2 + IBr, which is a product channel accessible energetically.[8,20]

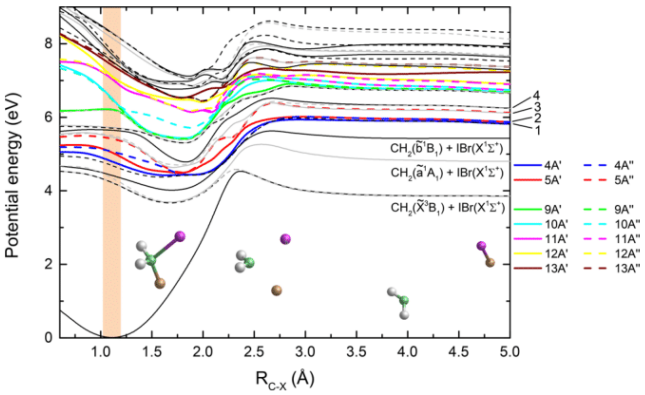

Figure 9. Computed CASSCF/MRCI potential energy curves for the direct formation of CH_2 + IBr, where the C−X distance is considered as the reaction coordinate, X being the geometrical center between the I and Br atoms. The solid lines correspond to the A' symmetry levels while the dotted lines correspond to the A'' symmetry. Colored curves correspond to the representative excited states. The shaded area indicates the Franck−Condon region. Numbered asymptotes are as follows: (1) $CH_2(\tilde{X}^3B_1)$ + IBr($A^3\Pi(2)$); (2) $CH_2(\tilde{X}^3B_1)$ + IBr($A^3\Pi(1)$); (3) $CH_2(\tilde{X}^3B_1)$ + IBr($B^3\Pi(0^+)$); (4) $CH_2(\tilde{X}^3B_1)$ + IBr($C^1\Pi(1)$).

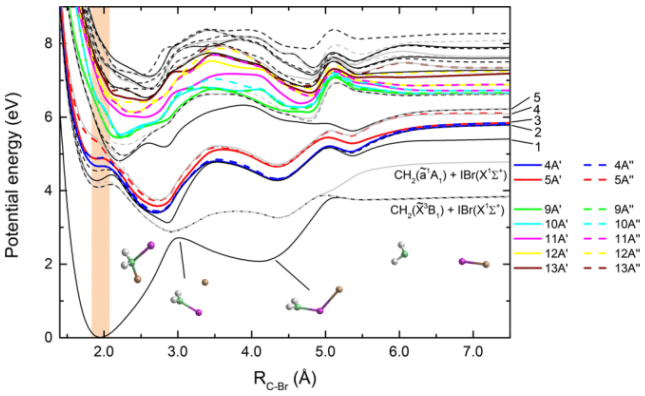

Figure 10. Computed CASSCF/MRCI potential energy curves for the isomerization after elongation of the C−Br bond, yielding CH_2−I−Br and finally breaking to CH_2 + IBr. The solid lines correspond to the A' symmetry levels while the dotted lines correspond to the A'' symmetry. Colored curves correspond to the representative excited states. The shaded area indicates the Franck−Condon region. Numbered asymptotes are as follows: (1) $CH_2(\tilde{b}^1B_1)$ + IBr($X^1\Sigma^+$); (2) $CH_2(\tilde{X}^3B_1)$ + IBr($A^3\Pi(2)$); (3) $CH_2(\tilde{X}^3B_1)$ + IBr($A^3\Pi(1)$); (4) $CH_2(\tilde{X}^3B_1)$ + IBr($B^3\Pi(0^+)$); (5) $CH_2(\tilde{X}^3B_1)$ + IBr($C^1\Pi(1)$).

Figure 9 shows the PECs associated with the symmetric stretch of both C−I and C−Br bonds, in terms of the C−X reaction coordinate, where X is the geometrical center between the I and Br atoms. These PECs provide us with possible pathways for direct dissociation into CH_2 + IBr upon excitation of the parent molecule at 193 nm. As can be seen, even if not completely forbidden, this mechanism is very unlikely since all electronic states show significant barriers in the C−X coordinate, while the elimination of Br is barrierless and straightforward, which explains the very low yields of the IBr and CH_2 fragments observed experimentally.[8,20] However, the symmetric stretch of both bonds may induce electronic relaxation to lower electronic states, in particular to the $7A'$, and may explain a very minor elimination of IBr. In this work we tried to detect $CH_2(\tilde{X}^3B_1)$ by (2 + 1) REMPI at 311.8 nm[51] without success. Although it is predicted in ref.[51] that the REMPI transition is weak and only low vibrational energies of the $CH_2(\tilde{X}^3B_1)$ fragment would be detected, which makes detection of this fragment, if present, rather difficult, it is also clear from the present calculations that production of ground state $CH_2(\tilde{X}^3B_1)$ in correlation with IBr is very unfavorable.

Finally, Figure 10 shows that an isomerization mechanism, where first the Br atom is expelled and then strip the I atom to form CH_2−I−Br and later on CH_2 + IBr, cannot be excluded. However, here again, all electronic states exhibit barriers in the reaction path to reach the CH_2 + IBr channel, while Br-atom elimination is barrierless. Therefore, formation of IBr, even if energetically allowed, appears to be dynamically unfavorable, and if it occurs, it is expected to be very minor and very hard to detect.

■ ANALYSIS AND DISCUSSION

In this section, the main experimental results will be further analyzed and discussed benefiting from the PECs computed as a function of the C−Br and C−I distances. The velocity map images along with the corresponding TEDs show three different contributions for the four fragments.

- Contribution *a*, slow-recoil Boltzmann-type structure which is assigned to multiphoton ionization processes in all cases.
- Contribution *b*, Gaussian-type contribution at intermediate translational energies which is associated with prompt dissociation upon one-photon excitation.
- Contribution *c*, Gaussian-type contribution at larger translational energies which is particularly observed for the Br/Br* fragments. As further discussed below, it can be assigned to secondary dissociation upon a second photon absorption. This contribution is almost indiscernible in the measured TEDs for the I/I* fragments. The anisotropy analysis clearly demonstrates that the contribution observed at larger translational energies for I* fragment, initially labeled *c*, is indeed part of the prompt dissociation process−contribution *b*.

The prompt dissociation mechanisms leading to C−Br and C−I bond cleavage are discussed first, while the secondary dissociation upon a second-photon absorption is then explored.

Direct Dissociation Processes. *The Br(^2P_J) + CH_2I Channels.* The most remarkable information provided by the present work is the similarity between the experimental results obtained at 193 nm (excitation energy of 6.424 eV, assigned to the 2_0^1 vibronic band of the $13A' \leftarrow \tilde{X}^1A'$ transition−see above), with those previously obtained at 266 and 210 nm for dissociation into Br(^2P_J) from the A and A' bands, respectively.[21]

In the mentioned work, the experimental TEDs for both spin−orbit Br(^2P_J) atoms were analyzed and interpreted in terms of three contributions. A low-recoil, Boltzmann-like contribution was assigned to REMPI-assisted multiphoton dissociative ionization. The *middle* contribution (translational energy of 0.25 eV at 266 nm and 0.5 eV at 210 nm), which constituted the main result,[21] was assigned, in the case of

https://doi.org/10.1021/acs.jpca.2c05897
J. Phys. Chem. A 2022, 126, 8404−8422

excitation at 266 nm (A band), to indirect dissociation via absorption to the $5A'$ state and subsequent curve crossing with upper excited dissociative states such as the $9A'$, while upon excitation at 210 nm (A' band), it was attributed to direct dissociation in the $9A'$ excited state. A third broad and faster contribution was tentatively interpreted in terms of secondary dissociation of the CH_2Br fragment upon an additional one-photon absorption. At 210 nm, no $I(^2P_J)$ signals were detected, and the experimental observation of $I(^2P_J)$ at 266 nm were plainly rationalized in terms of a single fast decomposition process through direct absorption and ulterior dissociation through the $5A'$ state for the I fragments, and $5A' \rightarrow 4A'/4A''$ nonadiabatic crossing for the I* fragments.[21]

The prompt dissociation mechanism for both $Br(^2P_J)$ (at 266 and 210 nm) and $I(^2P_J)$ (at 266 nm) species were characterized by a large vibrational and rotational excitation in the polyatomic coproduct, with no thermal distribution of rotational states. In the corresponding translational energy distributions, such energy partitioning is revealed by a significant shift between the rise of the distributions and the available energy. The observed energy distribution was explained in terms of the soft impulsive model, developed by Bush and Wilson[52] and improved by Butler and co-workers.[53] The soft impulsive model predicts the energy partitioning among the different degrees-of-freedom (DOF) of the products of a photodissociation process interceded by a high repulsive electronic surface. The CH_2BrI, in particular, is well described by the soft radical version of the model, where the majority of the available energy (~50%) is transformed into rotational excitation of the CH_2Br or CH_2I fragments;[52,53] the energy channeled into translation adds up to ~20% of the available energy and the remaining ~30% should be transformed into vibrational excitation of the polyatomic fragments. This was confirmed by high-level *ab initio* electronic structure calculations and full dimension on-the-fly trajectory calculations including surface hoping,[22] where an *anchor* effect due to the remaining halogen atom in the dissociating parent molecule imparts significant rotational motion and leads to a remarkable rotational energy of the nascent cofragment.

It should be noticed that the fraction of the available energy transferred into the vibrational modes of the polyatomic products is not explicitly predicted by the soft impulsive model. The vibrational activity of the products would be associated with the geometrical changes leading the ground parent molecule to the final configuration of the major polyatomic fragments. In the present case, for instance, the geometry of the CH_2BrI in the ground state is pseudotetrahedral—with angles differing from the theoretical 109.5° of the sp^3 hybridization of the carbon atom—while the CH_2X is fairly planar. The departure of the heavy halogen atom imprints a large torque and momentum to the CH_2X moiety which is, in turn, transformed into rotational and vibrational activity, respectively.[21,22]

The soft impulsive model describes quite accurately the contribution b observed in the $Br(^2P_J)$ TEDs shown in Figures 4 and 6, which is safely assigned to a prompt dissociation mechanism along a repulsive surface. Figures 4a and 6a include the vertical bars corresponding to the available energy obtained for the dissociation of CH_2BrI yielding CH_2I products in the $\tilde{X}$ ground state. The reference is located at significantly higher energies than the corresponding dissociation feature. Fast decomposition processes associated with prompt bond-breaking are commonly characterized by narrow translational energy distributions placed at energies slightly above the available energy reference. A large shift between the rise of the distributions and the maximum total available energy indicates that a substantial amount of the energy provided by the photon is communicated as internal energy of the photoproducts. The calculation of the fraction of the available energy channeled into internal DOF of the photofragments, f_{int}, for the prompt dissociation feature, provides values of 0.84 for both $Br(^2P_J)$ fragments, *i.e.*, ~1.2 higher than those obtained at longer wavelengths.[21] In all cases, the dissociation step involves a significant geometrical change of the CH_2I moiety, from distorted pyramidal in the ground and excited states to quasi-planar in the asymptotic dissociative limit (ground state CH_2I ($\tilde{X}$) radicals). The source of the contrast in the energy partitioning at the different dissociation wavelengths must be found in either the excitation step or in the adiabatic passage toward the asymptotic dissociation limit.

As discussed above, absorption at 193 nm takes the parent molecule to the bound $13A'$ state, where dissociation must occur through predissociation of any repulsive state correlating with CH_2I and $Br(^2P_J)$ products. The entanglement of curves which compose the adiabatic picture shown in Figure 7 might complicate the visualization of the decomposition process. It must be considered, however, that certain vibrational activity in the ground CH_2BrI species should most probably assist the absorption. Vibrational excitation in the parent molecule not only enhances the transition probabilities in the Franck–Condon (FC) region but also alters the excited state landscape, bending the symmetry and enabling nonadiabatic transitions between the PECs. Having such prospect in mind, fast decomposition pathways of the excited CH_2BrI can be visualized. Tentatively, the $13A'$ state might proceed successively through two curve crossings via $11A'/11A''$ or $12A'/12A''$, leading to direct dissociation through the $10A'/9A''$ toward the asymptotic CH_2I + Br and CH_2I + Br* limits, respectively. The proposed dissociation picture viewed in light of the soft impulsive model rationalizes the observed experimental features. The excited $13A'$ state is characterized by a CH_2I conformation close to that of the asymptotic limit (*i.e.*, with a Br–C–R angle and C–Br distance substantially different from those of the ground state). At 193 nm excitation, therefore, the geometrical change involved in the process occurs in the excitation step. Once in the excited state, prompt dissociation takes place as discussed above, and the energy accumulated in the distorted CH_2BrI is transferred as momentum (vibration) and torque (rotation) to the internal DOF of the CH_2I moiety.

At 266 nm excitation, CH_2BrI is promoted to the $5A'$ state, while at 210 nm it is excited to the $9A'$ state.[21] A close inspection of Figure 7 (also Figure 8 of ref 21) shows that excitation between 4.66 and 5.90 eV (266–210 nm) leads the parent molecule to a set of curves with a shallow well in the FC region. As such, the excitation step becomes less restricted by geometrical impositions than at 193 nm excitation; in other words, at 266 and 210 nm, the rather wide FC region covers a large range of C–Br distances and CH_2BrI geometries in the excited state. With an accommodated configuration of the excited CH_2BrI, the torque and momentum generated in the departure of the halogen atom would be, consequently, reduced.

The transition from the ground state to the excited $13A'$ state possesses parallel character and, consequently, a value close to the maximum of $\beta = 2$ should be expected for prompt dissociation (within the axial recoil limit). The mechanism described for contribution b involves adiabatic and nonadiabatic

https://doi.org/10.1021/acs.jpca.2c05897
J. Phys. Chem. A 2022, 126, 8404–8422

transitions between different potential energy curves. The geometrical demands of each passing deviate the recoil of the fragments from the axial limit, resulting in a reduced value for the anisotropy parameter.

The $a_0^2(\|)$ polarization parameter takes a value of ~0.8 for the *b* contribution (see Figure 6). The maximal values indicate that the $Br(^2P_{3/2})$ is exclusively populated in the $m_J = \pm 3/2$ states. Such result turns out to be exceptional if we consider that Br atom's cofragment is a polyatomic radical with high rotational content. The alignment of the $Br(^2P_{3/2})$ atom implies that the projection of the CH_2I rotational angular momentum—or, for all intents and purposes, the rotational angular momentum itself—is greatly constrained along the recoil direction. In light of the soft impulsive model, this constraint implies that the CH_2I fragment does not scramble isotropically; instead, the rotational angular momentum presents a narrow distribution of rotational states, strongly aligned along the recoil direction. The TED associated with a rotational distribution as the one previously described should not cover a broad range of internal energies and would be far from the available energy reference. The *b* component of the Br TED clearly matches those requirements.

The $I(^2P_J)$ + CH_2Br Channels. The TEDs of the $I(^2P_J)$ products present similar qualitative patterns than those of $Br(^2P_J)$, although differ significantly in certain relevant aspects. First of all, the C−I channel is closed at 210 nm excitation and reappears at 193 nm. Second, the TEDs reported at 266 nm show a single contribution—associated with the prompt dissociation mechanism—while at 193 nm the TEDs are qualitatively similar to those obtained for the $Br(^2P_J)$ species. The f_{int} values increase from ~0.65 at 266 nm to 0.85 at 193 nm for both $I(^2P_J)$ fragments, which supports the idea that the photodecomposition of CH_2BrI into $CH_2Br + I(^2P_J)$ and $CH_2I + Br(^2P_J)$ is ruled by a similar dynamics, and can be rationalized through the soft impulsive model explained in the previous paragraphs.

The vibrational-like structure observed for the prompt bond dissociation featured in the $I^*(^2P_{1/2})$ TED (Figure 6) deserves some further explanation. As discussed for the $Br(^2P_J)$ species, absorption at 193 nm takes the parent molecule to the bound $13A'$ state, where dissociation must occur, in this case, through fast internal conversion to lower excited states and further decomposition onto a repulsive surface (see Figure 8); predissociation through any repulsive state correlating with CH_2Br and $I(^2P_J)$ products seems somehow unreliable since, in contrast to the classical predissociation picture—valid for the $CH_2I + Br(^2P_J)$ channel—where the curve crossing takes place at bond distances close to that of the equilibrium (minima of the PECs), in the current situation the coupling should happen in the steep part of the curves, *i.e.*, far from the FC region. Assuming, therefore, fast internal conversion to a lower state and further dissociation, the vibrational-like structure observed for the $CH_2Br + I^*(^2P_{1/2})$ channel tags the quasi-bound $6A'$ state as the main candidate for the dissociative PEC. The vibrationally assisted diabatic coupling between bound states generates dissociative CH_2Br—I species excited in specific vibrational modes—those mediating in the diabatic coupling—which would unfold in the CH_2Br product. The $CH_2Br + I(^2P_{3/2})$ channel, with no participation of any dissociative-bound state, will show no vibrational structure, emulating the $CH_2I + Br(^2P_J)$ dissociation channels. The proposed dissociation picture explains the observed experimental features, in particular the f_{int} values, in light of the soft impulsive model, in a similar fashion than for the $Br(^2P_J)$ products.

The anisotropy analysis for the $I^*(^2P_{1/2})$ fragment can be drawn in similar terms of those employed for the $Br(^2P_J)$ products. In short, the difference between the experimental anisotropy value, $\beta \simeq 0.8$, and the maximum value of $\beta = 2$ is rationalized in terms of the orientation of the transition dipole moment with respect to the C-I bond as well as of the geometrical changes imposed by the different curve crossings that the molecule undergo in the decomposition pathway. The experimental values for the anisotropy parameter with regard to production of $I(^2P_{3/2})$ atoms show, however, an oscillating increasing tendency along the velocity region of the *b* component, with a maximum value of $\beta \simeq 1$ and a minimum value of $\beta \simeq 0.5$. The variation should be better understood if considered from right to left in the TED. The high energy limit of the distribution, where $\beta \simeq 1$, correlates with CH_2Br fragments with moderate internal energy, *i.e.*, with fragments which had spent less time wandering around the PECs mesh. Since the lost of anisotropy is associated with internal conversion processes, the said fragments will present higher β values. As the kinetic energy is reduced, the available energy transfer into internal DOF of the radical would increase, in parallel to the lost of anisotropy. Remarkably, the oscillations are associated with the vibrational coupling: A vibrational match would generate a fast curve transfer and a subsequent relative small reduction of lost anisotropy.

The $a_0^2(\|)$ polarization parameter takes a value of ~0 for contribution *b* in the TED of Figure 6. Following the discussion developed for the $Br(^2P_{3/2})$ photofragment, the value reported here indicates no preference of the angular momentum along the recoil direction, a fact that is associated with a broad and unconstrained CH_2Br rotational distribution. The momentum imparted by the I atom during the cleavage is not aligned with respect to any molecular axis, and as a result, the radical product rotates freely around the recoil direction. The corresponding TED shows a rather broad profile (blue and orange lines in Figure 6), in particular, when compared with the same component in the $Br(^2P_{3/2})$ profile.

Branching Ratios, Photofragment Polarization, and Secondary Dissociation. Undoubtedly, the most remarkable differences between the TEDs displayed in Figures 4 and 6 are the branching ratios between the three contributions. The slow-recoil contribution, which is significant for the $Br(^2P_J)$ species becomes particularly intense and strongly dominant for the $I^*(^2P_{1/2})$ and $I(^2P_{3/2})$ products, respectively. The shape of the distribution and the associated anisotropy suggest a multi-photon ionization process, which, in the $I(^2P_J)$ case should be assisted by a resonant excited state, enhancing the absorption of the laser radiation. An additional explanation should be considered, however. Boltzmann distributions in photodissociation processes are usually associated with slow internal conversion of the excited parent molecule to the ground state, where thermal dissociation should occur. The randomization of energy results in distributions characterized by little translational energy. The large branching ratio observed for the $I(^2P_J)$ fragments may be associated, therefore, to a hampered adiabatic dissociation attempt onto an excited PEC. In agreement with a statistical dynamics, the low-recoil contribution shows no particular photofragment polarization, with β and $a_0^2(\|)$ parameters equal to zero.

https://doi.org/10.1021/acs.jpca.2c05897
J. Phys. Chem. A 2022, 126, 8404−8422

The prompt dissociation feature dominates the $Br^*(^2P_{1/2})$ TEDs and is fairly visible in the $I(^2P_J)$ distributions. In the $Br(^2P_{3/2})$ curve, the feature is obscured by the previously undiscussed *c* component. Possible secondary dissociation of the CH_2I and CH_2Br radicals produced after primary C−Br and C−I bond cleavage, respectively, has been considered. Assuming that the polyatomic fragment absorbs a second 193 nm photon from the same pulse (nanosecond time duration), the corresponding energy balance can be written as follows

$$E_{av}^{2^{nd}} = h\nu - D_0(CH_2 - X) - E_{SO}(X) + E_i(CH_2X) - E_i(CH_2) \quad (9)$$

where $E_{av}^{2^{nd}}$ is the available energy in the secondary dissociation process, $D_0(CH_2{-}X)$ = 2.856 and 3.430 eV are the bond dissociation values for $CH_2{-}I$ and $CH_2{-}Br$, respectively.[54] The term $E_i(CH_2)$ represents the internal energy of the CH_2 coproduct, and $E_i(CH_2X)$ is the internal energy acquired by the polyatomic product on the primary dissociation event. Since the CH_2X fragment is produced with certain distribution of internal energy—represented in Figures 4 and 6 by the *b* contribution—the available energy for the halogen atom produced in the secondary process would vary accordingly.

Table 2. Available Energies, E_{av}, (in eV) for the Possible Primary and Secondary Dissociation Processes[a]

1st dissociation	E_{av}	2nd dissociation	E_{av-max}^{2nd}	E_{av-min}^{2nd}
CH_2I + Br*	3.03	CH_2 + I	6.48	5.51
		CH_2 + I*	5.54	4.57
CH_2Br + I*	3.09	CH_2 + Br	5.90	4.63
		CH_2 + Br*	5.44	4.17
CH_2I + Br	3.49	CH_2 + I	6.47	5.20
		CH_2 + I*	5.53	4.26
CH_2Br + I	4.04	CH_2 + Br	5.93	4.57
		CH_2 + Br*	5.47	4.11

[a] E_{av-max}^{2nd} and E_{av-min}^{2nd} represent the limiting values of the available energy corresponding to $E_i^{max}(CH_2X)$ and $E_i^{min}(CH_2X)$, respectively.

In Table 2, the available energies for the possible dissociation processes are gathered, where $E_{av-max}^{2^{nd}}$ and $E_{av-min}^{2^{nd}}$ represent the limiting values of the available energy corresponding to $E_i^{max}(CH_2X)$ and $E_i^{min}(CH_2X)$, respectively, in the threshold situation in which the CH_2 fragment is produced with no internal energy. The $E_{av}^{2^{nd}}$ references in either case are substantially high-energy shifted with respect of the associated *c* distributions, as expected for secondary processes.

Once the energy requirements have been checked, the $Br(^2P_J)$ and $I(^2P_J)$ images and the corresponding TEDs must be revisited to inspect the consistency of the secondary dissociation assumption. The relative intensity of the $Br(^2P_J)$ and $I(^2P_J)$ images may suggest that dissociation of the C−Br bond is greatly favored at 193 nm excitation with respect to C−I dissociation. The $Br(^2P_{3/2})$ TED provides relevant information which might help us to delve into the former statement, in particular when compared to the $I(^2P_{3/2})$ distribution. If the images shown in Figures 3 and 5 are analyzed in terms of the predominant feature—setting aside the low-recoil contribution—it should be concluded that (i) the overall intensity of the $Br(^2P_J)$ images is due to both the primary and secondary dissociation processes and (ii) the secondary dissociation of the CH_2I radical is highly unfavored (no secondary dissociation feature is observed in the $I^*(^2P_{1/2})$ TED). Therefore, it should not be overlooked the fact that although the C−Br bond cleavage is clearly preferred at 193 nm, most of the signal coming from the C−I dissociation is located at the center of the image (stochastic process) and that such signal adds to the secondary source of $Br(^2P_J)$ atoms. Notice that no quantitative branching ratios could be extracted from the present data taking into account the detection method used. Only qualitative comparisons can be done based on the intensity of the images. Further experiments employing other detection methods, such as one-photon VUV ionization, would be necessary to determine the branching ratios between the four atomic fragments.

The stereodynamical data presented in panels b and d of Figures 4 and 6 might illuminate the dynamics behind. Before we proceed, it must be stated that the validity of the photofragment analysis presented in this work is limited to one-photon dissociation processes. Some information for the secondary dissociation process can nevertheless be extracted, although without a proper mathematical treatment, the extension of the analysis is limited. At 193 nm excitation, CH_2BrI can undergo dissociation along both the C−Br and C−I coordinates. Involving two states of the same symmetry, the $13A' \leftarrow \tilde{X}$ transition possesses parallel character, the transition dipole moment $\tilde{\mu}$, however, would form a nonzero angle with either molecular axis. The dissociating bonds, as a consequence, will not be aligned along the polarization direction of the photolysis pulse. With regard to the primary dissociation event (*b* component in the TEDs), the preference for the C−Br bond dissociation suggests that the parent CH_2BrI is preferentially aligned along the C−Br axis in the excitation step at the expenses of the C−I axis, which is in excellent agreement with the different $a_0^2(\|)$ values found for both the $Br(^2P_{3/2})$ and $I(^2P_{3/2})$ fragments. Furthermore, assuming that the alignment produced by the photolysis pulse is lost due to the rotation during the dissociation step, it must be safely argued that in the steepest part of the PEC, where a second photon might be absorbed, the alignment of the ensemble should be little affected by rotation. If so, a subsequent dissociation of the partially aligned product ensemble would be greatly enhanced if the molecular axis of the dissociating product lies parallel to the polarization of the photolysis laser; and it would be strongly depleted if the said transition is perpendicular to the polarization of the photolysis laser. The relative intensity of the secondary $Br(^2P_J)$ and $I(^2P_J)$ signals fits into the former discussion. $CH_2Br{-}I$ dissociation is unfavored by geometrical restrictions; the CH_2Br species is produced, nonetheless, with the C−Br bond aligned along the photolysis pulse, and thus, the second absorption and consequent dissociation is highly favored. It could be easily argued that most molecules that dissociate through the C−I bond cleavage should undergo secondary C−Br dissociation. On the other hand, $CH_2I{-}Br$ dissociation is favored by geometrical restrictions; the CH_2I species would be produced with the C−I axis forming a significant angle with respect to the polarization of the photolysis laser. Secondary dissociation along the C−I bond would be, therefore, clearly hampered.

The former discussion provides a reasonable explanation of the observed branching ratios. To compose a whole picture of the dissociation dynamics, the assumptions made should find agreement with the remaining data provided by the TEDs,

https://doi.org/10.1021/acs.jpca.2c05897
J. Phys. Chem. A 2022, 126, 8404−8422

specifically the photofragment polarization and the energy partitioning. In the $Br(^2P_J)$ TEDs, the anisotropy parameter takes the maximum value of $\beta = 2$ for a parallel transition in the velocity range corresponding to the *c* component. This fact, in conjunction with the large branching ratio obtained for the component at issue, suggests that the CH_2Br radical behaves like a pseudodiatomic, with a well-defined parallel transition dipole moment leading to further dissociation along the C−Br coordinate. In addition, primary dissociation of CH_2BrI into CH_2Br and $I(^2P_J)$ takes place through two different processes, specifically, prompt C−I cleavage (*b* contribution) and slow internal conversion followed by thermal dissociation in the ground state (*a* contribution). In both cases, the CH_2Br fragment is produced with substantial internal (rotational and vibrational) excitation, although with different partitioning (the *b* profile reproduces specific rotational and vibrational excitation, while the *a* contribution is characterized by randomized distribution of the rovibrational excitation). Accordingly, a broad and unstructured translational distribution, located at substantial distance from the corresponding available energy reference (indicating the formation of CH_2 fragments with high internal energy), should be expected for the secondary dissociation of CH_2Br. The prediction reflects quite accurately the profiles obtained for the *c* component in panel b of Figures 4 and 6.

Likewise, a similar discussion may be developed for the $I(^2P_J)$ species. The *c* component in the corresponding TEDs might be considered almost negligible for both $I(^2P_J)$ products. In addition, the associated β parameter takes values close to zero. The reduced values of β suggest, as in the case of CH_2Br, that the CH_2I radical behaves like a pseudodiatomic, with a well-defined parallel transition dipole moment leading to further dissociation along the C−I coordinate; in this case, however, the absorption of a second photon would be highly hampered by the disadvantageous orientation of the C−I axis with respect to the polarization of the photolysis laser. The energy partitioning of the minor *c* component for the $I(^2P_J)$ species is explained in similar terms than that made for $Br(^2P_J)$. In short, the CH_2I fragments would be produced with significant internal energy, leading to broad TEDs associated with the formation of CH_2 fragments with high content of internal energy.

CONCLUSIONS

The main conclusions of the present work are summarized as follows: The translational energy distributions for the $Br(^2P_J)$ and $I(^2P_J)$ (with J = 3/2 and 1/2 for Br/I and Br*/I*, respectively) atomic photofragments are interpreted in terms of three contributions, associated to prompt C−X dissociation, a stochastic process and a secondary CH_2X dissociation process. At 193 nm excitation, those CH_2BrI molecules whose C−Br molecular axis is aligned parallel to the electric field of the photolysis pulse are preferentially excited. As a result, cleavage of the C−Br bond is greatly favored with respect to C−I dissociation for both CH_2XY and CH_2X (where X and Y are either halogen atom, Br or I) species. Prompt C−Br dissociation takes place after excitation at the $13A'$ electronic state and predissociation through the $11A'/11A''$ or $12A'/12A''$ states, leading to direct dissociation through the $10A'/9A''$ states for the CH_2I + Br and CH_2I + Br*, respectively.

Bond C−I dissociation takes place after excitation at the $13A'$ state but is not assisted by predissociation. Instead, fast internal conversion to lower electronic states and subsequent dissociation through the $6A'/6A''$ and $4A'/4A''$ results in relative fast $I(^2P_J)$ fragments and in a predominant low-recoil Boltzmann-like contribution associated to the partially frustrated prompt C−I bond cleavage.

The prompt bond dissociation dynamics is well interpreted in terms of the soft impulsive model which predicts a large fraction of the available energy transferred into rotation of the polyatomic CH_2X fragment. The CH_2X products show as well a considerable amount of vibrational energy due to the geometrical changes produced in the curve crossings leading to the dissociation limits. In the case of the first dissociation event (*b* contribution), the photofragment polarization analysis performed in terms of the $a_q^k(p)$ parameters suggest that the rotational angular momentum of the CH_2I species is produced with a high degree of alignment around the recoil direction.

ASSOCIATED CONTENT

Supporting Information

The Supporting Information is available free of charge at https://pubs.acs.org/doi/10.1021/acs.jpca.2c05897.

High-resolution UV−VUV gas phase CH_2BrI absorption spectrum and assignments. (PDF)

AUTHOR INFORMATION

Corresponding Author

Luis Bañares − *Departamento de Química Física (Unidad Asociada I+D+i al CSIC), Facultad de Ciencias Químicas, Universidad Complutense de Madrid, 28040 Madrid, Spain; Instituto Madrileño de Estudios Avanzados en Nanociencia (IMDEA-Nanoscience), 28049 Madrid, Spain;* orcid.org/0000-0002-0777-2375; Email: lbanares@ucm.es

Authors

Pedro Recio − *Departamento de Química Física (Unidad Asociada I+D+i al CSIC), Facultad de Ciencias Químicas, Universidad Complutense de Madrid, 28040 Madrid, Spain;* orcid.org/0000-0002-4867-2872

Javier Cachón − *Departamento de Química Física (Unidad Asociada I+D+i al CSIC), Facultad de Ciencias Químicas, Universidad Complutense de Madrid, 28040 Madrid, Spain*

Luis Rubio-Lago − *Departamento de Química Física (Unidad Asociada I+D+i al CSIC), Facultad de Ciencias Químicas, Universidad Complutense de Madrid, 28040 Madrid, Spain*

David V. Chicharro − *Departamento de Química Física (Unidad Asociada I+D+i al CSIC), Facultad de Ciencias Químicas, Universidad Complutense de Madrid, 28040 Madrid, Spain; Quantum Dynamics & Control, Max Planck Institute for Nuclear Physics (MPIK), 69117 Heidelberg, Germany*

Alexandre Zanchet − *Instituto de Física Fundamental, Consejo Superior de Investigaciones Científicas, 28006 Madrid, Spain*

Paulo Limão-Vieira − *Atomic and Molecular Collisions Laboratory, CEFITEC, Department of Physics, Universidade NOVA de Lisboa, 2829-516 Caparica, Portugal;* orcid.org/0000-0003-2696-1152

Nelson de Oliveira − *Synchrotron SOLEIL, L'Orme des Merisiers, 91192 Gif sur Yvette, France*

Peter C. Samartzis − *Institute of Electronic Structure and Laser, Foundation for Research and Technology-Hellas (FORTH-IESL), 70013 Heraklion, Greece;* orcid.org/0000-0001-8873-2326

Sonia Marggi Poullain − *Departamento de Química Física (Unidad Asociada I+D+i al CSIC), Facultad de Ciencias*

https://doi.org/10.1021/acs.jpca.2c05897
J. Phys. Chem. A 2022, 126, 8404−8422

Químicas, Universidad Complutense de Madrid, 28040 Madrid, Spain; orcid.org/0000-0001-6712-3628

Complete contact information is available at: https://pubs.acs.org/10.1021/acs.jpca.2c05897

Notes

The authors declare no competing financial interest.

■ ACKNOWLEDGMENTS

P.R. is grateful to Universidad Complutense de Madrid (UCM) for a Margarita Salas postdoctoral contract. J.C. and D.V.C. acknowledge financial support from Spanish Ministry of Science and Innovation under the FPI predoctoral program. P.L.-V. acknowledges Fundación Carolina for a mobility grant at UCM under the Programa de Movilidad de Profesores e Investigadores Portugueses (Fundación Endesa). Part of the experiments presented were performed at the DESIRS beamline at synchrotron SOLEIL under proposal number 20170473. We acknowledge SOLEIL for provision of synchrotron radiation facilities. This work was performed in part at the Institute of Electronic Structure and Laser, Foundation for Research and Technology-Hellas (IESL-FORTH) and received financial support from LaserLab Europe (Grant agreement No. 654148) through the ULF-FORTH002540 project. This research has been carried out within the Unidad Asociada Química Física Molecular between the Departamento de Química Física of Universidad Complutense de Madrid and CSIC. This project has received funding from the Spanish Ministry of Science and Innovation (Grants PGC2018-096444-B-I00 and PID2019-107115GB-C21).

■ ADDITIONAL NOTES

[a]The Br*($^2P_{1/2}$) or I*($^2P_{1/2}$) photofragments possess a total angular momentum $J = 1/2$ and cannot show angular polarization (alignment or orientation).

[b]The relationship between $A_q^k(p)$ coefficients and the $a_q^k(p)$ parameters can be found in eqs ^{4}a−^{4}d of ref 34.

■ REFERENCES

(1) Saiz-Lopez, A.; Plane, J. M. C.; Baker, A. R.; Carpenter, L. J.; von Glasow, R.; Gómez Martín, J. C.; McFiggans, G.; Saunders, R. W. Atmospheric Chemistry of Iodine. *Chem. Rev.* **2012**, *112*, 1773−1804.

(2) Simpson, W. R.; Brown, S. S.; Saiz-Lopez, A.; Thornton, J. A.; von Glasow, R. Tropospheric Halogen Chemistry: Sources, Cycling, and Impacts. *Chem. Rev.* **2015**, *115*, 4035−4062.

(3) Welz, O.; Savee, J. D.; Osborn, D. L.; Vasu, S. S.; Percival, C. J.; Shallcross, D. E.; Taatjes, C. A. Direct Kinetic Measurements of Criegee Intermediate (CH_2OO) Formed by Reaction of CH_2I with O_2. *Science* **2012**, *335*, 204−207.

(4) Eskola, A. J.; Wojcik-Pastuszka, D.; Ratajczak, E.; Timonen, R. S. Kinetics of the reactions of CH_2Br and CH_2I radicals with molecular oxygen at atmospheric temperatures. *Phys. Chem. Chem. Phys.* **2006**, *8*, 1416−1424.

(5) Jones, C. E.; Carpenter, L. J. Solar Photolysis of CH_2I_2, CH_2ICl, and CH_2IBr in Water, Saltwater, and Seawater. *Environ. Sci. Technol.* **2006**, *40*, 1372.

(6) Mossinger, J. C.; Shallcross, D. E.; Anthony Cox, R. UV−VIS Absorption Cross-Sections and Atmospheric Lifetimes of CH_2Br_2,CH_2I_2 and CH_2BrI. *J. Chem. Soc., Faraday Trans.* **1998**, *94*, 1391−1396.

(7) Man, S.; Kwok, W. M.; Phillips, D. L.; Johnson, A. E. Short-time photodissociation dynamics of A-band and B-band bromoiodomethane in solution: An examination of bond selective electronic excitation. *J. Chem. Phys.* **1996**, *105*, 5842.

(8) Butler, L. J.; Hintsa, E. J.; Shane, S. F.; Lee, Y. T. The electronic state-selective photodissociation of CH_2BrI at 248, 210, and 193 nm. *J. Chem. Phys.* **1987**, *86*, 2051.

(9) Lee, S. J.; Bersohn, R. Photodissociation of a molecule with two chromophores. CH_2IBr. *J. Phys. Chem.* **1982**, *86*, 728−730.

(10) Liu, K.; Zhao, H.; Wang, C.; Zhang, A.; Ma, S.; Li, Z. A theoretical study of bond selective photochemistry in CH_2BrI. *J. Chem. Phys.* **2005**, *122*, 044310.

(11) Liu, Y.-J.; Ajitha, D.; Krogh, J. W.; Tarnovsky, A. N.; Lindh, R. Spin−Orbit Ab Initio Investigation of the Photolysis of Bromoiodomethane. *ChemPhysChem* **2006**, *7*, 955−963.

(12) Tang, K.-C.; Peng, J.; Spears, K. G.; Sension, R. J. Photoinitiated bond dissociation of bromoiodomethane in solution: Comparison of one-photon and two-photon excitations and the formation of iso-CH_2Br−I and iso-CH_2I−Br. *J. Chem. Phys.* **2010**, *132*, 141102.

(13) Anderson, C. P.; Spears, K. G.; Wilson, K. R.; Sension, R. J. Solvent dependent branching between C-I and C-Br bond cleavage following 266 nm excitation of CH_2BrI. *J. Chem. Phys.* **2013**, *139*, 194307.

(14) Attar, A. R.; Piticco, L.; Leone, S. R. Core-to-valence spectroscopic detection of the CH_2Br radical and element-specific femtosecond photodissociation dynamics of CH_2BrI. *J. Chem. Phys.* **2014**, *141*, 164308.

(15) Horton, S. L.; Liu, Y.; Forbes, R.; Makhija, V.; Lausten, R.; Stolow, A.; Hockett, P.; Marquetand, P.; Rozgonyi, T.; Weinacht, T. Excited state dynamics of CH_2I_2 and CH_2BrI studied with UV pump VUV probe photoelectron spectroscopy. *J. Chem. Phys.* **2019**, *150*, 174201.

(16) Liu, Y.; Rozgonyi, T.; Marquetand, P.; Weinacht, T. Excited-state dynamics of CH_2I_2 and CH_2IBr studied with UV-pump VUV-probe momentum-resolved photoion spectroscopy. *J. Chem. Phys.* **2020**, *153*, 184304.

(17) Burt, M.; et al. Coulomb-explosion imaging of concurrent CH_2BrI photodissociation dynamics. *Phys. Rev. A* **2017**, *96*, 043415.

(18) Köckert, H.; et al. UV-induced dissociation of CH_2BrI probed by intense femtosecond XUV pulses. *J. Phys. B: At. Mol. Opt. Phys.* **2022**, *55*, 014001.

(19) Pan, C.; Zhang, Y.; Lee, J. D.; Kidwell, N. M. Imaging the dynamics of CH_2BrI photodissociation in the near ultraviolet region. *J. Phys. Chem. A* **2018**, *122*, 3728−3734.

(20) Muthiah, B.; Paredes-Roibás, D.; Kasai, T.; Lin, K.-C. Photodissociation of CH_2BrI using cavity ring-down spectroscopy: in search of a BrI elimination channel. *Phys. Chem. Chem. Phys.* **2019**, *21*, 13943.

(21) Marggi Poullain, S.; Chicharro, D. V.; Navarro, E.; Rubio-Lago, L.; González-Vázquez, J.; Bañares, L. Photodissociation dynamics of bromoiodomethane from the first and second absorption bands. A combined velocity map and slice imaging study. *Phys. Chem. Chem. Phys.* **2018**, *20*, 3490.

(22) Murillo-Sánchez, M. L.; Marggi Poullain, S.; Bajo, J. J.; Corrales, M. E.; González-Vázquez, J.; Solá, I. R.; Bañares, L. Halogen-atom effect on the ultrafast photodissociation dynamics of the dihalomethanes CH_2ICl and CH_2BrI. *Phys. Chem. Chem. Phys.* **2018**, *20*, 20766.

(23) de Oliveira, N.; Roudjane, M.; Joyeux, D.; Phalippou, D.; Rodier, J.-C.; Nahon, L. High-resolution broad-bandwidth Fourier-transform absorption spectroscopy in the VUV range down to 40 nm. *Nat. Photonics* **2011**, *5*, 149−153.

(24) Nahon, L.; de Oliveira, N.; Garcia, G. A.; Gil, J.-F.; Joyeux, D.; Lagarde, B.; Polack, F. DESIRS: a state-of-the-art VUV beamline featuring high resolution and variable polarization for spectroscopy and dichroism at SOLEIL. *J. Phys.: Conf. Ser.* **2013**, *425*, 122004.

(25) de Oliveira, N.; Joyeux, D.; Roudjane, M.; Gil, J.-F.; Pilette, B.; Archer, L.; Ito, K.; Nahon, L. The high-resolution absorption spectroscopy branch on the VUV beamline DESIRS at SOLEIL. *J. Synchrotron Rad.* **2016**, *23*, 887−900.

(26) de Oliveira, N.; Joyeux, D.; Phalippou, D.; Rodier, J. C.; Polack, F.; Vervloet, M.; Nahon, L. A Fourier transform spectrometer without a beam splitter for the vacuum ultraviolet range: From the optical design to the first UV spectrum. *Rev. Sci. Instrum.* **2009**, *80*, 043101.

(27) Gebhardt, C. R.; Rakitzis, T. P.; Samartzis, P. C.; Ladopoulos, V.; Kitsopoulos, T. N. Slice imaging: A new approach to ion imaging and velocity mapping. *Rev. Sci. Instrum.* **2001**, *72*, 3848−3853.
(28) Papadakis, V.; Kitsopoulos, T. N. Slice imaging and velocity mapping using a single field. *Rev. Sci. Instrum.* **2006**, *77*, 083101.
(29) Rodríguez, J. D.; González, M. G.; Rubio-Lago, L.; Bañares, L.; Samartzis, P. C.; Kitsopoulos, T. N. Stereodynamics of the Photodissociation of Nitromethane at 193 nm: Unravelling the Dissociation Mechanism. *J. Phys. Chem. A* **2013**, *117*, 8175−8183.
(30) Marggi Poullain, S.; González, M. G.; Samartzis, P. C.; Kitsopoulos, T. N.; Rubio-Lago, L.; Bañares, L. New insights into the photodissociation of methyl iodide at 193 nm: stereodynamics and product branching ratios. *Phys. Chem. Chem. Phys.* **2015**, *17*, 29958−29968.
(31) Kim, Y. S.; Jung, Y.-J.; Kang, W.; Jung, K.-H. Photoelectron imaging spectroscopy for (2 + 1) resonance-enhanced multiphoton ionization of atomic bromine. *Bull. Korean Chem. Soc.* **2002**, *23*, 189.
(32) Jung, Y.-J.; Shin Kim, Y.; Kyung Kang, W.; Jung, K.-H. Photoelectron imaging spectroscopy for (2 + 1) resonance-enhanced multiphoton ionization of atomic iodine produced from A-band photolysis of CH3I. *J. Chem. Phys.* **1997**, *107*, 7187.
(33) Rakitzis, T. P.; Zare, R. N. Photofragment angular momentum distributions in the molecular frame: Determination and interpretation. *J. Chem. Phys.* **1999**, *110*, 3341.
(34) Rakitzis, T. P. Direct measurements of photofragment alignment from unnormalized Abel-inverted images. *Chem. Phys. Lett.* **2001**, *342*, 121−126.
(35) Rakitzis, T. P.; Samartzis, P. C.; Kitsopoulos, T. N. Complete Measurement of $S(^1D_2)$ Photofragment Alignment from Abel-Invertible Ion Images. *Phys. Rev. Lett.* **2001**, *87*, 123001.
(36) Rakitzis, T. P.; Kitsopoulos, T. N. Measurement of Cl and Br photofragment alignment using slice imaging. *J. Chem. Phys.* **2002**, *116*, 9228.
(37) Rakitzis, T.; Samartzis, P.; Toomes, R.; Tsigaridas, L.; Coriou, M.; Chestakov, D.; Eppink, A.; Parker, D.; Kitsopoulos, T. Photofragment alignment from the photodissociation of HCl and HBr. *Chem. Phys. Lett.* **2002**, *364*, 115−120.
(38) Orr-Ewing, A.; Zare, R. N. Orientation and Alignment of Reaction Products. *Annu. Rev. Phys. Chem.* **1994**, *45*, 315−366.
(39) Samartzis, P. C.; Bakker, B. L. G.; Rakitzis, T. P.; Parker, D. H.; Kitsopoulos, T. N. Spin-orbit branching ratios for the Cl atom photofragments following the excitation of Cl_2 from 310 to 470 nm. *J. Chem. Phys.* **1999**, *110*, 5201.
(40) Werner, H.-J.et al.*MOLPRO, A Package of Ab Initio Programs*, ver. 2015.1; 2015.
(41) Werner, H.-J. Third-order multireference perturbation theory The CASPT3 method. *Mol. Phys.* **1996**, *89*, 645.
(42) Werner, H.-J.; Knowles, P. J. A second order multiconfiguration SCF procedure with optimum convergence. *J. Chem. Phys.* **1985**, *82*, 5053.
(43) Berning, A.; Schweizer, M.; Werner, H.-J.; Knowles, P. J.; Palmieri, P. Spin-orbit matrix elements for internally contracted multireference configuration interaction wavefunctions. *Mol. Phys.* **2000**, *98*, 1823.
(44) Lee, M.; Kim, H.; Lee, Y. S.; Kim, M. S. One-photon mass-analyzed threshold ionization spectroscopy of CH_2BrI: Extensive bending progression, reduced steric effect, and spin-orbit effect in the cation. *J. Chem. Phys.* **2005**, *123*, 024310.
(45) Penner, A.; Amirav, A. Rydberg state absorption spectroscopy of $Br(CH_2)_nI$ (n = 1−3). *J. Chem. Phys.* **1990**, *93*, 8576−8579.
(46) Man, S.-Q.; Kwok, W. M.; Phillips, D. L. Investigation of bond-selective electronic excitation in bromoiodomethane. *J. Phys. Chem.* **1995**, *99*, 15705−15708.
(47) Liu, Y.-J.; Ajitha, D.; Krogh, J. W.; Tarnovsky, A. N.; Lindh, R. Spin−Orbit Ab Initio Investigation of the Photolysis of Bromoiodomethane. *ChemPhysChem: A European Journal of Chemical Physics and Physical Chemistry* **2006**, *7*, 955−963.
(48) Zheng, X.; Phillips, D. L. Photoisomerization reaction of CH_2BrI following *A*-band and *B*-band photoexcitation in the solution phase: Transient resonance Raman observation of the iso-CH_2I−Br photoproduct. *J. Chem. Phys.* **2000**, *113*, 3194−3203.
(49) Sándor, P.; Zhao, A.; Rozgonyi, T.; Weinacht, T. Strong field molecular ionization to multiple ionic states: direct versus indirect pathways. *Journal of Physics B: Atomic, Molecular and Optical Physics* **2014**, *47*, 124021.
(50) Muckerman, J. T. J. Information Theoretic Prior Functions for Large Molecular Systems. *J. Phys. Chem.* **1989**, *93*, 179−184.
(51) Irikura, K. K.; Johnson, R. D.; Hudgens, J. W. Two new electronic states of CH_2. *J. Phys. Chem.* **1992**, *96*, 6131.
(52) Busch, G. E.; Wilson, K. R. Triatomic Photofragment Spectra. I. Energy Partitioning in NO_2 Photodissociation. *J. Chem. Phys.* **1972**, *56*, 3626−3638.
(53) Brynteson, M. D.; Womack, C. C.; Booth, R. S.; Lee, S.-H.; Lin, J. J.; Butler, L. J. Radical intermediates in the addition of OH to propene: photolytic precursors and angular momentum effects. *J. Phys. Chem. A* **2014**, *118*, 3211−3229.
(54) Lazarou, Y. G.; Prosmitis, A. V.; Papadimitriou, V. C.; Papagiannakopoulos, P. Theoretical calculation of bond dissociation energies and enthalpies of formation for halogenated molecules. *J. Phys. Chem. A* **2001**, *105*, 6729.

https://doi.org/10.1021/acs.jpca.2c05897
J. Phys. Chem. A 2022, 126, 8404−8422

Supplementary Information

Imaging the photodissociation dynamics and fragment alignment of CH_2BrI at 193 nm

Pedro Recio,[†] Javier Cachón,[†] Luis Rubio-Lago,[†] David V. Chicharro,[†,‡] Alexandre Zanchet,[¶] Paulo Limão-Vieira,[§] Nelson de Oliveira,[‖] Peter C. Samartzis,[⊥] Sonia Marggi Poullain,[†] and Luis Bañares[*,†,#]

[†]Departamento de Química Física (Unidad Asociada I+D+i al CSIC), Facultad de Ciencias Químicas, Universidad Complutense de Madrid, 28040 Madrid, Spain
[‡]Quantum Dynamics & Control, Max Planck Institute for Nuclear Physics (MPIK), Saupfercheckweg 1, 69117 Heidelberg, Germany
[¶]Instituto de Física Fundamental, Consejo Superior de Investigaciones Científicas, Serrano 123, 28006 Madrid, Spain
[§]Atomic and Molecular Collisions Laboratory, CEFITEC, Department of Physics, Universidade NOVA de Lisboa, 2829-516 Caparica, Portugal
[‖]Synchrotron SOLEIL, L'Orme des Merisiers, St. Aubin, BP 48, 91192 Gif sur Yvette, France
[⊥]Institute of Electronic Structure and Laser, Foundation for Research and Technology-Hellas (FORTH-IESL), Vassilika Vouton, 70013 Heraklion, Greece
[#]Instituto Madrileño de Estudios Avanzados en Nanociencia (IMDEA-Nanoscience), Cantoblanco, 28049 Madrid, Spain

*E-mail: lbanares@ucm.es

High-resolution UV-VUV gas phase CH_2BrI absorption spectrum and assignments

The room temperature high-resolution vacuum ultraviolet (VUV) photoabsorption spectrum of bromoiodomethane (CH_2BrI) (Figures S1–S4 and Tables S1-S6 for assignments) was recorded at the DESIRS beam line of the SOLEIL synchrotron facility.

The absolute photoabsorption cross-section (in units of Mb ≡ 10^{-18} cm^2) of CH_2BrI is shown in Figure S1, in the 5.0−11.0 eV photon energy range, with detailed sections depicted in Figures S2–S4. We have adopted the normal mode description and numbering from the vibrational analysis of Lee *et al*.,[1] and the electronic excitation above 6.0 eV shows fine structure assigned to the CH_2 scissoring and wagging modes ν_2' and ν_3', with ground state energies of (1374 cm^{-1}) and (1150 cm^{-1}).[2] Above 7.0 eV the observed rich structure is due to the overlap of different Rydberg electronic states and vibrational excitations contributing to the spectrum. These modes have also been assigned to the contribution of C–Br stretching ν_4', C–I stretching ν_5', and Br–C–I bending ν_6' modes, with ground state energies of (616 cm^{-1}), (517 cm^{-1}) and (144 cm^{-1}), respectively. The absorption bands are classified as excitations from the ground to valence but mainly Rydberg character. Due to the high flux, a few structures corresponding to signatures coming from photodissociation products of CH_2BrI can be observed. Even if weak, and difficult to assign due to the scarce literature, most of these photolysis signals have been identified and presented in Table S1. Tables S2-S4 show the energy values for the vibrational assignments in the different absorption bands of CH_2BrI. For the assignments of the vibronic structure, we will adopt the notation X_m^n, with *m* and *n* the initial and final vibrational states and *X* denotes the particular geometric change the molecule undergoes in the photoabsorption process.

The 5.0 – 7.0 eV photon energy range

The first absorption band, so-called *A* band, of bromoiodomethane lying in the 4-5 eV energy range is assigned to the $\sigma^*(\mathrm{C-I}) \leftarrow n_I(\mathrm{5p})$ transition and cannot be observed in the present photoabsorption spectrum. A first weak structureless band peaking at 5.837 eV (~212 nm) is observed in Figure S1 and assigned to the $\sigma^*(\mathrm{C-Br}) \leftarrow n_{Br}(\mathrm{4p})$ ($9A' \leftarrow \tilde{X}\ ^1A'$) transition.

The *A'*-band has been previously reported [2–8] where a general agreement is noted for its maximum position, yet the absolute cross-section values in the wavelength range 215–250 nm (5.767–4.959 eV) of Mössinger *et al.*[7] are 9–35% lower than the present high-resolution data (Figure S2). Additionally, this band has been also the subject of experimental[2,6,8] and theoretical[4,5,8] photodissociation dynamics studies, with relevant information about the energies of the activated vibrational modes. A close inspection of the photoabsorption spectrum, shows an enhancement of the background signal where the features are superimposed on a diffuse background reminiscent of a predissociative character of the absorption bands.

The results from the high-level *ab initio* calculations presented in the main manuscript are summarized in Table S5 and compared with other results in the literature, where other less intense electronic states may contribute to the underlying character of the *A'*-band, as previously noted by Man *et al.*[2] and Zheng and Phillips.[8]

A close inspection of the potential energy curves (PECs) in the article (Figures 7-10 of the main text) shows many avoided crossings, implying multiple conical intersections in the full multi-dimensional space. The PECs along the C–Br coordinate show that at the *A'*-band position in the adiabatic description, the dissociative character is already operative, which lends strong support to the absence of any fine structure. Note that in this energy band some minor dissociation may also lead to C–I bond excision[5] as well as to elimination of electronically excited BrI was also reported.[6] In the reaction coordinate yielding CH_2–BrI either through direct bond excision or isomerization mode, the multitude of excited electronic states crossing at ~ 6.5 eV, are responsible for predissociative character, which means some spectral signature of CH_2 scissoring and wagging modes ν_2' and ν_3' being excited. Yet, for a thorough description of the dissociation dynamics see Zheng and Phillips[8] resonance Raman experiments and Liu *et al.*[5] spin-orbit theoretical investigation of the photolysis of CH_2BrI.

The next band has been assigned to the $(6s \leftarrow n_I)$ Rydberg transition converging to the lowest ionisation energy (see discussion below), showing a modest fine structure (Figure S2) due to vibrational excitation with assignments in Table S2. Note that the present calculations indicate that this energy region is characterised by a valence transition with its vertical value tentatively placed at 6.529 eV. We have assigned this to the $\sigma^*(\mathrm{C-Br}) \leftarrow n_{Br}(4\mathrm{p})$ $\left(13A' \leftarrow \tilde{X}\ ^1A'\right)$

transition (see Table S5). The 0_0^0 origin band is tentatively assigned at 6.23(2) eV, with a 2_0^n (n = 0–3) progression of the CH_2 scissoring mode, ν_2', and an average spacing of 0.154 eV (1242 cm^{-1}). However, a contribution from the CH_2 wagging mode, ν_3', is also discernible (see Table S2). Other progressions at higher energy have also been assigned and are discussed below for the Rydberg transitions.

Above 7.0 eV photon energy range

The photoabsorption spectrum above 7.0 eV displays prominent Rydberg features (see below) and the calculations in Table S5 predict a valence transition at 8.04 eV. The experimental vertical value is at 7.488 eV (with a cross-section of 37.2 Mb), in reasonable agreement with the calculation given the level of accuracy used (±0.5 eV) and is assigned to the $\left(17A' \leftarrow \tilde{X}\ ^1A'\right)$ transition. Given the background contribution to the absorption band, the nature of this transition is reminiscent of a dissociation character. We are not aware of any other information in the literature to compare with the present finding.

Ionisation energies of bromoiodomethane

Lee *et al.*[1] mass-analysed threshold ionization (MATI) lowest-lying energy is at (9.5944±0.0006) eV with strong Br–C–I bending overtones (6^n) in this spectral region of the MATI spectrum, whereas the ionisation energy has been reported by Lago *et al.*[9] at (9.692±0.012) eV. According to Lee *et al.*,[1] the difference between the two measurements, (0.098±0.012 eV), is considerably large, given that MATI measurements of the ionisation energies of other aliphatic halides studied before are usually in agreement with photoelectron spectroscopy (PES) or photoelectron-photoion coincidence (PEPICO) results within error limits. Thus, those authors suggest that such difference is due to the fact that the 0_0^0 band is very weak and that the bending progression reaches the maximum intensity at a high overtone. It is likely that the (9.692±0.012 eV) value reported by Lago et al.[9] refers to the vertical ionisation energy.[1] Due to lack of information regarding any experimental values for the ionic electronic excited states, we have followed the high accuracy of the multireference configuration interaction calculations of Sándor *et al.*'s[10] These authors have obtained an energy difference of 0.57 eV between the neutral ground state and the first ionic states. Thus, for the latter we will use the value of 10.1644 eV and tentative Rydberg assignments are shown in Figures S3 and S4, and Table S6.

Rydberg transitions

Bromoiodomethane electronic excitation in the photon energy range studied in this work displays a prominent Rydberg character where a summary of the experimental energies, assignments and quantum defects can be found in Table S6. The peak positions have been tested using the Rydberg formula: $E_n = E_I - R/(n-\delta)^2$, where E_I is the ionisation energy, n is the principal quantum number of the Rydberg orbital of energy E_n, R is the Rydberg constant (13.61 eV), and δ is the quantum defect resulting from the penetration of the Rydberg orbital into the core. In order to avoid congestion in Figure S4, from the different members of the Rydberg series and the fine structure, relevant assignments have not been explicitly depicted, but rather are listed in Table S4. However, the normal mode description may lead to Fermi resonances, making assignments in the absorption spectrum particularly challenging.

The lowest-lying Rydberg transition is assigned to the promotion of iodine nonbonding n_I (5p) lone pair electrons to the 6s Rydberg state (Table S5), with the first member $n = 6$ at 6.529 eV, an effective quantum number $n^* = 2.11$ (Table S6) and extending up to n = 11. The energy region comprising the 6s Rydberg state shows a modest fine structure (see Figure S2) due to vibrational excitation, with assignments in Table S2. The features are assigned to the contribution of CH_2 scissoring and wagging modes ν_2' and ν_3', with an energy spacing from the origin band of ~ 0.144 eV (0.170 in the ground state[2]) and ~ 0.107 eV (0.143 eV in the ground state).[2] The first members of the np and nd series (Table S6) are associated with features at 7.27(4) eV and 7.922 eV ($n^* = 2.42$ and 2.85), and are accompanied by several quanta of the CH_2 scissoring and wagging ν_2' and ν_3', C–Br stretching ν_4' and C–I stretching ν_5' modes (Table S3).

The Rydberg series converging to the ionisation energy of 10.1644 eV state are listed in Table S6, and have been assigned to the ns, np and nd transitions. The first members of these series are associated with features at 6.913 eV ($n^* = 2.05$), 7.866 eV ($n^* = 2.43$) and 8.49(9) eV ($n^* = 2.86$). The present Rydberg (tentative) assignments have been made up to n = 12 for the ns and np series, where some of the features contribute to more than one series. Such a contribution may be noted from a close inspection of the absorption spectrum, where such features tend to appear broader due to contributions from vibrational modes (Table S4). The observed fine structure in these absorption peaks has been assigned to vibrational excitation involving the CH_2 scissoring ν_2', the CH_2 wagging ν_3', the C–Br stretching ν_4', the C–I stretching ν_5', and the Br–C–I bending ν_6' modes. These modes show an average spacing of

0.149 eV (1202 cm^{-1}), 0.120 eV (968 cm^{-1}), 0.074 eV (597 cm^{-1}), 0.035 eV (282 cm^{-1}) and 0.013 eV (105 cm^{-1}), respectively (see Table S4). From the vibrational frequencies of CH_2BrI cation in the ground electronic state calculated by Kim *et al.*[11] and Lee *et al.*,[1] the major difference to the Rydberg vibrational excitations in Tables S3 and S4 are due to the C–I stretching ν_5', mode. Those authors report average values of 0.062 eV (500 cm^{-1}) which are 44% higher than in the neutral excited Rydberg states. This is not surprisingly given the dominant repulsive nature of the neutral electronic excited states along the C–I coordinate above 7.0 eV as is clearly depicted in Figure S6.

Finally, not any other Rydberg tentative assignments have been performed above the lowest-lying ionic states of bromoiodomethane (Figure S5).

Figure S1. High-resolution VUV photoabsorption spectrum bromoiodomethane, CH_2BrI in the 5.0−11.0 eV photon energy range.

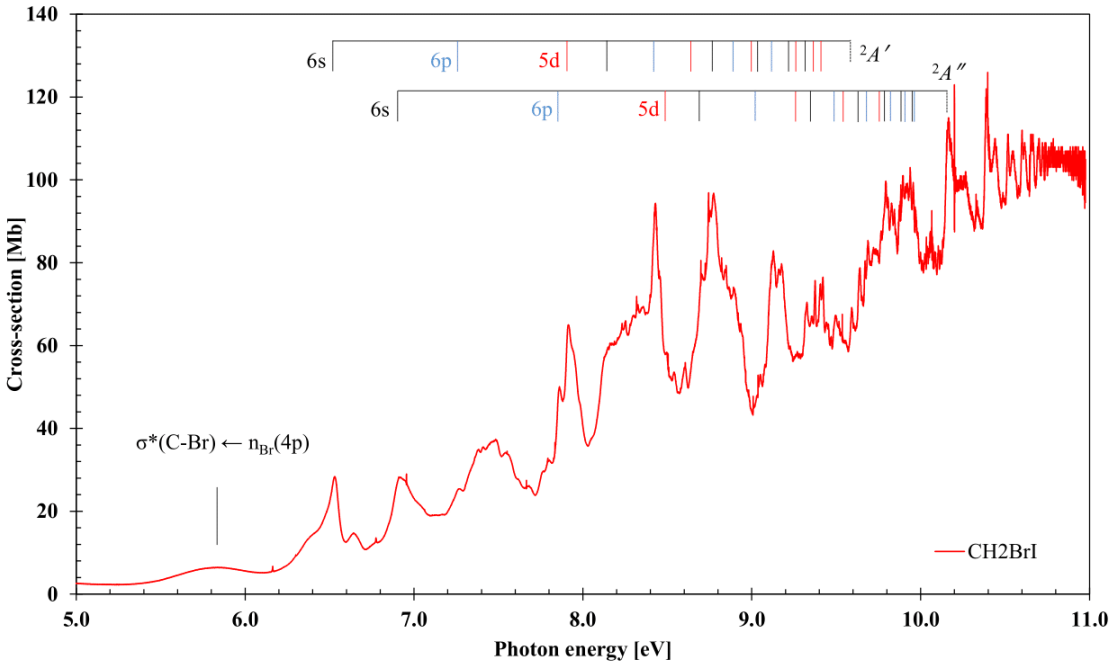

Figure S2. High-resolution VUV photoabsorption spectrum of bromoiodomethane, CH_2BrI in the 5.0−7.0 eV photon energy range with assignments.

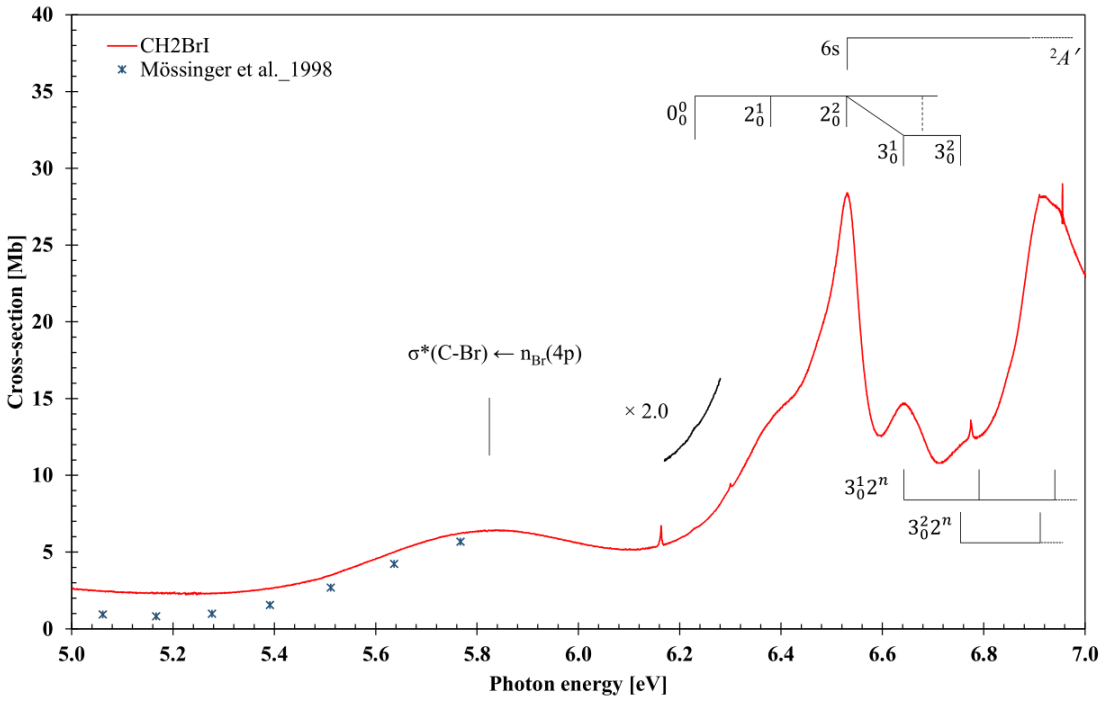

Figure S3. High-resolution VUV photoabsorption spectrum of bromoiodomethane, CH_2BrI in the 6.8−8.8 eV photon energy range with assignments.

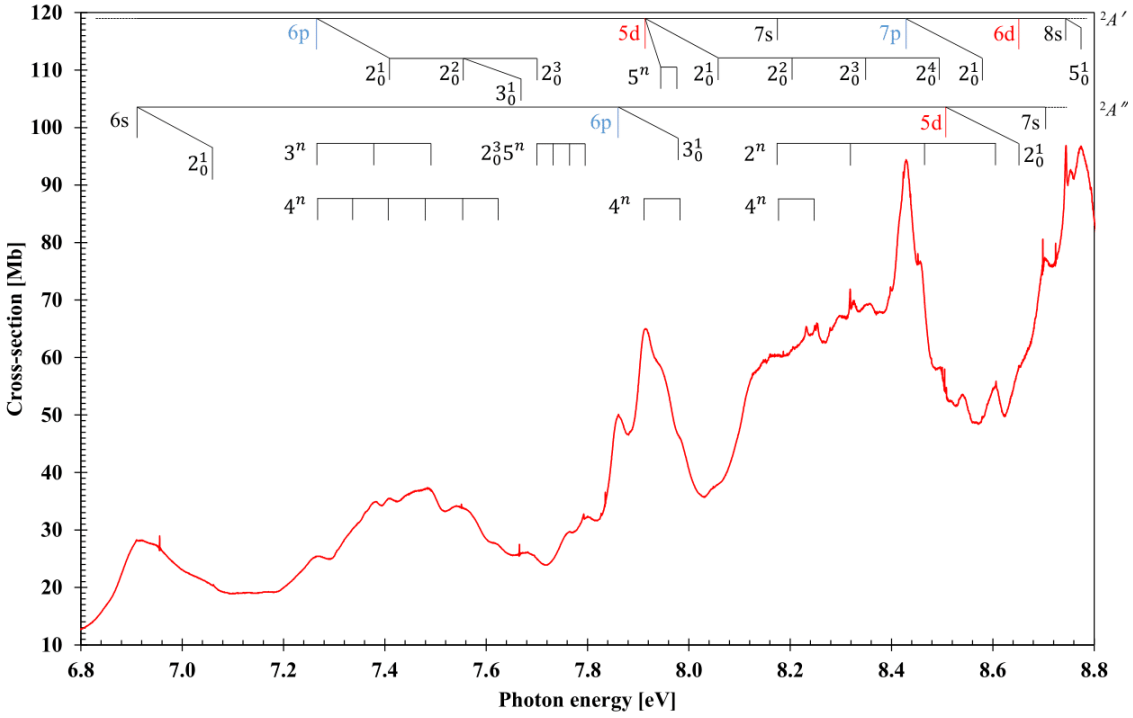

Figure S4. High-resolution VUV photoabsorption spectrum of bromoiodomethane, CH_2BrI in the 8.8−10.8 eV photon energy range with assignments.

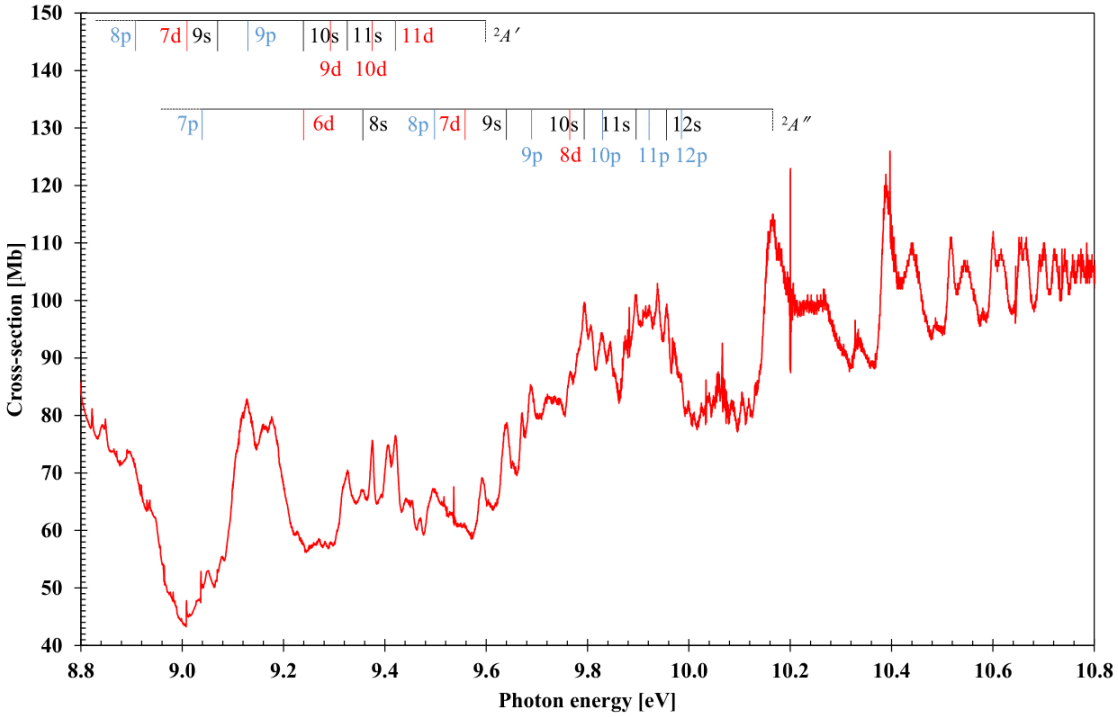

Table S1. Proposed assignment of the several structures of the spectrum corresponding to signals from photolysis products of CH_2BrI.

Energy (cm^{-1})	Energy (eV)	Photolysis Product
49704	6.163	CH_3I
50808	6.300	CH_3I
54633	6.774	I
54642	6.775	CH_3I
56092	6.955	I
56948	7.061	I_2
60896	7.551	I
61954	7.682	I_2
61819	7.665	I
62843	7.792	I_2
63120	7.826	I_2
63186	7.835	I
66386	8.231	I_2
66526	8.249	Not assign
66560	8.253	I_2
67084	8.318	HBr
67183	8.330	Not assign
67725	8.397	I_2
67930	8.423	I_2
68045	8.437	Not assign
68162	8.452	I_2
68376	8.478	I_2
68550	8.500	I
68588	8.504	I
68616	8.508	I
69405	8.606	Not assign
70151	8.698	I
70354	8.723	I
70517	8.744	HBr
71144	8.821	Not assign
71153	8.822	I_2
71357	8.848	I_2
71534	8.870	Not assign
71929	8.919	I_2
72018	8.930	I_2
72065	8.936	I_2
72294	8.964	I
72436	8.982	Not assign
72649	9.008	I_2
72879	9.036	I_2
75899	9.411	I

76903	9.535	I
79695	9.882	HBr
80916	10.033	Kr - beamline gas filter
81177	10.065	HBr
82259.5	10.200	H-Lyα
83292	10.328	HBr
83845	10.396	HBr
85846	10.644	Kr - beamline gas filter

Table S2. Proposed vibrational assignments in the 6.0−7.1 eV absorption bands of bromoiodomethane, CH_2BrI. Energies in eV.

energy[#]	assignment	ΔE (ν_2')	ΔE (ν_3')
6.23(2)(s)	0_0^0	–	–
6.38(9)(b)	2_0^1	0.157	–
6.529	2_0^2 / 6s ($^2A'$)	0.140	–
6.637	$2_0^2 + 3_0^1$ / 6s ($^2A'$) + 3_0^1	–	0.108
6.68(1)(s,w)	2_0^3	0.152	–
6.75(1)(s)	$2_0^2 + 3_0^2$ / 6s ($^2A'$) + 3_0^2	–	0.103
6.78(7)(b)	$2_0^2 + 3_0^1 + 2_0^1$ / 6s ($^2A'$) + $3_0^1 + 2_0^1$	0.150	–
6.913	$2_0^2 + 3_0^2 + 2_0^1$ / 6s ($^2A''$)	0.162	–
6.95(6)(b)	$2_0^2 + 3_0^1 + 2_0^2$ / 6s ($^2A'$) + $3_0^1 + 2_0^2$	0.169	–
7.05(9)(b)	$2_0^2 + 3_0^2 + 2_0^2$ / 6s ($^2A''$) + 2_0^1	0.146	–

[#]The last decimal of the energy is given in brackets for these less resolved features; (s) shoulder structure; (b) broad feature; (w) weak feature.

Table S3. Proposed vibrational assignments in the 6.8−8.8 eV absorption bands of bromoiodomethane, CH_2BrI. Energies in eV.

energy[#]	assignment	ΔE (ν_2')	ΔE (ν_3')	ΔE (ν_4')	ΔE (ν_5')	ΔE (ν_5')
7.27(4)(b)	6p ($^2A'$)	–	–	–	–	–
7.33(5)(s,w)	6p ($^2A'$) + 4_0^1	–	–	0.061	–	–
7.38(6)(b)	6p ($^2A'$) + 3_0^1	–	0.112	–	–	–
7.416	6p ($^2A'$) + 2_0^1 / 6p ($^2A'$) + 4_0^2	0.142	–	0.081	–	–
7.48(0)(b)	6p ($^2A'$) + 3_0^2 / 6p ($^2A'$) + 4_0^3	–	0.094	0.064	–	–
7.56(1)(b)	6p ($^2A'$) + 2_0^2 / 6p ($^2A'$) + 4_0^4	0.145	–	0.081	–	–
7.626	6p ($^2A'$) + 4_0^5	–	–	0.065	–	–
7.67(3)(b)	6p ($^2A'$) + 2_0^2 + 3_0^1	–	0.112	–	–	–
7.70(5)(s)	6p ($^2A'$) + 2_0^3	0.144	–	–	–	–
7.73(6)(s,w)	6p ($^2A'$) + 2_0^3 + 5_0^1	–	–	–	0.031	–
7.77(1)(s)	6p ($^2A'$) + 2_0^3 + 5_0^2	–	–	–	0.035	–
7.80(4)(b)	6p ($^2A'$) + 2_0^3 + 5_0^3	–	–	–	0.033	–
7.866	6p ($^2A''$)	–	–	–	–	–
7.98(2)(s)	6p ($^2A''$) + 3_0^1	–	0.116	–	–	–
7.922	5d ($^2A'$)	–	–	–	–	–
7.94(7)(s)	5d ($^2A'$) + 5_0^1	–	–	–	0.025	–

7.98(2)(s)	5d ($^2A'$) + 5_0^2 / 6p ($^2A''$) + 3_0^1 / 6p ($^2A''$) + 4_0^1	–	–	0.060	0.035	–
8.06(5)(s,b)	5d ($^2A'$) + 2_0^1	0.143	–	–	–	–
8.21(2)(w)	5d ($^2A'$) + 2_0^2	0.147	–	–	–	–
8.34(5)(b)	5d ($^2A'$) + 2_0^3	0.133	–	–	–	–
8.498	5d ($^2A'$) + 2_0^4	0.153	–	–	–	–
8.18(0)(b,w)	7s ($^2A'$)	–	–	–	–	–
8.255	7s ($^2A'$) + 4_0^1	–	–	0.075	–	–
8.327	7s ($^2A'$) + 2_0^1	0.147	–	–	–	–
8.46(3)(s)	7s ($^2A'$) + 2_0^2	0.136	–	–	–	–
8.606	7s ($^2A'$) + 2_0^3	0.143	–	–	–	–
8.432	7p ($^2A'$)	–	–	–	–	–
8.544	7p ($^2A'$) + 3_0^1	–	0.112	–	–	–
8.57(8)(s)	7p ($^2A'$) + 2_0^1	0.146	–	–	–	–
8.49(9)(s)	5d ($^2A''$)	–	–	–	–	–
8.65(7)(s)	7d ($^2A''$) + 2_0^1 / 6d ($^2A'$)	0.158	–	–	–	–
8.744	8s ($^2A'$)	–	–	–	–	–
8.756	8s ($^2A'$) + 6_0^1	–	–	–	–	0.012

8.776	8s ($^2A'$) + 5_0^1	–	–	–	0.032	–

[#]The last decimal of the energy is given in brackets for these less resolved features; (b) broad feature; (s) shoulder structure; (w) weak feature.

Table S4. Proposed vibrational assignments in the 8.8−10.8 eV absorption bands of bromoiodomethane, CH_2BrI. Energies in eV.

energy[#]	assignment	ΔE (ν_2')	ΔE (ν_3')	ΔE (ν_4')	ΔE (ν_5')	ΔE (ν_6')
8.90(2)(s)	8p ($^2A'$)	–	–	–	–	–
8.91(5)(s,w)	8p ($^2A'$) + 6_0^1	–	–	–	–	0.013
8.93(2)(s,w)	8p ($^2A'$) + 6_0^2	–	–	–	–	0.017
8.94(1)(s)	8p ($^2A'$) + 5_0^1	–	–	–	0.039	–
8.98(2)(s)	8p ($^2A'$) + 4_0^1 / 8p ($^2A'$) + 5_0^2	–	–	0.080	0.041	–
9.053	8p ($^2A'$) + 2_0^1	0.151	–	–	–	–
9.19(7)(s)	8p ($^2A'$) + 2_0^2	0.144	–	–	–	–
9.01(0)(s,w)	7d ($^2A'$)	–	–	–	–	–
9.08(5)(s)	7d ($^2A'$) + 4_0^1	–	–	0.075	–	–
9.16(8)(b)	7d ($^2A'$) + 2_0^1 / 8p ($^2A'$) + 2_0^1 + 3_0^1	0.158	0.115	–	–	–
9.178	7d ($^2A'$) + 2_0^1 + 6_0^1	–	–	–	–	0.010
9.31(6)(s)	7d ($^2A'$) + 2_0^2	0.148	–	–	–	–
9.471	7d ($^2A'$) + 2_0^3	0.155	–	–	–	–
9.07(1)(s)	9s ($^2A'$)	–	–	–	–	–
9.227	9s ($^2A'$) + 2_0^1	0.156	–	–	–	–
9.374	9s ($^2A'$) + 2_0^2 / 10d ($^2A'$)	0.147	–	–	–	–

9.501	9s ($^2A'$) + 2_0^2 + 3_0^1 / 10d ($^2A'$) + 3_0^1 / 8p ($^2A''$)	–	0.127	–	–	–
9.52(0)(s)	9s ($^2A'$) + 2_0^3 / 10d ($^2A'$) + 2_0^1	0.146	–	–	–	–
9.130	9p ($^2A'$) / 7d ($^2A'$) + 3_0^1	–	0.120	–	–	–
9.271	9p ($^2A'$) + 2_0^1 / 7d ($^2A'$) + 2_0^1 + 3_0^1 / 8p ($^2A'$) + 2_0^1 + 3_0^2	0.141	0.103	–	–	–
9.28(0)(w)	9p ($^2A'$) + 2_0^1 + 6_0^1	–	–	–	–	0.009
9.29(0)(w)	9p ($^2A'$) + 2_0^1 + 6_0^2	–	–	–	–	0.010
9.408	9p ($^2A'$) + 2_0^2	0.137	–	–	–	–
9.52(0)(s)	9p ($^2A'$) + 2_0^2 + 3_0^1	–	0.112	–	–	–
9.23(2)(s,w)	10s ($^2A'$) / 6d ($^2A''$)	–	–	–	–	–
9.359	10s ($^2A'$) + 3_0^1 / 6d ($^2A''$) + 3_0^1 / 8s ($^2A''$)	–	0.127	–	–	–
9.39(7)(s,w)	10s ($^2A'$) + 2_0^1 / 6d ($^2A''$) + 2_0^1	0.165	–	–	–	–
9.471	7d ($^2A'$) + 2_0^3 / 10s ($^2A'$) + 3_0^2 / 6d ($^2A''$) + 3_0^2 / 8s ($^2A''$) + 3_0^1	–	0.112	–	–	–
9.55(6)(w)	10s ($^2A'$) + 2_0^2 / 6d ($^2A''$) + 2_0^2	0.159	–	–	–	–
9.29(3)(w)	9d ($^2A'$)	–	–	–	–	–
9.408	9d ($^2A'$) + 3_0^1	–	0.115	–	–	–
9.442	9d ($^2A'$) + 2_0^1	0.149	–	–	–	–
9.45(5)(w)	9d ($^2A'$) + 2_0^1 + 6_0^1	–	–	–	–	0.013
9.590	9d ($^2A'$) + 2_0^2	0.148	–	–	–	–

9.74(4)(w)	9d ($^2A'$) + 2_0^3 / 11d ($^2A'$) + 2_0^1	0.154	–	–	–	–
9.329	11s ($^2A'$)	–	–	–	–	–
9.359	11s ($^2A'$) + 5_0^1 / 8s ($^2A''$)	–	–	–	0.030	–
9.442	11s ($^2A'$) + 3_0^1 / 9d ($^2A'$) + 2_0^1	–	0.113	–	–	–
9.48(3)(s)	11s ($^2A'$) + 2_0^1	0.154	–	–	–	–
9.56(1)(w)	11s ($^2A'$) + 3_0^2 / 7d ($^2A''$)	–	0.119	–	–	–
9.639	11s ($^2A'$) + 2_0^2 / 9s ($^2A''$)	0.156	–	–	–	–
9.65(4)(w)	11s ($^2A'$) + 2_0^2+ 6_0^1 / 9s ($^2A''$) + 6_0^1	–	–	–	–	0.015
9.78(2)(s)	9s ($^2A''$) + 2_0^1	0.143	–	–	–	–
9.920	9s ($^2A''$) + 2_0^2 / 11p ($^2A''$)	0.138	–	–	–	–
10.07(0)(b)	9s ($^2A''$) + 2_0^3 / 11p ($^2A''$) + 2_0^1	0.150	–	–	–	–
9.374	10d ($^2A'$)	–	–	–	–	–
9.48(3)(s)	10d ($^2A'$) + 3_0^1 / 11s ($^2A'$) + 2_0^1	–	0.109	–	–	–
9.53(6)(b)	10d ($^2A'$) + 2_0^1	0.162	–	–	–	–
9.590	10d ($^2A'$) + 3_0^2 / 9d ($^2A'$) + 2_0^2	–	0.107	–	–	–
9.423	11d ($^2A'$)	–	–	–	–	–
9.45(5)(w)	11d ($^2A'$) + 5_0^1	–	–	–	0.032	–
9.501	11d ($^2A'$) + 4_0^1 / 8p ($^2A''$)	–	–	0.078	–	–

9.53(6)(b)	11d ($^2A'$) + 3_0^1 / 10d ($^2A'$) + 2_0^1	–	0.113	–	–	–
9.590	11d ($^2A'$) + 2_0^1 / 9d ($^2A'$) + 2_0^2	0.167	–	–	–	–
9.60(5)(w)	11d ($^2A'$) + 2_0^1 + 6_0^1	–	–	–	–	0.015
9.65(3)(w)	11d ($^2A'$) + 3_0^2	–	0.117	–	–	–
9.691	9p ($^2A''$)	–	–	–	–	–
9.73(2)(b)	9p ($^2A''$) + 5_0^1	–	–	–	0.041	–
9.808	9p ($^2A''$) + 3_0^1	–	0.117	–	–	–
9.830	9p ($^2A''$) + 2_0^1	0.139	–	–	–	–
9.920	9p ($^2A''$) + 3_0^2 / 9s ($^2A''$) + 2_0^2 / 11p ($^2A''$)	–	0.112	–	–	–
9.970	9p ($^2A''$) + 2_0^2	0.140	–	–	–	–
10.037	9p ($^2A''$) + 3_0^3 / 11s ($^2A''$) + 2_0^1	–	0.117	–	–	–
10.105	9p ($^2A''$) + 2_0^3	0.135	–	–	–	–
9.769	8d ($^2A''$)	–	–	–	–	–
9.793	8d ($^2A''$) + 5_0^1	–	–	–	0.024	–
9.874	8d ($^2A''$) + 3_0^1	–	0.105	–	–	–
9.831	8d ($^2A''$) + 5_0^2 / 10p ($^2A''$)	–	–	–	0.038	
9.831	10p ($^2A''$)	–	–	–	–	–
9.844	10p ($^2A''$) + 6_0^1	–	–	–	–	0.013

9.894	10p ($^2A''$) + 4_0^1	–	–	0.063	–	–
9.938	10p ($^2A''$) + 3_0^1	–	0.107	–	–	–
9.970	10p ($^2A''$) + 4_0^2 / 9p ($^2A''$) + 2_0^2	–	–	0.076		
9.894	11s ($^2A''$)	–	–	–	–	–
10.037	11s ($^2A''$) + 2_0^1	0.143	–	–	–	–
10.17(8)(s)	11s ($^2A''$) + 2_0^2	0.141	–	–	–	–
9.956	12s ($^2A''$)	–	–	–	–	–
10.06(6)(b)	12s ($^2A''$) + 3_0^1	–	0.110	–	–	–
10.17(8)(s)	12s ($^2A''$) + 3_0^2 / 11s ($^2A''$) + 2_0^2 + 3_0^1	–	0.112	–	–	–
9.97(1)(s)	12p ($^2A''$)	–	–	–	–	–
10.118	12p ($^2A''$) + 2_0^1	0.147	–	–	–	–

[#]The last decimal of the energy is given in brackets for these less resolved features; (b) broad feature; (s) shoulder structure; (w) weak feature.

Table S5. Calculated vertical excitation energies (present calculations; see main text) and transition moments of CH_2BrI compared with experimental data. See text for details.

state	E (a.u.)	E-E_0 (a.u.)	E-E_0 (cm^{-1})	E-E_1 (a.u.)	E-E_1 (cm^{-1})	E-E_1 (eV)	mdz	E (eV)[4]	E (eV) expt.	Cross-section (Mb)
$\tilde{X}$ A′	-749.66499241	-0.00133519	-293.04	0.00000000	0.00	0.0000	0.048296			
2 A′	-749.51310869	0.15054854	33041.58	0.15188372	33334.62	4.1330	-0.002323			
3 A′	-749.50625581	0.15740142	34545.62	0.15873661	34838.66	4.3194	-0.084574			
4 A′	-749.49208682	0.17157041	37655.35	0.17290559	37948.39	4.7050	-0.050217			
5 A′	-749.48373766	0.17991957	39487.78	0.18125476	39780.82	4.9322	-0.225248			
6 A′	-749.46765264	0.19600459	43018.04	0.19733978	43311.07	5.3699	0.113071			
7 A′	-749.46038075	0.20327647	44614.03	0.20461166	44907.07	5.5678	-0.084537			
8 A′	-749.45770321	0.20595402	45201.68	0.20728921	45494.72	5.6406	-0.022001			
9 A′	-749.43997305	0.22368418	49093.00	0.22501937	49386.04	6.1231	0.441189		5.837	6.4
10 A′	-749.43030826	0.23334897	51214.18	0.23468416	51507.22	6.3861	0.053209			
11 A′	-749.40906841	0.25458882	55875.79	0.25592401	56168.83	6.9640	-0.089582			
12 A′	-749.40738477	0.25627245	56245.30	0.25760764	56538.34	7.0099	-0.022801			
13 A′	-749.39591538	0.26774185	58762.54	0.26907703	59055.58	7.3220	0.261517	6.685	6.529	28.2
14 A′	-749.39212539	0.27153184	59594.35	0.27286703	59887.39	7.4251	-0.021596			
15 A′	-749.38677202	0.27688521	60769.28	0.27822039	61062.32	7.5708	-0.095617			
16 A′	-749.38501918	0.27863805	61153.98	0.27997324	61447.02	7.6185	0.109960			
17 A′	-749.36948917	0.29416806	64562.43	0.29550324	64855.47	8.0411	0.553953		7.488	37.2
18 A′	-749.36521189	0.29844534	65501.18	0.29978052	65794.22	8.1574	-0.297283			

Table S6. Energy value (eV), and effective quantum number (n*) of the Rydberg series converging to the ionic electronic ground ($^2A'$) and first excited ($^2A''$) states of bromoiodomethane, CH_2BrI[a].

vertical energy	n*	assignment	vertical energy	n*	assignment	vertical energy	n*	assignment
IE_1 = (9.5944±0.0006) eV[b]								
6.529	2.11	6s ($^2A'$)	7.27(4)(b)	2.42	6p ($^2A'$)	7.922	2.85	5d ($^2A'$)
8.18(0)(b,w)	3.10	7s ($^2A'$)	8.432	3.42	7p ($^2A'$)	8.65(7)(s)	3.81	6d ($^2A'$)
8.744	4.00	8s ($^2A'$)	8.90(2)(s)	4.43	8p ($^2A'$)	9.01(0)(s,w)	4.83	7d ($^2A'$)
9.07(1)(s)	5.07	9s ($^2A'$)	9.130	5.41	9p ($^2A'$)	–	–	–
9.23(2)(s,w)	6.12	10s ($^2A'$)	–	–	–	9.29(3)(w)	6.72	9d ($^2A'$)
9.329	7.16	11s ($^2A'$)	–	–	–	9.374	7.86	10d ($^2A'$)
–	–	–	–	–	–	9.423	8.91	11d ($^2A'$)
IE_2 = (10.1644±0.0006) eV[c]								
6.913	2.05	6s ($^2A''$)	7.866	2.43	6p ($^2A''$)	8.49(9)(s)	2.86	5d ($^2A''$)
8.699	3.05	7s ($^2A''$)	9.03(6)(s)	3.47	7p ($^2A''$)	9.23(2)(s,w)	3.82	6d ($^2A''$)
9.359	4.11	8s ($^2A''$)	9.501	4.53	8p ($^2A''$)	9.56(1)(w)	4.75	7d ($^2A''$)
9.639	5.09	9s ($^2A''$)	9.691	5.36	9p ($^2A''$)	9.769	5.87	8d ($^2A''$)
9.793	6.05	10s ($^2A''$)	9.831	6.39	10p ($^2A''$)	–	–	–
9.894	7.09	11s ($^2A''$)	9.920	7.46	11p ($^2A''$)	–	–	–
9.956	8.08	12s ($^2A''$)	9.97(1)(s)	8.39	12p ($^2A''$)	–	–	–

[a] (b) broad feature; (w) weak feature; (s) shoulder structure (the last decimal of the energy value is given in brackets for these less-resolved features); [b] adiabatic value from Ref.[1]; [c] value from Ref.[10] (see text for details).

References

(1) Lee, M.; Kim, H.; Lee, Y. S.; Kim, M. S. One-Photon Mass-Analyzed Threshold Ionization Spectroscopy of CH_2BrI: Extensive Bending Progression, Reduced Steric Effect, and Spin-Orbit Effect in the Cation. *J. Chem. Phys.* **2005**, *123*, 024310. https://doi.org/10.1063/1.1954770.

(2) Man, S. Q.; Kwok, W. M.; Lee Phillips, D.; Johnson, A. E. Short-Time Photodissociation Dynamics of A-Band and B-Band Bromoiodomethane in Solution: An Examination of Bond Selective Electronic Excitation. *J. Chem. Phys.* **1996**, *105*, 5842–5857. https://doi.org/10.1063/1.472426.

(3) Penner, A.; Amirav, A. Rydberg State Absorption Spectroscopy of $Br(CH_2)_NI$ (N=1-3). *J. Chem. Phys.* **1990**, *93*, 8576–8579. https://doi.org/10.1063/1.459243.

(4) Liu, K.; Zhao, H.; Wang, C.; Zhang, A.; Ma, S.; Li, Z. A Theoretical Study of Bond Selective Photochemistry in CH_2BrI. *J. Chem. Phys.* **2005**, *122*, 044310. https://doi.org/10.1063/1.1835955.

(5) Liu, Y. J.; Ajitha, D.; Krogh, J. W.; Tarnovsky, A. N.; Lindh, R. Spin-Orbit *Ab Initio* Investigation of the Photolysis of Bromoiodomethane. *ChemPhysChem* **2006**, *7*, 955–963. https://doi.org/10.1002/cphc.200500654.

(6) Man, S. Q.; Kwok, W. M.; Phillips, D. L. Investigation of Bond-Selective Electronic Excitation in Bromoiodomethane. *J. Phys. Chem.* **1995**, *99*, 15705–15708. https://doi.org/10.1021/j100043a002.

(7) Mössinger, J. C.; Shallcross, D. E.; Cox, R. A. UV–VIS Absorption Cross-Sections and Atmospheric Lifetimes of CH_2Br_2,CH_2I_2 and CH_2BrI. *J. Chem. Soc., Faraday Trans.* **1998**, *94*, 1391–1396.

(8) Zheng, X.; Phillips, D. L. Photoisomerization Reaction of CH_2BrI Following *A*-Band and *B*-Band Photoexcitation in the Solution Phase: Transient Resonance Raman Observation of the Iso-CH_2I–Br Photoproduct. *J. Chem. Phys.* **2000**, *113*, 3194–3203. https://doi.org/10.1063/1.1286920.

(9) Lago, A. F.; Kercher, J. P.; Bödi, A.; Sztáray, B.; Miller, B.; Wurzelmann, D.; Baer, T. Dissociative Photoionization and Thermochemistry of Dihalomethane Compounds Studied by Threshold Photoelectron Photoion Coincidence Spectroscopy. *J. Phys. Chem. A* **2005**, *109*, 1802–1809. https://doi.org/10.1021/jp045337s.

(10) Sándor, P.; Zhao, A.; Rozgonyi, T.; Weinacht, T. Strong Field Molecular Ionization to Multiple Ionic States: Direct versus Indirect Pathways. *J. Phys. B At. Mol. Opt. Phys.* **2014**, *47*, 124021. https://doi.org/10.1088/0953-4075/47/12/124021.

(11) Kim, H.; Park, Y. C.; Lee, Y. S. Spin-Orbit Effects on the Structure of Haloiodomethane Cations CH_2XI^+ (X=F, Cl, Br, and I). *Bull. Korean Chem. Soc.* **2014**, *35*, 775–782. https://doi.org/10.5012/bkcs.2014.35.3.775.

Chapter 5 General Conclusions

In this PhD Thesis, the photodissociation dynamics of methylamine (CH_3NH_2) and the photodissociation dynamics and stereodynamics (atomic photofragment alignment) of several alkyl iodides (linear and ramified RI, R=C_nH_{2n+1}, n=1-4) and the dihalocarbon CH_2BrI, have been studied by performing velocity map imaging and slice imaging experiments together with resonance enhanced multiphoton ionization detection of atomic and molecular photofragments using nanosecond pump-probe laser pulses. In addition, high level *ab initio* calculations of potential energy curves of the ground and electronically excited states of the title molecules have been carried out to disentangle the experimental results and associated mechanisms.

In the case of the **photodissociation dynamics of methylamine (CH_3NH_2)** excited to the blue-edge of the first absorption band, the main conclusions are the following:

- The photodissociation dynamics of methylamine (CH_3NH_2) focusing on the **H-atom elimination channel** reveals complex pathways influenced by the excitation wavelengths employed. The study identifies three distinct reaction pathways: direct dissociation through the $\tilde{A}$ state to form $CH_2NH(\tilde{X})$, dissociation after passage through a conical intersection (CI) resulting in dissociation in the ground state, and a newly observed threshold dissociation leading to $CH_2NH(\tilde{A})$. High-level *ab initio* calculations and experimental results demonstrate that N–H bond cleavage is predominant, facilitated by an initial structural change in the NH_2 group. The branching ratios and anisotropy parameters suggest that at the shortest excitation wavelengths ($\lambda \leq 210$ nm), the molecule acquires sufficient translational energy to enhance prompt dissociation through the CI. In contrast, longer excitation wavelengths ($\lambda \geq 210$ nm) result in a higher probability of the molecule to being trapped in the upper cone of the CI, leading to a slower statistical dissociation process. These findings provide a comprehensive understanding of the energy-dependent photodissociation pathways in methylamine to produce H-atoms, highlighting the critical role of the CI and the excitation energy in determining the reaction dynamics.

- The photodissociation dynamics of CH_3NH_2 leading to the **C–N bond cleavage** have been thoroughly investigated upon photoexcitation in the 198–204 nm range. This study reveals two primary dissociation mechanisms: a minor prompt dissociation channel through a conical intersection (CI), resulting in $NH_2(\tilde{A}) + CH_3(\tilde{X})$, and a major slow dissociation mechanism, leading to $NH_2(\tilde{X})+CH_3(\tilde{X})$, characterized by Boltzmann-type translational energy distributions. The anisotropy analysis supports the presence of both direct dissociation and statistical dissociation pathways. High-level ab initio calculations confirm the presence of an energy barrier and a CI along the C–N coordinate, consistent with the experimental results. These findings provide a comprehensive understanding of the C–N bond photodissociation pathways in CH_3NH_2, highlighting the critical role of molecular geometry changes and the CI in the reaction dynamics. Future investigations involving on-the-fly trajectory calculations would further elucidate the proposed mechanisms and their contributions to the overall photodissociation process.

- The photodissociation of methylamine in the blue edge of the A-band via the **NH + CH_4 channel** is dominated by roaming-mediated processes, where hydrogen migration plays a critical role prior to C–N bond cleavage. Detailed analysis shows that the translational energy distributions (TEDs) exhibit low kinetic energy release, indicating significant retention of energy in the internal degrees of freedom of the NH and CH_4 fragments. The angular distributions of the fragments suggest partial isotropy, consistent with a roaming dissociation mechanism involving extended molecular rotation and slower dynamics compared to direct dissociation pathways. Furthermore, the NH radicals are predominantly formed in specific low rotational quantum states, highlighting a constrained energy partitioning during the dissociation process. These findings provide detailed insights into the mechanisms driving the NH + CH_4 channel, emphasizing the importance of roaming dynamics and energy redistribution in the overall photodissociation dynamics of methylamine

In the case of the **photodissociation dynamics and atomic photofragment alignment of the family of alkyl iodides (RI, R=C_nH_{2n+1}, n=1-4) and the dihalocarbon CH_2BrI**, the main conclusions are the following:

- The **photodissociation dynamics** of **alkyl iodides** in the A-band have been studied by measuring the impact of molecular structure on the energy disposal and the **atomic photofragment alignment**. By employing slice imaging and resonance-enhanced multiphoton ionization, the dissociation of several linear and branched alkyl iodides at 254 and 268 nm was analyzed. The results reveal that linear structures couple more efficiently with the C-I reaction coordinate, resulting in higher translational energy distributions, while branched structures demonstrate a significant coupling with additional vibrational modes, indicating a multidimensional dissociation process. Furthermore, the presence of conical intersections or avoided crossings play a crucial role in the non-adiabatic dynamics, with smaller linear alkyl iodides, such as CH_3I and C_2H_5I, exhibiting substantial rotational alignment, whereas larger and branched alkyl iodides display varied alignment parameters. The findings highlight the importance of molecular structure in determining the photodissociation pathways and energy distributions, contributing valuable insights into the stereodynamics of alkyl iodides.

- The study on the **photodissociation dynamics and atomic fragment alignment of CH_2BrI** at 193 nm reveals complex dissociation pathways influenced by molecular geometry and excitation wavelength. Using slice imaging and resonance-enhanced multiphoton ionization, the experimental results demonstrate three distinct dynamical regions corresponding to different dissociation mechanisms: a slow-recoil statistical decay, a prompt C-X bond cleavage, and a high kinetic energy pathway. High-level *ab initio* calculations support the experimental findings, indicating that the C-I and C-Br bond cleavages occur through different electronic states and potential energy curves. The observed photofragment polarization and alignment parameters show the angular momentum constraints along the recoil direction, highlighting the role of conical intersections and internal conversion processes in the dissociation dynamics. This investigation improves our understanding of the stereodynamics and energy partitioning in the photodissociation of dihalocarbons, providing valuable

insights into their atmospheric reactivity and the fundamental processes governing their photochemistry.

References

[1] R. Schinke, *Photodissociation Dynamics*. Cambridge University Press, Cambridge, 1993.

[2] H. H. Telle, A. G. Ureña, and R. J. Donovan, *Laser Chemistry: Spectroscopy, Dynamics and Applications*. John Wiley & Sons, Chichester, 2007.

[3] J. Durá Díez, *Fotodisociación en tiempo real de moléculas y agregados con pulsos láser de femtosegundos y técnicas de imágenes de iones*, Tesis Doctoral, Universidad Complutense de Madrid, Madrid, 2009.

[4] R. D. Levine, R. B. Bernstein, and Y. T. Lee, *Molecular Reaction Dynamics and Chemical Reactivity*, Phys. Today, **41**, 90–92 (1988).

[5] R. D. Levine, *Molecular Reaction Dynamics*. Cambridge University Press, Cambridge, 2005.

[6] J. W. Hudgens, T. G. DiGiuseppe, and M. C. Lin, *Two photon resonance enhanced multiphoton ionization spectroscopy and state assignments of the methyl radical*, J. Chem. Phys., **79**, 571–582 (1983).

[7] R. N. Dixon, *The determination of the vector correlation between photofragment rotational and translational motions from the analysis of Doppler-broadened spectral line profiles*, J. Chem. Phys., **85**, 1866–1879 (1986).

[8] R. N. Zare and D. R. Herschbach, *Doppler line shape of atomic fluorescence excited by molecular photodissociation*, Proceedings of the IEEE, **51**, 173–182 (1963).

[9] R. Schmiedl, H. Dugan, W. Meier, and K. H. Welge, *Laser Doppler spectroscopy of atomic hydrogen in the photodissociation of HI*, Zeit. Phys. A, **304**, 137–142 (1982).

[10] R. N. Zare*, Angular Momentum. Understanding Spatial Aspects in Chemistry and Physics*, Wiley-Interscience, New Jersey, 1989.

[11] R. N. Zare, *Photoejection dynamics*, Mol. Photochem., **4**, 1–37 (1972).

[12] T. P. Rakitzis, *Direct measurement of photofragment alignment from unnormalized Abel-invertible images*, Chem. Phys. Lett., **342**, 121–126 (2001).

[13] T. P. Rakitzis and R. N. Zare, *Photofragment angular momentum distributions in the molecular frame: Determination and interpretation*, J. Chem. Phys., **110**, 3341–3350 (1999).

[14] T. P. Rakitzis, P. C. Samartzis, and T. N. Kitsopoulos, *Complete Measurement of $S(^1D_2)$ Photofragment Alignment from Abel-Invertible Ion Images*, Phys. Rev. Lett., **87**, 123001 (2001).

[15] T. P. Rakitzis, P. C. Samartzis, R. L. Toomes, L. Tsigaridas, M. Coriou, D. Chestakov, A. T. J. B. Eppink, D. H. Parker, T. N. Kitsopoulos, *Photofragment alignment from the photodissociation of HCl and HBr*, Chem. Phys. Lett., **364**, 115–120 (2002).

[16] T. P. Rakitzis and T. N. Kitsopoulos, *Measurement of Cl and Br photofragment alignment using slice imaging*, J. Chem. Phys., **116**, 9228–9231 (2002).

[17] Sirah Lasertechnik, *Pulsed Dye Laser's Manual,* Version 2.0.4

[18] J. L. Kinsey, *Fourier transform Doppler spectroscopy: A new means of obtaining velocity-angle distributions in scattering experiments*, J. Chem. Phys., **66**, 2560–2565 (1976).

[19] D. W. Chandler and P. L. Houston, *Two-dimensional imaging of state-selected photodissociation products detected by multiphoton ionization*, J. Chem. Phys., **87**, 1445–1447 (1987).

[20] D. W. Chandler and P. L. Houston, *Two-dimensional imaging of state-selected photodissociation products detected by multiphoton ionization*, J. Chem. Phys., **87**, 1445–1447 (1987).

[21] A. T. J. B. Eppink and D. H. Parker, *Methyl iodide A-band decomposition study by photofragment velocity imaging*, J. Chem. Phys., **109**, 4758–4767 (1998).

[22] W. C. Wiley and I. H. McLaren, *Time-of-flight mass spectrometer with improved resolution*, Rev. Sci. Inst., **26**, 1150–1157 (1955).

[23] D. W. Chandler, J. W. Thoman Jr., M. H. M. Janssen, and D. H. Parker, *Photofragment imaging: The 266 nm photodissociation of CH_3I*, Chem. Phys. Lett., **156**, 1445–1447 (1989).

[24] A. G. Suits, L. S. Bontuyan, P. L. Houston, and B. J. Whitaker, *Differential cross sections for state-selected products by direct imaging: Ar+NO*, J. Chem. Phys., **96**, 8618–8620 (1992).

[25] D. P. Baldwin, M. A. Buntine, and D. W. Chandler, *Photodissociation of acetylene: Determination of D_0^0(HCC-H) by photofragment imaging*, J. Chem. Phys., **93**, 6578–6584 (1990).

[26] A. T. J. B. Eppink and D. H. Parker, *Velocity map imaging of ions and electrons using electrostatic lenses: Application in photoelectron and photofragment ion imaging of molecular oxygen*, Rev. Sci. Inst., **68**, 3477–3484 (1997).

[27] D. W. Chandler, M. H. M. Janssen, S. Stolte, R. N. Strickland, J. W. Thoman, and D. H. Parker, *Photofragment imaging: the 266-nm photolysis of CD_3I*, J. Phys. Chem., **94**, 4839–4846 (1990).

[28] M. A. Buntine, D. P. Baldwin, and D. W. Chandler, *Photodissociation dynamics of doubly excited Rydberg states of molecular hydrogen*, J. Chem. Phys., **96**, 5843–5856 (1992).

[29] T. N. Kitsopoulos, M. A. Buntine, D. P. Baldwin, R. N. Zare, and D. W. Chandler, *Reaction Product Imaging: The H + D_2 Reaction*, Science, **260**, 1605–1610 (1993).

[30] S. Deshmukh, J. D. Myers, S. S. Xantheas, and W. P. Hess, *Investigation of acetyl chloride photodissociation by photofragment imaging*, J. Phys. Chem., **98**, 12535–12544 (1994).

[31] C. Sparling and D. Townsend, *Tomographic reconstruction techniques optimized for velocity-map imaging applications*, J. Chem. Phys., **157**, 114201 (2022).

[32] V. Ferrari, R. Sousa, M. Pereira, J. P. L. de Carvalho, J. N. Amaral, J. Moreira, G. Araujo, *Advancing Direct Convolution Using Convolution Slicing Optimization and ISA Extensions*, ACM Trans. Arch. Code Opt., **20**, 1–26 (2023).

[33] V. Dribinski, A. Ossadtchi, V. A. Mandelshtam, and H. Reisler, *Reconstruction of Abel-transformable images: The Gaussian basis-set expansion Abel transform method*, Rev. Sci. Inst., **73**, 2634–2642 (2002).

[34] L. M. Smith, D. R. Keefer, and S. I. Sudharsanan, *Abel inversion using transform techniques*, J. Quant. Spectrosc. Radiat. Transf., **39**, 367–373 (1988).

[35] C. Sparling, D. Rajak, V. Blanchet, Y. Mairesse, and D. Townsend, *Fourier–Hankel–Abel Nyquist-limited tomography: A spherical harmonic basis function approach to tomographic velocity-map image reconstruction*, Rev. Sci. Inst., **95**, 053301 (2024).

[36] V. Dribinski, A. Ossadtchi, V. A. Mandelshtam, and H. Reisler, *Reconstruction of Abel-transformable images: The Gaussian basis-set expansion Abel transform method*, Rev. Sci. Inst., **73**, 2634–2642 (2002).

[37] A. N. Tikhonov, *Solution of incorrectly formulated problems and the regularization method*, Dokl. Akad. Nauk. USSR, **151**, 1035-1038 (1963).

[38] G. A. Garcia, L. Nahon, and I. Powis, *Two-dimensional charged particle image inversion using a polar basis function expansion*, Rev. Sci. Inst., **75**, 4989–4996 (2004).

[39] C. R. Gebhardt, T. P. Rakitzis, P. C. Samartzis, V. Ladopoulos, and T. N. Kitsopoulos, *Slice imaging: A new approach to ion imaging and velocity mapping*, Rev. Sci. Inst., **72**, 3848–3853 (2001).

[40] D. Townsend, M. P. Minitti, and A. G. Suits, *Direct current slice imaging*, Rev. Sci. Inst., **74**, 2530–2539 (2003).

[41] J. J. Lin, J. Zhou, W. Shiu, and K. Liu, *Application of time-sliced ion velocity imaging to crossed molecular beam experiments*, Rev. Sci. Inst., **74**, 2495–2500 (2003).

[42] M. N. R. Ashfold, N. H. Nahler, A. J. Orr-Ewing, O. P. J. Vieuxmaire, R. L. Toomes, T. N. Kitsopoulos, I. A. Garcia, D. A. Chestakov, S.-M. Wu, D. H Parker, *Imaging the dynamics of gas phase reactions*, Phys. Chem. Chem. Phys., **8**, 26–53 (2006).

[43] K. Tonokura and T. Suzuki, *Slicing photofragment spatial distribution by laser sheet ionization*, Chem. Phys. Lett., **224**, 1–6 (1994).

[44] T. Kinugawa and T. Arikawa, *Three-dimensional velocity analysis combining ion imaging with Doppler spectroscopy: Application to photodissociation of HBr at 243 nm*, J. Chem. Phys., **96**, 4801–4804 (1992).

[45] K. T. Lorenz, D. W. Chandler, J. W. Barr, W. Chen, G. L. Barnes, and J. I. Cline, *Direct measurement of the preferred sense of NO rotation after collision with argon*, Science, **293**, 2063–2066 (2001).

[46] R. Campargue, *Progress in overexpanded supersonic jets and skimmed molecular beams in free-jet zones of silence*, J. Phys. Chem., **88**, 4466–4474 (1984).

[47] V. Papadakis and T. N. Kitsopoulos, *Slice imaging and velocity mapping using a single field*, Rev. Sci. Inst., **77**, 083101 (2006).

[48] L. Rubio-Lago, A. García-Vela, A. Arregui, G. A. Amaral, and L. Bañares, *The photodissociation of CH_3I in the red edge of the A-band: Comparison between slice*

imaging experiments and multisurface wave packet calculations, J. Chem. Phys., **131**, 174309 (2009).

[49] M. G. González, J. D. Rodríguez, L. Rubio-Lago, A. García-Vela, and L. Bañares, *Slice imaging and wave packet study of the photodissociation of CH_3I in the blue edge of the A-band: Evidence of reverse $^3Q_0 \leftarrow {}^1Q_1$ non-adiabatic dynamics*, Phys. Chem. Chem. Phys., **13**, 16404–16415 (2011).

[50] M. G. González, J. D. Rodríguez, L. Rubio-Lago, and L. Bañares, *Imaging the stereodynamics of methyl iodide photodissociation in the second absorption band: fragment polarization and the interplay between direct and predissociation*, Phys. Chem. Chem. Phys., **16**, 26330–26341 (2014).

[51] S.P. Sander, J. P. D. Abbatt, J. R. Barker, J. B. Burkholder, R.R. Friedl, D.M. Golden, R. E. Huie, M. J. Kurylo, G. K. Mortgat, V. L. Orkin, P. H. Wine, *Chemical kinetics and photochemical data for use in atmospheric studies*, Evaluation number 18, JPL Publication No 15-10, Pasadena, California (2011)

[52] J. V. Michael and W. A. Noyes, *The Photochemistry of Methylamine*, J. Am. Chem. Soc., **85**, 1228–1233 (1963).

[53] P. Recio, J. Cachón, A. Zanchet, S. Marggi Poullain, and L. Bañares, *Photodissociation dynamics of methylamine in the blue edge of the A-band. I. The H-atom elimination channel*, J. Chem. Phys., **158**, 234304 (2023).

[54] J. Cachón, P. Recio, A. Zanchet, S. Marggi Poullain, and L. Bañares, *Photodissociation dynamics of methylamine in the blue edge of the A-band. II. The NH_2 + CH_3 channel*, J. Chem. Phys., **159**, 064302 (2023).

[55] L. Rubio-Lago, A. García-Vela, A. Arregui, G. A. Amaral, and L. Bañares, *The photodissociation of CH_3I in the red edge of the A-band: Comparison between slice imaging experiments and multisurface wave packet calculations*, J. Chem. Phys., **131**, 174309 (2009).

[56] H.-J. Werner and P. J. Knowles, *A second order multiconfiguration SCF procedure with optimum convergence*, J. Chem. Phys., **82**, 5053–5063 (1985).

[57] S. G. Clement, M. N. R. Ashfold, C. M. Western, R. D. Johnson, and J. W. Hudgens, *Triplet Rydberg states of the imidogen radical characterized via two-photon resonance-enhanced multiphoton ionization spectroscopy*, J. Chem. Phys., **97**, 7064–7072 (1992).

[58] J. O. Thomas, K. E. Lower, and C. Murray, *Formation of Vibrationally Excited Methyl Radicals Following State-Specific Excitation of Methylamine*, J. Phys. Chem. A, **118**, 9844–9852 (2014).

[59] A. Zanchet, O. Roncero, E. Karabulut, N. Solem, C. Romanzin, R. Thissen, C. Alcaraz*, The role of intersystem crossing in the reactive collision of $S^+(^4S)$ with H_2*, J. Chem. Phys., **161**, 044302 (2024).

[60] J. O. Thomas, K. E. Lower, and C. Murray, *Observation of NH $X^3\Sigma^-$ as a Primary Product of Methylamine Photodissociation: Evidence of Roaming-Mediated Intersystem Crossing?*, J. Phys. Chem. Lett., **3**, 1341–1345 (2012).